Department of Physics
University College London
University of London

Scanning Tunnelling Microscopy of Bilayer Manganites

Benjamin E. M. Bryant

Submitted in partial fulfilment of the requirements
for the degree of Doctor of Philosophy
at University College London

September 14, 2009

I, Benjamin Earl Maurice Bryant, confirm that the work presented in this thesis is my own. Where information has been derived from other sources, I confirm that this has been indicated in the thesis.

Abstract

This thesis describes experimental work carried out on bilayer manganites with the general composition $R_{2-2x}A_{1+2x}Mn_2O_7$, where R is a trivalent rare earth cation and A is a divalent alkaline-earth cation. Experiments have been carried out primarily using Scanning Tunnelling Microscopy (STM) and Spectroscopy (STS); bulk electrical transport, MPMS and LEED measurements have also been made.

The primary results are obtained from single crystal samples of $PrSr_2Mn_2O_7$. This compound provides a surface suitable for STM study when cleaved at low temperature in ultra-high vacuum: atomic resolution can be readily achieved. The expected square lattice is observed, together with a larger scale surface modulation which is not presently explained. In some areas of the $PrSr_2Mn_2O_7$ surface a population of adatoms and surface vacancies is observed. STS data indicate that adatoms carry a negative charge compared to the rest of the surface, and vacancies a positive charge: the adatoms and vacancies are interpreted as oxygen adatoms and oxygen vacancies. A detailed study is made of the oxygen adatoms and vacancies: this is believed to be the first such study made on a manganite surface. Oxygen adatoms on the $PrSr_2Mn_2O_7$ surface are found to be mobile: hopping and adatom-vacancy recombination are observed.

Additional results are reported on the layered manganite compound $La_{2-2x}Sr_{1+2x}Mn_2O_7$ at a range of cation doping x. For the $LaSr_2Mn_2O_7$ compound (x = 0.5) spectroscopic variation has been identified in a variable-temperature STS survey. This indicates the coexistence of two surface electronic phases, possibly the charge ordered and antiferromagnetic phases.

Acknowledgements

I would like to thank Christoph Renner and Gabriel Aeppli, for their patient supervision and inspirational guidance. Thankyou to everybody who helped me with the experiments, particularly Charles Bird, Katsuya Iwaya, Mark Ellerby, Marc Warner and Silvia de Santis. Thanks to the STM lab team at the London Centre for Nanotechnology, Cyrus Hirjibehedin, Neil Curson, Steven Schofield and Philipp Studer. Thanks to Matthias Fenner at Omicron for setting up the Cryogenic STM, and to Steffen Wirth for invaluable tips on how to get it to work.

Thankyou to my parents, Richard Bryant and Carolyn Heighway, for making it possible for me to study at UCL.

Finally the greatest thanks are due to Martina Avellino, for supporting me and putting up with me during the course of this work. PhD study can be a lonely road, but we walked it together.

Contents

Chapter 1

The Physics of Manganites

1.1 Introduction to Manganites

Manganese oxides, or manganites, have been the subject of a great deal of experimental and theoretical work, due to their remarkable properties such as colossal magnetoresistance and phase separation [12,29,56]. Manganites adopt a perovskite or layered perovskite crystal structure, and have the general formula $R_{n-nx}A_{1+nx}Mn_nO_{3n+1}$, where R is a trivalent rare earth cation and A is a divalent alkaline-earth cation. The fundamental "building block" of these manganites is the perovskite unit cell as shown in figure 1.1a: this consists of a cube with R or A ions at the vertices, a Mn ion at the body centre, and oxygen ions at the face centres. The Mn ion is thus surrounded by an oxygen octahedron. The three dimensional perovskite structure $R_{1-x}A_xMnO_3$ is formed at $n = \infty$: layered compounds are formed by inserting an additional rock-salt-type layer $(R_{1-x}A_x)_2O_2$ between every n^{th} MnO_2 sheet [32]. The bilayer compound $R_{2-2x}A_{1+2x}Mn_2O_7$ is formed at n = 2: figure 1.1 shows the structure of the n = 2 and $n = \infty$ compounds. The convention adopted for labelling the crystal directions is indicated. In layered compounds the c-axis is perpendicular to the layers, and the a and b axes are parallel to the layers. The various compounds are commonly defined by their relative (R,A), Mn and O content, so the cubic perovskite structure is referred to as 113 and the bilayer is 327. The rare earth and alkaline earth ions are referred to as occupying the A sites in the crystal, whilst the manganese ion sites are the B sites.

Structural phase transitions to lower symmetry states can occur in manganites. The basic perovskite structure is cubic, but the Jahn-Teller effect (see section 1.3) and also the mismatch between ionic radii may cause the crystal to undergo an orthorhombic distortion, whereby the oxygen octahedra tilt with respect to one another. Figure 1.2 shows the distortion caused by the Jahn-teller effect in $LaMnO_3$. The (100) plane of undistorted cubic $LaMnO_3$ is shown in figure 1.2a, and the (101) plane of orthorhombic $LaMnO_3$ is shown in figure 1.2b.

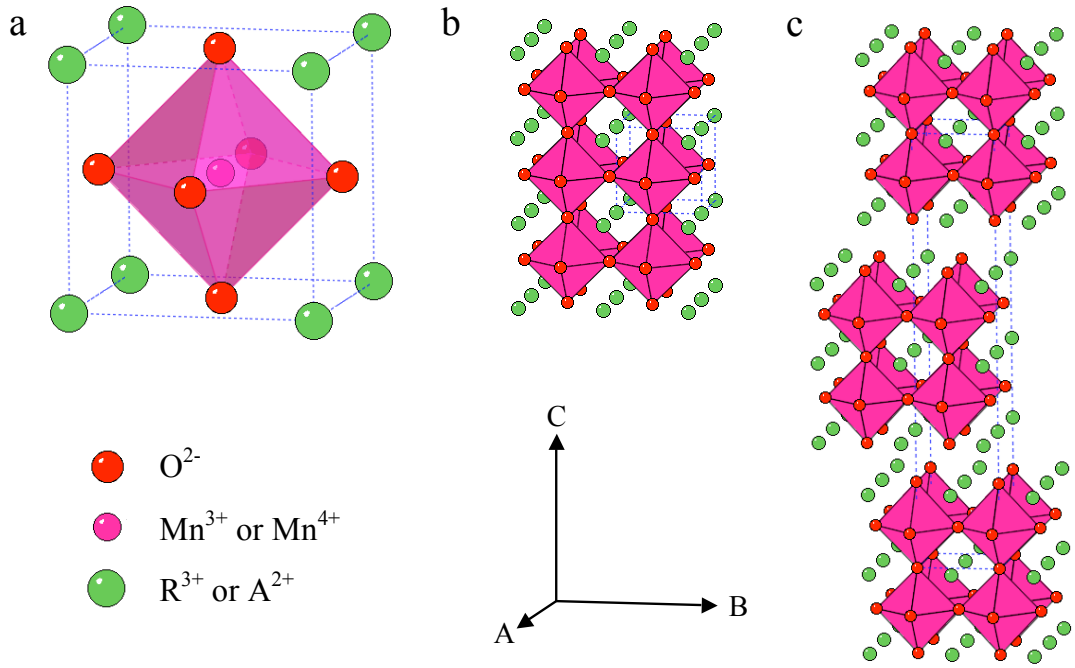

Figure 1.1: Crystal structure of $R_{n-nx}A_{1+nx}Mn_nO_{3n+1}$. (a) cubic perovskite unit cell (b) cubic ($n = \infty$) structure (c) n = 2 bilayer structure. Unit cells are shown as dotted lines. The convention adopted for labelling crystal directions is shown: the c-axis is perpendicular to the layers, and the a and b axes are parallel to the layers.

1.2 Cation Doping and Electron Bandwidth

The cation doping x is critical for determining the properties of manganites. As x is increased, Mn^{3+} is progressively replaced by Mn^{4+}. At x = 0 and x = 1, Mn is only present in a single valence state and super-exchange via oxygen sites causes the material to become an antiferromagnetic insulator (AFI). At some intermediate doping levels ($0 < x < 1$), due to the mixed manganese valency (Mn^{3+} and Mn^{4+} are both present in the material) double exchange may dominate. In this case the ground state of the manganite is a ferromagnetic metal (FM) [7]. Above the Curie or Néel temperature, all compounds revert to a paramagnetic insulating (PI) state. In addition to these states, a charge ordered state is often observed at $x \geq 0.5$. This state is thought to comprise spatial segregation of Mn^{4+} and Mn^{3+} ions. The charge ordered (CO) state may also exhibit orbital and spin order: the charge, spin and orbitally ordered state is referred to as the CE state [21]. The charge ordered state competes strongly with the metallic state [13].

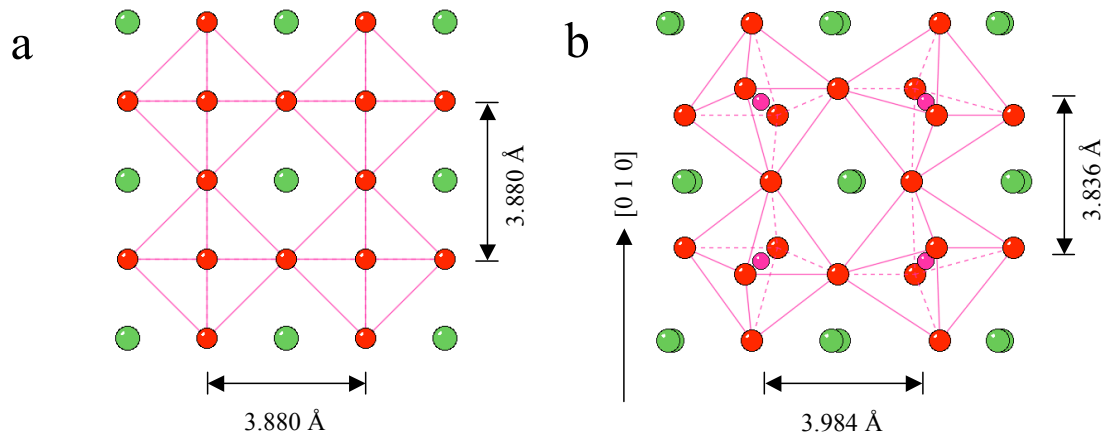

Figure 1.2: (a) (100) plane of cubic $LaMnO_3$ without Jahn-Teller distortion (b) orthorhombically distorted structure of $LaMnO_3$: the (101) plane is shown. La is green, Mn purple and O red. The dimensions are the Mn-Mn spacing in the indicated direction

The choice of the trivalent and divalent A-site cations is equally as important as the cation doping level. An important factor in the effect of different cations is the ionic radius: ionic radii of various ions are listed in table 1.1. Oxygen ions have a tendency to sit closer to the A-site when it is occupied by a smaller ion: this causes the oxygen octahedron to distort, producing a structural phase transition. The distortion of the oxygen octahedra can be quantified by a geometric factor Γ. This is defined as $\Gamma = d_{A-O}/\sqrt{2}d_{Mn-O}$, where d_{A-O} is the distance between the A-site and the nearest oxygen ion, and d_{Mn-O} is the distance between the Mn site and the closest oxygen ion [12]. For an undistorted cube as shown in figure 1.1a, $\Gamma = 1$. When small A-site cations are selected, d_{A-O} decreases and $\Gamma \leq 1$. The Mn-O-Mn angle θ also decreases from 180°: as θ decreases, the electron hopping amplitude for the Mn-O-Mn bond decreases. This is because the oxygen p orbital is involved, so there is a cos θ term in the hopping amplitude: if $\theta \neq 180$ the p orbital cannot point towards both Mn ions at once. Thus as the A-site ionic radius is decreased, Γ decreases, θ decreases, the electron hopping amplitude is reduced, and the material becomes less conductive. Γ is thus a measure of the single electron bandwidth. As Γ decreases charge-ordered states can become stabilised, and metallic phases are less common. Clearly manganite compounds have a rich three dimensional phase diagram, with many electronic, magnetic and structural phases manifested as functions of temperature, cation doping and choice of rare earth and alkaline earth

Ion	Crystal Radius (Å)	Ionic Radius (Å)
La^{3+}	1.172	1.032
Bi^{3+}	1.17	1.03
Pr^{3+}	1.13	0.99
Nd^{3+}	1.123	0.983
Pb^{2+}	1.33	1.19
Sr^{2+}	1.32	1.18
Ca^{2+}	1.14	1.00
Mn^{3+}	0.785	0.645
Mn^{4+}	0.67	0.53
O^{2-}	1.26	1.40

Table 1.1: Ionic and Crystal Radii in Ångstroms, for six-fold coordination. Note close match between Pr^{3+} and Ca^{2+} [68].

species.

Since manganites can exhibit so many different phases, much research has been undertaken to study the possibility of *phase separation* in these materials, where two competing phases coexist, forming an inhomogeneous state [12]. The coexisting phases can be magnetic, for example the coexistence of ferromagnetic and antiferromagnetic regions in $La_{2-2x}Sr_{1+2x}Mn_2O_7$ is thought to comprise the "canted" antiferromagnetic state (see section 1.6). Metallic and insulating or semiconducting phases may coexist near a metal-insulator transition as a result of a "percolative" phase transition, where the transition will occur at slightly different temperatures in different parts of the sample, due to variations in doping or nucleation of the new phase by defects. This leads to a phase transition which is broad in temperature. Such phase coexistence has been studied using STM/STS (section 2.2.1). It can be argued that a percolative phase transition does not represent phase separation *per se*, and is a simple consequence of a second-order phase transition in a system with some disorder (defects, etc.): however this is largely a matter of terminology.

1.3 Jahn Teller Effect and Polarons

At intermediate doping levels ($0 < x < 1$) the manganese ions in the manganite crystal are in a mixed valence state of Mn^{3+} and Mn^{4+}, which have configurations $3d^4$ ($t_{2g}^3 e_g^1$) and $3d^3$ ($t_{2g}^3 e_g^0$), and spin states 2 and 3/2 respectively. In Mn^{3+}, the interaction between the orbital state of the additional e_g electron and the crystal field of the surrounding oxygen octahedra causes a Jahn-Teller distortion. As the partly filled e_g orbitals ($d_{x^2-y^2}$, $d_{3z^2-r^2}$) are oriented towards the oxygen sites, the overall energy can be lowered if the octahedron spontaneously distorts, as shown in figure 1.3. Mn^{4+} has only a filled t_{2g} shell, so the Jahn-Teller effect does not occur in this ion. The Jahn-Teller effect results in a large electron-phonon interaction, since the presence of the e_g electron causes a large lattice distortion. It has long been recognised that this electron phonon interaction is crucial for understanding the properties of manganites: for example double exchange alone cannot explain the metallic state of $La_{1-x}Sr_xMnO_3$ [44].

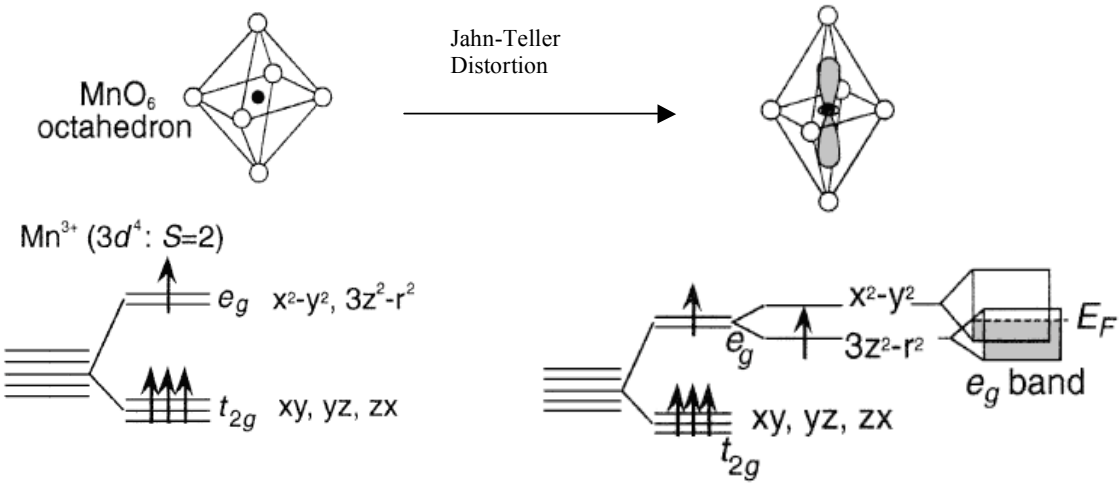

Figure 1.3: The Jahn-Teller effect in the Mn^{3+} ion. Adapted from [29]

Since the Jahn-Teller distortion introduces a strain field, it can be energetically advantageous for the whole crystal to distort: this is known as the co-operative Jahn-Teller effect. Structural phase transitions can thus occur in manganites as a function of cation doping, or as a function of temperature at fixed doping. The Jahn-Teller effect can also influence the magnetic ground state of a manganite. Antiferro-

magnetic cubic perovskite crystals commonly adopt G type antiferromagnetic order (figure 1.4b), as this preserves antiferromagnetic coupling for all nearest-neighbour interactions. However $LaMnO_3$ shows A type ordering (1.4a), with ferromagnetic coupling in the (010) planes, and antiferromagnetic coupling between these planes. This occurs because the Jahn-Teller distortion results in alternating long and short Mn-O bonds in the (010) planes (see figure 1.2b). This means that the d orbitals on a Mn ion are oriented differently to its neighbouring Mn ion, leading to an occupied orbital on one ion interacting with an unoccupied orbital on the other. In this case super-exchange can lead to a ferromagnetic in-plane interaction [7].

Since it is the e_g electrons which are itinerant in manganites, the charge carriers in Jahn-Teller active manganites are electrons with an accompanying lattice distortion: this can be regarded as a quasiparticle called a polaron. A polaron is essentially a bound state of an electron and a phonon, and has a much larger effective mass than a bare electron. The transition to the metallic, magnetic state from the paramagnetic insulating (PI) state can be understood as a polaronic effect [7, 44], whereby the PI state is dominated by polarons which are self-trapped in the lattice, and the transition to the low T metallic state occurs when these polarons are unbound.

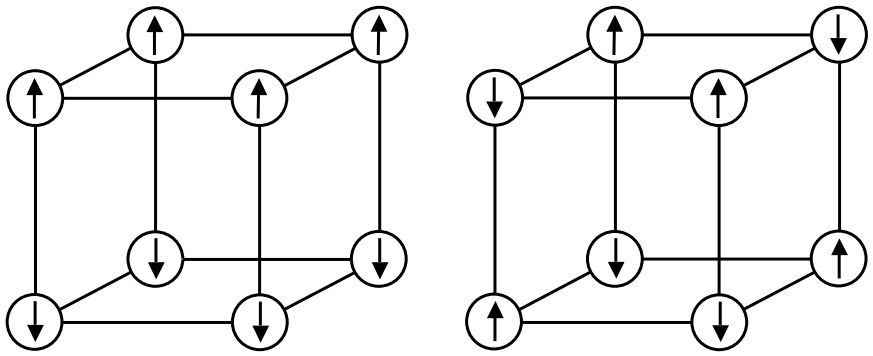

Figure 1.4: Two types of antiferromagnetism which can occur on a simple cubic lattice. The direction of the magnetic moment of each ion relative to the lattice may vary from that shown, but the relative orientation from ion to ion is preserved.

1.4 Colossal Magnetoresistance

A remarkable property of several manganite compounds is negative colossal magnetoresistance (CMR), a very large reduction in electrical resistance upon application of a magnetic field. The magnitude of magnetoresistance effects is normally given as the fractional change in resistance upon application of magnetic field. Either $\Delta R/R_H$ or $\Delta R/R_0$ may be quoted, where R_0 is the resistance at zero field, R_H the resistance at maximum field, and $\Delta R = (R_0 - R_H)$. The phenomenon of negative magnetoresistance in manganites was first noted in 1954 [81]: magnetoresistance ratios of order $\Delta R/R_H = 0.1$ at 0.3 T were found for polycrystalline $La_{1-x}Sr_xMnO_3$ samples. Large negative magnetoresistance effects were identified in a manganite compound in 1989 [33], in single crystal samples of $Nd_{0.5}Pb_{0.5}MnO_3$: this compound shows a magnetoresistance ratio of $\Delta R/R_H \approx 9$ at 11 T. Later studies identified magnetoresistance ratios of $\Delta R/R_H = 1.5$ at 7 T in thin films of $La_{0.67}Ba_{0.3}MnO_3$ [82], and $\Delta R/R_H = 1$ at 1 T in thin films of $La_{0.72}Ca_{0.25}MnO_3$ [9]. In all cases the largest magnetoresistance effect is found at temperatures close to the metal-insulator transition. The first truly colossal magnetoresistance effect was reported in a $La_{0.67}Ca_{0.33}MnO_3$ thin film [27], with $\Delta R/R_H > 1000$ at 6 T and 77 K. This film was optimised for the largest possible CMR effect by annealing under an O_2 atmosphere: this seems to have shifted the PI to FM phase transition from around 200 K to 95 K. Annealing in vacuum or in oxygen can profoundly change the properties of manganite films or crystals, because it can respectively decrease or increase the oxygen content of the material: this can in turn change the effective cation doping level. Since this publication even larger CMR effects have been found. In $Nd_{0.7}Sr_{0.3}MnO_3$ thin films $\Delta R/R_H > 10,000$ was reported, at 60 K and 6 T [84]. In this case a magnetoresistive memory effect was also seen, whereby the low temperature resistivity at zero field, after field cooling, was 10^{-3} times the initial zero field cooled resistivity.

The currently favoured explanation [13] for the CMR phenomenon is as a boundary effect at the phase transition from the FM metal state to the PI state, or from the FM metal to the CO state. A simple phenomenological explanation for CMR is that the magnetic field can align the Mn spins, and hence enhance the double-exchange hopping probability (proportional to $cos(\theta/2)$, where θ is the angle between adjacent Mn spins) [7]. Just below the transition temperature some spin disorder will remain:

this disorder can be suppressed by an applied magnetic field, effectively shifting the transition to a higher temperature and producing the negative MR effect [17]. This simple explanation is obviously not sufficient: a full model must include the effects of the strong electron-phonon coupling, *i.e.* polaronic effects, which may dominate the PI state [7, 44], and the fact that different competing phases may coexist near the phase boundary.

1.5 Charge Ordering

In manganites with certain values of the cation doping, notably x = 0.5, the CE-type charge ordered state may be stabilised at low temperature. This state is thought to comprise spatial segregation of Mn^{4+} and Mn^{3+} ions. The state is also thought to be orbitally ordered, with the e_g electron occupying $d_{3x^2-r^2}$ and $d_{3y^2-r^2}$ orbitals on alternate sites, and to have antiferromagnetic spin ordering [21, 52]. Thus it is sometimes referred to as the CEAFM state. The charge and orbital ordering of the charge ordered state are illustrated in figure 1.5. Ordering of the Mn^{3+} and Mn^{4+} ions produces a $\sqrt{2}a$ x $\sqrt{2}a$ unit cell, where a is the basic unit cell size. Including the effect of orbital order gives a $2\sqrt{2}a$ x $\sqrt{2}a$ unit cell, as shown in figure 1.5. Although strictly the CE type of order implies spin and orbital order as well as charge order [21], it has been frequently used in the literature [36] to mean just the $\sqrt{2}a$ x $\sqrt{2}a$ charge ordering, hence the use of "CEAFM" to denote a state which is also spin ordered.

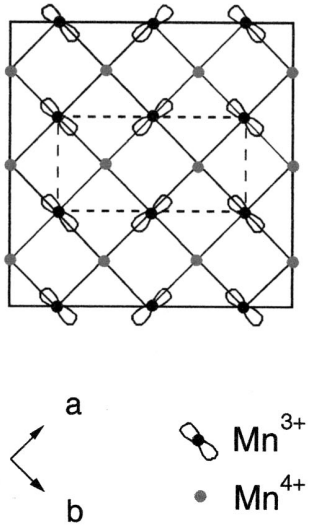

Figure 1.5: the CE charge ordered state, showing distribution of Mn^{3+} and Mn^{4+}, and orientation of Mn^{3+} e_g orbitals. [28]

CE-type order as described above implies spatial segregation of formal Mn^{3+} and Mn^{4+} ions, producing a commensurate superlattice. An alternate model [40] regards charge order as a charge density wave, with a much smaller variation in charge from one Mn site to the next [18]. This allows for incommensurate charge ordering: this has been observed in $La_{1-x}Ca_xMnO_3$ for x $\geq$ 0.5 by electron diffraction [40].

1.6 The Phase Diagram of $La_{2-2x}Sr_{1+2x}Mn_2O_7$ as a Function of Cation Doping

Bilayer manganites exhibit a variety of electronic and magnetic phases. Figure 1.6 shows the phase diagram of $La_{2-2x}Sr_{1+2x}Mn_2O_7$ [37], indicating phases manifested as a function of cation doping x and temperature. The compound is a paramagnetic insulator at room temperature for all doping levels. At x = 0.3, $La_{2-2x}Sr_{1+2x}Mn_2O_7$ is an antiferromagnetic metal (AFM) below the Néel temperature of 100 K: in the region $0.32 < x < 0.4$ the material is a ferromagnetic metal (FM) at low temperature. Between x = 0.42 and x = 0.66 there is an antiferromagnetic insulator state (AFI) below the Néel temperature: this is an A-type AF state (see figure 1.4) with an additional phase transition to a canted antiferromagnetic state at a lower temperature between x = 0.42 and x = 0.48. This CAF state can be interpreted as phase-separated mixture of ferromagnetic and antiferromagnetic states [12]. Figure 1.7 illustrates the spin alignment in the region 0.3 < x < 0.5. At x = 0.5 there is a charge ordered state with a transition temperature of 210 K: this state seems not to be stable to zero temperature however, reverting to the AFI state at around 100 K [28]. This charge ordered state will be examined in more detail in section 1.6.3. In the region $0.66 < x < 0.74$ there is a frustrated spin state, with no long range spin order at all. At high doping, between x = 0.74 and x = 1, two different AFI states are seen, which are thought to overlap near x = 0.9. Also, a structural phase transition takes place at high temperature between x = 0.74 and x = 0.94, from a tetragonal to a lower symmetry orthorhombic structure. This transition is not complete, and the tetragonal and orthorhombic phases coexist even at low temperature.

Bilayer manganites with x = 0.3 are antiferromagnetic at low temperature as noted above: this AF state comprises ferromagnetic bilayer planes which have antiferromagnetic interlayer coupling (see figure 1.7). Neutron diffraction has been used to determine the spin orientation as a function of temperature [2]. It was found that at the Néel temperature of 100 K, the spins are oriented at 43° to the c-axis: this angle decreases with temperature to a minimum of 13° at 5 K. Thus the spin arrangement is never exactly as depicted in figures 1.4 or 1.7, with spins oriented exactly in the c direction. Regardless of the spin angle though, the antiferromagnetic interlayer

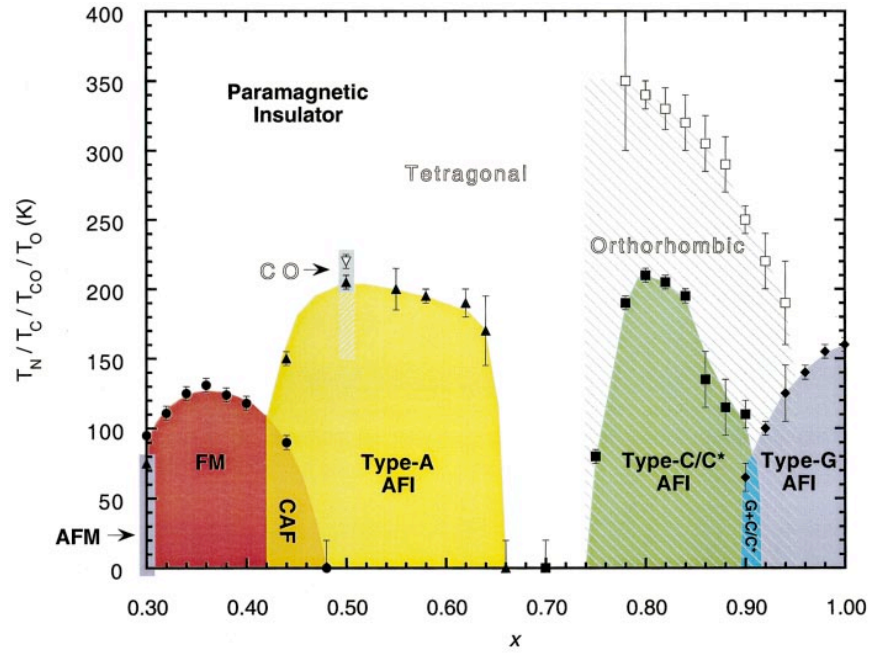

Figure 1.6: the phase diagram of $La_{2-2x}Sr_{1+2x}Mn_nO_7$, showing electronic and structural phases. From [37]

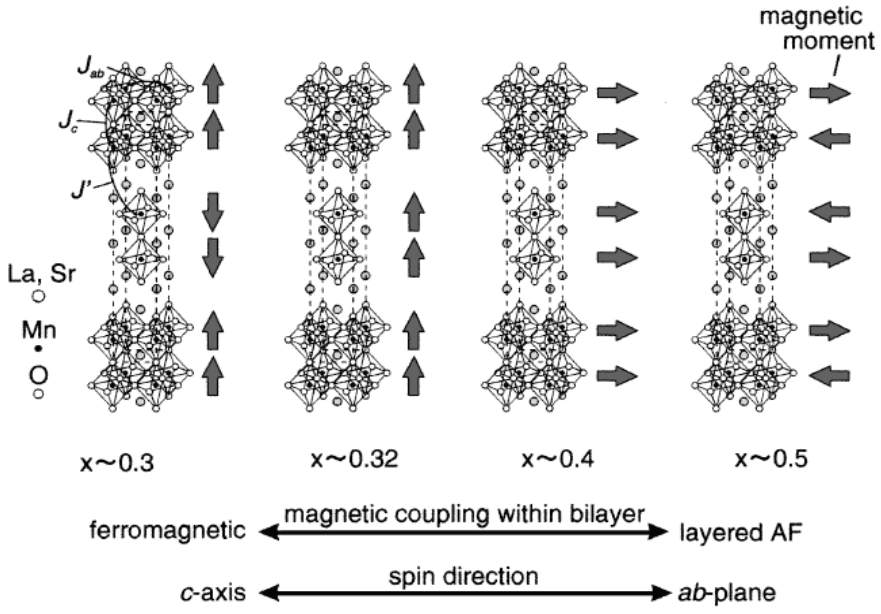

Figure 1.7: schematic of spin orientation in $La_{2-2x}Sr_{1+2x}Mn_nO_7$, in the doping region $0 < x < 0.5$. The spin ordering at x = 0.5 is A-type antiferromagnetic. From [29]

coupling is preserved. Spin polarised SEM has been used to directly observe the layered antiferromagnetic structure of the x = 0.3 compound [31]: this study verified the temperature dependence of the spin orientation. Both studies [2, 31] identified ferromagnetic inclusions, representing regions with higher ($0.3 < x < 0.32$) cation doping. Since it is difficult to determine the real doping level accurately, one must be cautious in interpreting experimental data in regions within a few percent in x of phase transitions.

1.6.1 Anisotropic Electrical Transport Properties of Bilayer Manganites

Bilayer manganites possess highly anisotropic electrical transport properties, with the resistivity parallel to the c axis (perpendicular to the bilayer planes) ρ_c several orders of magnitude higher than that parallel to the a or b axis, ρ_{ab}. Figures 1.8 and 1.9 illustrate this anisotropy in $La_{2-2x}Sr_{1+2x}Mn_2O_7$ at x = 0.4 and x = 0.3. This anisotropy can be attributed to the layered structure of the material: the $(R,A)_2O_2$ rock-salt type oxide layers are insulating, and electrons moving parallel to the c-axis need to tunnel through these layers. This simple picture is complicated slightly by the polaronic nature of electrical transport in these materials. Only a bare electron, not a polaron, can tunnel between the layers: polarons are therefore confined to the perovskite bilayers. For the electron to move out of the bilayer an energy cost equivalent to the polaron binding energy must be paid [59]. This energy cost is manifested as a pseudogap, observed in c-axis transport measurements. Due to this highly anisotropic gap, at some doping levels and temperature ranges bilayer manganites may be regarded as two-dimensional metals, with metallic transport only parallel to the ab planes. This occurs in $La_{1.4}Sr_{1.6}Mn_2O_7$ (x = 0.3), as shown in figure 1.9: ρ_c has a maximum at around 100 K (T^c_{max}), corresponding to the metal-insulator transition, whereas ρ_{ab} peaks at around 270 K (T^{ab}_{max}). Near T^{ab}_{max} the conductance anisotropy $\rho_c/\rho_{ab} = 104$. Between T^c_{max} and T^{ab}_{max} the material behaves like a metal ($d\rho/dT > 0$) in the ab direction, and a semiconductor ($d\rho/dT < 0$) in the c direction.

The model of $La_{1.4}Sr_{1.6}Mn_2O_7$ (x = 0.3) as a two-dimensional metal has been disputed. Li *et al.* [35] made transport measurements of $La_{2-2x}Sr_{1+2x}Mn_2O_7$ samples with x = 0.3 and 0.38, which have antiferromagnetic and ferromagnetic ground states respectively. Multi-terminal conductivity measurements were made on both compounds for a range of temperatures and magnetic fields: these measurements are a variation on six-terminal measurement methods. No evidence was found for different transition temperatures in the c and ab plane directions, contrary to the previous findings by Kimura *et al.* [30]. The authors suggest that the previously observed difference between T^c_{max} and T^{ab}_{max} is an artefact of four-terminal conductivity measurements with slightly misaligned contacts. However, optical conductivity measurements [26] show clear differences between the ab-plane and c axis directions. In

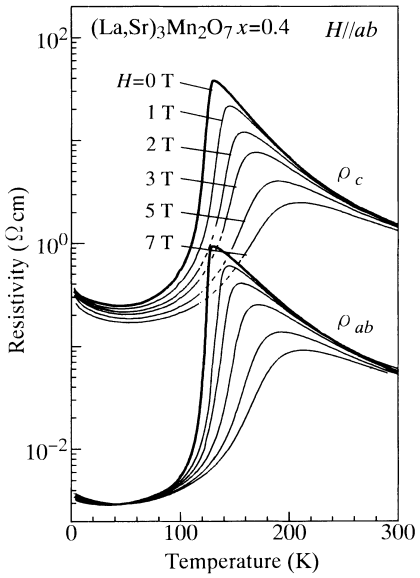

Figure 1.8: Temperature and magnetic field dependence of ρ_c and ρ_{ab} in x = 0.4 $La_{2-2x}Sr_{1+2x}Mn_2O_7$, showing CMR effect and anisotropic resistivity. [46]

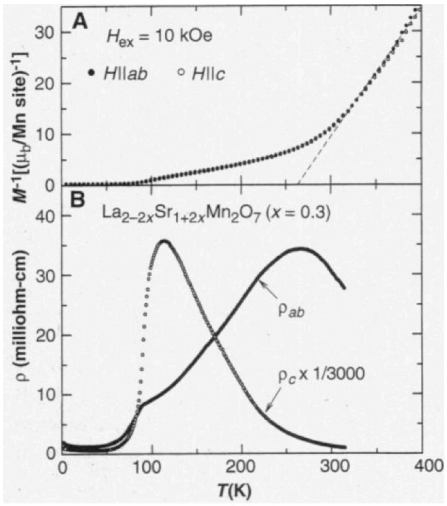

Figure 1.9: Temperature dependent resistivity in x = 0.3 $La_{2-2x}Sr_{1+2x}Mn_2O_7$, showing different behaviour of ρ_c and ρ_{ab}. [30]

particular an increase in optical conductivity at low frequencies is noted below 90 K: this is associated with a metallic state and is only observed in the ab-plane direction, not in the c-axis direction [59]. This is consistent with the electrical transport measurements by Kimura *et al.* [30], and provides evidence in favour of the model of $La_{1.4}Sr_{1.6}Mn_2O_7$ as a two-dimensional metal, crucially without requiring electrical contacts. The drop in the c-axis conductivity below 90 K, as shown in figure 1.9, is thought to be due to shunting of the c-axis current along the metallic ab planes (see section 2.2.3 and [59]).

The experiment by Li *et al.* [35] reveals a very large conductance anisotropy for the x = 0.3 compound, around 10,000 below 30 K at zero field. This is far in excess of the value for the x = 0.38 compound of 230. The high field (7 T) anisotropies of the two compounds are similar, indicating that the high c-axis resistivity of the x = 0.30 compound arises due to the antiferromagnetic interlayer coupling. The conductance anisotropy of the x = 0.38 compound, and the residual high-field anisotropy of the x = 0.3 compound, are attributed to the effect of greater Mn-Mn distance in the c-axis on double exchange transport.

1.6.2 Magnetoresistance of x = 0.3 and x = 0.4 Bilayered Manganites

Bilayer manganites exhibit a large magnetoresistance effect at some doping levels, in a similar way to the cubic perovskite manganites (section 1.4). Colossal magnetoresistance has been observed in $La_{2-2x}Sr_{1+2x}Mn_2O_7$ single crystals with cation doping x = 0.4 [46]. The CMR effect is attendant on the metal-insulator transition at 125 K. A magnetoresistance ratio R_0/R_H of up to 200 was measured at 129 K, under an applied field of 7 T. This is ten times larger than that measured in $La_{1-x}Sr_xMnO_3$ single crystals at the same doping level, implying that the bilayer structure somehow enhances the CMR effect. Magnetoresistance can be observed in both the c axis and ab plane resistivity (ρ_c and ρ_{ab}), with a similar R_0/R_H in each direction (figure 1.8). Here the magnetic field is applied parallel to the ab plane, along the easy axis of ferromagnetic spin alignment in the low temperature ferromagnetic phase (see figure 1.7).

The magnetoresistance of $La_{2-2x}Sr_{1+2x}Mn_nO_7$ single crystals with x = 0.3 has also been investigated [30]. In contrast to the x = 0.4 compound, where the temperature dependence of ρ_c is largely identical to ρ_{ab} (figure 1.8), at x = 0.3 they are fundamentally different, as discussed in the previous section, and shown in figure 1.9. Under a magnetic field, applied parallel to the c-axis, a magnetoresistance effect is seen in $La_{1.4}Sr_{1.6}Mn_2O_7$ in both ρ_c and ρ_{ab}: near T^{ab}_{max} = 270 K the effect is isotropic and relatively small [30]. Close to T^{c}_{max} = 100 K the MR effect is enhanced by proximity to the metal-insulator transition, and is observed to be highly anisotropic, with R_0/R_H (c-axis) as high as 100 and R_0/R_H (ab plane) around 3 at 5 T. At 4.2 K, where the material should be fully antiferromagnetic, an anisotropic magnetoresistance effect is still observed, with R_0/R_H (c axis) = 3.4 and R_0/R_H (ab plane) = 1.1 at 0.5 T. This anisotropic magnetoresistance is unusual, and it occurs even far from the phase transition. It can be modelled [29,30] by regarding the material as a stack of ferromagnetic metal-insulator-ferromagnetic metal junctions (FM/I/FM), through which spin-polarized electrons tunnel. Since the interlayer spin coupling is antiferromagnetic, the interlayer tunnelling probability under zero applied field is very small. The coupling is weak however, and can be overcome by an applied magnetic field of 1.5 T [50]. A fully three dimensional ferromagnet is thus created, and the interlayer tunnelling probability is greatly increased. The ferromagnetic

state has spins oriented in the ab plane, similar to the ground state of the x = 0.4 compound at zero field (see figure 1.7). This effect is referred to as tunnelling magnetoresistance to distinguish it from the CMR effect seen in perovskite manganites close to the metal-insulator transition temperature.

1.6.3 The Charge Ordered Phase in $LaSr_2Mn_2O_7$

At x = 0.5 $La_{2-2x}Sr_{1+2x}Mn_2O_7$ contains equal numbers of Mn^{3+} and Mn^{4+} ions, which below the charge ordering temperature T_{CO} = 210 K are thought to occupy alternate ion sites, forming a CE-type charge ordered state. The charge ordered phase of $LaSr_2Mn_2O_7$ was determined, by x-ray diffraction and bulk conductivity, to form at around 210 K, and collapse with decreasing temperature at 70-100 K [28, 34]. This collapse is referred to as re-entrant behaviour. Figure 1.10 shows the dependence of the ab-plane resistivity on temperature and magnetic field. The low temperature re-entrant temperature transition is observed to be hysteretic, with the transition occurring at higher temperature on warming than cooling. Above 210 K the material is a paramagnetic insulator (PMI): the low temperature phase is an A-type antiferromagnetic (AFM) insulator. Similar behaviour has been identified by neutron scattering [1]: in addition the CE and AFM phases are observed to coexist below 170 K. At around 125 K, the two phases exist in roughly equal proportions. A substantial negative magnetoresistive effect is observed in $LaSr_2Mn_2O_7$ below 210 K, as can be seen in figure 1.10. This effect is observed in the temperature range in which charge order is active, and is associated with a field-induced transition to the AFI state [28, 72]. The charge ordered state can be completely suppressed by the application of a field of 20 T [28].

Recent data from conductivity, magnetization, neutron and x-ray diffraction experiments at the Argonne National Laboratory [36] indicate that the CE state is in fact continuously stable to zero temperature, but only in a very narrow doping region very close to 50% hole doping. Both re-entrant and non re-entrant crystals have been produced by this group: non re-entrant crystals do not exhibit a collapse of the charge ordering at low temperature: neither is there any appreciable hysteresis. Non re-entrant crystals retain a high proportion of CE-type order at low temperature: A-type AFM order (AAFM) is present but is a minority phase, accounting

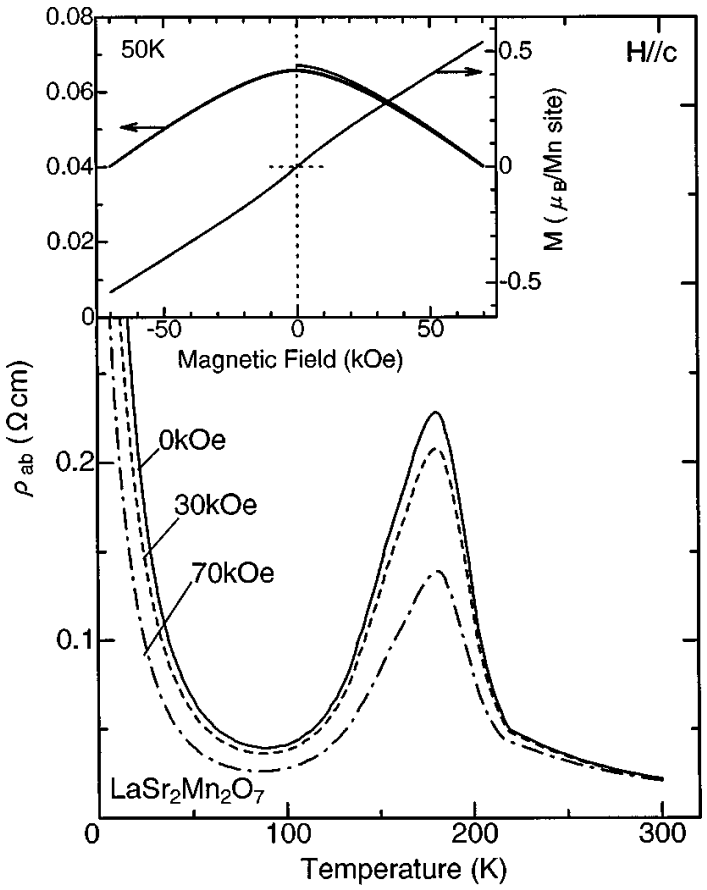

Figure 1.10: Temperature and magnetic field dependence of the ab-plane resistivity of $LaSr_2Mn_2O_7$. [28]

for just a few percent of the volume of the crystal. Oxygen level seems to be critical to the nature of the samples, as indicated by a crystal which was transformed from re-entrant to non re-entrant type by annealing in an oxygen atmosphere. The effective formula is therefore $La_{2-2x}Sr_{1+2x}Mn_2O_{7-\delta}$, and the critical parameter is the hole doping level $h = x - \delta$. In this interpretation, it is only deviation from $h = 0.5$ which causes re-entrance to the AFM state. No significant coexistence of CE and AAFM order was seen, either in re-entrant or non re-entrant samples: the phase coexistence seen by other groups is attributed to spatial variation in $h = x - \delta$. The revised phase diagram around $h = 0.5$ is shown in figure 1.11: the supposed doping level of re-entrant and non re-entrant crystals is marked as A and B respectively: "coexistent" indicates the probable distribution of h in samples exhibiting phase coexistence. The Néel temperature is measured as 130K, so above this temperature

the CE state is paramagnetic (CEPM). At h = 0.5 the material is charge, orbital and spin ordered (CEAFM) only below 130 K. At slightly higher or lower h re-entrance occurs and the CE state disappears below around 100 K. As at h = 0.5 the CEPM state is found above around 130 K: the CEAFM state below 130 K is metastable, and is only observed on cooling: on warming the crystal transforms directly from the AAFM state to CEPM, accounting for the hysteretic transition previously reported in [28].

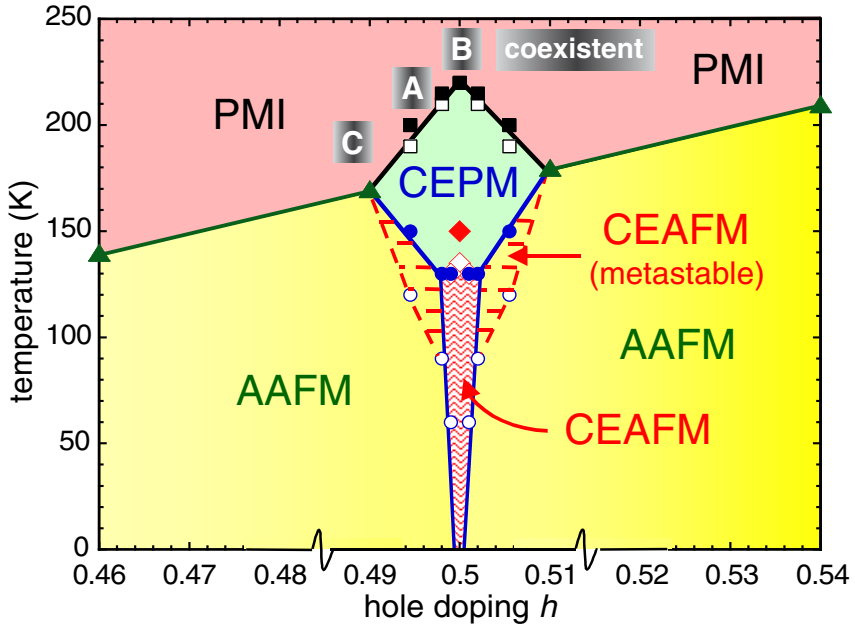

Figure 1.11: revised phase diagram of $La_{2-2x}Sr_{1+2x}Mn_nO_{7-\delta}$ near h = $x - \delta = 0.5$, from [36]

1.7 The Phase Diagram of $Pr(Sr_{1-y}Ca_y)_2Mn_2O_7$ as a Function of Bandwidth

The properties of manganites can be tuned by varying the choice of divalent alkaline-earth cation as well as by varying the cation doping: this has the effect of changing the electron bandwidth as discussed in section 1.2. The series $Pr(Sr_{1-y}Ca_y)_2Mn_2O_7$ demonstrates this effect: with increasing y, Sr is progressively replaced by the smaller Ca, and the electron bandwidth decreases. Figure 1.12 [79] shows the charge and spin order phases manifested by the manganite as a function of Ca content, y. Ca rich crystals are orthorhombically distorted since the small size of the Ca ion means the geometric factor (see section 1.2) $\Gamma \leq 1$: the line marked T_S in figure 1.12 shows where the crystal structure changes from tetragonal *I4/mmm* to orthorhombic *Amam*.

In this series of compounds the cation doping is always x = 0.5, *i.e.* equal quantities of Mn^{3+} and Mn^{4+} are present. At this doping level CE-type charge ordered compounds are expected to be stabilised: however charge order is only observed in $Pr(Sr_{1-y}Ca_y)_2Mn_2O_7$ for $y \geq 0.4$. This may be attributed to disorder in the Sr-rich compounds caused by the mismatch between the ionic radius of Sr and Pr. As can be seen in table 1.1, there is a much better match in ionic radius between Ca and Pr: thus the Ca-rich compounds have low disorder. Charge order may be stabilised in the Ca-rich compounds by the orthorhombic distortion or the smaller electron bandwidth at large y. Below y = 0.4 the manganite is a paramagnetic insulator at room temperature, and an A-type antiferromagnet (A-AF) below the Néel temperature of 100-130 K. The A-AF state is sometime referred to as psuedometallic as the resistivity drops upon cooling through T_N, but upon further cooling starts to diverge again (see figure 1.13).

Although $Pr(Sr_{1-y}Ca_y)_2Mn_2O_7$ does not exhibit CE-type charge ordering for $y < 0.4$, in $PrSr_2Mn_2O_7$ a charge-stripe state is observed at 125 K. This has been observed using x-ray diffraction (figure 1.13): scattering peaks are observed at h=0.24 and k=0.24, suggesting twinned domains of a stripe-type charge order with periodicity $\approx$ 4a as shown in figure 1.13b. The temperature dependence of the peak intensity is shown in figure 1.13b: the peak is strongest at $T_N = 125$ K. The exact nature of these stripes has not yet been identified: simple stripe charge order seems unlikely

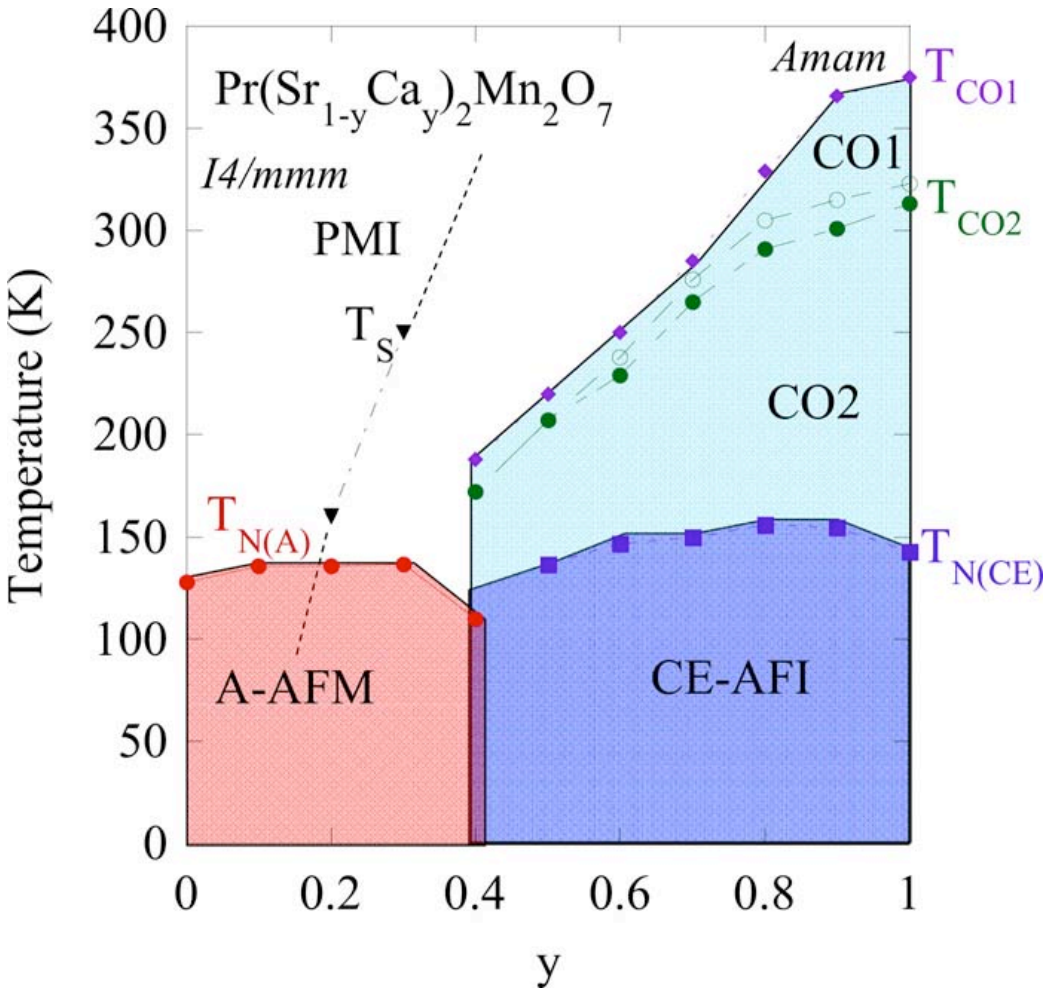

Figure 1.12: Phase diagram of $Pr(Sr_{1-y}Ca_y)_2Mn_2O_7$ as a function of Ca content, y. Cation doping x = 0.5 throughout. [79]

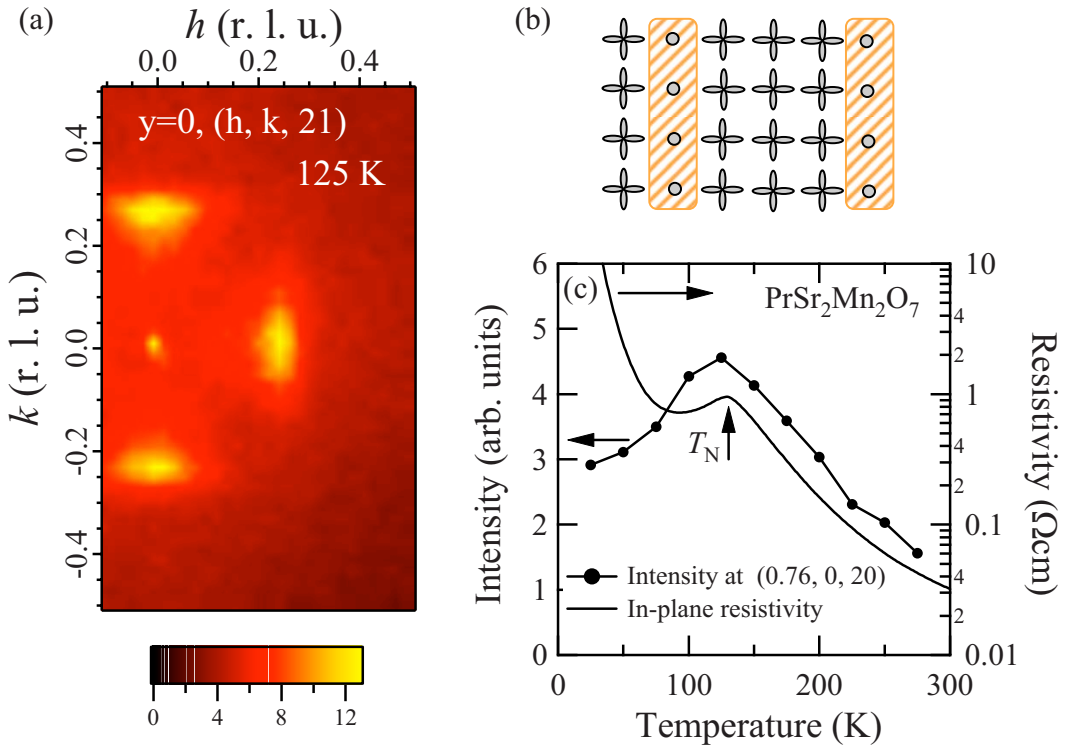

Figure 1.13: (a) Contour map of x-ray scattering for $PrSr_2Mn_2O_7$ (b) Schematic of possible charge stripes (c) Temperature dependence of peak intensity at (0.76, 0, 20) and ρ_{ab} [79]

as this would result in a 3:1 ratio between Mn^{3+} and Mn^{4+}, rather than 1:1.

For y $\geq$ 0.5 two charge order/orbital order (CO-OO) states are observed, identified as CO1 and CO2 (figure 1.12): these have identical charge ordering but between CO1 and CO2 the orbital order rotates by 90°. This rotation can be observed in a polarised optical microscope image [78]. The charge ordering temperatures are much higher than in $LaSr_2Mn_2O_7$, with CO1 as high as 375 K at y = 1: this is understandable as $PrCa_2Mn_2O_7$ will have a much smaller geometric factor Γ and smaller bandwidth, which will stabilise the charge ordered state. The state does not exhibit spin order (CE-type AFM) until lower temperatures, with T_N from 130-150 K depending on y. The intervening region is presumably a paramagnetic CO-OO state.

1.8 Manganite Based Memory Devices

Much research is currently being undertaken to determine if manganites are good materials from which to construct memory devices. Manganites that exhibit *resistance switching* may form the basis for novel types of solid-state memory such as Resistive RAM (ReRAM). A ReRAM element, or resistive memory device, is simply a two-terminal resistor that can be switched between two or more resistance states by the application of bias [60]. The resistance states should be stable, so the memory is non-volatile. A resistive memory device necessarily exhibits hysteretic electrical conductance: close to the switching voltage it will demonstrate negative differential resistance. The device can also be said to exhibit electroresistance as its resistance is changed by application of bias and therefore by an electric field.

Devices based on metal oxides have been known since 1962 to exhibit negative differential resistance [25][1], but it is not until more recently that oxide materials have been investigated for their potential applications in resistive memory devices [5, 39]. Two terminal devices constructed using thin films of the semiconducting perovskite manganite $Pr_{0.7}Ca_{0.3}MnO_3$ (PCMO) have been shown to exhibit resistance switching [3, 23, 39, 47, 48, 60–62, 69]. The devices consist simply of a manganite thin film or crystal sandwiched between two metal electrodes, which may be made from different metals. Such devices can be reversibly switched, by the application of a bias voltage, from a high resistance state (HRS) to a low resistance state (LRS). The switching exhibited is bipolar, meaning that the direction of state switching is dependent upon the polarity of the applied bias as well as the amplitude. Devices made with one low work function metal (Ti or Al) electrode [23, 60–62, 69] can form a Schottky diode at the metal-manganite interface. The metal electrode can become oxidised at the interface, producing an insulating metal oxide layer [23, 69]. In such devices a "forming process", whereby a large bias is applied to the device, may be necessary before resistance switching can be observed. It has been shown [63] that the switching effect in these devices occurs at the interface between the metal contact and the semiconducting manganite. Figure 1.14 shows room-temperature current-voltage plots for a PCMO based resistance switching device, with a Ti top electrode [60]. The PCMO and deposited Ti were patterned into "mesa" structures

[1] For a comprehensive review of differential negative resistance, resistance switching and memory effects in oxide devices up to 1970 see [14]

between 100 x 100 μm^2 and 500 x 500 μm^2 in size [60, 62]. Diode-like behaviour is observed: resistance state switching between HRS and LRS produces a hysteretic I(V) curve. Diode behaviour and resistance switching is only observed for a Ti top electrode, not Au or $SrRuO_3$.

There is evidence that oxygen content, and motion of oxygen ions, play important roles in resistance switching: for example, devices which have been annealed in an oxygenated atmosphere cease to exhibit resistance switching [60]. TEM was used to study the interface between the Ti electrode and the PCMO [69] in a resistance switching device: a 10 nm thick amorphous TiO_x layer is observed to form spontaneously at the Ti:PCMO interface. EELS measurements indicate that the O originates from the PCMO, which shows a decrease in Mn valence caused by O deficiency: the forming process is observed to further decrease the Mn valence near the interface, implying that O migrates from the PCMO to the TiO_x layer under applied bias during the forming process, thickening the oxide layer. The proposed mechanism for resistance switching in this case is that electrochemical migration of oxygen ions under applied bias causes oxidation or reduction of the TiO_x layer: the HRS represents a fully oxidised TiO_x layer, LRS a reduced layer. The PCMO acts as an oxygen reservoir. In an alternate model for interface-type resistance switching [61], oxygen vacancies form interface states which can be charged or discharged according to the applied bias, changing the effective width of the Schottky barrier. Oxygen vacancies may accumulate at the interface during the forming process as a result of electrochemical migration.

Another potential application of two-terminal resistance switching devices is as the fourth fundamental circuit element, the memristor. The possibility of an additional fourth passive circuit element, in addition to the resistor, capacitor and inductor, was first suggested by Leon Chua in 1971 [10]. As there are four fundamental circuit variables, current I, voltage V, charge Q and magnetic flux ϕ, Chua reasoned by symmetry that there should be a fourth circuit element to provide the relationship between charge and flux. This element is the memristor, which has a "memristance" M: the relationship is $\mathrm{d}\phi = Mdq$. If M is a constant, the memristor simply functions as a resistor. If M is a function of q however, a frequency-dependent hysteretic current-voltage curve results. In this case the inclusion of memristors in a passive circuit allows the circuit to perform functions which would otherwise require active elements [10, 70]. This means that the development of a working memristor would

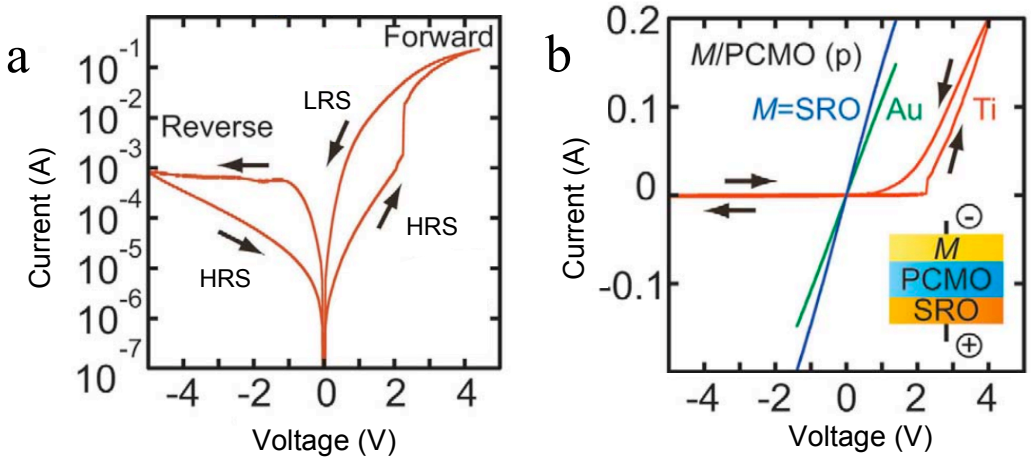

Figure 1.14: (a) figure from [60] showing bipolar switching between Low Resistance State (LRS) and High Resistance State (HRS) in a $Pr_{0.7}Ca_{0.3}MnO_3$ based device (b) the same plot on a linear scale, showing diode behaviour. Resistance switching and diode behaviour are only observed for Ti top electrodes

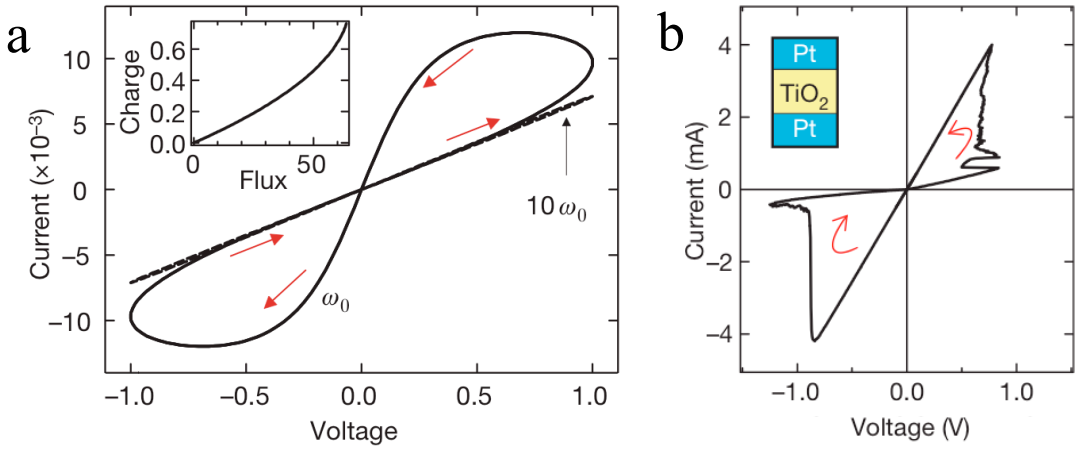

Figure 1.15: (a) simulation of the operation of a memristor. The inset shows the relationship between charge and magnetic flux, which is non-linear [70] (b) Current-voltage curve of a Pt-TiO_2-Pt device, which may be suitable as a memristor [70]

allow simplified circuit design. Figure 1.15a shows a simulated current-voltage curve for a memristor: the inset shows the relationship between charge and flux [70]. The hysteretic I(V) relationship collapses at high frequency. The resistance of the device is dependent on applied voltage, and also on the voltage history: the device thus has a memory, hence the name "memristor". A candidate device for a real memristor has been proposed [70]: this device consists of a TiO_2 element between two Pt electrodes. The TiO_2 is reduced to TiO_{2-x} close to one Pt contact: oxygen ions migrate under applied bias from the TiO_2 to the TiO_{2-x}, changing the overall device resistance. Figure 1.15b shows an I(V) curve from a Pt-TiO_2-Pt memristor device.

The similarity between memristors and ReRAM devices is clear: both are two-terminal resistive "memory" devices which exhibit hysteretic current-voltage curves. Similar physics may be at work, with electrochemical migration of oxygen ions playing an important role. Resistance switching manganite devices may be suitable as memristors as well as ReRAM elements.

1.9 Questions in Manganite Physics

Some of the most important questions in manganite physics may be summarised as:

- Does phase separation occur at the metal-insulator transition temperature, or at the charge ordering temperature, for any, or all manganite compounds?
- Which manganite compounds exhibit charge ordering, and at what temperatures?
- Is charge ordering best described by the traditional model of spatial segregation of Mn^{3+} and Mn^{4+} ions [21, 52], or by a charge density wave type model [40]?
- Are the electronic properties of manganite surfaces representative of the bulk properties?
- Do surface defects play a major role in the electronic properties of manganite surfaces?
- What are the technological applications of manganite compounds?

Chapter 2

Scanning Tunnelling Microscopy of Manganites

2.1 Introduction to Scanning Tunnelling Microscopy

The Scanning Tunnelling Microscope (STM) provides a way to study the topographic and electronic features of a surface with atomic resolution. The basic physical principles the STM relies upon are vacuum tunnelling and piezoelectricity. The mechanism of the STM is relatively simple: it consists of a sharp metal tip mounted on piezoelectric positioners, which can be brought within a few Ångstroms of a conducting sample surface. A bias voltage is applied between the tip and the sample: a quantum mechanical *tunnel current* can flow between the tip and the sample, due to the small separation between the two. The magnitude of this current is exponentially dependent on the tip-sample separation. The piezoelectric positioners ("piezos") allow the tip to be moved in three dimensions: the tip can thus be raster scanned across the sample surface. The basic architecture of the STM is shown schematically in figure 2.1a. The most common mode of operation is constant current mode. In this mode a feedback loop on the tunnel current is used to control the tip height (Z), by constantly adjusting the voltage supplied to the Z piezo so as to keep the tunnel current constant. As the tip is raster scanned across the sample surface the Z height thus tracks the height of the surface: an image of the surface can be built up in this way from the Z height data. Since the tunnel current is exponentially dependent on the tip-sample distance, a small change in the height of the surface results in a large change in current: typically the tunnel current will decrease by an order of magnitude if the tip is withdrawn by one Ångstrom. This means the STM can resolve very small changes in height. This makes it possible for atoms to be resolved by the STM, since the corrugation due to the atomic lattice can be imaged. A resolution of 0.01 Å can be achieved in the Z direction, and around 0.1 Å in the X and Y directions. An alternative mode of operation is constant height mode: in this mode the feedback loop is turned off (or more practically reduced in response), the tip is scanned over the surface, and the varying tunnel current signal is used to build up an image. Both modes of operation are illustrated in figure 2.1.

The magnitude of the tunnel current is not just determined by the tip-sample separation and the bias voltage: the electronic structure of both the tip and the sample is important. The electron density of states of the sample may not be uniform, but

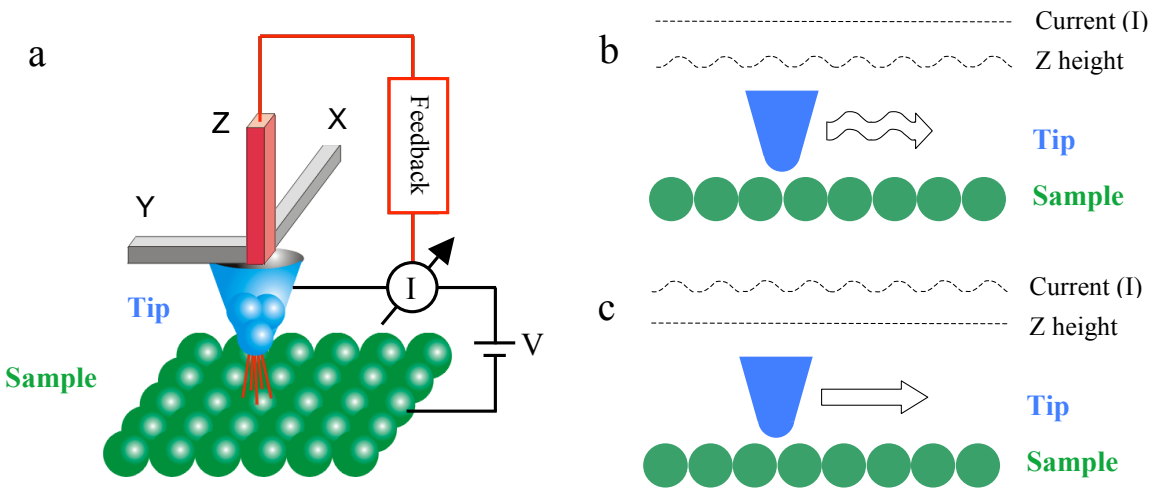

Figure 2.1: (a) schematic of STM construction (b) STM operation: constant current mode (c) STM operation: constant height mode

can vary across the surface under study: thus an STM image built up from Z height or tunnel current data does not represent a simple topographic map, but rather a convolution of the surface topography with variations in density of states. For example, a flat metal surface could be prepared with patches of some semiconducting material deposited on top of it. A constant-current STM image will show the semiconducting patches as lower than the surrounding metal, despite the fact that they are physically higher: this is because they have a lower electron density of states, are less conductive, and so the tip has to move closer to the surface to maintain the tunnel current.

According to the Wentzel, Kramers and Brillouin (WKB) approximation [22, 83] at zero temperature the tunnel current (I) at some location (r) can be expressed as a function of tip-sample separation (d), bias voltage (V), and the electronic density of states of both the tip and the sample, denoted by $N_T(r, E)$ and $N_S(r, E)$ respectively.

$$I = \int_0^{eV} N_S(r, E) N_T(r, E - eV) P(E, eV, r) dE \tag{2.1}$$

$P(E, eV, r)$ is the tunnelling transmission probability.

$$P(E, eV) = exp\left(\frac{-2d\sqrt{2m}}{\hbar}\sqrt{\frac{\phi_S + \phi_T}{2} + \frac{eV}{2} - E}\right) \tag{2.2}$$

ϕ_S and ϕ_T are the barrier heights of the sample and tip respectively: note the exponential dependence on the tip-sample spacing d. Conventionally the bias voltage V is assumed to be applied to the sample, with the tip at ground. At positive sample bias ($eV > 0$), electrons tunnel from the occupied states of the tip into unoccupied states of the sample: at negative bias ($eV < 0$) the tunnel current is from occupied sample states into unoccupied tip states. At negative bias the tunnelling transmission probability $P(E, eV, r)$ is dominated by electrons tunnelling from the Fermi level ($E = 0$) of the sample: at positive bias it is dominated by electrons with $E = eV$, tunnelling from the Fermi level of the tip. The current (2.1) is thus also dominated by electrons with energy $E = 0$ or $E = eV$. If we assume a metal tip so that $N_T(E)$ is approximately constant, then for constant current mode the tip follows a contour of constant $N_T(E)$. This means that a constant-current STM image is a contour map of sample electron density of states. Strictly speaking this is an approximation which is valid only at low voltages [76], but in most cases it is a valid model.

Since the STM image can be regarded as a density of states contour map, it is a convolution of electronic and topographic (height) information. It can be difficult to deconvolve these two, *i.e.* to determine which contrast features are electronic in origin and which are topographic. One method is to vary the bias voltage applied to the sample. Different sample electronic states will be probed at different biases, which may result in a change in the contrast, if it is of electronic origin: an image dominated by topographic contrast will appear similar at different biases. Images at different biases can be acquired "simultaneously" by changing the bias between successive scan lines, thus interlacing images of different bias. In particular, images at positive and negative bias can be interlaced: under positive sample bias sample empty states are probed, and filled states are probed under negative bias. This is sometimes known as "dual mode" imaging.

2.1.1 Scanning Tunnelling Spectroscopy

Instead of holding the tunnel current constant and moving the tip, the STM can be used to produce a tunnelling spectrum by holding the tip in one position and changing the voltage: this is known as Scanning Tunnelling Spectroscopy or STS. Normally this is achieved by temporarily suspending the feedback loop, ramping the voltage across the required range and measuring the tunnel current. A plot of current against voltage I(V) can thus be produced: this allows the sample density of states to be locally measured. Often dI/dV(V) spectra are used: from equation (2.1) dI/dV is proportional to the sample density of states $N_S(r, E)$. dI/dV can be measured directly using lock-in techniques, or calculated numerically from a measured I(V) curve.

It is not generally possible to extract an absolute measurement of the local density of states from an STS measurement, since in general the density of states of the tip is unknown, and the voltage dependence of the tunnelling probability is unknown. However, the real strength of STS as a technique is the ability to combine spectroscopy measurements with the high spatial resolution of the STM. The STM can be programmed to take an array of spectra at the same time as a topographic image: the tip can be paused at predetermined points in the image and spectra recorded at these points. The normal procedure is for the tip to move under feedback (constant-current) control for image acquisition: at the spectra positions the feedback loop is suspended and the spectrum is measured. Once the spectrum is complete the feedback loop is re-established and image acquisition resumes. This process is all undertaken automatically by the STM control system: dense arrays of spectra can be collected automatically. Thus a high-resolution I(V) or dI/dV(V) map of the sample surface can be built up. Any spatial variation of the sample density of states ($N_S(r)$ in 2.1) will be apparent in the spectroscopy map. Since it is the spatial variation of N_S which is of most interest in such a study, the inability to measure the absolute sample density of states is not normally a disadvantage.

In a real tunnelling spectroscopy experiment the energy resolution of an STS measurement will be fundamentally limited by thermal smearing of the electron density of states of the tip and the sample. For finite temperature we should write in equation 2.1 $N_S(r, E, T)$ and $N_T(r, E-eV, T)$. If we adopt the FWHM of the first derivative of the Fermi function as the energy resolution ΔE, this gives $\Delta E = 3.5\ kT$. At

300 K this means an energy resolution of $\Delta E = 91$ meV. Therefore STS experiments are often performed at cryogenic temperatures: at 2 K $\Delta E = 0.6$ meV. Note that the Fermi distributions of the tip and the sample will both be thermally smeared: therefore it is important that if the sample is cooled then the tip is cooled as well, otherwise the desired improvement in the energy resolution will not be achieved.

2.2 Existing STM Work on Manganites

Scanning Tunnelling Microscopy (STM) and Scanning Tunnelling Spectroscopy (STS) are powerful tools for studying manganites, since they allow the electronic properties of the material to be probed at Ångstrom length scales. This makes STM ideal for addressing some of the most interesting questions in manganite research:

- STM can be used to study phase separation, since coexisting electronic phases can be discerned using high-resolution STS.
- Charge ordering can also be studied, as the atomic resolution achievable with STM allows the charge order superlattice to be directly imaged.
- STM is a surface sensitive technique: when combined with bulk probes such as optical spectroscopy and bulk electrical transport it can provide information of how the surface electronic structure compares with the bulk.

STM and STS require the sample surface to be very clean, so since manganite surfaces are reactive, scanning is usually carried out in an Ultra High Vacuum (UHV) of 10^{-10} mbar or less. There are various methods for preparing the sample surface: perovskite single crystals can be cleaned or scratched in a solvent to expose a fresh surface before loading to UHV: thin films may be studied *in situ*, with the STM vacuum connected to the growth chamber. Bilayer manganites may be cleaved *in situ* in the STM UHV chamber, as we will see later.

2.2.1 STS Studies of Perovskite Manganites

STM and STS have been used by several groups to study perovskite ($n = \infty$) manganite compounds. Spatially resolved STS studies (STS maps) enable Ångstrom resolution measurements of the local conductance, and hence the electron Local Density of States (LDOS). This is ideal for studying the nature of the paramagnetic insulator (PI) to ferromagnetic metal (FM) phase transition and the attendant colossal magnetoresistance (CMR) effect, by identifying the possible coexistence of insulating and metallic regions near T_C.

Thin films and single crystals of $La_{1-x}Ca_xMnO_3$ ($0.25 \leq x \leq 0.3$) were studied by Fäth *et al.* using STS [17]. These materials are known to exhibit CMR. No topographic images are shown in this paper: the surface roughness of the films and single crystals is quoted as < 20 nm. This implies a significantly rough surface since an atomically flat surface studied by STM would be expected to have a roughness of less than 0.1 nm. STS maps were taken at a range of temperatures from well above the metal-insulator transition (MIT) at $T_C \approx 200$ K down to 4 K, and in magnetic fields up to 9 T. dI/dV maps at finite bias (3V) were used to measure local conductance variations. Such maps taken just below T_C show inhomogeneity in dI/dV, interpreted as a coexistence of metallic and semiconducting phases. These regions of differing conductance were 10-100 nm in size. Upon application of a magnetic field, some semiconductive regions can be converted into metallic regions: however some remain semiconducting in fields up to 9 T, implying that the CMR effect is not saturated. Similarly, some regions remain semiconducting at temperatures far below T_C. Figure 2.2 shows this effect in an $x = 0.27$ thin film.

A study by Becker *et al.* [6] investigated $La_{0.7}Sr_{0.3}MnO_3$ and $La_{0.7}Ca_{0.3}MnO_3$ thin films using spatially resolved STS. Topographic STM images of the thin films show a microstructure with a grain size of order 40 to 60 nm: the overall surface roughness is around 30 nm (peak-peak), though the r.m.s. roughness on single grains is of order 2-3 nm. Neither atomic resolution nor clear images of atomic terraces were reported. dI/dV was measured at zero bias, at a temperature range from 48 K to room temperature. The LSMO films were observed via transport measurements to undergo the metal-insulator transition at 300 K. On the LSMO films at 87 K, spatially segregated insulating and metallic phases were observed, with insulating "filaments" about 21 nm across. With increasing temperature, the insulating regions grow and connect, as would be expected for a percolative phase transition. No obvious correlation was seen between the topographic scan and the conductance map on either LSMO or LCMO.

A similar study by Capua *et al.* [15] also used spatially resolved STS on $La_{0.7}Sr_{0.3}MnO_3$ thin films, at 77 K and at room temperature. These thin films exhibited a metal-insulator transition at around 300 K. STM was performed in an inert helium environment rather than UHV: topographic images show a roughness of around 1.5 nm (peak-peak) over areas up to 400 nm^2. This represents a flatter surface than either Fäth or Becker *et al.*, though neither atomic resolution nor clear

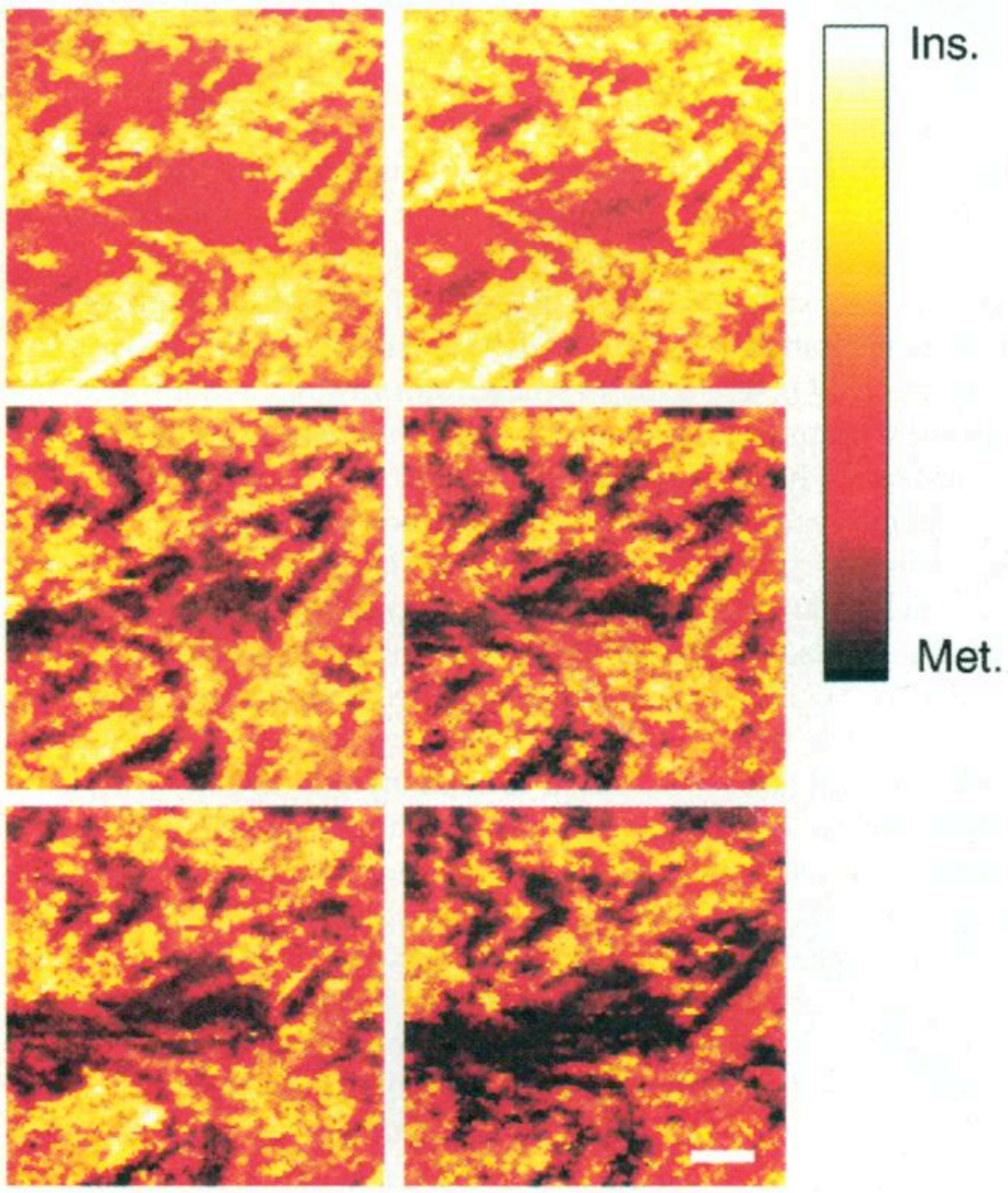

Figure 2.2: Conductance maps of $La_{0.73}Ca_{0.27}MnO_3$, 610 nm x 610 nm, bias voltage 3 V, various magnetic fields. [17]

images of atomic terraces are reported. dI/dV at zero bias was used to investigate LDOS variation. At 77 K, dI/dV maps were highly homogeneous: by contrast at 297 K large spatial inhomogeneities in dI/dV were observed. This was interpreted as phase separation in FM and PI domains, with the PI domains still observed slightly below the transition temperature. The typical size of the domains was 100-300 nm, much larger than the filaments observed by Becker et. al. [6]. It should be noted however that the films used by Capua et. al were flatter over a larger area than those used by Becker *et al.*, and also that additional small scale modulations in dI/dV over 10-20 nm were reported. The authors are confident that the observed effect is phase coexistence rather than observation of a chemical inhomogeneity, since in addition to the homogeneous spectroscopic maps seen at 77 K, there is a very low two dimensional correlation coefficient between the dI/dV maps and the simultaneously acquired topographic images.

It seems likely from STS studies that the FM to PI phase transition in LSMO and LCMO is a percolative one, with PI regions nucleating far below the transition temperature, possibly due to some structural disorder such as variations in oxygen content [17]. The existence of a percolative transition, and coexistence of metallic and insulating regions, seems to account for the observed broad metal-insulator transition [6]. However, a recent STS study [45] on $La_{0.7}Ca_{0.3}MnO_3$ films, indicated no phase coexistence near the metal-insulator transition at 268 K. These films were grown on a $NdGaO_3$ substrate, which is supposed to result in a less strained film than the $SrTiO_3$ substrate used by [17], or the MgO substrate used by [6]. This implies that the type of phase separation seen by Fäth and Becker is not intrinsic to cubic LCMO, but is strain-induced. It should be pointed out though that Fäth *et al.* [17] studied single crystal samples as well as films, and reported phase separation in both sets of samples. An STS study [85] using $La_{0.67}Sr_{0.33}MnO_3$ and $La_{0.7}Sr_{0.3}MnO_3$ films studied in ambient conditions reported no significant variation in dI/dV: it is suggested that phase separation reported in UHV studies such as [6] may be due to oxygen loss at the surface, which could produce insulating regions. However, STS studies performed in inert gas environments [15], which should not cause deoxygenation, also report phase coexistence.

It is worth noting that often metallic and insulating regions are assigned in a fairly arbitrary way, either by setting an explicit cutoff value in dI/dV [6] or by presenting a colour map of dI/dV values optimised for maximum contrast [17]. Thus it is

generally not clear if there is a continuous distribution of dI/dV values, or a genuinely bimodal distribution of density of states. Capua *et al.* [15] performed the most thorough analysis to demonstrate the existence of two distinct phases, and there does appear in this case to be a bimodal distribution of dI/dV values. In addition, at room temperature, the more conductive phase was found to have a similar dI/dV at zero bias to the homogeneous state at low temperature, lending support to the interpretation of this state as the FM phase. The surfaces which have been studied using STS are generally quite rough, with peak-peak roughness of 20-30 nm [6,17] or 1.5 nm [15]. Flat terraces are not seen, and atomic resolution is not achieved: this makes it difficult to verify the nature of the surface, which may be contaminated or damaged. This in turn makes it difficult to make any conclusions about the presence or absence of phase separation, since the effects seen may not be intrinsic to the material, but may arise as a result of contamination. Since these publications however, STS work has been done on some better defined manganite surfaces.

Recent STS work [57,58] has revealed an unusual phase transition in $Pr_{1-x}Pb_xMnO_3$. In this material in the range $0.23 \leq x \leq 0.32$, the metal to insulator transition and the ferromagnetic to paramagnetic transition do not occur at the same temperature. The electronic transition temperature T_{MI} is separated by up to 50K from the Curie temperature T_C. Between T_{MI} and T_C there is a paramagnetic metal (PM) region. The MI transition is relatively sharp, with a width of 15 K. Single crystal samples with $x = 0.32$ were studied using STM: flat terraces of unit cell height are observed in topographic images. At this doping $T_C = 210$ K and $T_{MI} = 255$ K. STS maps well above T_{MI} show homogeneous dI/dV, with a finite zero bias conductance (G_0): well below T_C, dI/dV are homogeneous with G_0 close to zero. The homogeneity here is determined by plotting a histogram of G_0 and demonstrating that it has a single narrow peak. Between T_{MI} and T_C, inhomogeneous STS maps are found: the inhomogeneities have a length scale of 2-3 nm. In this temperature range the G_0 histogram shows a much broader peak at finite conductance, and a weak peak at zero bias, indicating the presence of phase separation. (See figure 2.3). This is strongly indicative of the PM phase being formed from the coexistence of PI and FM regions. High resolution STM topographs taken at room temperature show stripe-like features with periodicity 4-5 Å: these are attributed to short-range ordering of Mn^{3+} and Mn^{4+}, *i.e.* a localised charge ordering. Mn^{4+} sites should appear bright in STM images of unoccupied states, due to localised holes.

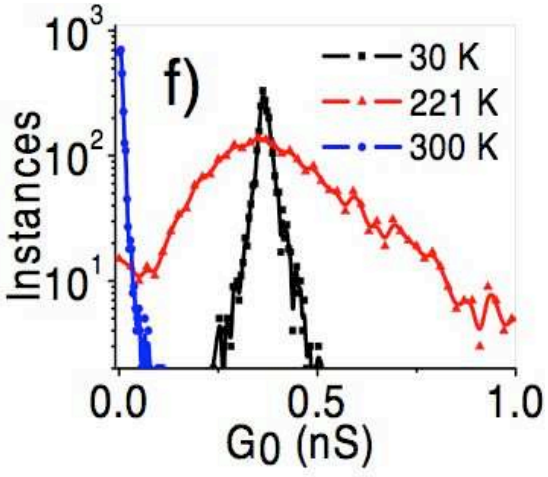

Figure 2.3: Histograms of zero bias conductance derived from STS data on $Pr_{0.68}Pb_{0.32}MnO_3$, at a range of temperatures. Note bimodal distribution of conductance at 221 K [57]

A more recent STS study on $La_{0.7}Ca_{0.3}MnO_3$ films [64] used strained films grown on $SrTiO_3$, which have a metal-insulator transition at $T_p = 147$ K. Atomic resolution could not be achieved in the STM topographic scans, but well-defined unit cell high terraces are observed. In the STS experiment gapped spectra were observed both above and below Tp: fully metallic spectra were not observed at any temperature, and a finite zero-bias conductance was only measured at 297 K. In the insulating regime above T_p, where transport is expected to be polaronic, the gap measured by STS is in agreement with the polaron binding energy estimated from the resistivity. The insulating gap is observed to narrow near Tp, but then increase again below the transition. This indicates that the charge carriers in the metallic phase are also polaronic, contrary to the standard model where polarons are unbound below the metal-insulator transition [44]. A similar effect was previously seen in bilayer manganites, see section 2.2.2. Conductance (dI/dV) spectra of $La_{0.7}Ca_{0.3}MnO_3$ show band edge peaks above and below Tp: these peaks are much sharper in the metallic phase, indicating a well-defined binding energy and hence a coherent polaron state. The temperature dependence of the gap in the metallic phase was found to be consistent with polaron binding energies obtained from optical reflectivity data. As the temperature is increased these band edge peaks soften: at 297 K they have vanished. This is interpreted as the melting of the coherent polaron state into a polaron liquid: this is consistent with neutron scattering data which indicated such

a melting transition at around twice T_p. At all temperatures, including close to the MIT, the distribution of gap values is found to be Gaussian, indicating no phase separation in this compound.

2.2.2 Atomically Resolved STM Studies of Perovskite Manganites

There are relatively few reports of STM studies of manganites which demonstrate atomic resolution, compared either to the number of non-atomically resolved STS studies, as discussed in the previous section, or to atomically resolved STM studies of cuprate superconductor materials [19].

Renner *et al.* [54] studied single crystal samples of $Bi_{1-x}Ca_xMnO_3$, with x = 0.76, using variable temperature STM and STS. This compound is a paramagnetic insulator (PI) at room temperature: upon cooling samples undergo a charge ordering transition at $T_{CO} = 250$ K, and a transition to an antiferromagnetic state at around $T_N = 120$ K [4]. The samples were prepared by cleaning the surface with ethanol before loading into the vacuum chamber. Atomic resolution could be achieved across terraces a few hundred nm^2 in area: at room temperature (299 K) a cubic lattice with spacing 3.8 ± 0.6 Å was observed, in good agreement with the X-ray diffraction lattice spacing of 3.77 Å. A larger square lattice of spacing $\sqrt{2}$ x 3.77 Å was also seen in room temperature scans, corresponding to a doubling of the unit cell along the cell diagonal. This unit cell doubling was observed to coexist with the normal lattice, and is interpreted as local CE-type charge ordering, *i.e.* segregation of Mn^{3+} and Mn^{4+} ions to alternate lattice sites. A height difference between Mn^{3+} and Mn^{4+} sites is expected, due to both the Jahn Teller effect, which will distort the oxygen octahedra about Mn^{3+} ions only, and the modulation of the tunnel current due to the different charge and orbital states of the Mn^{3+} and Mn^{4+} ions. Tunnelling spectra obtained on the $\sqrt{2}$ x $\sqrt{2}$ lattice areas were systematically more insulating than those on the normal lattice, as would be expected for a charge ordered state. In addition the magnitude of the energy gap in these areas was similar to that measured by optical spectroscopy in $Bi_{1-x}Ca_xMnO_3$ (x = 0.82) at 150 K, where the majority of the sample is in the CO state [38]. These data all support the idea that these unit cell doubled regions are local nucleations of the CO state at room temperature. STM topographic scans showing a phase boundary between a charge ordered area and a disordered (normal cubic lattice) area were obtained: (figure 2.4) such images are direct evidence for phase separation at atomic length scales.

STM topographic scans of $Bi_{0.24}Ca_{0.76}MnO_3$ performed at 146 K by Renner *et al.* [54]

reveal that the $\sqrt{2}$ x $\sqrt{2}$ lattice is the dominant atomic resolution feature below T_{CO}. The gap measured in STS on this surface is very similar to that measured in the CO regions at room temperature. At low temperature it also becomes possible to resolve a zigzag pattern in the atomic sites, where short and long interatomic distances alternate. The bright atoms in the STM images of the $Bi_{0.24}Ca_{0.76}MnO_3$ surface are thought to correspond to the oxygen atoms at the apex of the oxygen octahedra: the zigzag pattern is thus inferred to be direct imaging of tilting of the oxygen octahedra due to an orthorhombic distortion of the crystal (see section 1).

It should be noted that the CO state observed in (4) is consistent with a doping level of x = 0.5, *i.e.* a CE type state [21], whereas the nominal bulk doping of the sample is x = 0.76. Elsewhere on the surface of $Bi_{1-x}Ca_xMnO_3$ stripe-like patterns were in fact observed [55], with a periodicity of around 1.1 nm. This is close to the periodicity of the $2\sqrt{2}$ charge ordered stripe phase expected from X-ray diffraction data [71]. The stripe phase is only observed at low temperature: it has not been observed to coexist with the square lattice at room temperature, as has the $\sqrt{2}$ x $\sqrt{2}$ checkerboard lattice. The checkerboard charge ordered phase may be stabilised by defects or surface effects, explaining its appearance at doping x $\neq$ 0.5, and at room temperature.

An atomic resolution STM study of $La_{0.325}Pr_{0.3}Ca_{0.375}MnO_3$ has been made [42]. These films were made by laser MBE and were studied *in situ*. This compound undergoes a transition from a PI to a CO state at around 210 K [80]: STM measurements were performed at room temperature, with the films in the PI phase. Atomic resolution topographic scans were obtained, showing a cubic lattice of spacing 4 Å (figure 2.5). Filled state (positive tip bias) and empty state (negative tip bias) images were acquired simultaneously by using dual bias mode, where scans at two different bias voltages are interlaced. Two types of lattice sites were observed in the topographic scans, distinguished by a high or low height contrast. High contrast raised sites in the negative bias image were observed to become depressed sites in the positive bias image, corresponding to an increased tunnel current from unoccupied states and a decreased current from filled states. It is suggested that the high contrast sites are associated with Mn^{4+}, and the low contrast sites with Mn^{3+}. Since Mn^{4+} has an unoccupied e_g state, this will increase the tunnel probability at negative tip bias dramatically compared to the Mn^{3+} sites. At positive bias where the filled states are probed, the contrast is inverted since Mn^{3+} has an extra filled

e_g state. The contrast is also smaller at positive bias since both valence states have three t_{2g} electrons which contribute to tunnelling from filled states. Thus in this case STM allows localised doped holes to be imaged with atomic resolution.

A statistical analysis was performed on the positioning of the localised holes, to determine whether there is any tendency for the holes to order into a CE type charge ordered state, similar to that observed by Renner *et al.* [54]. Neighbouring holes along the [110] or [1-10] directions (see figure 2.5) were regarded as belonging to CE clusters, and holes with neighbours along the [100] or [010] directions to non CE regions. It was found that the observed hole distribution has a significantly higher proportion of CE clusters than a random distribution, indicating a tendency for nanoscale CE regions to form even well above the charge ordering transition.

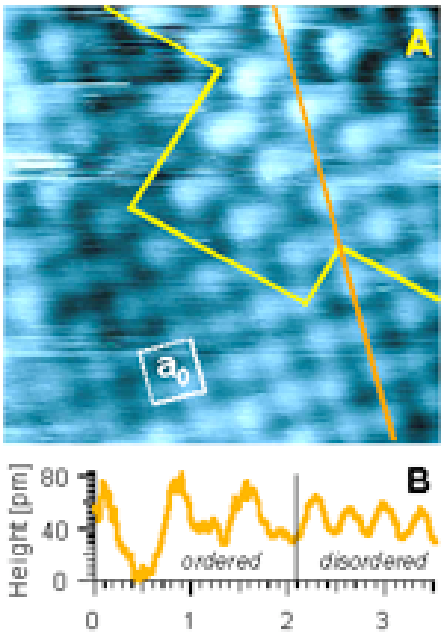

Figure 2.4: Coexistence of PI (disordered) and CO (ordered) states at room temperature. [54]

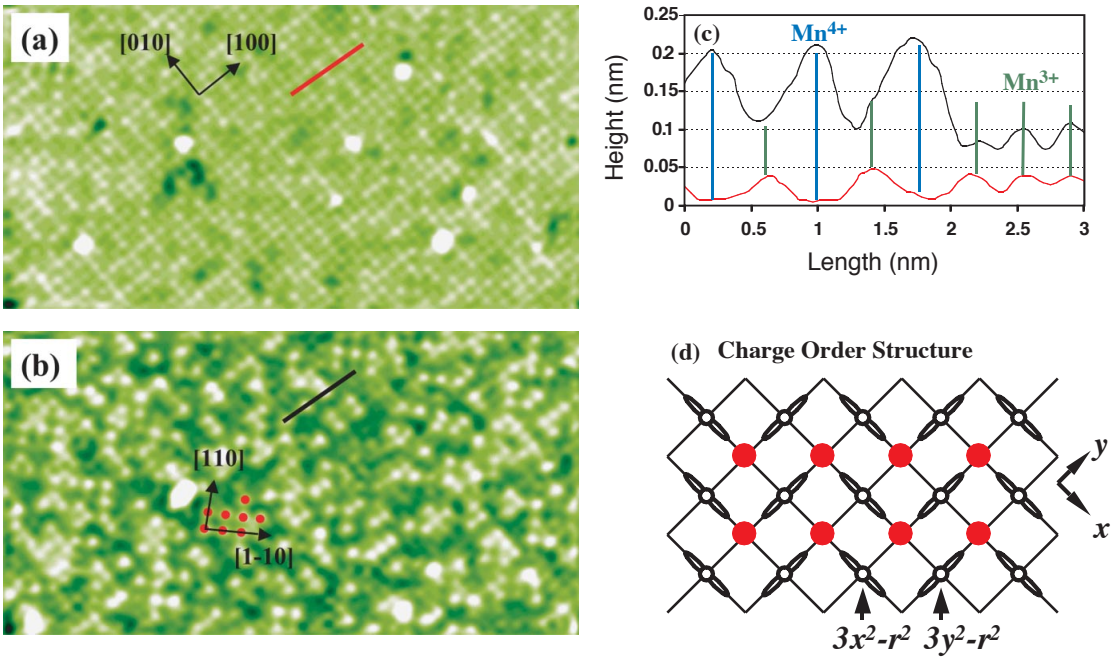

Figure 2.5: Dual bias images of LPCMO, showing occupied states (a) and unoccupied (b). Cross sections through both images are also shown (c), together with the CE-type charge ordered structure (d) [42]

2.2.3 STM Studies of Bilayer Manganites

All of the STM studies discussed so far have been performed on cubic (n=∞) perovskite manganites. Bilayer manganites – the 327 compound, with n = 2 – have been very little studied with STM. This is despite the fact that layered manganite compounds have a clear advantage for surface studies, since the crystals can be cleaved parallel to the bilayers. This allows a clean surface to be prepared in UHV by *in situ* cleave of a bulk single crystal sample. To date only one such STM study has been reported [59]. In this paper $La_{2-2x}Sr_{1+2x}Mn_2O_7$ single crystal samples with x = 0.3 were studied using variable temperature STM and STS, and also bulk electrical transport measurements.

The compound studied undergoes a transition at 90 K from a high temperature paramagnetic insulator phase, to a low temperature antiferromagnetic metal phase. As mentioned in section 1.6, this antiferromagnetic phase consists of ferromagnetic bilayers with antiferromagnetic inter-bilayer coupling. In the paramagnetic phase, below room temperature, the electrical resistance in the c direction ρ_c exhibits an insulator type temperature dependence ($d\rho/dT < 0$) while the ab direction resistance ρ_{ab} is metallic ($d\rho/dT > 0$). However, this behaviour does not continue to zero temperature: ρ_c drops sharply at the insulator-metal transition rather than diverging. This is not as expected since the pseudogap for interplane hopping will always be present, so the c-axis transport should always be thermally activated. A model to explain this inconsistency has been developed [59], by assuming a parallel conduction channel. The bilayer ferromagnetic domains will be of finite size, and may not coincide from layer to layer: therefore there will be regions where the local interlayer coupling is ferromagnetic and interlayer hopping is enhanced. Above T_C these crossover regions contribute only weakly to ρ_c since the spins are largely disordered: with decreasing temperature however a large portion of the c-axis conduction will be shunted via these regions along the metallic bilayers. This is shown schematically in figure 2.6a. By adding this parallel conduction channel to the thermally activated c-axis resistance, a good fit can be obtained for ρ_c across the whole temperature range (figure 2.6b).

In the STM study [59], it was found that an *in situ* cleave in UHV gave a clean surface, with atomically flat micrometre sized terraces. However, atomic resolution was not achieved across most of the surface: only in small (2-3 nm) regions could the

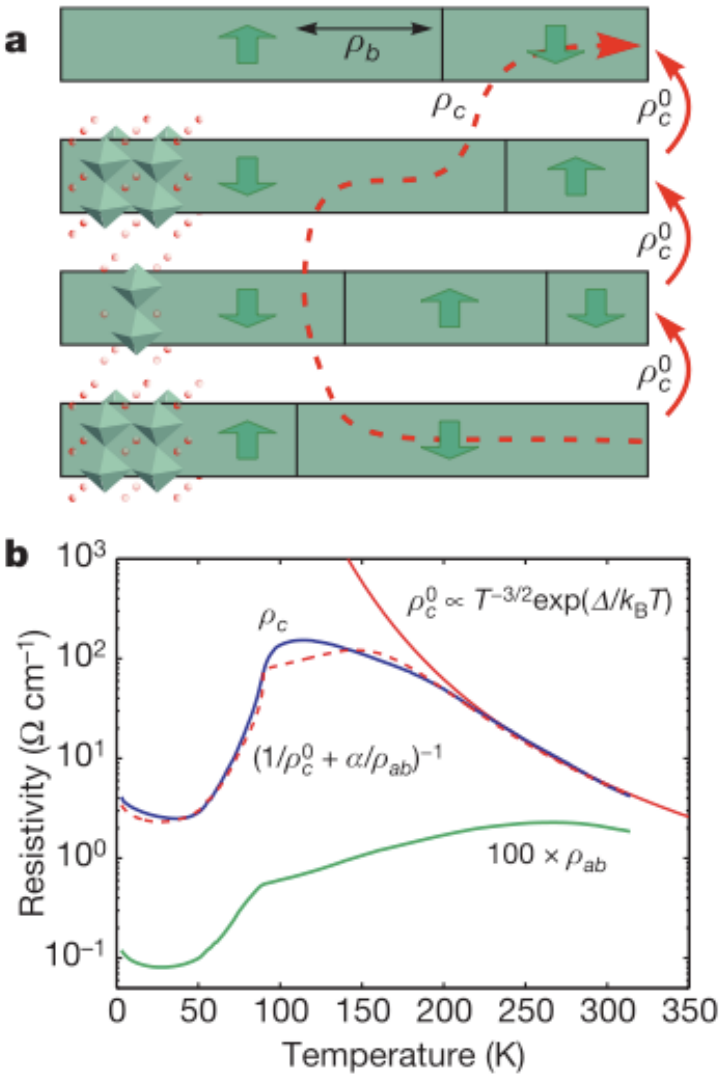

Figure 2.6: (a) domain model for c axis transport in $La_{1.4}Sr_{1.6}Mn_2O_7$ (b) ρ_c and ρ_{ab} as a function of temperature, with fits for ρ_c assuming purely activated behaviour (red) and a parallel in plane shunt resistance (dashed red) [59]

atomic lattice be seen. In these small islands though a cubic lattice of spacing 3.86 Å could be observed, in excellent agreement with the lattice spacing from diffraction experiments [30]. These islands were observed at various temperatures above T_C, in the paramagnetic regime. Extensive STS data were acquired, on both atomically resolved and non atomically resolved regions, at temperatures above and below Tc. Representative spectra at 44 K and 283 K are shown in figure 2.7a and b: the spectra measured are highly homogeneous. The zero-bias conductance as a function

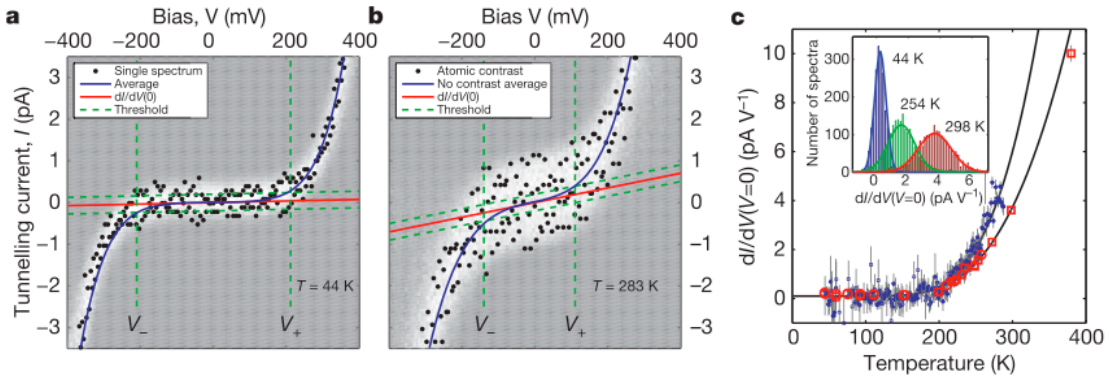

Figure 2.7: (a) STS of $La_{1.4}Sr_{1.6}Mn_2O_7$ at 44 K (b) at 283 K. White band is average data from many spectra: points are data from individual spectra. (c) Temperature dependence of zero bias tunnelling conductance: red points are averages from many spectra taken at fixed temperatures: blue are from single spectra taken whilst slowly warming [59]

of temperature is plotted in figure 2.7c.

It is obvious that the tunnelling spectra are gapped below T_C, in the metallic state: in fact the gap at 44 K is double that at room temperature, in apparent contradiction to the bulk conductivity data. Fitting a thermally activated conductance to the data (figure 2.7c) gives a gap of 196 ± 12 meV. This gap is consistent with the purely thermally activated part of the bulk c-axis conductivity, found to be 188 meV. The measured gap also corresponds to that measured by c-axis optical conductivity [26]. Both these results are evidence that the STS data are representative of the bulk sample and not some insulating surface state. The temperature dependence of the STS conductance is at odds with the bulk conduction result: this can be explained however since the parallel conduction channel cannot operate in an STS measurement, as the STS signal is dominated by the tunnel junction between the tip and the topmost bilayer. Only a bare electron can tunnel from sample to tip, so for polaronic transport a pseudogap will always be observed, since an energy equivalent to the polaron binding energy must always be supplied to extract an electron. This result indicates that in this compound the charge carriers are polarons both above and below the metal-insulator transition.

No spectroscopic difference between atomically resolved and non atomically resolved regions was observed in this study. In addition, the conductance distribution (inset,

figure 2.7c) has a single peak for each temperature studied, so there is no evidence for phase separation in this material. The general inability to resolve atomic features across much of the $La_{1.4}Sr_{1.6}Mn_2O_7$ surface is explained as being due to screening: if transport within the bilayers is metallic then charge screening will reduce the atomic contrast to below measurable levels [59]. The atomic resolution islands would therefore represent regions where screening is locally relieved, perhaps due to some lattice defect. Since the charge carriers in the bilayers are polarons, these islands may be viewed as polarons trapped by lattice defects: indeed the size of the islands is similar to the polaron size as measured by neutron and X-ray scattering [8, 51].

2.3 Open Problems in Research on Manganite Surfaces

This section will summarise the existing state of research in manganite surfaces, with a particular emphasis on STM results.

- Phase separation. In principle STM and STS studies are ideal for investigating the nature of phase separation of metallic and semiconducting phases in manganites, since they allow the local density of states to be probed with very high spatial resolution. However, as noted in section 2.2.1 many of the STS studies published showing phase separation [6, 15, 17] suffer from major flaws, and have been disputed [45, 65, 85]. The most serious problems are the high surface roughness of the materials studied, and the lack of a true bimodal distribution of gap or conductance values. The demonstration of such a bimodal distribution, collected on a well-defined surface showing either atomic resolution or clear atomic terraces, would constitute reasonable evidence for phase separation. To date the work by Rößler *et al.* [57] on $Pr_{1-x}Pb_xMnO_3$ comes closest to satisfying these criteria. This may be regarded as a special case, since phase separation in this compound was observed in the paramagnetic metal phase between T_{MI} and T_C. Phase separation of charge-ordered and disordered regions has also been observed in $Bi_{1-x}Ca_xMnO_3$ [54], but tracking the development of phase separation through the metal-insulator transition by STM and STS remains an outstanding challenge.

- Charge ordering. For $La_{1-x}Ca_xMnO_3$ with $x \geq 0.5$ an incommensurate charge ordering has been found [40], by electron diffraction. This suggests that charge ordering may be regarded as charge density wave, with a much smaller difference in charge between Mn ion sites than in the traditional CE-type model, involving spatial segregation of Mn^{3+} and Mn^{4+} charges [21, 52]. However, for $Bi_{1-x}Ca_xMnO_3$ with $x = 0.76$ [54], STM imaging showed a charge ordered state similar to the CE-type model. Further high-resolution STM imaging on other manganite compounds may reveal whether charge ordered states are commensurate or incommensurate with the atomic lattice. Possibly, some compounds exhibit CE-type order, and some a charge density wave type order.

- Surface electronic properties compared to bulk properties. In some cases the surface of manganites may show different properties to the bulk: Freeland *et al.* [20] demonstrated using X-ray and point contact data that the topmost layer of a ferromagnetic, metallic bilayered manganite may behave like a non-magnetic insulating layer. However these data were not obtained under UHV conditions, and samples were cleaving in air, raising the possibility of surface contamination. The result is contradicted by spin-polarized scanning electron microscopy results which show that the top layer is ferromagnetic [31], and by the close agreement of STS, bulk transport and optical data [59], indicating that the surface layer has similar electronic properties to the bulk. Clean-surface, UHV STM data on further manganite compounds, combined with bulk probes, will demonstrate whether this is a typical result.

- Surface defects. Surface defects, for example oxygen vacancies, have a profound effect on the electronic structure of oxide surfaces and have extensively studied in other systems (for example, TiO_2: for a comprehensive review see [16]). In particular, defects may play a crucial role in pinning charge carriers such as polarons [59]. To the best of the author's knowledge vacancies have not been studied on manganite surfaces using STM.

- Surface preparation. The reliable preparation of clean, atomically flat surfaces in UHV is one of the major challenges for STM on manganites, and also for the fabrication of devices based on manganites. Layered manganites ought to provide a method for clean surface preparation, by cleaving single-crystal samples *in situ*. However, few reports have been published on STM on such materials [59, 73]. This may be contrasted with the situation with the layered cuprate superconductors, where a large body of atomic resolution STM data exists. (For a review on STM on high-T_c superconductors see [19]). The reason for this apparent difficultly in cleaving layered manganites, compared to cuprates, is not apparent.

- Technological applications for manganites. Giant Magnetoresistance (GMR) and Tunnelling Magnetoresistance (TMR) sensors in hard disk read-write heads have been phenomenally successful (for a recent review on GMR see [77]). Colossal magnetoresistance manganite materials are unlikely to replace GMR devices in read-write heads in the foreseeable future, due to the high

magnetic fields they require to operate. However they may find applications in magnetic sensors and large area input devices, where the use of a homogeneous magnetoresistive material would be advantageous. Manganite-based electroresisistive devices are currently being developed (see section 1.8) and may be used as Resistive RAM elements [60], or memristors [70].

Chapter 3

Experimental Equipment

3.1 STM Systems

Three scanning tunnelling microscopes were used for experiments on bilayer manganites: all three are operated in an Ultra High Vacuum (UHV) of 10^{-10} mbar or better: they can also all be operated at low temperature. The Oxford Instruments UHV STM was initially a commercial instrument, but has been extensively modified. The LT-STM and the Cryogenic STM are commercial instruments built by Omicron Nanotechnology[1] and have been used without substantial modification. The Cryogenic STM did however require lengthy commissioning and testing, which is described here.

3.1.1 The Oxford Instruments UHV STM

The Oxford Instruments UHV STM was originally designed by Oxford Instruments[2], according to specifications provided by Prof. G. Aeppli[3], and was first assembled in 1998 at NEC labs in Princeton. The system has been substantially rebuilt by Prof. C. Renner[4]: this STM has already been used for several studies of manganites [54, 55, 59]. The STM stage consists of a piezo tube scanner and a single-axis piezo slip-stick drive for coarse tip approach. The vacuum system consists of two main chambers, one housing the STM: the other is a preparation chamber housing a sample heater, allowing samples to be vacuum annealed, and an Argon ion sputter gun for cleaning sample surfaces. A third chamber opening from the preparation chamber is a fast-entry load-lock. Both tips and samples can be exchanged in vacuum using a wobblestick: all three chambers (STM, preparation and load-lock) have sample carousels allowing several samples and tips to be loaded and stocked in UHV. The base pressure in the STM chamber is around 10^{-10} mbar: to achieve this pressure the system is baked to 110° C for around 72 hours. The STM can be cooled using a flow cryostat, which can be operated using liquid helium or liquid nitrogen. Base temperature at the sample is around 5 K when using liquid helium. A heater is mounted close to the helium bath, to allow the STM temperature to be controlled: temperature control is provided by an Oxford Instruments ITC unit, and stable

[1] Omicron NanoTechnology GmbH, Limburger Strasse 75, D - 65232 Taunusstein, Germany
[2] Oxford Instruments plc, Tubney Woods, Abingdon, Oxfordshire OX13 5QX
[3] London Centre for Nanotechnology, London WC1H 0AH
[4] Department of Condensed Matter Physics, University of Geneva

temperatures can be achieved anywhere between 5 K and 400 K by careful choice of the cryogen flow rate and the control PID settings. A 100 L helium dewar will last for around 3 days with the STM at 5 K, or around two weeks with the STM at 50 K. The STM sample stage and scanner are fully shielded by two concentric thermal shields: the stage, scanner and inner shield are all held at the same temperature, providing good temperature stability.

Upon initial installation in the Physics Department at UCL some problems were identified with the UHV STM. The main problem was with excess low-frequency vibrational noise being transmitted to the STM: this noise could be observed in STM topographic scans and STS spectra. The primary frequency observed was around 2 Hz. Two reason were identified for this problem: firstly the vibration environment of the Physics building, and secondly resonances within the vibration isolation system used on the STM. A vibration survey showed that the Physics building generates substantial vibration noise in the 2 Hz range: this is common in older buildings and is supposed to be due to the movement of large numbers of people around the building, particularly up and down stairs. The vibration isolation system initially installed on the Oxford UHV STM consisted of in-vacuum spring suspension with eddy current damping for the STM stage, plus the entire vacuum system was mounted on an air table, similar to an optical bench. Unfortunately the resonant frequencies of the air legs and the in-vacuum spring suspension were similar, and both close to 2 Hz. This caused the low frequency vibrational noise at the floor to be *amplified* by the vibration isolation system. Running the STM with either the spring suspension clamped or the air legs deflated was not desirable since this resulted in an increase in high frequency noise: therefore it was decided to replace the air table with a new active damping table.

Active damping is able to offer superior vibration isolation at low frequencies (1-10 Hz) compared to passive damping (air legs or springs). An active damping unit consists of springs which support the weight of the system, a piezoelectric accelerometer and electromagnetic actuators. A control unit monitors the vibration of the unit via the accelerometer: a feedback circuit supplies a signal to the actuators in antiphase with the vibration, to cancel it out. Active damping units and a custom welded frame for the Oxford UHV-STM were sourced from Halcyonics[5]: design work

[5]Halcyonics GmbH, Tuchmacherweg 12, D-37079 Goettingen, Germany: supplied by Stratton Technologies, 45 London Road, Biggleswade, SG18 8ZN, UK

on the active damping system was done by Dr. Charles Bird. The installation of the active damping system coincided with the move into new laboratories in the London Centre for Nanotechnology: these labs have been purpose built to provide a low-vibration environment. The active damping table was installed in the new lab: the STM was dismounted from the old air table, transported to the new lab and reassembled on the new damping table. Vibration measurements were made in the new lab using an accelerometer: figure 3.1 shows the results of this measurement. Vibration along the vertical axis is shown, in velocity units (μm/s), measured on the floor and on top of the table, with the active damping on and off. The noise spectrum on the floor shows a broad peak around 6 Hz, rather than 2 Hz in the case of the old Physics lab: this may be attributed to the improved vibration environment of the new Nanotechnology building. The table with the active damping off can be seen to amplify this vibration: in this case it is behaving like a simple damped resonator, as it is a sprung table: presumably the resonant frequency of the table is close to 6 Hz. Turning on the active damping produces a dramatic decrease in transmitted vibration in the range 2-100 Hz. The maximum reduction is seen at 7.5 Hz, where the velocity drops by a factor of 200 upon activating the damping. Above 100 Hz the damping is not effective: however in this range the spring suspension of the STM should be able to efficiently damp vibrations. Thus the two vibration isolation systems complement each other, being effective in different frequency ranges and having no resonances between them.

The control electronics of the Oxford STM have also been upgraded. Initially the system used the Oxford Instruments TOPSystem controller, with a proprietary variable-gain preamplifier. The control unit was not found to be reliable, particularly when collecting STS maps: often the controller would crash during a scan. In addition the preamplifier introduced excess electrical noise: the design consisted of two amplifier stages, one close to the STM with a fixed gain of 10^7 Ohms and another separated by 1 m of cable providing additional variable gain from zero to 10^3, plus filtering. This has the advantage of variable gain, but noise picked up between the two stages can be amplified at the second stage. It was therefore decided to completely replace the control unit and the preamplifier. Largely for reasons of compatibility with the other STM systems being purchased, an Omicron Nanotechnology MATRIX control unit was sourced to control the Oxford STM. A commercial fixed-gain preamplifier was also purchased from Femto: this provides 2x10^9 Ohm

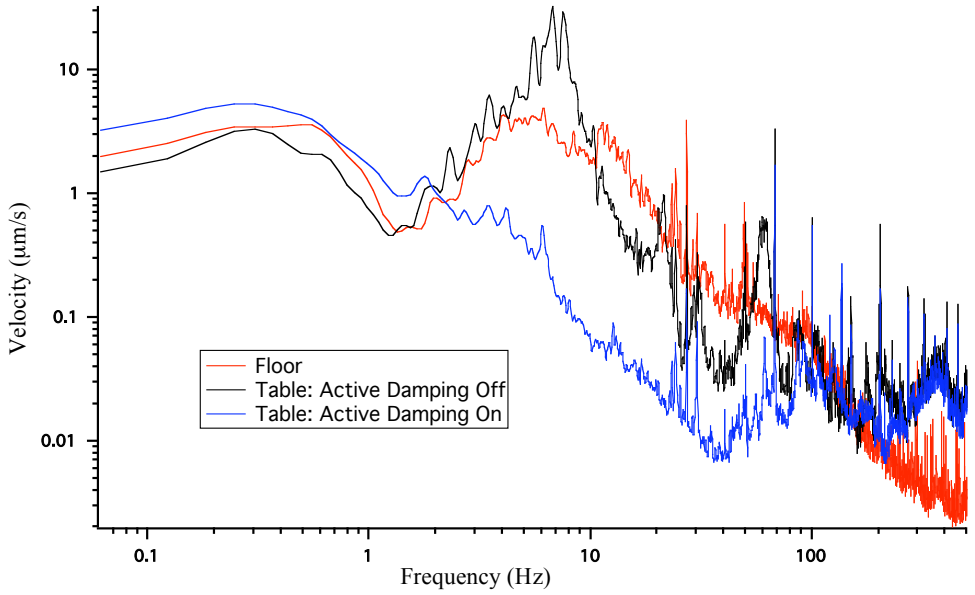

Figure 3.1: Vibration about the vertical axis in the Nanotechnology Lab, plotted in velocity units. Vibration levels were measured on the floor, on top of the vibration isolation table with the active damping off, and on top of the table with the active damping on.

gain. Integrating the Oxford STM with the MATRIX was largely a matter of ensuring that the voltage range and polarity of the signals supplied by the MATRIX to the piezos was suitable: this could be achieved by adjusting the hardware and software settings of the MATRIX to match the old TOPSystem (see appendix A.3). This was possible since the STMs produced by Omicron have a similar architecture to the Oxford STM, with a piezo tube scanner and piezo slip-stick drives for coarse positioning of the tip. The only major problem encountered was that the MATRIX supplies separate X,Y and Z voltages to the tube scanner, whereas the Oxford STM requires Y+Z and X+Z signals. This is because the Omicron STMs have a separate Z electrode, along the centre of the scan tube: in the Oxford STM this electrode is grounded. For testing purposes therefore an adapter circuit board was assembled: this uses operational amplifiers to add the Z signal to the X and Y signals inside the MATRIX. The function of this board is illustrated schematically in figure 3.2. The circuit board sums the Z signal from the feedback controller and the X and Y signals from the raster scan generator, before the signals are amplified: the amplifier inverts the -X and -Y signals, so the required signals from the adapter circuit are

(X/Y + Z) and (X/Y - Z).

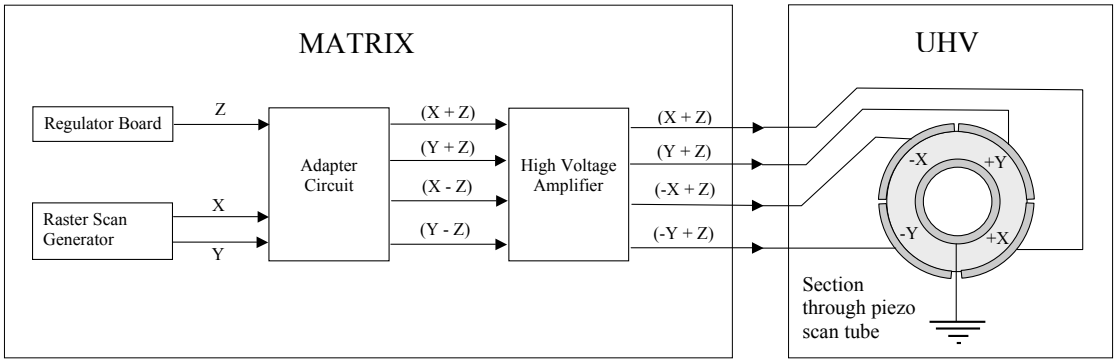

Figure 3.2: Schematic showing function of adapter circuit for Oxford STM MATRIX control unit. The arrangement of electrodes at the piezo scan tube is shown: on Omicron STMs the Z signal is carried by the central electrode, which is earthed here. Note that the high voltage amplifier inverts the (X-Z) and (Y-Z) signals

Once it was established that the MATRIX could be used with the Oxford STM, a modified high voltage amplifier was supplied by Omicron which adds the Z signal into the X and Y signals in the same way as the adapter board, so the board is no longer required (for settings see appendix A.3). The MATRIX unit has subsequently proved to be reliable: it also offers additional scan modes such as dual mode, where different bias voltages are applied when scanning forward and backward, allowing scans at two different biases to be interlaced.

In summary, the Oxford STM has been substantially upgraded, to reduce both vibrational and electrical noise, and provide improved reliability. The MATRIX control unit provides compatibility with the LT-STM and Cryogenic STM control systems, and allows for scan modes such as dual mode.

3.1.2 The Omicron Nanotechnology LT-STM

The Omicron Low Temperature STM (LT-STM) is a commercial UHV STM which can be operated at cryogenic temperatures. The design shares many features with the Oxford STM: there are separate STM, preparation and load-lock vacuum chambers, the STM stage is vibrationally isolated using springs and eddy current damping, and the STM head is surrounded by concentric thermal shields so that the scan tube, sample and innermost shield are held at the same temperature. The STM scanner is a piezo tube design, and there are piezo slip-stick drives to prove coarse positioning of the tip. Vacuum performance is better than the Oxford STM, with the base pressure better than $5x10^{-11}$ mbar in the STM chamber. The vacuum system is baked to 150°C to achieve this pressure. The STM is cooled using a storage cryostat rather than a flow cryostat: this can be operated using liquid nitrogen or liquid helium. The cryostat consists of an inner tank which can be filled with nitrogen or helium, which cools the STM and innermost shield, and an outer jacket which is filled with nitrogen: this cools the outer thermal shield and reduces thermal load on the inner tank. The advantage of a storage cryostat is that it is simpler to operate and easier to achieve a stable temperature, since active temperature control is not necessarily needed: also no pumps are required, which may introduce vibrational noise. The disadvantage is that the full temperature range is not accessible. A heater is mounted on the STM stage for temperature control, but for example, counter heating when cooling with liquid helium to achieve an STM temperature of 50 K will result in excessive helium consumption. Attainable temperature ranges are 4.5 K to 50 K and 77 K to 200 K using liquid helium and nitrogen respectively: the STM can also be operated at room temperature, but cannot be operated higher than 300 K. When running at helium temperature the helium must be refilled every 24 hours, or more often if the sample is exchanged: nitrogen must be refilled every 18hrs. When running at nitrogen temperature the inner tank can hold for 3-4 days, but the outer jacket will still boil off in 18 hrs.

The Omicron STM has some features which are particularly useful for the study of layered manganites. Firstly, full X-Y-Z positioning of the tip is possible thanks to orthogonal piezo slip-stick drives. An in-vacuum cleave of a layered manganite may not yield a homogeneous surface: some areas of the surface may be rough and unsuitable for STM. With the Oxford STM only approximate positioning in the X

direction can be done, by shifting the sample on the STM stage using the wobblestick: often a well-cleaved part of the sample surface would remain inaccessible. The X-Y tip positioning of the LT-STM means that if any part of the sample presents a good surface, it can be accessed: this allows experiments can be done more reliably. The second feature is a cold cleaving stage. In the Oxford STM, although samples can be studied at low temperature, layered samples are always cleaved at room temperature: in some cases a sample surface exposed in vacuum at room temperature may not be stable, as it may undergo some sort of surface reconstruction. The LT-STM features a cleaving stage which can be cooled with liquid helium using a flow cryostat: samples can be cleaved at less than 20 K and rapidly transferred to the STM stage using the wobblestick. It is possible to transfer the sample without its temperature rising above 77 K, by clamping the wobblestick to the sample plate whilst it is cooled: the STM temperature is observed to drop from 77 K when the sample is loaded in this way, showing that the sample is cooler than the STM stage.

Sample preparation such as annealing can be carried out on the manipulator on the LT-STM system, either in the STM chamber or the Prep chamber. Silicon samples can be prepared by direct current heating: Si(111) or Si(100) provides a useful test sample for calibration and tip preparation. The manipulator can also be cooled using a liquid helium flow cryostat to around 20 K. A Low Energy Electron Diffraction (LEED) screen is fitted to the preparation chamber, allowing surface diffraction studies to be undertaken. As the manipulator can be cooled and heated, LEED can be done at a range of temperatures.

3.1.3 The Omicron Nanotechnology Cryogenic STM

The third STM in the London Centre for Nanotechnology laboratories is the Omicron Nanotechnology Cryogenic STM. This is a specially commissioned instrument, unlike the LT-STM which is essentially "off the shelf". The Cryogenic STM features a three-axis superconducting magnet: this can apply a field of 6 T perpendicular to the sample surface (Z direction), or 1 T in either direction parallel to the surface (X & Y directions). The maximum combined field which can be applied is 2 T in the Z direction plus 1 T in each of the X and Y directions. A field of up to 1 T can therefore be applied in any direction. The STM stage can be cooled to 2 K, and is held in UHV at better than $5x10^{-11}$ mbar. In addition to the low-temperature performance, the temperature of the STM can be varied continuously between 2 K and 350 K: the magnetic field can still be applied with the STM head at any temperature in this range. Thus the Cryogenic STM provides full access to the phase space of temperature and magnetic field.

To achieve this temperature and magnetic field performance a complex cryogenic system is required: an Oxford Instruments cryostat is used. The STM was integrated with the cryostat by Matthias Fenner at Omicron Nanotechnology in Taunnstein: the whole system was then shipped to the London Centre for Nanotechnology and reassembled. A schematic of the cryogenic system is shown in figure 3.3. The cryostat comprises a tank holding 135 litres of liquid helium, in which the magnets are immersed. There are three magnet coils, one 6 T solenoid to provide the vertical (Z axis) field and two 1 T split coils to provide the horizontal (X & Y) field. The helium tank is surrounded by a liquid nitrogen jacket, to reduce the thermal load on the helium, and a vacuum space (Outer Vacuum Can) for insulation. A UHV tube is inserted through the bore of the cryostat: the STM is suspended inside this tube. A UHV chamber (STM chamber) is located underneath the cryostat: to exchange tips and samples, the STM is lowered out of the cryostat using a large Z-manipulator (fig. 3.3, no. 11), into the STM chamber where there is a wobblestick. To reach low temperature the STM is raised back into the cryostat: there are spring-loaded thermal doors (12) which close behind the STM once it is raised, ensuring there is no line of sight from the warm STM chamber into the cryostat. The STM is cooled by a helium pot (4), which is fed with a capillary (3) from the main helium tank: the flow of helium is controlled by a needle valve (1) controlled by a stepper motor

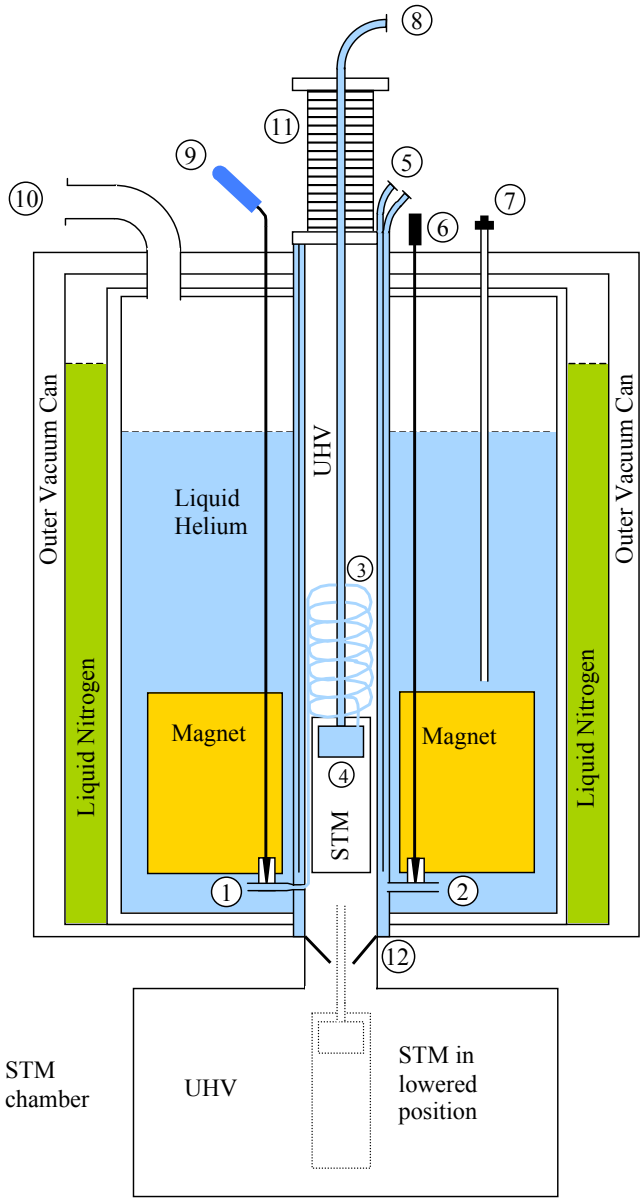

1. Auto Needle Valve for STM Helium pot
2. Manual needle valve for annular space
3. STM Helium capillary
4. STM Helium pot
5. Pumping ports for inner and outer annular spaces (2 x KF 16)
6. Manual needle valve control
7. Helium siphon port
8. Pumping port for STM helium pot (KF 25)
9. Auto needle valve motor
10. Helium vent port (Large KF)
11. Z manipulator
12. Thermal doors

Figure 3.3: Schematic of the Cryogenic system of the Omicron Cryogenic STM. The areas coloured blue comprise the helium space, nitrogen space is green

(9). To allow for the movement of the STM the capillary is coiled inside the UHV tube. The STM helium pot is pumped via a KF flange on top of the Z-manipulator (8). The Oxford Instruments cryostat allows for room-temperature bore operation: the UHV tube is in fact a triple walled tube, which encloses two annular pumped helium spaces within the walls of the tube. A second needle valve (2) admits helium from the main tank into both annular spaces, which are joined at the bottom: the helium spaces are pumped via two separate KF flanges at the top of the cryostat (5). The helium flow through the annular spaces is controlled manually via the needle valve and by regulating the pumping pressure. The UHV tube can thus be cooled to liquid helium temperature, separately of the STM head. This allows the STM to be cooled to 2 K, as it is very well thermally shielded. It also allows the STM to be run at higher temperatures under a magnetic field, without causing excessive boil-off of liquid helium from the magnet tank, as the UHV tube shields the magnet tank from the warm STM.

The cryogenic STM head itself is of a highly compact cylindrical design to fit inside the UHV tube. The STM is suspended from the helium pot on springs to provide vibration isolation: no eddy current damping system is fitted however, due to the requirement that the head be non-magnetic. A heater is mounted on the STM head to allow the temperature to be controlled. The STM scanner is a piezo tube design, similar to the other two STMs: coarse motion is provided by two orthogonal piezo slip-stick drives. These move the sample stage in the Z and X directions only: full three-dimensional positioning as with the LT-STM is not possible. With the STM lowered into the STM chamber, two clamps mounted on the chamber are used to hold the STM head fast so that tips and samples can be exchanged, using the wobblestick.

The cryogenic STM chamber is attached to a preparation chamber and load-lock in a similar way to the LT-STM and Oxford STM. A manipulator with sample heating capability is mounted on the preparation chamber to allow samples to be annealed in vacuum. No cold cleaving stage or cooled manipulator is fitted however. To achieve UHV conditions the whole UHV system must be baked to at least 110° C: this presents unique challenges due to the cryogenic system. The UHV tube running through the cryostat must be baked, in addition to the STM and preparation chambers, and the Z-manipulator on top of the cryostat. Baking the UHV tube is achieved by blowing hot compressed air through the annular spaces. This is the

reason for a triple walled UHV tube with two annular spaces: during bakeout the needle valve (figure 3.3, no. 2) is closed and hot air at 195° C is pumped into one of the pumping ports (5) and allowed to escape through the other. The rest of the system is baked using electric heaters and removable insulation panels, plus integral heaters mounted on the thermal shield at the base of the cryostat. The vacuum chambers are baked to 145° and the cryostat thermal shield to 110°. The STM stage is heated by the UHV tube, and typically reaches 130-135°: the STM heater (normally used to control the STM temperature during cryogenic operation) can be used additionally to boost the STM temperature to 145°. Although the cryostat is heated by its integral heaters and the UHV tube during bakeout, the superconducting magnets cannot be allowed to warm up much above room temperature, as this could damage their electrical insulation. Therefore during bakeout the magnet tank is filled with liquid nitrogen to keep the magnets cool: due to the hot environment of the cryostat about 50 L of nitrogen boils off per day, so it must be kept topped up during the bake.

The Cryogenic STM has largely been used as supplied, with minimal modifications so far. One alteration that has been made is to increase the capacity of the load-lock. Originally there were no positions in the load-lock where samples or tips could be stocked, meaning that only one tip *or* one sample could be loaded at a time, leading to a very slow turnaround time for experiments. Therefore a simple insert was constructed for the load-lock to allow two tips and one sample to be stocked. This is illustrated in figure 3.4. The insert comprises a stainless steel arm which can be inserted into the load-lock via a 51 mm travel UHV manipulator. A tip stage machined from oxygen-free Copper and a sample stage are fixed to the end of the arm. The load-lock wobblestick is used to load samples and tips onto the positions provided: the insert can be moved out of the loadlock using the manipulator, allowing samples and tips to be transferred to the preparation chamber.

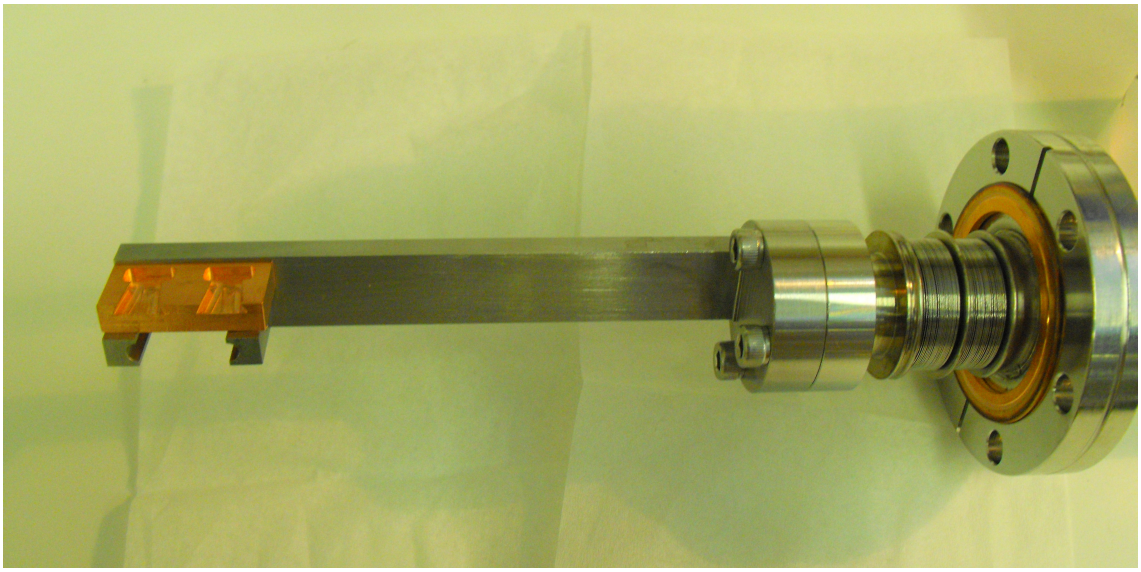

Figure 3.4: Load-lock insert fabricated for the Cryogenic STM

3.1.4 Cryogenic STM Testing

A thorough series of test experiments were carried out on the Cryogenic STM, to ensure that it was operating correctly. The objectives were to test that atomic resolution could be achieved, that spectroscopy could be performed at high spatial and energy resolution, and that the cryogenic system and superconducting magnets were performing properly. It was decided to use 2H-$NbSe_2$, a layered superconductor, as a test sample. This compound is a type-II superconductor with $T_c = 7.2$ K: it also shows a surface charge density wave (CDW) state below 33 K [24]. This CDW has a periodicity $\approx$ 3a where a is the hexagonal lattice spacing of 3.45 Å. The NbSe2 samples were grown by Helmut Berger[1]. $NbSe_2$ samples can be cleaved in UHV, giving atomically flat terraces $> 1\ \mu m^2$. Atomic resolution can readily be achieved at a wide range of temperatures from 1.3 K to 300 K [53].

A $NbSe_2$ crystal was mounted onto a sample plate using conducting epoxy[2]: a cleaving post, consisting of a cylinder of magnetic stainless steel (10 mm long x 2 mm diameter), was mounted onto the top of the sample. The sample was loaded into the STM chamber of the Cryogenic STM: the wobblestick was then used to knock the cleaving post off, cleaving the sample and exposing a fresh uncontaminated surface. The sample was then loaded to the STM stage, which was then raised into the cryostat to enable low-temperature operation. A W tunnelling tip was used: this was prepared by AC electrochemical etching in KOH (see section 4.2.1).

Figure 3.5a shows a 7 x 7 nm constant current STM topographic image of $NbSe_2$, taken at a bias voltage of 50 mV and a tunnel current of 50 pA, at a temperature of 2.33 K. Low-frequency noise is visible in the image as near-horizontal stripes. Figure 3.5b shows the same image, after selective Fourier filtering has been used to remove the noise signal. Atomic resolution can be observed, together with the $\approx$ 3a charge density wave. A lattice defect can also be seen in the image. As can be seen from image 3.5a, the low frequency noise signal is substantial. The noise signal is contained in the difference between the raw image and the Fourier filtered image: by analysing this image, the noise can be measured. The primary frequency is found to be 5.5 $\pm$ 0.3 Hz, and the amplitude is 17 pm peak-peak (6 pm RMS). This is comparable to the measured atomic corrugation of 10 pm peak-peak, so

[1] EPFL, Lausanne, Switzerland

[2] Epo-Tek 4110 conducting silver epoxy

the noise can "swamp" the atomic signal. The most likely source of this noise is coupling-in of external vibrational noise, similar to that experienced on the Oxford STM. As we have seen in section 3.1.1 the floor in the Nanotechnology labs is found to supply vibrational noise in a wide band around 6 Hz. This frequency may not be effectively damped by the Cryogenic STM's air legs, nor by the integral spring suspension, which as noted (section 3.1.3) does not include eddy current damping. Fortunately the 5.5 Hz noise is found to be intermittent, indicating that it is driven by some variable source of noise e.g. heavy traffic outside the laboratory. Also some tunnelling tips seem particularly sensitive to the low-frequency noise, perhaps due to lower rigidity. Finally, to some extent the effect of the 5.5 Hz noise on collected data can be avoided by careful choice of imaging scan rate, or voltage ramp speed for tunnelling spectroscopy. This approach has been adopted for data collected on manganite samples.

Having verified that it is possible to achieve atomic resolution at low temperature, despite low-frequency noise pickup, the next step was to test the operation of the STM under magnetic field. Image 3.5c shows an unfiltered 12.4 x 12.4 nm STM topographic image taken at 2.48 K and a magnetic field of 6 T in the z-axis: the bias voltage is 20 mV and the tunnel current 100 pA. Atomic resolution here is very clear, and there is no sign of low-frequency noise, so clearly the operation of the STM is not impaired by operation in magnetic field. Three defects can be seen in the image, but the CDW is not clearly visible: there may be a multiple tip effect, as the defects show a similar, extended shape. After acquiring this image, the tip was retracted, the magnetic field ramped down to zero, and tunnelling was re-established at the same sample location. Image 3.5d shows the same area as 3.5c, at zero field. Three effects are apparent: firstly very little drift has occurred in ramping the field from 6T to zero, as the same defects are visible: cross-correlation analysis indicates that the tip has moved by less than 0.5 nm relative to the sample. This indicates that the the non-magnetic construction of the cryogenic STM head has been successful. Secondly the zero-field image is much noisier: this includes low-frequency noise at around 6.5 Hz. This implies that the application of magnetic field actually stabilises the STM stage: this may be due to eddy currents being induced in the STM head. The effect of the applied magnetic field on the tunnel current noise is examined in more detail in appendix A.1.

As a final test, vortex imaging on $NbSe_2$ was attempted using the Cryogenic STM.

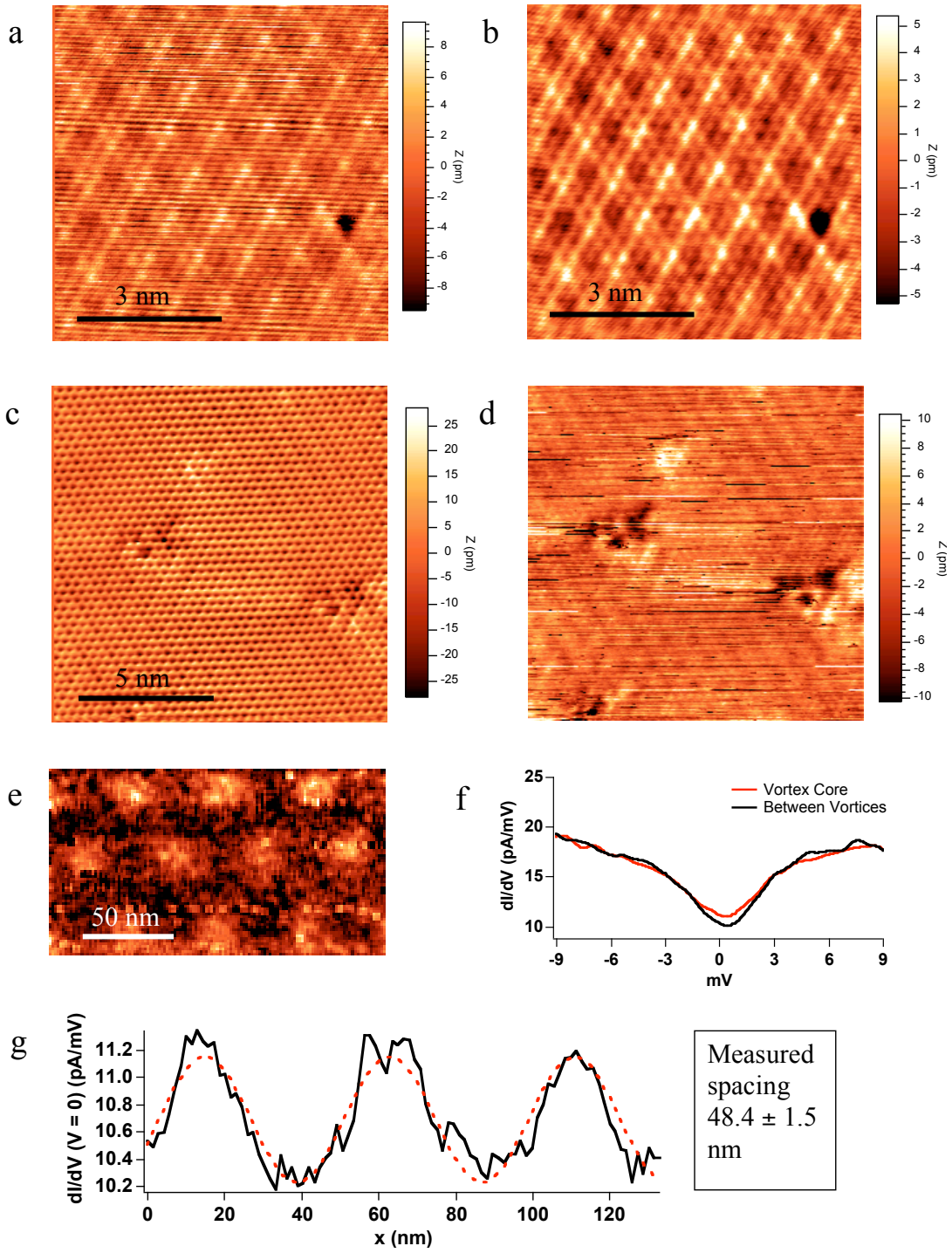

Figure 3.5: Testing the Cryogenic STM using $NbSe_2$. See text for details

$NbSe_2$ is a type-II superconductor, and as such has two critical magnetic field strengths below T_c, H_{c1} and H_{c2}. For $H < H_{c1}$ the material is superconducting: for $H > H_{c2}$ is is in the normal, non-superconducting state. For $H_{c1} < H < H_{c2}$ the type-II superconductor is in a mixed state: in this state the magnetic field can penetrate the sample, forming an array of flux lines called a vortex lattice. This is commonly a hexagonal lattice as this allows for the densest packing of vortices. Each vortex carries one quantum of magnetic flux, $\phi_0 = h/2e = 2.068^{-15}$ Wb: this allows the vortex spacing to be easily calculated. If the vortices form a hexagonal lattice with spacing a_V, each vortex lattice unit cell has an area of $\sqrt{3}/2\ a_V$. The vortex lattice is thus given as a function of magnetic field density H by:

$$a_V = \left(\frac{2}{\sqrt{3}}\frac{\phi_0}{H}\right)^{1/2} = 48.86\ H^{-1/2} \tag{3.1}$$

For a_V in nm and H in Tesla. In the centre of each vortex (the vortex core) the material is in the normal state: between vortices the material is superconducting. The vortex lattice can be imaged using STM by using spatially resolved STS (STS mapping): the local electron density of states, and hence the zero bias conductivity, will be higher in the vortex core than between the vortices, as the superconducting gap is suppressed in the vortex cores.

STS maps were collected on a $NbSe_2$ sample at a temperature of 2.4 K, with magnetic fields of 0.5 T and 1 T applied in the z-direction (perpendicular to the sample surface). At this temperature, the upper critical field H_{c2} is around 3 T [24]. Maps consisting of arrays of 128 x 128 I(V) spectra were collected: the I(V) spectra were subsequently individually numerically differentiated to produce dI/dV maps. Lock-in modulation techniques, to produce dI/dV data directly, were also tried but it was found that due to the limited bandwidth of the Cryogenic STM preamplifier ($\approx$ 800 Hz), it took too long to produce dI/dV spectra with a reasonable signal to noise level. Also, rapid measurement of I(V) curves ($\approx$ 0.1 s per curve) allowed low frequency noise to be avoided, whereas the relatively slow voltage sweep required for modulation techniques (several seconds per curve) introduced low frequency noise to the spectra. Figure 3.5e shows a 183 x 100 nm zero-bias dI/dV map at 1 T, showing the hexagonal flux lattice. The dI/dV map is obtained by numerical differentiation of an I(V) map: each spectrum has been smoothed by averaging it with its eight

neighbouring spectra: this reduces noise but also reduces spatial resolution. The spectra are also smoothed during differentiation by convolution with a Gaussian with FWHM of 0.9 mV. The resulting image is still noisy but a hexagonal lattice can clearly be seen: brighter areas correspond to higher zero-bias density of states. Figure 3.5g shows a cross section through 3.5e, with a sine wave fit. The measured lattice spacing is 48.4 $\pm$ 1.5 nm. This is in good agreement with the calculated value from equation 3.1 of 48.86 nm. A similar measurement at 0.5 T yielded a lattice spacing of 69.0 $\pm$ 0.6 nm, in good agreement with the calculated value of 69.10 nm. Figure 3.5f shows two example spectra from the dI/dV map shown in Figure 3.5e, one in the centre of a vortex core and one between vortices. The voltage resolution is insufficient to resolve the superconducting gap clearly: the superconducting gap energy has previously been measured via STS as 1.11 $\pm$ 0.03 meV [24], whereas our achieved resolution is worse than 1 meV. Nonetheless, a decrease in dI/dV is clearly seen around zero bias. Due to the poor energy resolution a clear difference between the vortex core and normal superconducting spectra is not seen: however the gap is suppressed at the vortex core. Finer spectroscopic features of the superconducting and vortex spectra such as the peaks either side of the superconducting gap, and the zero bias peak in dI/dV seen at the vortex core [24] are not observed.

We can conclude that it is possible to achieve atomic resolution with the Cryogenic STM at a range of temperatures and magnetic fields. For non-magnetic samples, the field can be ramped and the same scan area retained. The vortex lattice experiment demonstrates that samples can be studied in a superconducting state: it also shows that the magnetic field density at the sample is correct. Many problems remain, notably the low frequency vibration and the poor spectroscopic energy resolution. Attempts to improve the vibration damping performance of the Cryogenic STM are discussed in appendix A.1. The energy resolution may be improved by using a Au or Pt/Ir tip instead of W. Tungsten tips may have a surface oxide layer, which can affect the properties of the tunnel junction at low bias. Au tips have been found to give the best resolution for STS measurements on superconductors [53].

Chapter 4

STM experiments on Bilayer Manganites

4.1 Introduction

STM experiments on bilayer manganites were carried out at the London Centre for Nanotechnology. Single crystals of $PrSr_2Mn_2O_7$ with x = 0.5 were studied: the Omicron LT-STM, Omicron Cryogenic STM and the Oxford STM were used for experiments on $PrSr_2Mn_2O_7$. Thin films and single crystals of $La_{2-2x}Sr_{1+2x}Mn_2O_7$ were also studied, in the doping range $0.3 \leq x \leq 0.5$. The Omicron Cryogenic STM and the Oxford STM were used for experiments on $La_{2-2x}Sr_{1+2x}Mn_2O_7$. Sample characterisation experiments were performed both by the sample growers, Y. Tokura, T. Kimura and Y. Takamura, and at the London Centre for Nanotechnology: details of these experiments are given in the sections for the specific samples.

4.2 Experimental Methods

Some experimental methods are common to all the STM experiments performed, and are described in this section. These include the preparation of tunnelling tips, the calibration of the piezo scanners and the preparation of single crystal samples.

4.2.1 Preparing Tunnelling Tips

For STM experiments on manganites tunnelling tips made from tungsten (W) were used. These were electrochemically etched in potassium hydroxide (KOH) to make them sharp enough for STM experiments. Tungsten wire obtained from Goodfellow at 99.9 % purity was used. Initially an AC voltage etch method was used. This method uses a platinum ring electrode around 4 cm in diameter immersed in KOH solution, prepared at a concentration of 1 mol/l. A length of W wire is cut and lowered into the solution via a screw drive: the end of the wire is dipped about 1 mm into the KOH. The wire and the electrode are then connected to a 23 V, 50 Hz power supply: the current flowing through the wire is monitored using an RMS ammeter. The current decreases as the end of the tungsten wire is etched away, forming a sharp tip. Once the current reaches 0.18 mA the power is cut: the tip is rapidly removed from the KOH and rinsed in distilled water to prevent the tungsten being further etched. The tip is then cleaned by immersion in Isopropanol in an ultrasound bath, taking care not to blunt the tip. This is to remove any organic deposits which may occur during the etching process. The tip is inspected under an optical microscope for any defects and then mounted onto the tip carrier and loaded into the STM vacuum chamber.

Later a more reliable DC etch method was developed, largely by Dr Katsuya Iwaya at the London Centre for Nanotechnology. This uses a smaller 1 cm diameter platinum ring electrode held close to the surface of the KOH solution: the KOH is prepared at 3 mol/l. A piece of tungsten wire is lowered 1 mm into the KOH solution, into the centre of the ring electrode: the wire and the electrode are both held by micrometer heads giving accurate height control. A DC voltage of 4.5 V is applied between the wire and the electrode, with positive voltage applied to the wire. A LabView-based computer interface controls the voltage and monitors the current. The LabView interface is programmed to cut the voltage when the current drops suddenly, below a threshold of 6mA. This indicates that the end of the W wire has dropped off into the solution, leaving a sharp tip. By using computer control to cut the power as quickly as possible over-etching of the tip can be avoided and the most reproducible results obtained. Once the tip has been etched it is rapidly removed from the KOH, and rinsed and cleaned as for AC etched tips. The tip can then be mounted and loaded into the STM chamber.

4.2.2 Calibration of the STM Piezo Scanners

The STM piezo tube scanners require calibration to determine the piezo coefficients, the ratios between voltage applied to the piezo scanner and distance moved by the tip. The scanners are typically supplied with an approximate calibration, but for studies of new materials precise calibration in the X, Y and Z directions is important for measuring lattice parameters. The X and Y directions are defined as being in the plane of the sample surface, and the Z direction as perpendicular to the surface.

The piezo scanner can be calibrated in the X and Y directions by making atomically resolved topographic scans of a test sample which has a known lattice constant. The apparent lattice parameters can be measured from the scans: the ratios of the real to apparent lattice constants can be calculated. These ratios can be used as correction factors for further measurements. Fourier analysis can be used to measure the apparent lattice spacing accurately. In the Oxford STM Highly Oriented Pyrolytic Graphite (HOPG) samples were used as test samples. A clean HOPG surface can be readily prepared by cleaving the sample with adhesive tape in air. In the Cryogenic STM the $NbSe_2$ samples used for commissioning tests were used as calibration samples.

Calibrating the piezo scanners of the Oxford and Cryogenic STMs in the Z direction proved more problematic. The standard method for calibrating piezo scanners in the Z direction is to measure the apparent terrace step height of a material with well defined atomic terraces, with steps of known height. The apparent step height can be measured accurately by plotting a histogram of the Z height of an image, and measuring the spacing between peaks. HOPG is not ideal for Z calibration as it does not always present well defined terrace edges. Terrace edges were not observed on $NbSe_2$ despite scan areas several hundred nm across. Ultimately scans of $PrSr_2Mn_2O_7$ yielded reliable step heights and hence Z-calibration information: the step height of $PrSr_2Mn_2O_7$ has been well determined from scans taken using the LT-STM, which is accurately calibrated in Z (see below). However only a limited number of images of $PrSr_2Mn_2O_7$ showing step edges were collected using the Oxford and Cryogenic STM, so the Z calibration is less accurate than for the LT-STM.

In the LT-STM, silicon surfaces can be prepared by annealing in UHV: the Si(100) (2x1) surface was therefore used to calibrate the LT-STM piezo scanner. This surface

is ideal for STM calibration, as in addition to the clear resolution of dimer rows which can be achieved on Si terraces, allowing accurate X-Y calibration, clear terrace edges can also be seen which can be used to calibrate the scanner in the Z-direction. Due to the diamond structure of Si, the direction of the dimer rows changes direction from one terrace to the next: this makes it possible to identify multiple steps. The Z calibration for the LT-STM is therefore more accurate than that of the Cryogenic STM or Oxford STM. Si(111) is also used to calibrate the scanner in the X and Y directions, and to check the tip condition.

Piezo coefficients change with temperature: this must be taken into account when using a low temperature STM in which the piezo scanner is also cooled. The response of the piezo scanner to a fixed voltage may change by as much as a factor of four between room temperature and 4 K. Ideally calibration scans should be taken at every temperature studied, but this is not always possible. An approximate correction for the effect of changing temperature on the piezo constants is given by a cubic dependence on temperature. The following relation has been sourced from the Omicron LT-STM manual [49].

$$\frac{P(T)}{P(293K)} = 0.18 + 2.21 \times 10^{-3}\,T - 1.63 \times 10^{-6}\,T^2 + 1.26 \times 10^{-8}\,T^3 \qquad (4.1)$$

P(293K) is the piezo coefficient at 293 K and P(T) is the coefficient at some temperature T $\leq$ 293 K. Note that the piezo coefficient is much smaller at low temperature than at room temperature, so for a given voltage the tip will move a much shorter distance. This relation was used to generate variable temperature piezo calibrations for the Cryogenic STM and Oxford STM, based on room-temperature calibration data. For the Cryogenic STM X-Y calibration data were also available at $\approx$ 2K from the test data on $NbSe_2$. For the Oxford STM calibration data (from HOPG) were available for 44 K, 75 K and 300 K. For the LT-STM a full cubic fit was made based on data acquired from $PrSr_2Mn_2O_7$: this is detailed in appendix A.2.

As mentioned above a standard method for measuring the lattice parameters of an atomically resolved image is to use Fourier analysis. A Fast Fourier Transform (FFT) can be taken of a topographic image: the lattice parameters can be determined from the position of the peaks in the Fourier image. This method also allows us to estimate the best accuracy of a measurement of lattice parameters from a single

image. The size of pixels in the Fourier image, and hence the maximum accuracy of a measurement of peak positions, is equal to $1/d$ where d is the image size. For a lattice with spacing x the Fourier image peaks will be at $1/x$. The fractional accuracy in a measurement of x is thus x/d, and the absolute accuracy is x^2/d. The best accuracy can therefore be achieved by having the maximum number of unit cells in an image. This is subject to the critical (Nyquist) sampling limit of two pixels per unit cell. For example, calibration images of Si(111) taken using the LT-STM are 50 nm x 50 nm. The atomic spacing $x = 0.384$ nm. The fractional error is therefore 0.768 % and the absolute error in x is $\pm$ 0.003 nm. The total error on an experimental measurement will be the combination of the calibration and measurement errors.

4.2.3 Cleaving Single Crystal Samples

Single crystal samples of layered manganites can be cleaved in Ultra High Vacuum, exposing a clean surface for STM study. The method adopted for cleaving the crystals was to mount the sample to a titanium or molybdenum sample plate using non-conducting epoxy (Varian TorrSeal), and then apply conducting epoxy (EpoTek 4110) around the edge of the sample to provide electrical contact. A cleave post, consisting of a magnetic stainless steel cylinder 10mm x 2mm diameter, was then mounted onto the top of the crystal, again using TorrSeal. This arrangement is illustrated in figure 4.1. The sample is loaded into the vacuum chamber and cleaved by applying a lateral force to the top of the cleaving post using the wobblestick. The reason for using TorrSeal is that it is stronger than the conducting epoxy and provides a better bond to the manganite crystals: the crystals require some force to cleave and EpoTek 4110 was not strong enough to cleave the crystals. A good electrical contact is still provided since the EpoTek contacts the sides of the samples, allowing current to flow along the a-b planes.

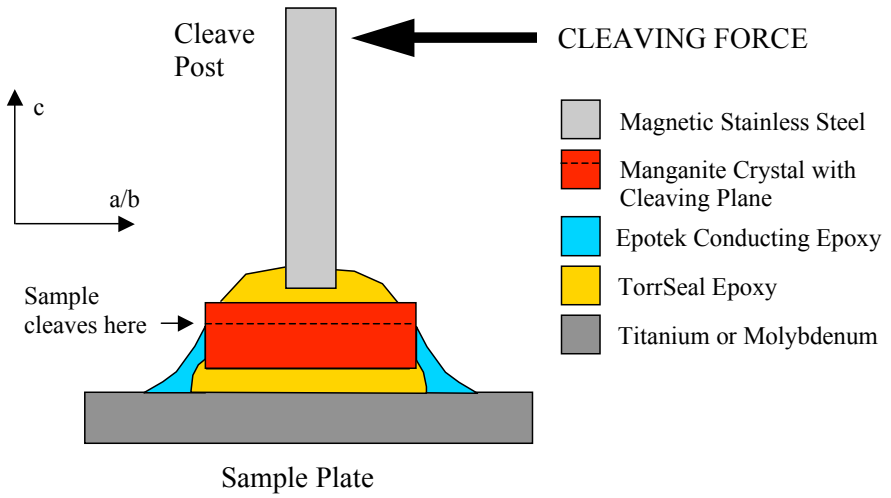

Figure 4.1: Schematic of method used for in-situ cleave of single crystal manganite samples. Crystal directions are shown: the crystals cleave parallel to the a/b planes

Chapter 5

STM Experiments on $PrSr_2Mn_2O_7$

5.1 Characterisation of $PrSr_2Mn_2O_7$ Samples

Single crystal samples of the bilayer manganite $Pr_{2-2x}Sr_{1+2x}Mn_2O_7$ were studied by STM. These samples were grown by Y. Tokura[1,2,3,4,5] and Y. Tokunaga[1,2]. The samples were grown by a floating zone method [79]. These samples have cation doping $x = 0.5$: in the phase diagram shown in figure 1.12 this is the $y = 0$ compound.

Single crystal samples were characterised at the London Centre for Nanotechnology using bulk electrical conductivity and magnetic susceptibility measurements. An Oxford Instruments MagLab was used to make conductivity measurements, and a Quantum Design MPMS based on a Superconducting Quantum Interference Device (SQUID) was used to make susceptibility measurements. The SQUID measurements were performed by Marc Warner.

Figure 5.1 shows results from an MPMS measurement of a $PrSr_2Mn_2O_7$ single crystal sample. The magnetic moment is shown as a function of temperature for various magnetic field strengths: moment is given in units of the Bohr magneton μ_B, per Mn ion. $PrSr_2Mn_2O_7$ shows a monotonic increase of magnetic moment with decreasing temperature, with a steeper slope below around 125 K corresponding to the antiferromagnetic state. No significant difference in this behaviour is seen between 0.025 T and 1 T.

Bulk conductivity measurements were made on $PrSr_2Mn_2O_7$ single crystals, to verify the temperature dependence of the conductivity and hence T_N: a peak should be observed in the resistivity at T_N [79]. This also appears to coincide with the temperature at which the charge-stripe phase is most prevalent [79]. $PrSr_2Mn_2O_7$ crystals were cleaved in air: gold contacts were then thermally evaporated into the cleaved surface. Two-point resistivity measurements were made using the MagLab, in a temperature range 20 K - 260 K: resistivity is recorded on both the upwards and downwards temperature sweep. Figure 5.2 shows the results of these measurements. In 5.2a resistivity in the ab plane (ρ_{ab}) is plotted: the c-axis resistivity ρ_c is shown

[1]Multiferroics Project, ERATO, Japan Science and Technology Agency (JST), Bunkyo-ku, Tokyo 113-8656, Japan
[2]Spin Superstructure Project, ERATO, JST, Tsukuba, Ibaraki 305-8562, Japan
[3]Correlated Electron Research Center (CERC), National Institute of Advanced Industrial Science and Technology (AIST), Tsukuba, Ibaraki 305-8562, Japan
[4]Department of Applied Physics, University of Tokyo, Bunkyo-ku, Tokyo 113-8656, Japan
[5]Joint Research Centre for Atom Technology, Tsukuba, Ibaraki 305,Japan.

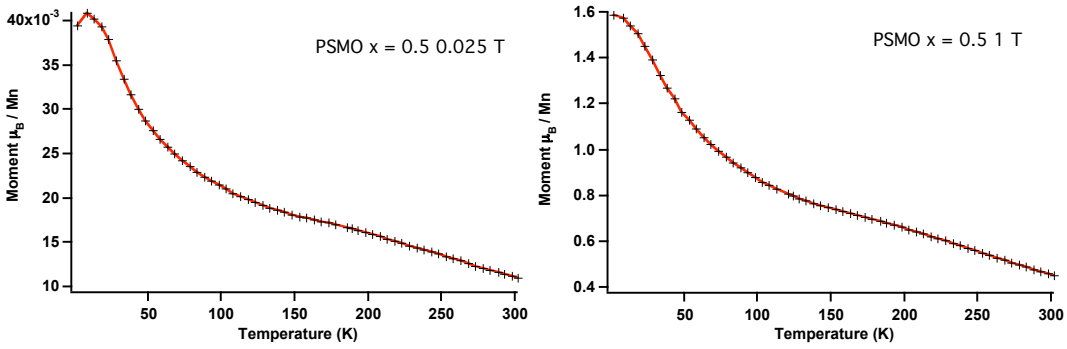

Figure 5.1: Magnetic moment of x = 0.5 $PrSr_2Mn_2O_7$ single crystal samples, measured as a function of temperature using the SQUID at the LCN, at fields of 0.025 T and 1 T

in figure 5.2b. It should be noted that these two measurements were not taken at the same time: the c-axis measurement was taken some months after the ab-plane measurement. A clear peak is not observed in ρ_{ab}, but an inflection is observed at around 140 K. There is an apparent hysteresis in the resistivity curve: this is likely an artefact of the measurement however, as the actual sample temperature lags slightly behind the temperature sensor. This amounts to an uncertainty in the temperature measurement of $\pm$ 4 K. A similar inflection is seen in ρ_c, at a slightly lower temperature of 120 $\pm$ 4 K. It is not clear if this apparent difference in the critical temperature between ρ_{ab} and ρ_c is genuine or a result of the sample ageing between the two sets of measurements. From these results, and the magnetic moment measurements, we can conclude that T_N is in the range 120 - 140 K.

Two differences can be seen between this measurement and that done by Y.Tokunaga [79]. Firstly although an inflection in ρ is seen at T_N in our measurement, the resistivity does not decrease below T_N. Secondly the a-b plane resistivity we measure is substantially higher: at 125 K we have measured $\rho_{ab} = 12 \pm 1$ Ω cm, whereas the published value [79] is around 0.2 Ω cm. These differences might be due either to a change in the sample properties, or to the experimental procedure. Manganite crystal samples can change their properties over time, due largely to changes in oxygen content, but this seems unlikely in this case since T_N does not seem to have shifted substantially. There may be some variation from crystal to crystal, and it is possible that the crystal we have measured contains a higher than usual number of

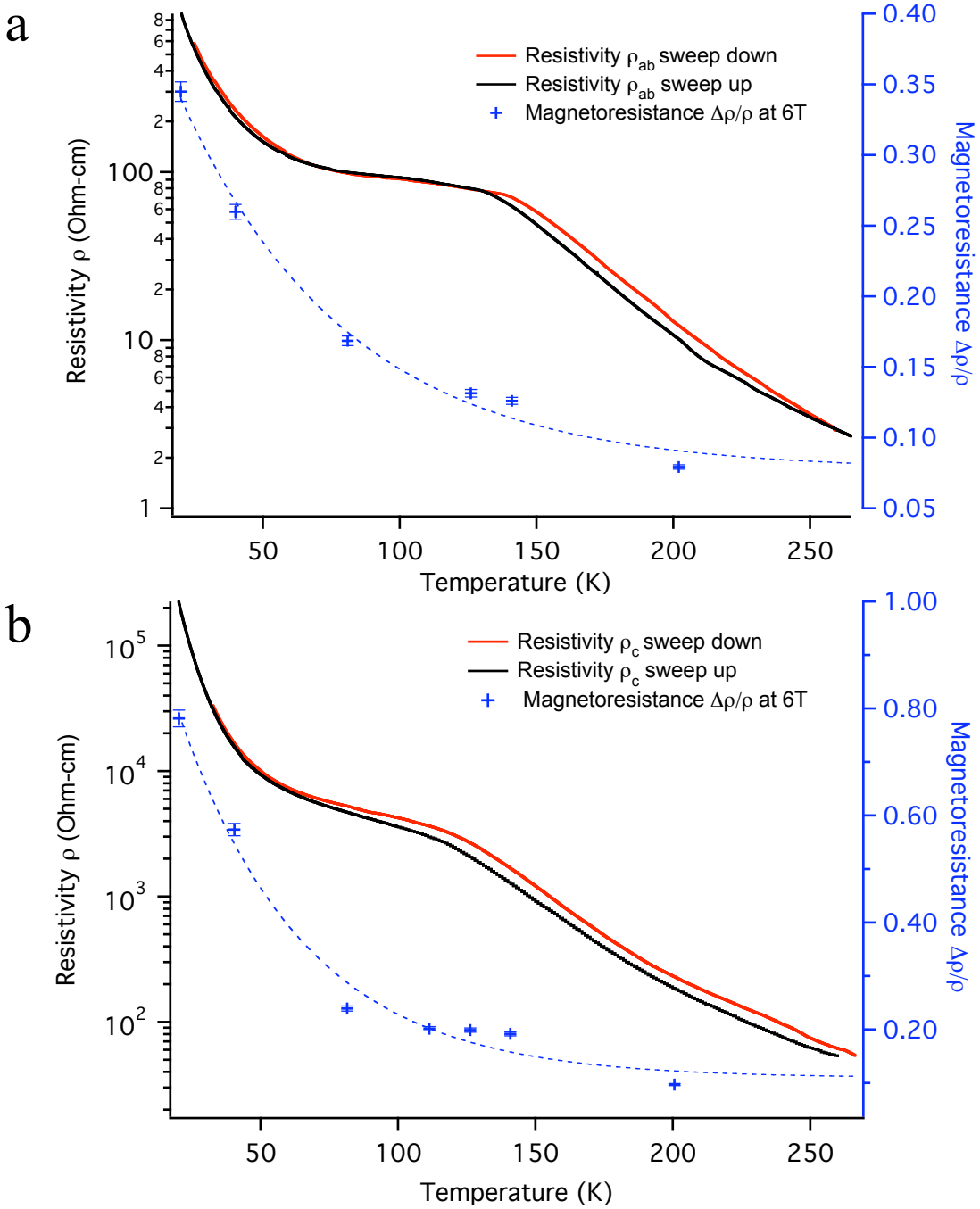

Figure 5.2: (a) ab plane resistivity ρ_{ab}, and magnetoresistance $\Delta\rho_{ab}/\rho_{ab}$ at 6T, as a function of temperature for a single crystal sample of $PrSr_2Mn_2O_7$ (b) c-axis resistivity ρ_c, and magnetoresistance $\Delta\rho_c/\rho_c$ at 6T. Magnetic field applied perpendicular to the sample surface in both experiments. Exponential fits are shown for $\Delta\rho/\rho$ vs. T. for both ab plane and c-axis magnetoresistance

impurities or defects. One possibility is the presence of a significant volume fraction of some impurity state: the presence of single layer (n = 1: $(R,A)Mn_2O_4$) or cubic perovskite (n = ∞: $(R,A)MnO_3$) intergrowths can cause phase transitions to become less sharp (see section 6.1.1). The presence of n = 1 or n = ∞ intergrowths will be apparent in STM images, as these will result in different step heights at terrace edges. The increased ab-plane resistance of the sample may be explained by the experimental geometry: both contacts are on the top of the sample, and due to the anisotropic resistivity of the crystal ($\rho_c > \rho_{ab}$) the current will be shunted through the top layers of the sample, reducing the effective thickness of the sample and increasing its resistance.

Magnetoresistance measurements were also made on $PrSr_2Mn_2O_7$ single crystals using the Maglab. The magnetic field was swept to 6 T at a range of fixed temperatures, and the sample resistivity (ρ_c or ρ_{ab}) plotted. The magnetic field is applied perpendicular to the sample surface. Figure 5.2 shows the magnetoresistance, defined as the fractional change in resistivity $\Delta\rho/\rho_0$ between zero field and 6 T, where ρ_0 is the resistance at zero field, plotted as a function of temperature for both ρ_{ab} and ρ_c. The c-axis magnetoresistance is larger than the ab plane value, with maximum values at 20 K and 6 T of $\Delta\rho_c/\rho_c = 0.78$ and $\Delta\rho_{ab}/\rho_{ab} = 0.34$. Magnetoresistance is observed to increase monotonically with decreasing temperature: this is in contrast to the colossal magnetoresistance observed in $La_{2-2x}Sr_{1+2x}Mn_2O_7$, which peaks close to the metal-insulator transition (see section 1.6). The temperature dependence of $\Delta\rho/\rho$ is roughly exponential in T for both ρ_{ab} and ρ_c : figure 5.2a shows exponential fits of the form $exp(-T/\tau)$ to the magnetoresistance data. For the ab plane magnetoresistance $\tau = 63 \pm 12$ K, for the c-axis $\tau = 46 \pm 9$ K: there does not seem to be any significant difference in the temperature dependence of $\Delta\rho/\rho$ between the ab plane and c-axis directions. Close to T_N a slight excess in $\Delta\rho/\rho$ is observed over the exponential fit. This might indicate that the magnetoresistance is enhanced by proximity to T_N. Alternatively this may simply reflect the increased resistivity near T_N, suggesting that that the magnetoresistance is dependent on resistivity rather than temperature.

5.2 STM Studies of $PrSr_2Mn_2O_7$

A major limiting factor in the study of manganites by STM is the reliable preparation of sample surfaces. Bilayer manganites do not always cleave well, leaving large, atomically flat surfaces: sometimes only a small proportion of the cleaved sample will present a flat surface, and often many cleaves will be necessary before a good surface can be obtained. Typically surfaces do not remain pristine indefinitely, even in UHV, but are observed to degrade, sometimes within hours. This limits the scope of STM experiments. Therefore a major experimental objective is to find a sample preparation method, and a specific manganite compound, that will reliably yield surfaces suitable for STM experiments. The bilayer compound $PrSr_2Mn_2O_7$ is observed upon cleaving in air to give large optically flat (mirror-smooth) surfaces far more often than most of the $La_{2-2x}Sr_{1+2x}Mn_2O_7$ compounds: it was therefore decided to study this compound using STM.

The initial objective of STM experiments on $PrSr_2Mn_2O_7$ was to see if the sample surface can be reliably prepared, to reproducibly yield atomically flat surfaces on which atomic resolution can be achieved. Variable temperature STM topography and STS were performed to search for signatures of the charge-stripe phase, observed to be strongest at 125 K [79]. This might be observed directly in topographic imaging as a stripe structure with spacing $\approx$ 4a, where a = 3.8535 nm is the ab plane lattice spacing. We also carried out variable temperature LEED: any surface charge stripes should appear as satellite spots in the LEED pattern.

5.2.1 The Surface of $PrSr_2Mn_2O_7$

Single crystal $PrSr_2Mn_2O_7$ samples were studied using the Omicron LT-STM, at temperatures between 77 K and 195 K. The piezo scanner was calibrated in X, Y and Z by recording topographic images of the (2x1) reconstructed Si(100) surface. $PrSr_2Mn_2O_7$ samples were cleaved in the STM chamber using the cold cleaving stage, at a temperature of $\leq$ 20 K and a pressure of 5 x 10^{-11} mbar or better. The $PrSr_2Mn_2O_7$ samples were found to cleave more reliably than the $La_{2-2x}Sr_{1+2x}Mn_2O_7$ single crystals, with five out of the eight cleaves performed yielding good surfaces with atomically flat terraces. Figure 5.3a shows a 560 x 610 nm topographic image

of $PrSr_2Mn_2O_7$ showing several terraces: the step height is measured as 1.01 ± 0.02 nm, in good agreement with the value from X-ray diffraction of c/2 = 0.9964 nm [79]. Figure 5.3b shows a 22 x 24 nm topographic image, recorded at +0.8 V sample bias (empty states). Two general characteristics can be identified: firstly a square atomic lattice can be observed across the whole image, with spacing a = 0.396 ± 0.007 nm. This is in reasonable agreement with the value from X-ray diffraction of a = b = 0.38535 nm [79]. Secondly a larger scale modulation is observed, with a length scale of around 4 nm. By using Fourier analysis to separate the atomic lattice from this larger modulation, the relative Z-corrugation of the two components can be measured. The atomic lattice has a peak to peak corrugation of ≈ 4 pm, whilst the larger modulation has a peak to peak corrugation of ≈ 20 pm. The atomic lattice appears superposed upon the modulation, being visible across the whole image. Figure 5.3c shows the atomic lattice and larger modulation in more detail, in a 10 x 11 nm topographic image collected at 78 K. The sample bias voltage is +0.5 V, so empty states are being probed: figure 5.3d shows the same area imaged in filled states at -0.5 V. These two images were collected simultaneously using "dual mode" to interlace scans at two different biases: positive bias is applied as the tip sweeps left to right, and negative bias as the tip travels from right to left. A delay time is imposed between the left and right scans (typically 50-100 ms) to eliminate any transient effects of the bias change. Most features remain the same between filled and empty state images: some features are more prominent in filled states however. Cross sections are shown of both 5.3c and d: since *most* features remain the same between positive and negative bias, cross-correlation analysis can be used to align the sections, correcting for the effect of piezo hysteresis between the left-to-right and right-to-left scan. A depression visible in the filled state image (d) between 6 and 7 nm in the section is not visible in the empty state section (c).

Similar topographic features can be observed on the $PrSr_2Mn_2O_7$ surface at 125 K. Figure 5.3e shows a 4 x 4 nm area imaged at +0.5 V sample bias at 125 K: atomic resolution can be clearly seen. The cross-section shows that the peak-peak corrugation is ≈ 4 pm. Figure 5.3f shows a 16 x 18 nm image of the $PrSr_2Mn_2O_7$ surface, imaged at + 0.8 V sample bias (empty states) at 125 K. Figure 5.3g shows the same area imaged simultaneously at -0.8 V (filled states). The atomic lattice and the longer-scale modulation can both be seen in both images. Cross sections of 5.3f and g are shown: cross correlation analysis has been used to align the section location.

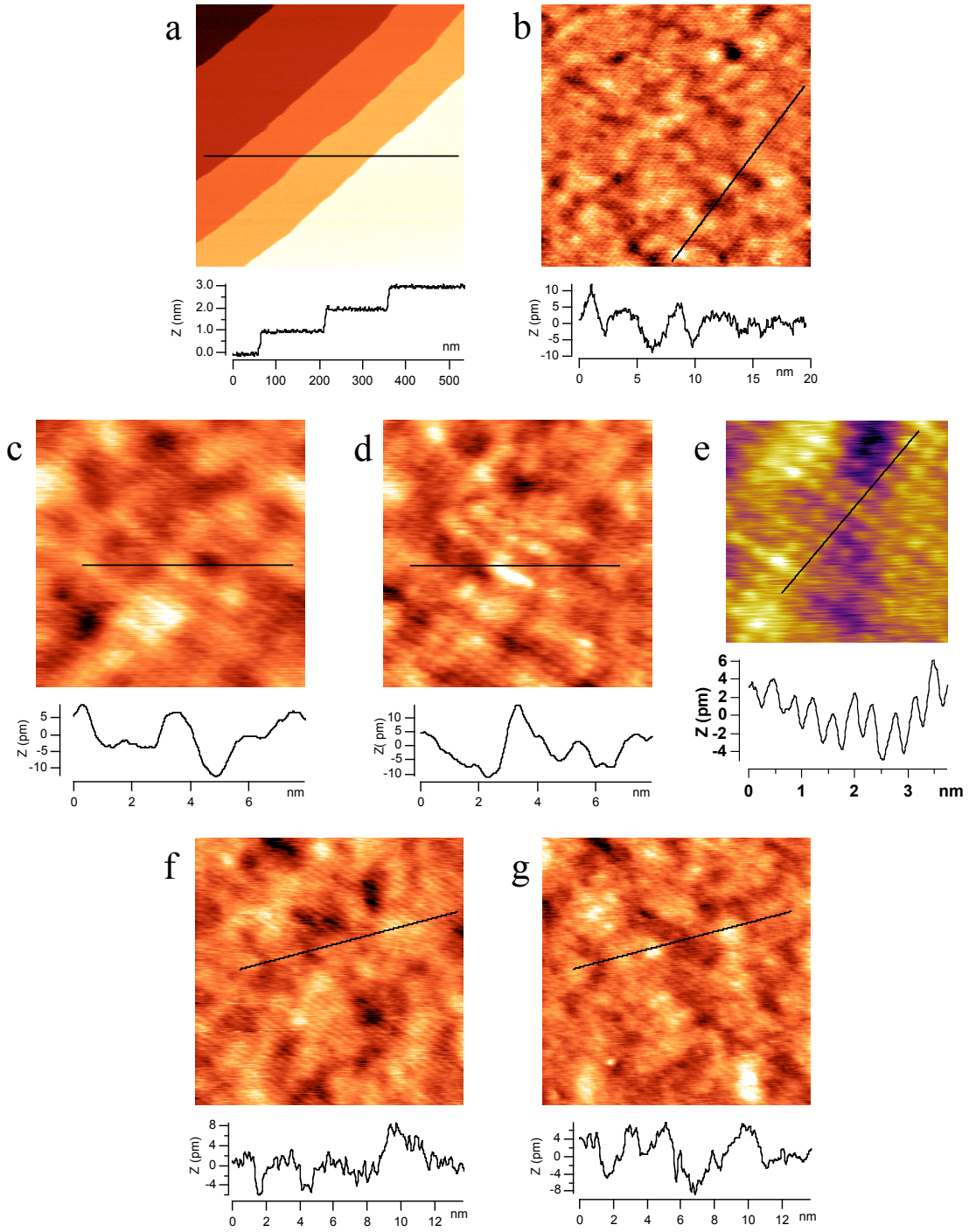

Figure 5.3: (a) 560 x 610 nm topographic image of $PrSr_2Mn_2O_7$ taken at 78 K: step height is 1 nm (b) 22 x 24 nm image taken at 78 K, sample bias + 0.8 V, tunnel current 50 pA (c) 10 x 11 nm image taken at 78 K, + 0.5 V (d) same area at - 0.5 V (e) 4 x 4 nm image taken at 125 K, +0.5 V (f) 16 x 18 nm image taken at 125 K, + 0.8 V (g) same area at - 0.8 V

As at 78 K some features can be seen to change contrast between positive and negative bias: two raised features are visible at around 3 and 5 nm in the filled state image (g), which are not visible in the empty state image (f).

Step heights on the $PrSr_2Mn_2O_7$ surface are always multiples of 1 nm: no other atomic lattice is seen other than the a = 0.396 nm square lattice. This means that we can be confident that we are studying a $PrSr_2Mn_2O_7$ surface, and not that of some inclusion or impurity phase, for example single layer (n = 1: (Pr,Sr)Mn_2O_4) or cubic perovskite (n = ∞: (Pr,Sr)MnO_3) intergrowths. As described by Loviat *et al.* [41] for the $La_{1.4}Sr_{1.6}Mn_2O_7$ surface, the expected cleaving plane in bilayer manganites is between (R,A)O layers in the rock-salt layer. This is the most energetically advantageous crystal plane to cleave along: this argument is supported by x-ray photoelectron spectroscopy data collected on the cleaved $La_{1.4}Sr_{1.6}Mn_2O_7$ surface [41]. In addition, in this experiment and STM experiments on $La_{1.4}Sr_{1.6}Mn_2O_7$ [59] step heights of $\approx$ 1 nm are observed, together with atomically flat surfaces of roughness $\leq$ 30 pm. Only two mirror planes are available to produce a step height of 1 nm, namely in between (R,A)O layers in the rock-salt layer, or along the (R,A)O layer in the middle of the bilayer (see figure 5.4). Cleaving through the centre of a bilayer will produce a surface with peak-peak roughness around 0.2 nm as the cleave is along a (R,A)O layer, and by symmetry half of the ions in the layer must be left on the surface. As this is not observed we can conclude that the surface exposed upon cleaving $PrSr_2Mn_2O_7$ represents the topmost (Pr,Sr)O layer of a bilayer.

The nature of the $\approx$ 4 nm modulation seen in STM topographic images of $PrSr_2Mn_2O_7$ has not yet been adequately determined. The modulation appears irregular and is not commensurate with the atomic lattice, although some alignment of modulation features to the atomic lattice is visible in figures 5.3b,c and d. We observe that there is some bias dependence in images of this modulation, but only some features are observed to change between positive and negative bias. Several possible sources of this modulation may be postulated. $PrSr_2Mn_2O_7$ is a mixed valence material and includes both Mn^{3+} and Mn^{4+} ions. The distribution of these two ions below the surface might cause the observed modulation. This could be a physical modulation due to the surface oxygen ions sitting closer to the Mn^{4+} sites, or an electronic effect caused by the additional e_g electron of the Mn^{3+} ion. A physical modulation would not seem sufficient to supply the observed 20 pm modulation as the difference in ionic radius between Mn^{3+} and Mn^{4+} (table 1.1) is only

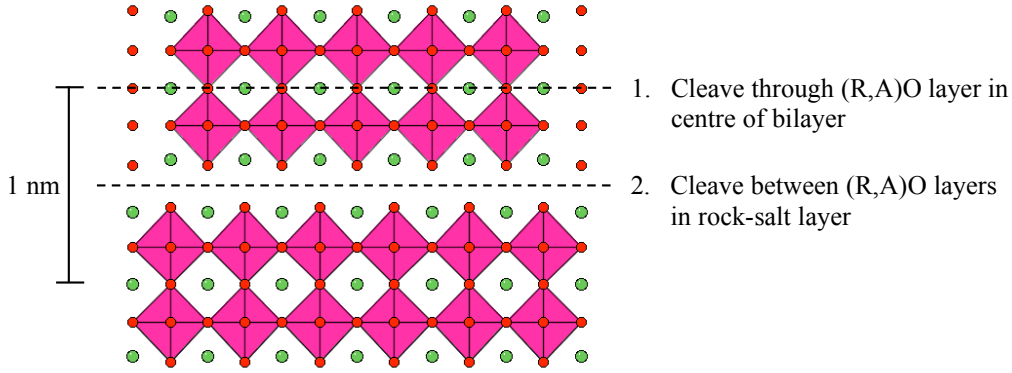

Figure 5.4: There are only two possible cleaving planes for $R_{2-2x}A_{1+2x}Mn_2O_7$ which will produce 1 nm step height, as observed in $La_{1.4}Sr_{1.6}Mn_2O_7$ [59] and $PrSr_2Mn_2O_7$. Cleaving plane 1 will produce a rougher surface than is observed, so $PrSr_2Mn_2O_7$ and $La_{1.4}Sr_{1.6}Mn_2O_7$ must cleave along plane 2.

11.5 pm. As noted in section 2.2.2, Ma *et al.* [42] have identified Mn^{3+} and Mn^{4+} sites at the surface of $La_{0.325}Pr_{0.3}Ca_{0.375}MnO_3$. Mn^{4+} ions show a much larger contrast between positive and negative bias images than Mn^{3+} ions: this is attributed to the additional e_g electron of the Mn^{3+} ion. This effect could be responsible for the bias dependent portion of the modulation. The second possible source is the distribution of Pr^{3+} and Sr^{2+} ions in the surface layer. In this case the difference in ionic radius is 19 pm so it is possible that ionic size effects alone could account for the modulation. This could account for the non-bias dependent portion of the modulation. As the 4 nm modulation shows some features that change with bias and some that do not, it may be necessary to include the effects of both the Mn^{3+}/ Mn^{4+} and the Pr^{3+}/ Sr^{2+} distributions to fully explain the modulation.

Alternatively the observed $\approx$ 4 nm superstructure might be due to trapped polarons, as postulated for the similar structures observed on the $La_{1.36}Sr_{1.64}Mn_2O_7$ surface (see section 6.3). In STM studies of $La_{1.4}Sr_{1.6}Mn_2O_7$ [59] raised "islands" displaying atomic resolution were attributed to the trapping of polarons by point defects. Electrical transport in $PrSr_2Mn_2O_7$ is expected to be polaronic since there is a large electron-phonon interaction via the Jahn-Teller effect. $PrSr_2Mn_2O_7$ is much more resistive than $La_{1.4}Sr_{1.6}Mn_2O_7$, so we might expect polarons to be trapped more easily, resulting in a higher surface density of topographic features. However, at

present it is unclear if such an explanation can account for the bias dependence of the superstructure.

5.2.2 Bias Dependent Imaging of the $PrSr_2Mn_2O_7$ Atomic Lattice

Atomically resolved topographic images can be obtained on the $PrSr_2Mn_2O_7$ surface at both positive and negative sample bias. Figure 5.5 shows two 5 x 5 nm images (a and b), collected simultaneously using dual bias mode, at 125 K and ± 0.5 V sample bias. This is the same area as shown in figure 5.3e. Clear atomic resolution, plus the larger modulation, can be seen: a square lattice with spacing a = 0.39 nm is seen in both images. Cross-sections through both images are shown in 5.5c: the atomic corrugation is similar in positive and negative bias at around 4 pm peak to peak. To correct for the effect of piezo hysteresis the images shown in figures 5.5a and b have been aligned in the horizontal direction, using the large scale modulation as a reference. The alignment correction is calculated by measuring the position of maximum correlation between images a and b, where the images have been filtered so that the atomic lattice is no longer visible but the large scale modulation is visible.

The topmost atomic layer of cleaved $PrSr_2Mn_2O_7$ (see section 5.2.1) consists of Pr^{3+}, Sr^{2+} and O^{2-} ions, as shown in figure 5.5f. The observed a = 0.39 nm square lattice can be reproduced if either the Pr/Sr sites, or the O sites, are represented by topographic peaks. Although the same square lattice is seen in positive and negative bias it is possible that different ion sites are imaged: for example if the positive bias lattice represented the Pr or Sr ions, and the negative bias lattice the O ions, the same lattice would be observed at positive as at negative bias, but offset by $a/\sqrt{2}$ along the unit cell diagonal. From figure 5.5c it is clear that there is some offset between positive and negative bias images: cross-correlation analysis of the two sections gives an offset of 0.12 nm or 0.31a. A more accurate measurement of the offset can be obtained by performing a two-dimensional cross-correlation analysis on the full images shown in 5.5a and b. This analysis gives the offset as 0.09 nm or 0.24a, at 4° to the lattice direction. An identical analysis was performed on two further images, shown in figure 5.5d and e. These images were collected at 78 K at ± 0.8 V sample bias. Atomic resolution is visible in both images, though less clearly

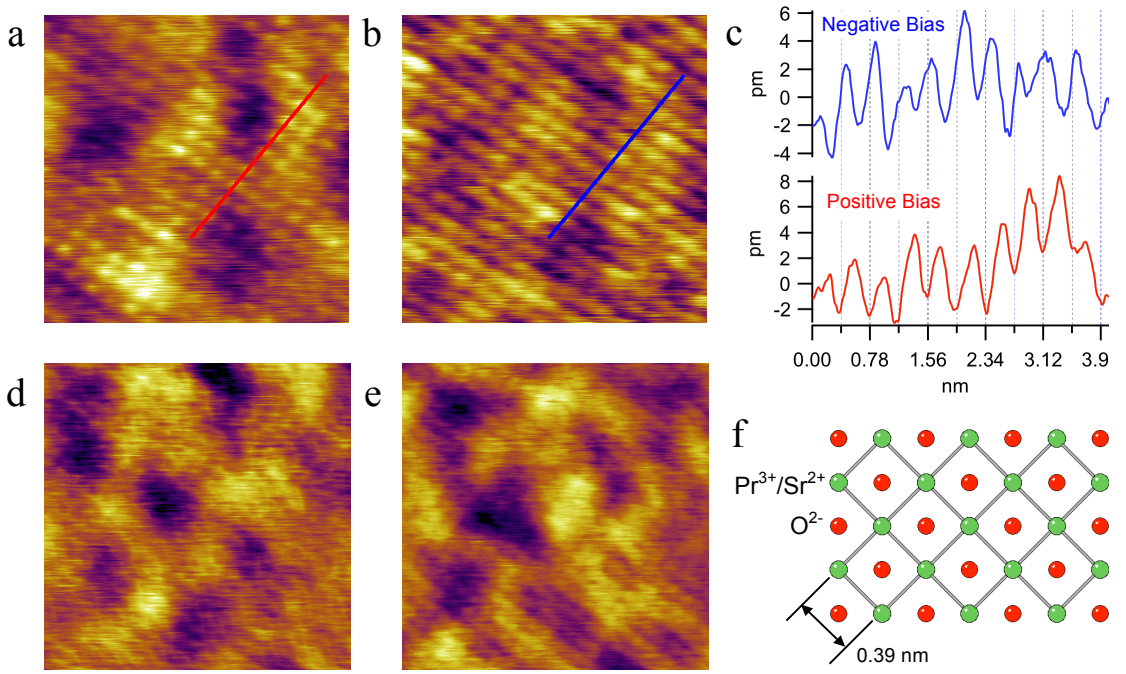

Figure 5.5: (a) 5 x 5 nm STM topographic image of $PrSr_2Mn_2O_7$ collected at 125 K and +0.5 V (b) same area imaged at -0.5 V. Cross sections through these images are shown in (c), with vertical grid lines at the atomic lattice spacing (d) 8 x 8 nm STM topographic image collected at 78 K and +0.8 V (e) same area imaged at -0.8 V (e) schematic of expected surface lattice of $PrSr_2Mn_2O_7$: O sites are in red and Pr/Sr in green

than in 5.5a and b. In this case a different approach has been used to correct for piezo hysteresis. STM images were collected immediately before the images shown, on the same area, without using dual mode, but with all other scan parameters the same. The forward and backward non-dual bias images are identical except for the effects of piezo hysteresis. This enables the horizontal offset to be extracted via cross-correlation from the non-dual bias images, then applied to the dual bias images. Cross correlation analysis on 5.5d and e gives the offset between the positive and negative bias images as 0.15 nm or 0.39a, at 16° to the lattice direction.

Both results above are somewhat inconclusive since there is no clear alignment of the positive and negative bias lattices, either to zero offset, or offset to the unit cell body centre, 0.71a at 45° to the atomic lattice. In addition the two results do not agree well, indicating that the accuracy of the method may be insufficient to determine sub-atomic offsets. However in both cases the maximum correlation

position is closer to zero offset than to the body centre. This indicates that the same ion sites are imaged at positive and negative bias. At present it is not known whether it is the Pr, Sr or O ions which are responsible for the observed lattice.

Clearly both pairs of images shown here suffer from the weakness of needing to correct for piezo hysteresis. In future a more accurate measurement of the offset of positive and negative bias images may be possible by interlacing scans collected with the same scan direction, thus eliminating piezo hysteresis. This mode of imaging has not so far been possible with the Omicron MATRIX control units. Alternatively the scan axes could be aligned with the atomic lattice and the phase shift between the lattice in the y (non-hysteretic) direction can be measured: the scan axes can then by rotated 90° and the corresponding measurement made in the x-direction.

5.2.3 Adatoms and Vacancies on the $PrSr_2Mn_2O_7$ Surface

Some regions of the $PrSr_2Mn_2O_7$ surface show a rougher surface, with a peak to peak roughness of around 0.2 nm. Figure 5.6a shows a 55 x 60 nm topographic image of such a region. The increased roughness can be seen to be due to a distribution of features around 1 nm across and 0.1 nm high. Features this size are large enough to be atoms adsorbed on the surface, so these features will henceforth be referred to as "adatoms". This rougher surface has been observed on the same sample as the atomically flat surface, at different locations on the sample. The rougher surface is in fact more common than the atomically flat surface, and has been observed on most of the samples studied. Atomic resolution is difficult to achieve on this rougher surface due to the high density of adatoms, however a Fourier transform of Figure 5.6a shows peaks due to a square lattice of spacing a = 0.380 ± 0.005 nm, similar to the lattice which was observed on flatter areas. By performing an inverse Fourier transform the atomic lattice can be extracted and its average peak to peak corrugation measured: this is found to be around 1 pm. Atomic resolution can sometimes be achieved in areas between adatoms: atomic rows can be seen in figure 5.6b, a 4 x 4 nm topographic image. The row spacing is 0.37 ± 0.02 nm and the peak to peak corrugation is around 8 pm: the spots in the Fourier transform of image 5.6a may thus be due to many such areas of atomic resolution between adatoms. In addition to adatoms, holes or vacancies are also observed in the $PrSr_2Mn_2O_7$ surface. Figure 5.6b shows several adatoms, and also several vacancies: a cross section through a vacancy is shown. Roughly the same number of vacancies as adatoms are observed: vacancies are around 1 nm across and 60 pm deep.

The density of adatoms varies, but has a maximum density of around one adatom every 66 unit cells. One possible source of this rougher adatom/vacancy surface might be a cleave through the centre of a bilayer instead of between bilayers, *i.e.* cleaving plane 1 rather than 2 in figure 5.4. However, by symmetry such a cleave would produce a surface with a 50 % coverage of Pr, Sr and O ions, rather than the 1.5 % coverage of adatoms seen here. Thus we conclude that the adatom/vacancy surface represents a cleave between bilayers (cleave plane 2 in figure 5.4), as with the atomically flat surface.

Adatoms have been observed on the $PrSr_2Mn_2O_7$ surface immediately after cleaving, making it unlikely that the adatoms arise by deposition or contamination from the

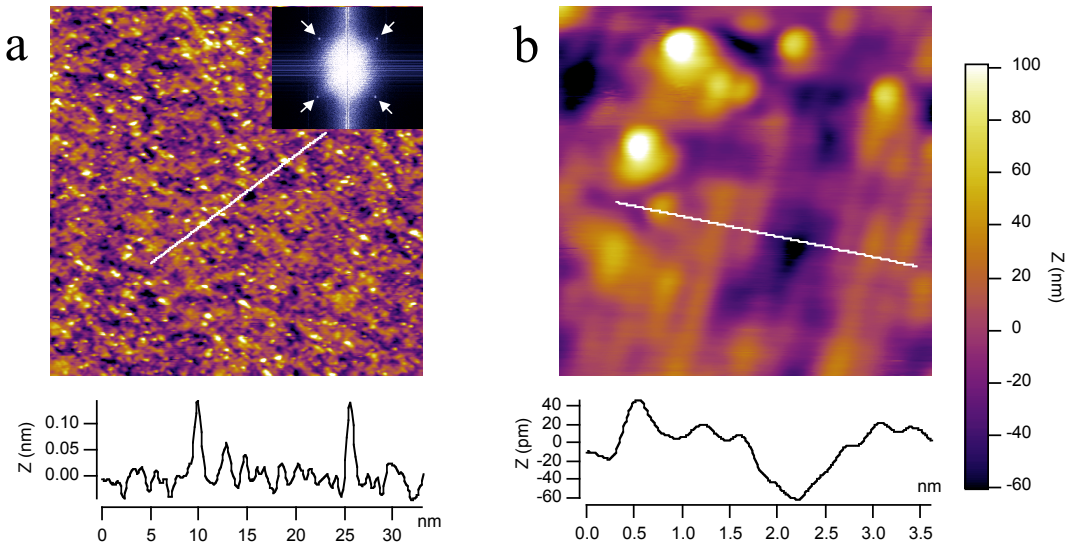

Figure 5.6: In some STM images of $PrSr_2Mn_2O_7$ a rougher surface is observed. This is due to a partial coverage of the surface with adatoms, and also vacancies in the surface. (a) 55 x 60 nm topographic image showing adatoms: 78 K. A Fourier transform of this image (inset) shows spots (arrowed) corresponding to a lattice spacing of a = b = 0.39 nm. (b) 4 x 4 nm image showing adatoms, atomic rows and vacancies at 78 K.

UHV chamber. Also, the density of adatoms on a given area is not observed to increase significantly even over experiments lasting several weeks. Thus the adatoms and vacancies are likely to be intrinsic to $PrSr_2Mn_2O_7$: one possibility is that when the crystal is cleaved, some of the atoms of the (Pr,Sr)O layer from the cleaved-off part are left behind. By symmetry some atoms in the (Pr,Sr)O surface should remain attached to the cleaved-off part: this would account for the observation of vacancies as well as adatoms, as well as why the two are observed in roughly equal numbers. The atoms which are left behind on the surface could therefore be either Pr, Sr or O.

5.2.4 Nature and Origin of Adatoms and Vacancies

It was decided to study the adatoms and vacancies apparent on the $PrSr_2Mn_2O_7$ surface in more detail. The initial objective was to identify the chemical species comprising the adatoms. Initially dual bias mode was used to record topographic images of adatom and vacancy areas in both filled and empty states. Figure 5.7a shows a negative bias (filled state) topographic image of $PrSr_2Mn_2O_7$: 5.7b shows a positive bias (empty state) image simultaneously acquired at the same location. The images were collected at 78 K and ± 0.8 V, from the same region shown in figure 5.6a. The images have been aligned by cross-correlation to correct for the effect of piezo hysteresis. Adatoms are clearly visible in both filled and empty states. This indicates that the adatoms are physical entities rather than purely electronic contrast features. This is in contrast with the observation of Mn^{4+} sites at the surface of $La_{0.325}Pr_{0.3}Ca_{0.375}MnO_3$ by Ma *et al.* [42]. In this case the Mn^{4+} sites were observed to stand ≈ 0.1 nm proud of the surface, but only in empty states: in filled states the Mn^{4+} sites are visible as depressions in the topographic image. Adatoms are more clearly resolved in filled states than in empty states: the cross sections shown in figure 5.7 show that in filled states the adatoms have a height of around 0.14 nm, whilst in empty states the height is around 0.11 nm. In addition some adatoms visible in filled states are not visible in empty states: for example the adatom at 6 nm in the cross section of figure 5.7a is not visible in 5.7b. Thus there is an electronic component as well as a physical component to the imaging contrast.

In order to further investigate this bias dependence, STS I(V) maps were collected on areas showing adatoms, at a range of temperatures. Maps of conductance G = dI/dV were extracted from the STS data, either at zero or finite bias. Figure 5.8a shows a 14 x 14 nm filled state (sample bias = -0.8 V) topographic image collected at 140 K. The image is shown in a high contrast colour scale: adatoms appear blue and vacancies dark red. An I(V) map was collected on the same area: figure 5.8b shows a conductance map calculated from this I(V) map, plotted in filled states at -0.77 V. The colour scale is shown in the histogram of this map in 5.8d. Substantial variation in conductance is observed: also areas of high conductance (blue) can be observed to correspond with the positions of adatoms in the topographic image. Figure 5.8c shows typical spectra collected on adatoms and on the "normal" (neither adatom nor vacancy) surface. Note that the current set point is defined at +0.8

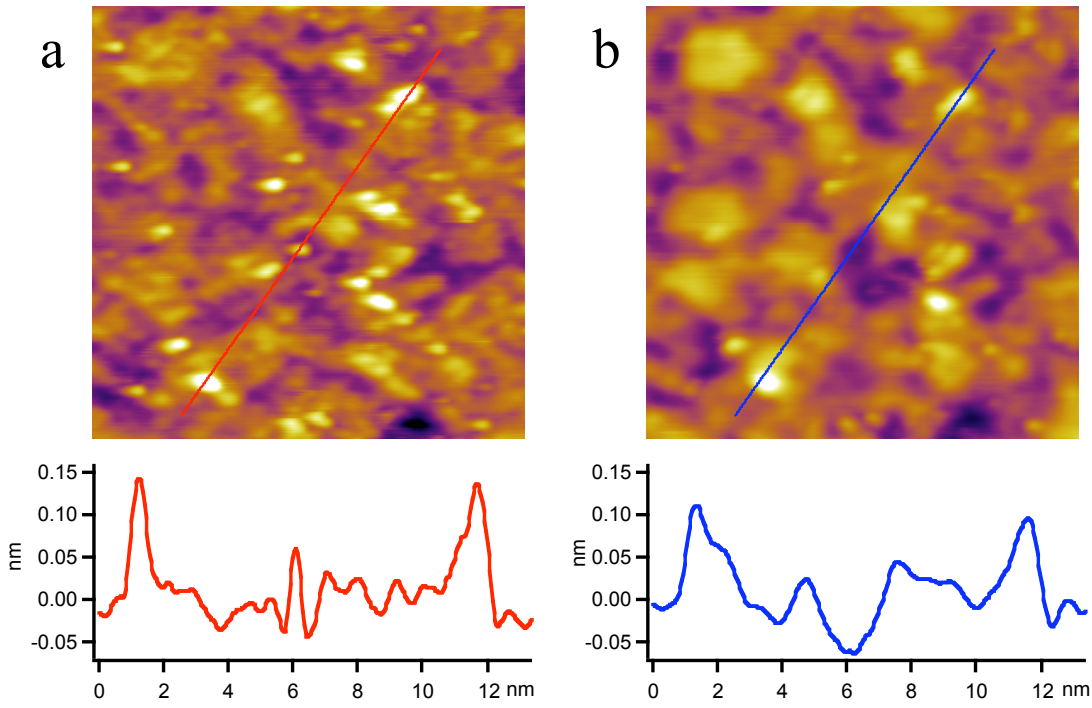

Figure 5.7: (a) Negative bias (filled state) topographic image of $PrSr_2Mn_2O_7$ at 78 K, showing adatoms (b) simultaneously acquired positive bias (empty state) image. Adatoms appear in both images, but are more prominent in the filled state image. Bias voltage ± 0.8 V

V bias, so the current is "pinned" at this bias. Clearly spectra from adatoms have substantially larger tunnel current and dI/dV in filled states, at negative bias. Since the tunnel current is proportional to the integrated density of states (equation 2.1) this indicates that the adatoms have a higher integrated density of states in filled states than the general surface. This criterion could be fulfilled if the adatoms carry a negative charge relative to the rest of the surface. This would explain the increased image contrast seen in filled state topographic images compared to empty state images (figure 5.7): when imaging filled states, the negatively charged adatoms will produce an enhancement in the tunnel current, causing the tip to ride higher over the adatoms to maintain the tunnel current. The physical and electronic contrast mechanisms operate in the same sense, producing an enhanced contrast. When imaging in empty states, the negatively charge adatoms will suppress the tunnel current, leading to the tip moving closer to the adatom, and producing a reduced contrast.

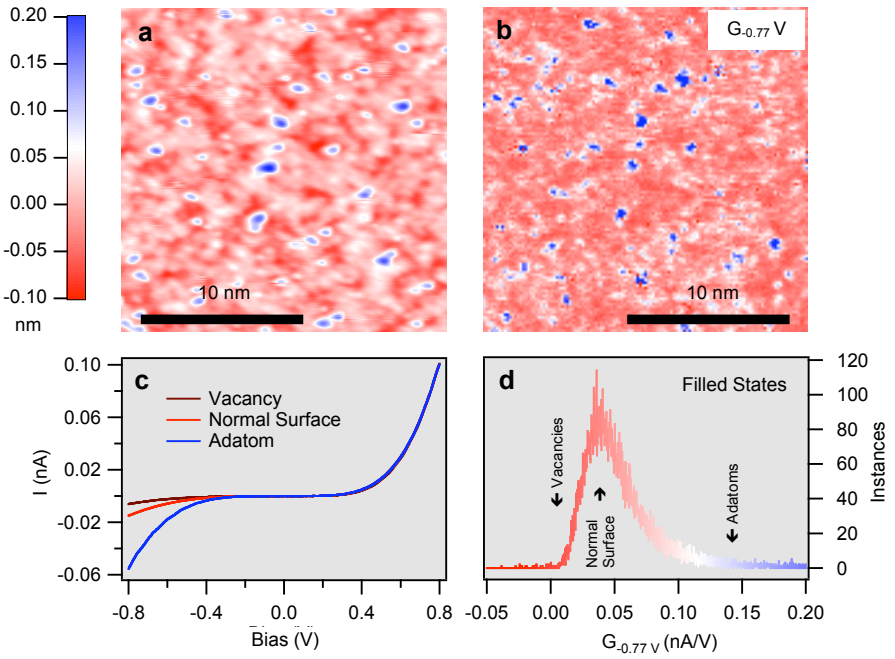

Figure 5.8: (a) 14 x 14 nm filled state topographic image collected at 140 K (b) conductance map generated from IV array collected on the same area, plotted at -0.77 V (filled states) (c) typical spectra on cavities, adatoms and the normal surface (d) histogram of conductance values from (b)

As discussed in the previous section it is unlikely that adatoms arise as a result of contamination or deposition. Therefore they arise from the chemical species present in $PrSr_2Mn_2O_7$. The only one of these chemical species capable of holding a negative charge is oxygen. Therefore we conclude that the adatoms observed on the surface of $PrSr_2Mn_2O_7$ are negatively charged oxygen ions. These may arise as a result of an uneven cleave between bilayers, which produces oxygen adatoms (figure 5.9). By symmetry the cleave must also produce oxygen vacancies.

Oxygen vacancies would be expected to carry a positive charge compared to the normal surface, and hence show an excess of tunnel current in empty states (positive bias). In the I(V) array results shown in figure 5.8 the spectra are effectively normalised at +0.8 V by the tunnel current setpoint. This means that vacancies would be expected to show a decreased tunnel current in empty states compared to the normal surface: this is observed, and is shown in figure 5.8c. However the conductance difference at -0.77 V between the vacancies and the normal surface is much smaller than between the adatoms and the normal surface, so it is difficult to

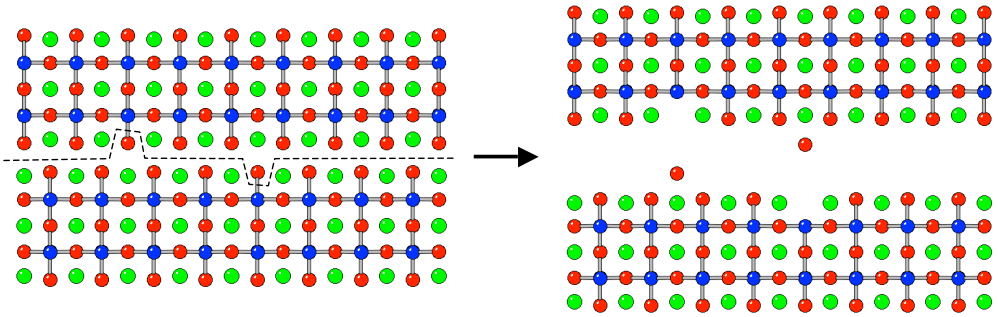

Figure 5.9: Schematic showing how an uneven cleave between bilayers in $PrSr_2Mn_2O_7$ may produce oxygen adatoms and vacancies on the surface. O is shown in red, Pr/Sr in green and Mn in blue

see the effect in the conductance map or histogram. This reduced contrast arises because the current setpoint is set here at positive bias (empty states): this means the STM tip is positioned closer to the negatively charged adatoms than the positively charged vacancy positions. A better contrast in tunnel current or dI/dV for vacancy positions can be achieved by applying the current setpoint at negative sample bias. In fact the MATRIX control system allows the functions of dual mode imaging and STS mapping to be combined, allowing two STS I(V) maps at different setpoints to be collected simultaneously. This was carried out on a 10 x 10 nm area, at 78 K: a detail of this area is shown in figure 5.6b: adatoms and vacancies are visible. Figure 5.10 shows the results of this dual mode STS study. Example spectra of adatoms, vacancies and the normal surface are shown, collected with the setpoint set at positive bias (5.10a) and at negative bias (5.10b). A section through a filled state topographic image is shown in figure 5.10c : this shows one adatom and three vacancies. A model of the proposed adatom and vacancy structure produced by cleaving $PrSr_2Mn_2O_7$ is also shown. Sections through the two I(V) maps are shown along the same axis as the topographic section. The "filled state" section is derived from the I(V) array collected with the current setpoint set at positive bias, as in the spectra shown in 5.10a: the section shows the current at -0.8 V of every spectrum along the section line. The "empty state" section is from the I(V) array collected with the current setpoint set at negative bias, as in the spectra shown in 5.10b: the current at +0.8 V is plotted along the same line. The sections are representative of integrated density of states in filled and empty states respectively.

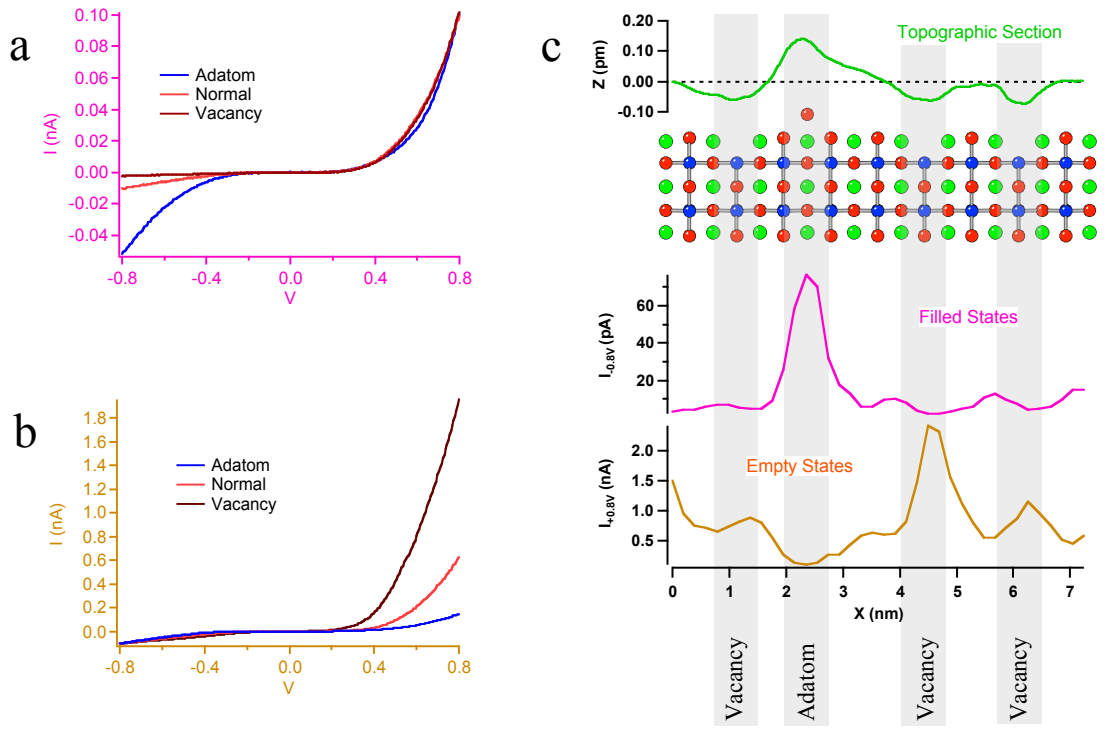

Figure 5.10: (a) Example spectra of adatoms, vacancies and the normal surface collected with the current setpoint set at positive bias. (b) Example spectra collected with the setpoint set at negative bias. (c) Top to bottom: a section through a filled state topographic image: a model of the suggested adatom and vacancy structure: a filled state tunnel current section section derived from an I(V) array, collected with the current setpoint set at positive bias, as in (a): an empty state tunnel current section from an I(V) array, collected with the current setpoint set at negative bias, as in the spectra shown in (b). The current at ± 0.8 V is shown.

It can clearly be seen that the position of the adatom corresponds to a large increase in tunnel current in filled states, and a decrease in empty states. The vacancy positions correspond to an increase in tunnel current in empty states and a slight decrease in filled states. This is consistent with the model that the adatoms are negatively charged oxygen ions, and the vacancies are positively charged oxygen vacancies.

Clearly the normal surface spectra in figures 5.8 and 5.10 are asymmetric with voltage, showing a much larger magnitude of the tunnel current at positive bias than negative bias. The value of the asymmetry in the current is around 10:1 at ± 0.8 V. Similar spectra are obtained from the atomically flat surface. This indicates

that the whole surface has an increased density of states in empty states, suggesting that the surface carries a positive charge. This might be expected since the surface layer exposed on cleaving is the (Pr,Sr)O layer. Each unit cell of this surface contains one O^{2-} ion and one Pr^{3+} or Sr^{2+}: in total there are twice as many Sr^{2+} as Pr^{3+} ions. Assuming that the A-site cations are totally randomly distributed, this means an average charge of $+1/3$ per surface unit cell. The adatoms and vacancies on the $PrSr_2Mn_2O_7$ surface have negative and positive charges respectively *relative* to the surface.

5.2.5 Probability of Adatom Formation

If the adatoms observed in STM images are accepted to be oxygen ions derived from the $PrSr_2Mn_2O_7$ crystal, it is reasonable to ask why we observe the adatom and vacancy coverage we do, and why there is such variation in coverage. If oxygen ions can be separated from an atomic layer to form adatoms and vacancies, why doesn't this occur for all surface oxygen ions? A simple model can be constructed to investigate this. Figure 5.11 shows the lattice environment of the suggested site for adatom/vacancy formation, before and after cleaving. The adatom is placed at the location it would occupy if it has not moved after the sample is cleaved. The nearest neighbours of the oxygen ion which is removed to form a vacancy are four Pr/Sr sites (referred to as A sites), four O sites and one Mn site. The nearest neighbours of the adatom are four oxygen sites and one A site. There will be an energy cost to removing the oxygen ion to form a vacancy, and an energy gain in creating an adatom. The electrostatic energy gain in forming an adatom will be maximised if the nearest A site to the O^{2-} adatom is occupied by a Pr^{3+} ion rather than a Sr^{2+} ion: the energy cost in forming the corresponding vacancy will be minimised if all four of the nearest A sites are occupied by Sr^{2+} ions rather than Pr^{3+}. If the A sites are randomly populated with Pr^{3+} and Sr^{2+} ions according to the stoichiometric composition, then the probability of this configuration occurring is 0.066[1]. The charge of the Mn ion adjacent to the oxygen vacancy site has not been considered for this calculation, since $PrSr_2Mn_2O_7$ is conductive, and it is the Mn e_g electrons which are the charge carriers (see section 1.3): the charge state of each Mn ion will thus rapidly change between Mn^{3+} and Mn^{4+}. Charge ordering is neglected. If we

[1]The stochiometric composition is 2:1 Sr:Pr. $(2/3)^4(1/3) = 0.066$

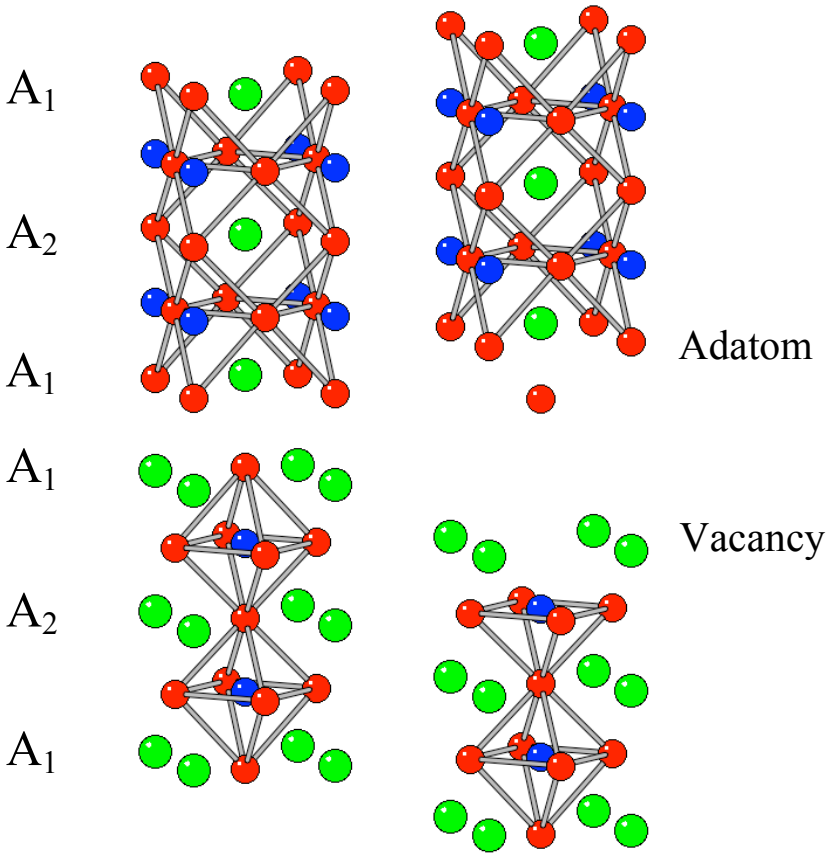

Figure 5.11: Detail of proposed adatom/vacancy formation before and after cleaving. O ions are red, Pr/Sr green and Mn blue. The two types of A sites (green) are differentiated as the 12-coordinate A_2 site and the 9-coordinate A_1 site

assume that the minimum energy configuration is required to form adatoms, this would imply a surface adatom density of 1 per 15 unit cells.

This calculated coverage is higher than the observed maximum adatom density of one per 66 unit cells. However, we have assumed that the probability of an A site in the topmost layer being occupied by a Pr^{3+} ion is 1/3. This is not necessarily the case: some X-ray diffraction studies of bilayer manganites [66,67] show that the divalent ions preferentially occupy the 9-fold co-ordination A sites at the edge of the bilayer and the trivalent ions have a tendency to occupy the 12-fold co-ordination A sites in the centre of the bilayer. This is a form of partial A-site ordering. We will denote the 9-fold co-ordination A site at the edge of the bilayer as A_1, and the 12-fold

co-ordination A sites in the centre of the bilayer as A_2, as shown in figure 5.11. There is a greater tendency to decreased trivalent-ion occupancy of A_1 sites in compounds with trivalent ions of smaller radius: for example in $Pr_{1.2}Sr_{1.8}Mn_2O_7$ the Pr ions have a lower occupancy of the A_1 sites than the La ions do in $La_{1.2}Sr_{1.8}Mn_2O_7$ [67]. Thus it is plausible that A-site ordering of this kind may occur in $PrSr_2Mn_2O_7$: this means the probability of finding a Pr ion in a random A_1 site in the surface layer could be less than 1/3. If we define this probability, equal to the mean Pr occupancy of an A_1 site, as x and adopt the model described above, the probability of an adatom being formed in one surface unit cell is $(1-x)^4\,x$. This is plotted in figure 5.12. This represents an oxygen ion being removed from a site where its nearest neighbours are four Sr^{2+} ions, and being deposited on a surface site above a Pr^{3+} ion. Note that the changing density of Pr ions in the surface layer does not change the average Mn valence as we have not changed the *total* number of Pr and Sr ions. To achieve the observed density of one adatom per 66 unit cells the required Pr occupancy is x = 0.016.

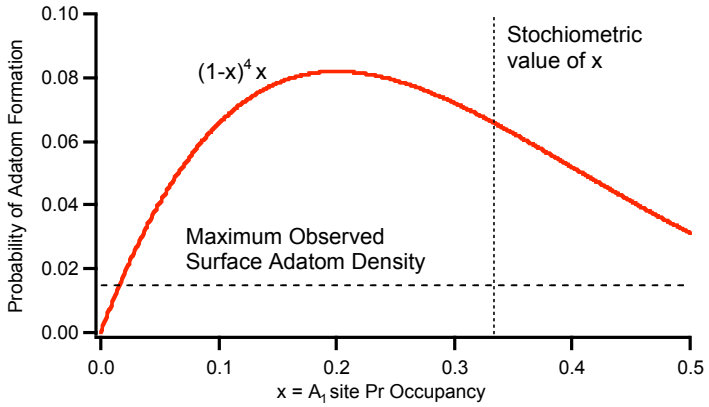

Figure 5.12: Probability of adatom formation according to a simple model, as a function of Pr^{3+} occupancy of A_1 sites, x. The stoichiometric value of x = 1/3 would imply a much higher value for the surface adatom density than is observed.

If the Pr occupancy in the surface A_1 sites x is reduced to zero then the probability of adatom formation is also zero. This represents a fully ordered state where all the A_2 sites are occupied by Pr^{3+} and the A_1 sites are occupied by Sr^{2+}. If such an ordered state exists this could produce the atomically flat surface observed by STM. A completely ordered state may be unlikely however as some mixture of Pr and Sr ions in the surface layer may be necessary to explain the modulation observed in

atomically resolved STM images (see section 5.2.1) and the excess of empty state density of states over filled states on the general surface (see section 5.2.4). One might postulate a Pr surface A_1 site occupancy high enough to produce the observed modulation and density of states asymmetry, but not high enough to produce an observable density of adatoms. There may be natural variation of the Pr^{3+} A_1 site occupancy x in a single sample, due to slight variations in growth conditions, for example temperature. This may produce the different surfaces observed. Areas of high x, which will produce an adatom-vacancy surface, may represent A-site disorder frozen-in during growth, since the crystal growth temperature may provide enough energy to move ions out of their ordered state positions. Theoretical investigations into the role of A-site ordering in adatom formation are currently underway.

5.2.6 Ordering of Oxygen Adatoms on the $PrSr_2Mn_2O_7$ Surface

The analysis of the previous section indicates that adatoms are most likely to sit above Pr^{3+} ions. If oxygen adatoms have a preferred binding site on the $PrSr_2Mn_2O_7$ surface, then ordering of the adatom positions might be expected: adatoms should occupy positions which are commensurate with the atomic lattice. Furthermore, ordering of adatoms may reflect any charge ordering effect in the underlying surface. Image analysis was carried out to identify any possible ordering. Igor Pro software by Wavemetrics, and Scanning Probe Image Processing (SPIP) software by Image Metrology were used. Initially the atomic lattice was extracted from STM images showing adatoms: the adatom positions were compared with this lattice. This analysis showed that the adatoms do not all occupy the same lattice sites: if the atomic lattice were offset to align it with one adatom, then neighbouring adatoms would not be aligned to the lattice. This indicates either that adatoms are not ordered, that the ordering is partial, or that the ordering is incommensurate with the atomic lattice.

Autocorrelation analysis was used to investigate adatom ordering further. An autocorrelation image shows the correlation coefficient of an image mapped onto itself with every possible offset. The autocorrelation image of an STM image of $PrSr_2Mn_2O_7$ which shows adatoms should reveal if the adatoms have any tendency to form self-similar patterns. Figure 5.13a shows a 36 x 37 nm STM topographic image of $PrSr_2Mn_2O_7$ featuring adatoms, collected at 78 K. This is the same area shown in figures 5.6a and 5.7, but the image has been rotated in software after the data were acquired, to align it to the lattice directions. Figure 5.13b shows an autocorrelation image of 5.13a. Two peaks are visible in this image, which might indicate tendency for adatoms to maintain the same spacing in one direction. However, we cannot be sure that these autocorrelation peaks are due to the adatoms rather than some other feature of the $PrSr_2Mn_2O_7$ image. Therefore we need a way to isolate the adatom positions and analyse them separately from the rest of the image. To do this the grain analysis tool in SPIP was used to assign coordinates to every part of the image above a threshold level: these coordinates represent the adatom positions. The coordinates can then be converted into a sparse matrix, *i.e.* an image which is zero everywhere apart from at the adatom positions, with each

adatom being represented by a 1. This image is then smoothed by convolution with a 2D Gaussian to form a synthetic image of the adatoms suitable for image analysis. Such an image is shown in figure 5.13c: the spots represent the adatom positions in figure 5.13a. An autocorrelation image of this synthetic adatom image is shown in figure 5.13d: the same peaks are visible as in 5.13b, demonstrating that they are indeed due to a common adatom spacing in one direction. A section through these peaks is shown in 5.13e: the position of the section is shown as a red section in figure 5.13d. The peaks indicate a spacing of 6.39 ± 0.11 nm at 44.3 ± 0.7° to the lattice direction. This does not seem to correspond to any integer multiple of $\sqrt{2}\times$a where a is the $PrSr_2Mn_2O_7$ lattice spacing of 0.385 nm. These peaks have a maximum correlation coefficient of 0.12. There are some weaker peaks closer to the central peak in the autocorrelation image, aligned to the lattice to ± 4°. A section through these peaks is shown in 5.13f: the position of the section is shown as a blue section in figure 5.13d. These peaks show a spacing of 0.83 ± 0.11 nm, which corresponds to 2a = 0.77 nm. The maximum correlation coefficient is only 0.064 however.

In this image at 78 K we have identified an incommensurate ordering of adatoms at 45° to the atomic lattice, and a weak tendency for adatoms to order with a spacing of 2a in the lattice direction. However other images of the $PrSr_2Mn_2O_7$ surface do not show the same adatom ordering. Figure 5.14 shows another topographic image of $PrSr_2Mn_2O_7$ collected at 78 K, together with an autocorrelation image. The topographic image has been aligned to the atomic lattice as for figure 5.13a. The peaks in this autocorrelation image are clearly different from those in figure 5.13b. The strongest peaks are at 2.64 ± 0.12 nm at -8.6 ± 0.7 ° to the atomic lattice: these are shown in section 5.14c and have a correlation coefficient of 0.34. Further peaks are at 2.74 ± 0.12 nm at 61.0 ± 0.7 ° to the atomic lattice: these are shown in the section 5.14d and have a correlation coefficient of 0.10. These peaks are not orthogonal to each other and seem to be incommensurate with the atomic lattice. Autocorrelation images have been derived from many further areas, and are observed to produce yet more different peak positions. No common autocorrelation peaks are observed. We may therefore conclude that, based on autocorrelation data, there is no significant, consistent ordering of adatoms at 78 K. No signature of the ≈ 4a charge stripe order observed in X-ray diffraction data [79] is identified in the autocorrelation data.

Images of adatoms on the $PrSr_2Mn_2O_7$ surface were collected at a range of temper-

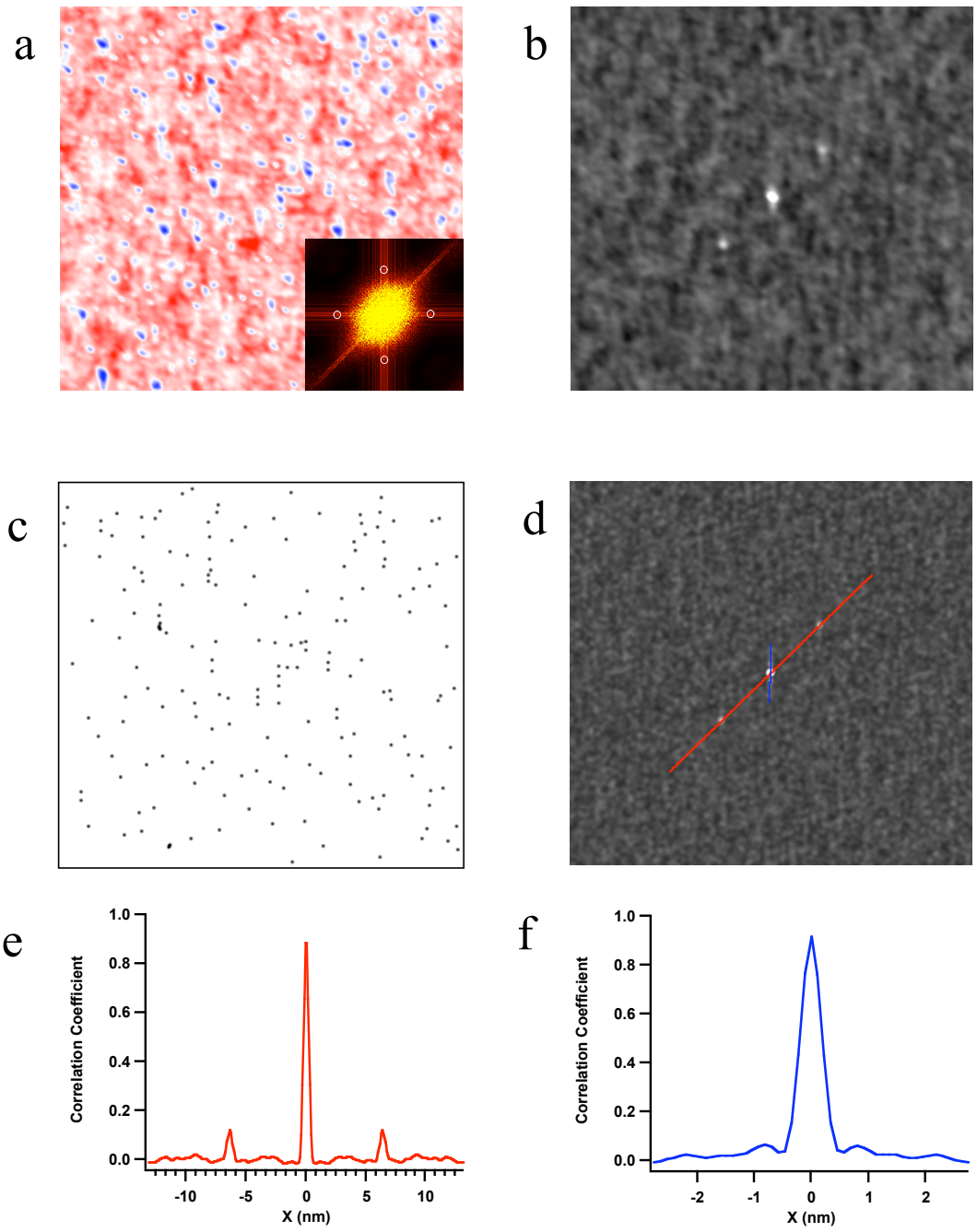

Figure 5.13: (a) 36 x 37 nm STM topographic image at 78 K showing adatoms in blue, vacancies in dark red. The image has been rotated to be aligned to the atomic lattice: a Fourier transform is shown (inset) with the lattice spots indicated (b) Autocorrelation image derived from the topographic image. (c) Synthetic image showing adatom positions only. (d) Autocorrelation image derived from the synthetic image. Section positions are indicated by colour coded lines. (e) Section through (d), showing correlation peaks at 6.39 nm. (f) Section through (d) showing weak peaks at 0.83 nm.

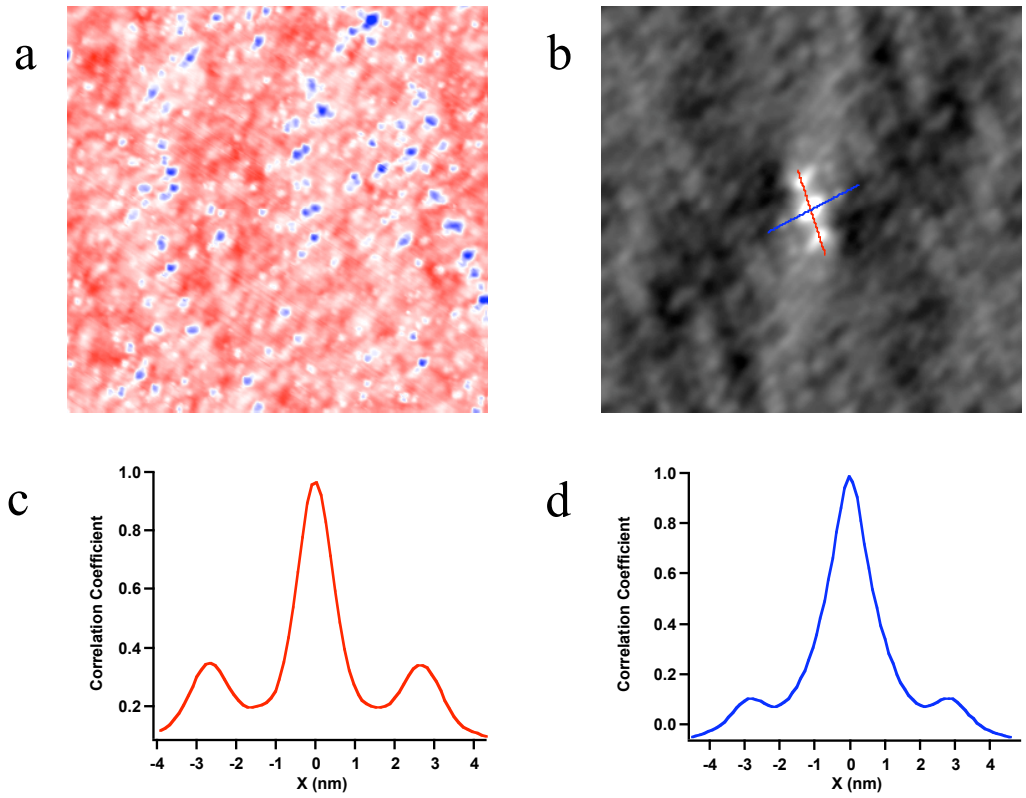

Figure 5.14: (a) 38 x 38 nm STM topographic image at 78 K showing adatoms in blue, vacancies in dark red. The image has been rotated to be aligned to the atomic lattice. (b) Autocorrelation image derived from the topographic image. Section positions are indicated by colour coded lines. (c) Section through (b), showing correlation peaks at 2.64 nm. (d) Section through (b) showing peaks at 2.74 nm.

atures from 78 K to 195 K. Images 50 x 50 nm across were analysed, containing around 300 adatoms each. All images show sharp peaks in the Fourier transform, corresponding to the atomic lattice. Various autocorrelation peaks were observed, but no consistent ordering of adatoms was observed from autocorrelation data at any temperature.

Some further analysis methods were used to investigate any possible ordering of adatoms. The analysis method described above to extract the adatom positions produces x,y coordinates for each adatom: we can therefore calculate the nearest neighbour spacing of adatoms. This analysis was carried out for the full range of temperatures studied: for each image at each temperature the nearest neighbour

distance of each adatom r_A was measured. A histogram of r_A can then be produced: this should reveal if there is any tendency for adatoms to group at a specific distance from each other, as this would be visible as a sharp peak in the histogram. Figure 5.15a shows example histograms of r_A at 78 K and 195 K. The histograms do not reveal any special value of r_A, nor is this seen at any intermediate temperature. Mean and median adatom nearest neighbour spacings can be measured for each data set. Figure 5.15b shows these values plotted against temperature. Two results are apparent: firstly, the spacing of adatoms increases with temperature, accompanying a decrease in the number of adatoms per unit area. At 78 K this is equivalent to one adatom per 66 unit cells: at 195 K, one adatom per 89 unit cells. This result will be discussed in section 5.2.7. Secondly, at low temperatures the median value is substantially less than the mean: at higher temperatures the two averages are closer in value. This may be attributed to the fact that r_A cannot be less than zero. At low temperature where the mean value $\bar{r}_A$ is smaller, this results in an asymmetric distribution with the median smaller than the mean. This can be observed in 5.15a where the histogram for 78 K is substantially more asymmetric about the median than that for 195 K. This result does not therefore imply any significant change with temperature in the ordering of adatoms.

We can perform a numerical test based on the mean nearest neighbour spacing $\bar{r}_A$ to determine if adatoms are randomly distributed, ordered or clustered. This test is based on comparing the measured mean nearest neighbour spacing $\bar{r}_A$ with a mean spacing calculated from a random Poisson distribution of points, $\bar{r}_E$. The test is discussed in detail by Clark and Evans [11]: we will state the main results here. If the density of points per unit area is given by ρ, then:

$$\bar{r}_E = \frac{1}{2\sqrt{\rho}} \tag{5.1}$$

We can then use the ratio $\mathrm{R} = \bar{r}_A/\bar{r}_E$ to quantify the degree of ordering of points. If $\mathrm{R} = 1$ then the distribution of points is indistinguishable from a random distribution. If $\mathrm{R} < 1$ the mean nearest neighbour distance is less than the random value, so the points must be grouped into clusters. If R >1 the mean nearest neighbour distance is larger than the random value, so there must be some ordering or anti-clustering behaviour. For example, if the points are ordered into a regular square lattice, R

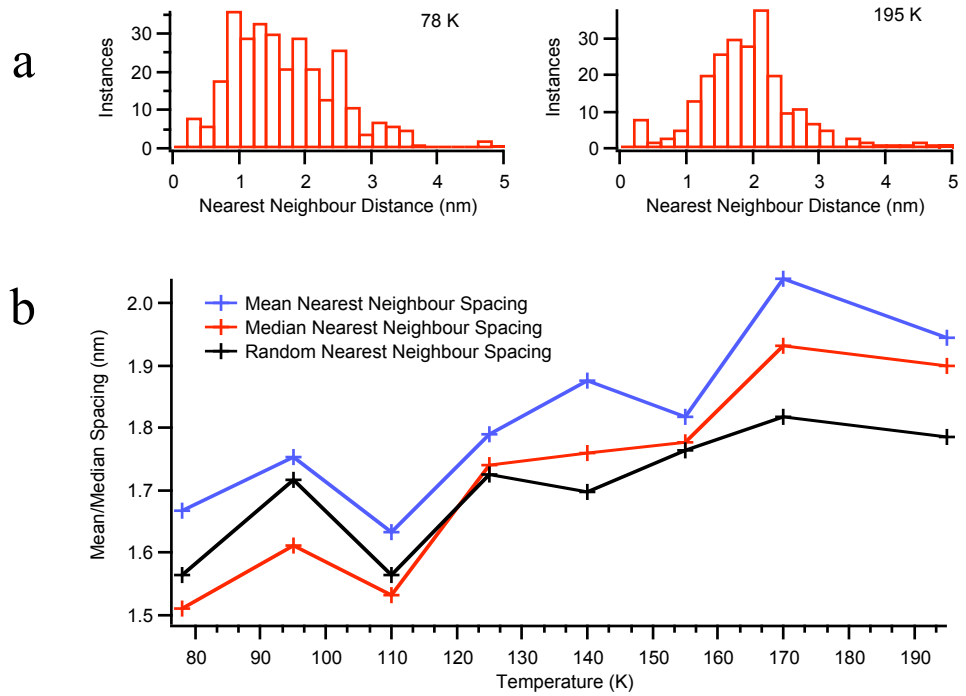

Figure 5.15: (a) Example histograms of adatom nearest neighbour spacing r_A at 78 K and 195 K (b) Mean adatom nearest neighbour spacing $\bar{r}_A$ as a function of temperature. The calculated spacing based on a random Poisson distribution, $\bar{r}_E$, and the Median nearest neighbour spacing are also shown.

Temperature (K)	$\bar{r}_A$ (nm)	$\bar{r}_E$ (nm)	R	N	ρ (nm^{-2})	c
78	1.668	1.563	1.067	306	0.102	2.24
95	1.753	1.717	1.021	206	0.085	0.57
110	1.632	1.565	1.043	334	0.102	1.51
125	1.791	1.725	1.038	270	0.084	1.19
140	1.877	1.697	1.106	276	0.087	3.36
155	1.819	1.764	1.031	252	0.080	0.95
170	2.040	1.818	1.122	231	0.076	3.55
195	1.944	1.785	1.089	239	0.078	2.63

Table 5.1: Table showing variation in measured mean nearest-neighbour adatom spacing $\bar{r}_A$ with temperature. The calculated spacing based on a random Poisson distribution of adatoms $\bar{r}_E$ is also given, together with R = $\bar{r}_A/\bar{r}_E$. N is the number of adatoms in each image, ρ is the number of adatoms per nm^2. The statistical significance of the deviation of R from 1, c is given in in standard deviations

= 2. If the points are ordered into a hexagonal lattice, maximising mean nearest neighbour spacing, R = 2.1491 [11]. Table 5.1 gives $\bar{r}_A$, $\bar{r}_E$ and $R = \bar{r}_A/\bar{r}_E$ for the full range of temperatures studied. These data are derived from images approximately 50 x 50 nm in size: the total number of adatoms in each image N, and the areal density of adatoms ρ are also given. For all temperatures R > 1, implying a degree of order in the placement of adatoms. R ranges from 1.02 to 1.12: there does not seem to be any clear dependence of R on temperature.

We can perform a statistical test to determine if the deviation of R from 1 is significant in this case. This test is also discussed by Clark and Evans [11]. The standard variate of the normal distribution c, measured in standard deviations, is given in this case as:

$$c = \frac{\bar{r}_A - \bar{r}_E}{\sigma_{\bar{r}_E}} \tag{5.2}$$

Where $\sigma_{\bar{r}_E}$ is the standard error of the mean nearest neighbour distance in a randomly distributed population, which is given by:

$$\sigma_{\bar{r}_E} = \frac{0.26136}{\sqrt{N\rho}} \tag{5.3}$$

The derivation of $\bar{r}_E$ and $\sigma_{\bar{r}_E}$ is given by Clark and Evans [11]. The standard variate c has been calculated for all temperatures studied: this is listed in table 5.1. Considerable variation is observed in c, but since no clear temperature dependence is seen in R or c, it is reasonable to average over all images. The mean value of c is equal to 2.00, greater than the 95% confidence interval of c = 1.96. Therefore we may conclude that when averaged over temperature there is a statistically significant tendency for oxygen adatoms on the $PrSr_2Mn_2O_7$ surface to adopt an anti-clustered arrangement. The average value of R is only 1.06 however, so this must be regarded as weak anti-clustering. This result does not necessarily imply that oxygen adatoms are ordered, it may simply indicate that adatoms repel one another, as would be expected if they all carry a negative charge.

5.2.7 Oxygen Adatom Motion

STM topographic images of $PrSr_2Mn_2O_7$ showing adatoms and vacancies were obtained using the LT-STM at a range of temperatures, from 78 K to 195 K. It can be observed that oxygen adatom positions do not all remain fixed, but change over time. Figure 5.16a shows a time series of STM images collected at 170 K, covering 16 minutes: several adatoms can be observed to appear and disappear. From frame to frame most adatoms remain in the same position: this allows the use of cross-correlation to align the images and correct for the effects of drift. Such time series were collected at a range of temperatures. Figure 5.16b shows how the hopping rate, defined as the fraction of visible adatoms appearing or disappearing per frame averaged over many frames, varies with temperature. All other parameters such as image size, tunnel current and applied bias voltage were constant. The area for study was randomly selected at each temperature: due to thermal effects it was not possible to study the same area at all temperatures. One temperature point was measured per day, in order of increasing temperature. The error bars represent one standard error $\sigma/\sqrt{n}$, where σ is the standard deviation of the hopping rate and n is the number of frames the measurement is averaged over. The mobility increases from nearly zero at 78 K to around 4% of visible adatoms at 125 K. Further increase in temperature does not seem to produce much increase in mobility: the reason for this is not known, but may be related to the inflection in resistivity at $T_N \approx$ 130 K (section 5.1). The sample resistivity decreases sharply upon increasing the temperature above 130 K, indicating a transition to a more insulating state in which there may be a stronger interaction between the surface and adatoms. Clearly it is not possible to accurately measure an activation energy from these data.

The observation of mobile adatoms in STM images does not represent a passive measurement. The STM tip will exert a force on the surface adatoms, and the motion of the tip may drag or push adatoms around on the surface. The tunnel junction properties (bias voltage and tunnel current) will affect the force exerted by the tip upon adatoms. Unfortunately attempts to study the bias and tunnel current dependence of adatom mobility have largely been inconclusive due to the small number of mobile adatoms and the substantial natural variation in mobility. However, there is a clear dependence of mobility on sample bias polarity. The same area of the $PrSr_2Mn_2O_7$ surface was repeatedly scanned at a range of biases at 170 K,

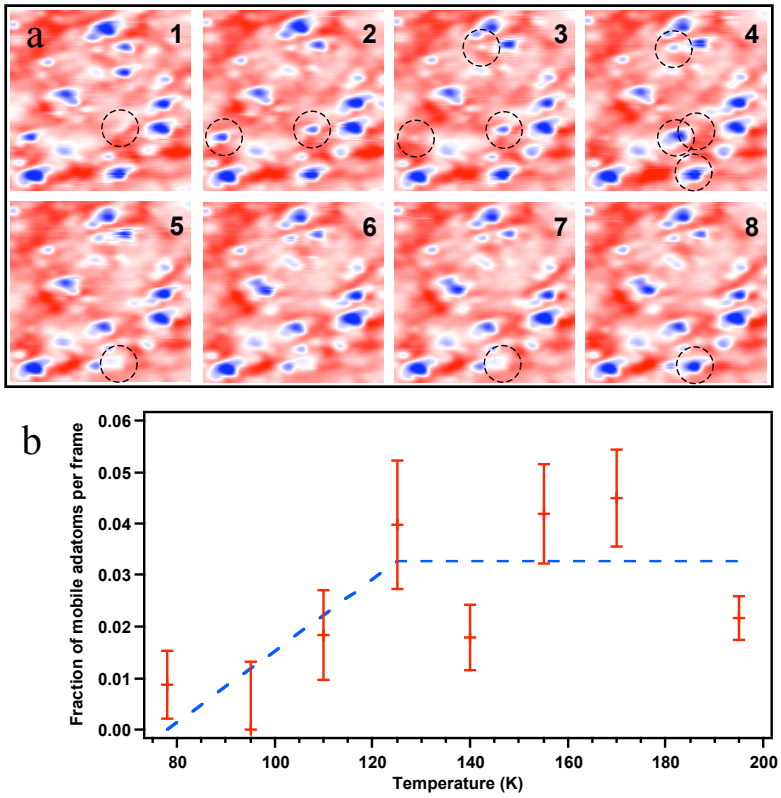

Figure 5.16: (a) A time series of filled state STM topographic images, 10 x 10 nm, collected at 170 K. Total time covered is 16 minutes: adatoms which move from one frame to the next are outlined (b) number of adatom "hops" (appearances or disappearances) per frame as a function of temperature: dashed line is a guide to the eye.

and the hopping rate measured for each bias. At positive sample bias the hopping rate is minimal, less than 0.8 % and does not display any dependence on bias in the range +0.5 V to +0.8 V. Once the sample bias is switched to -0.8 V the hopping rate increases to 9 %. This dependence on bias polarity may be due to two factors. Firstly at negative sample bias oxygen ions will be repelled from the $PrSr_2Mn_2O_7$ surface and attracted to the tip, which may increase mobility. Secondly due to the asymmetric density of states (see section 5.2.4) at negative sample bias the tip will move closer to the surface to maintain the tunnel current setpoint. This will result in a larger force being exerted on the adatoms by the tip. However, it is worth noting that the mobility does not increase at lower positive bias. In I(V) spectra a sample bias of +0.5 V results in a similar magnitude of tunnel current to -0.8 V, indicating that when scanning at +0.5 V the tip is a similar distance from the

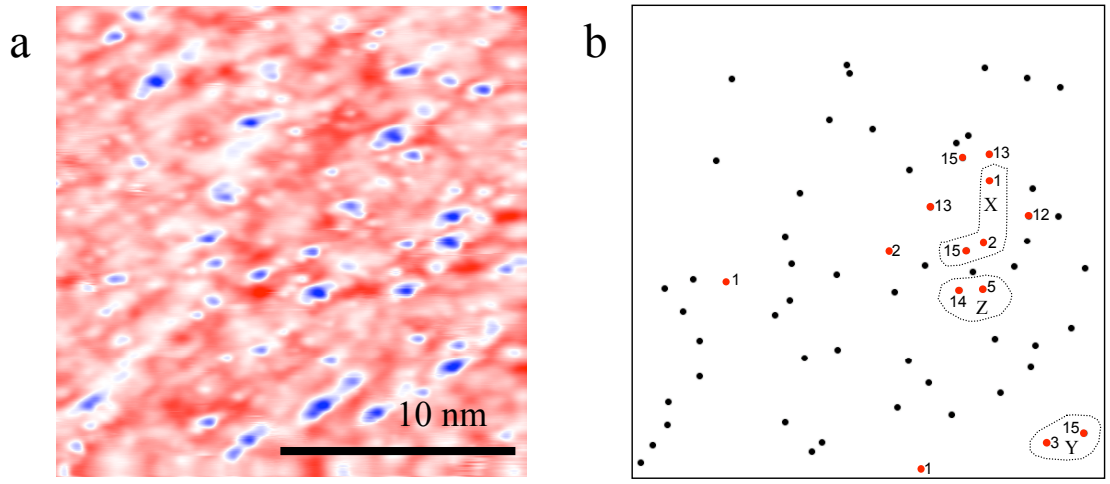

Figure 5.17: (a) 20 x 20 nm filled state topographic image. One of a time series of 18 images collected at 170 K: the images shown in figure 5.16 show a detail of this time series (b) time series analysis. Black markers indicate an adatom present for all 18 frames: red markers indicate an adatom position occupied only for a limited number of frames. This occupancy number is indicated next to the marker.

surface as when scanning at -0.8 V. This would indicate that electrostatic effects are important in determining oxygen adatom mobility. So far it has not been possible to deliberately manipulate oxygen adatoms with the STM tip.

From time series such as figure 5.16a it is not clear if adatoms are hopping from one site to an adjacent site, or randomly appearing and disappearing. One way to distinguish these two possibilities is by studying the time series to see if there is any correlation between the locations of sites where adatoms appear and disappear. Some detailed analysis on a time series of images was therefore carried out. Figure 5.16a is a detail of a series of larger images: one of these 20 x 20 nm filled state images is shown in figure 5.17a. The full time series consists of 18 frames, covering a time interval of 36 minutes. The analysis was carried out as follows. Each frame was reduced to a sparse matrix as detailed in section 5.2.6, zero everywhere apart from at the adatom positions, with each adatom being represented by a 1. The complete set of matrices is summed to produce the image shown in figure 5.17b. Adatoms that do not move are represented by a pixel value, or occupation number, of 18. Adatom positions that are only occupied for part of the time series have an occupation number of less than 18. In figure 5.17b the pixels representing the adatom positions have been enlarged to make them more visible: positions with an

occupation number of less than 18 are marked red, and the number is indicated. Positions with an occupation number of 18 are black. Several conclusions can be made: firstly there is a clear correlation of the positions of partly-occupied sites with one another: there is a cluster of mobile adatoms in the centre right of the image. Secondly pairs and groups of sites can be identified which indicate a clear hopping path for a single adatom. These can be identified as groups of sites which show sequential occupation, *i.e.* where the total occupancy is 18 and no two sites are simultaneously occupied. Two such groups are identified in figure 5.17b and are labelled as X and Y. Thirdly adatom positions which are vacated are sometimes reoccupied later. Group Z in figure 5.17b indicates an adatom which has hopped from one site to its neighbour: the original site is then re-occupied by another adatom. The total occupancy of the group is therefore 19.

There is clear evidence that adatoms hop from site to site rather than appearing and disappearing at random. The appearance and disappearance of adatoms are clearly correlated and cascades can be observed where adatoms appear to sequentially hop from one site to another. Adatoms may diffuse over the surface, or they may hop onto the STM tip and then off again at a different location: if adatoms hop onto the apex of the tip however this would be expected to affect the imaging conditions, which is not observed in these time series. It is worth noting that at 170 K only 22% of adatoms are mobile, with most remaining fixed.

The fact that vacated adatom sites are later reoccupied indicates that adatoms do *not* sit at random sites on the surface, but have preferred positions. Based on the evidence of the previous section however it would appear that adatoms do not display any ordering which is commensurate with the atomic lattice. There are therefore preferred adatom positions which do not bear a simple relationship to the surface lattice. We may relate these preferred binding sites to the larger scale ($\approx$ 4 nm) modulation seen in atomically flat STM images of the $PrSr_2Mn_2O_7$ surface (see section 5.2.1). This modulation is not observed in images of $PrSr_2Mn_2O_7$ which show adatoms and vacancies, but it may simply be masked by the much larger z-signal of the adatoms. Oxygen vacancies may preferentially occupy potential energy minima created by the modulation. The $\approx$ 4 nm modulation is in turn likely related to a disordered or partially ordered arrangement of Pr^{3+}, Sr^{2+}, Mn^{4+} and Mn^{3+} ions at or near to the $PrSr_2Mn_2O_7$ surface (sections 5.2.1 and 5.2.5). Negatively charged oxygen adatoms may find potential energy minima at sites above Pr^{3+} ions,

above pairs or groups of Pr^{3+} ions, or sites defined by a more complex combination of A-site cations and Mn ions.

5.2.8 Recombination of Oxygen Adatoms and Vacancies

Image analysis can be used to calculate the coverage of adatoms and vacancies on the $PrSr_2Mn_2O_7$ surface, and to determine if this coverage is constant with time and temperature. Two methods can be used to determine the adatom or vacancy coverage. Firstly the grain analysis method can be used as for the previous time series and temperature dependence analyses. In this method a threshold level is set: all areas higher than this are designated as adatoms: these areas are identified and counted. The advantage of this method is that the coordinates of the adatoms are determined, so statistics on their nearest-neighbour spacing can be collected. The method requires that the images used are carefully calibrated in Z so that the same threshold can be used for all images. The calibration used must take account of the changing piezo constant with temperature.

This method has been used in section 5.2.6 to plot the coverage of adatoms only as a function of temperature. Coverage is measured from single images at each temperature. The coverage of adatoms is observed to decrease with increasing temperature, from one adatom per 66 unit cells at 78 K to one adatom per 89 unit cells at 195 K. The observed decrease in adatom coverage is a function both of temperature and time: the temperature dependent data took a total of eight days to collect. One temperature was measured per day, in order of increasing temperature. At a fixed temperature of 78 K the coverage of adatoms has been observed to decrease over time between images collected three days apart, but only by 3 %. In the temperature dependent experiment we see the coverage decrease by 35 % over seven days, so there is a clear effect of elevated temperature.

The grain analysis threshold method works well for adatoms, but not for vacancies. Vacancies often join into pairs or groups, leading to an underestimate of the vacancy coverage by the threshold method. The method also relies on accurate Z-calibration information being available. An alternate method is to analyse the height (Z) histogram of an image: this contains information on the coverage of the image by adatoms and vacancies. An example Z histogram is shown in figure 5.18. The cen-

tral portion of the histogram arises due to the "normal" surface, not adatoms or vacancies: this can be fitted with a Gaussian function, shown as a dotted line in the histogram in figure 5.18. The central portion is defined as the region within the half maximum of the histogram. The Gaussian function then gives a reference for analysing the rest of the histogram. In an image with a high density of adatoms, the histogram will show an excess over the Gaussian fit at the positive end of the distribution: a high vacancy density will result in an excess over the fit at the negative side. The coverage of adatoms and vacancies can be measured by integrating the area under the histogram at each end: this integrated area is equal to the area of the image covered in adatoms and vacancies. The adatom and vacancy coverage is thus determined by integrating the regions of the Z histogram at each end and expressing this value as a fraction of the total integrated area under the histogram, which is equal to the total area of the image. The end regions are defined as those areas where the Gaussian fit is 5% or less of its peak value. Thus the adatom and vacancy coverage are determined by analysing the shape of the image height histogram, so the result is independent of the Z-calibration of the image. This method has been applied to a time series of images, collected on the same area at a fixed temperature. The same time series as used for figure 5.17 has been used: the series consists of 18 frames collected over 36 minutes at 170 K. Figure 5.18 shows that the coverage of both adatoms and vacancies decreases during this time series. The coverage of adatoms decreases from 5.59 % to 5.05 %, and the coverage of vacancies decreases from 1.15 % to 0.76 %. The vacancy coverage as measured by this method is lower than the adatom coverage since vacancies are shallower than adatoms are high, but the same cut-off value of 5 % has been used for both.

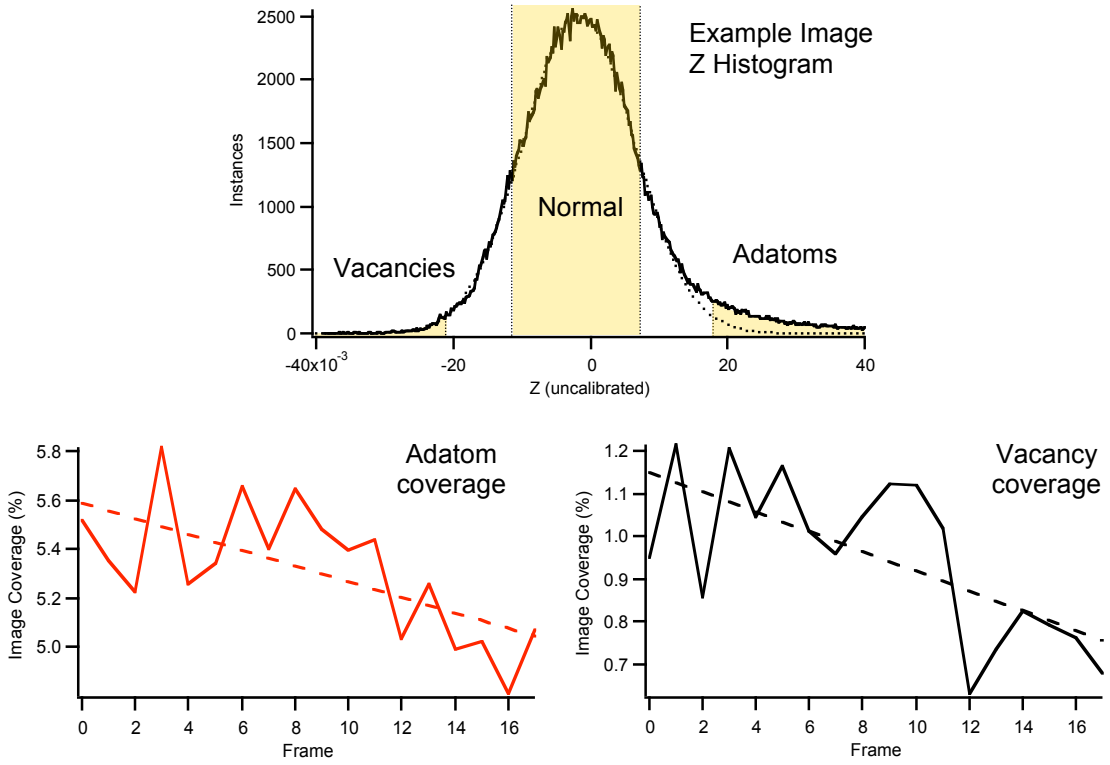

Figure 5.18: Analysis of adatom and vacancy coverage as a function of time within a time series of STM images (frames). The height (Z) histogram of each image is analysed to produce an areal coverage of adatoms and vacancies for each frame. The coverage of both adatoms and vacancies is observed to decrease with time. The time series covers 36 minutes.

Over a time series of images the density of both adatoms and of vacancies decreases. It is logical to postulate that adatom-vacancy recombination may be taking place, where adatoms fall into vacancies, producing a reduction in the coverage of both. This process may also explain the decrease in coverage with increasing temperature. As the adatom mobility appears to be thermally activated, recombination will occur more rapidly at higher temperatures, resulting in more rapid depletion of adatom and vacancy densities at elevated temperature. The recombination of adatom/vacancy pairs has been observed by STM. Figure 5.19 shows two successive frames of a time series: in (a) an adatom and a vacancy are visible in close proximity; in (b) both the adatom and the vacancy have vanished, suggesting that the adatom has filled in the vacancy.

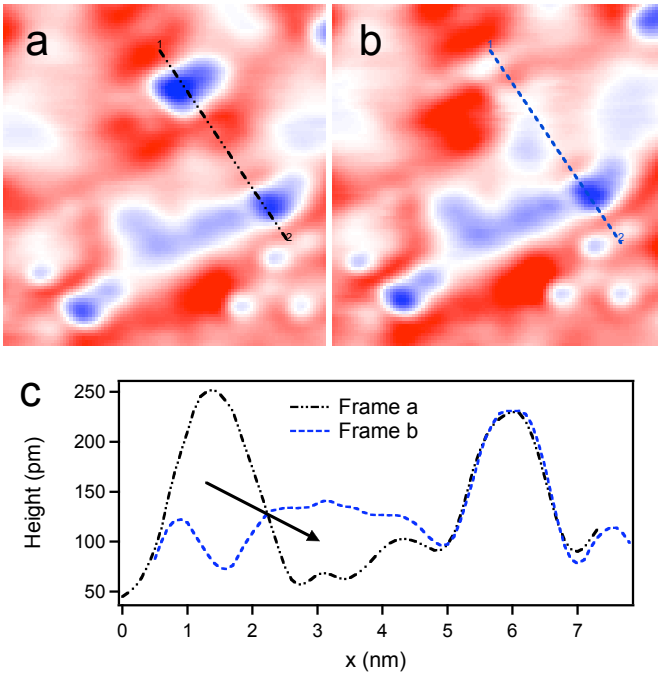

Figure 5.19: (a) and (b): successive frames in a time series showing recombination of an adatom/vacancy pair (c) line profiles through (a) and (b) showing that both the adatom and the adjacent vacancy vanish

5.2.9 Bistable Oxygen Adatoms

In addition to adatom hopping observed in a time series of images, bistable adatoms are observed in single STM images and I(V) spectra. Such adatoms can switch between two adjacent positions several times during a single topographic scan, within a time frame of a few minutes. Figure 5.20 shows an STM topographic image collected at 125 K, showing a bistable adatom: the adatom appears streaky because it moves between one scan line and the next. The STM tip takes around 10 s to scan over the adatom. Also shown are I(V) spectra collected on the bistable adatom, a stable adatom and the normal surface: spectrum positions are marked on the topographic image. Voltage was swept from positive to negative bias. A discontinuity is observed in the I(V) curve because the adatom switches position during the I(V) measurement. The measured spectrum switches between that typical of an oxygen adatom and that of the underlying surface. This occurs faster than the time resolution of the I(V) measurement of 1 ms. This discontinuity can be used to measure the bias voltage needed to switch the adatom: switching of bistable atoms is not observed at low bias, but only at bias voltages higher than 300 mV. It may not be possible to discern switching at lower biases however since this is will be within the gap of the I(V) spectrum, and tunnel current will be very low. Switching has been observed at both positive and negative bias, and when sweeping the bias voltage in either direction.

The mechanism behind the discontinuity observed in I(V) spectra is assumed to be the motion of the oxygen ion under applied bias: as the bias between the sample and the tip is increased, the adatom moves towards or away from the tip. So far attempts to determine the preferred direction of switching have not been successful: no clear dependence of the switching direction upon bias polarity or the direction that the bias is swept in has been established. Bistable oxygen adatoms and discontinuous I(V) spectra have been observed at 78 K, 125 K and 140 K, but so far there is insufficient data to determine the temperature dependence of this phenomenon.

One problem with studying bistable adatoms with I(V) spectroscopy is that the bias voltage needs to be re-applied after each I(V) measurement, in order to continue imaging: this voltage may move the adatom again, introducing uncertainty into the voltage and position history of the adatom. It would be advantageous to be able to scan the $PrSr_2Mn_2O_7$ surface at a low sample bias, < 300 mV, since this

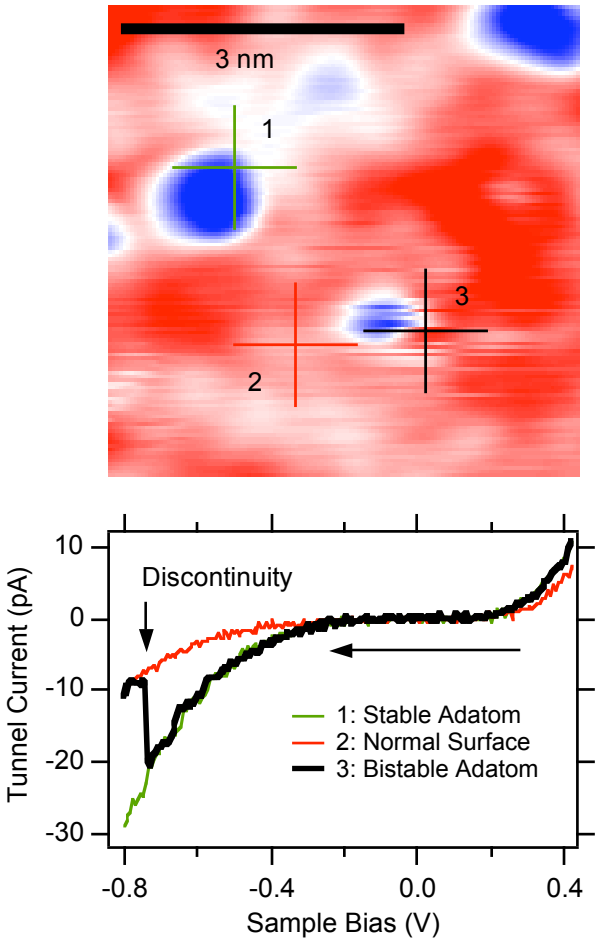

Figure 5.20: 5 x 5 nm STM topograph collected at 125 K, 100 pA, -0.8 V sample bias. Position 1 shows a stable adatom, position 3 a bistable adatom. I(V) Spectra from these positions are shown, together with a spectrum from the normal surface (position 2). Spectrum 3 shows the characteristic discontinuity caused by motion of the adatom: the spectrum can be seen to switch between that of an adatom and that of the normal surface.

would reduce electrostatic forces exerted on adatoms: switching of bistable adatoms has not been observed below this voltage. Performing STM at less than 300 mV bias voltage may not be possible however, as due to the low tunnel current at this bias the tip will likely crash. In future, it is planned to upgrade the LT-STM at the London Centre for Nanotechnology to include Q-plus AFM capability. This enables atomic resolution AFM to be carried out in the same low-temperature, UHV environment as STM. In addition combined AFM-STM experiments can be carried out, for example imaging may be performed using AFM mode, but tunnelling I(V)

spectra may be collected as well. AFM capability would allow images to be collected at zero bias, to establish a "baseline" mobility: the voltage dependence of the adatom mobility could then be studied in detail. In addition, it would be possible to measure accurately the voltage required to move single adatoms on the $PrSr_2Mn_2O_7$ surface. Adatom positions could be determined using AFM mode: voltage pulses could then be applied to the adatoms, and the voltage required to move the adatom determined from the discontinuity in the tunnel current, without the uncertainty in the voltage history of the adatom inherent in the STM measurement.

5.2.10 Effect of High Temperatures on the $PrSr_2Mn_2O_7$ Surface

Imaging the $PrSr_2Mn_2O_7$ surface using the LT-STM at temperatures above 195 K has proved problematic. Imaging was attempted at 220 K: terraces can still be observed, with 1 nm high steps. The overall surface roughness is around 0.2 nm, consistent with the adatom/vacancy $PrSr_2Mn_2O_7$ surface. Higher resolution images were very noisy however, with many changes of contrast, likely due to some instability of the STM tip. A few stable images were obtained at 220K: figure 5.21 shows a short time series of images, covering around 3 minutes. Adatoms can clearly be seen in these images, and are around 150 pm high. Clearly the adatoms are mobile: we can identify up to 8 appearances or disappearances of adatoms per frame: the fraction of mobile adatoms is 69 $\pm$ 15 %, far higher than the mobility observed at lower temperatures. The coverage of adatoms varies within the short time series shown in figure 5.21 but is in the range $0.04 \leq \rho \leq 0.07$ nm^{-2}, or between one per 100 and one per 165 surface unit cells[2]. This compares to one adatom per 86 unit cells at 195 K. Both the increased mobility and decreased coverage fit with the temperature trends previously identified: there is clearly a dramatic increase in mobility between 195 K and 220 K though. Figure 5.22 shows the fraction of mobile adatoms as defined in section 5.2.7, including the hopping rate at 220 K. The same guide to the eye as figure 5.16b has been shown for 78 K $\leq$ T $\leq$ 195 K in the inset to figure 5.22. An activated fit of the form $exp(-E_A/k_bT)$ has been made for the full temperature range. The activated fit is shown in figure 5.22: the activation energy

[2]The same counting method and height threshold has been used to evaluate the adatom density at 220 K as for the lower temperature data in section 5.2.6

$E_A = 140$ meV. There is a poor fit to the lower temperature adatom mobility. Due to this poor fit the measurement of the activation energy is not accurate: however the likely range of the activation energy can be estimated by making several activated fits. This method yields $100 \leq E_A \leq 260$ meV. The poor fit suggests that adatom mobility is not a simple thermally activated process.

There is a decreased coverage of adatoms at 220 K, with between 11 % and 46 % fewer adatoms than at 195 K. The $PrSr_2Mn_2O_7$ surface was studied at 220 K as part of the same experiment as the lower temperature studies: the 220 K data were collected the day after the data for 195 K. For 78 K $\leq$ T $\leq$ 195 K the average decrease of adatom coverage in a 25 K interval was around 5 %. This indicates that loss of adatom coverage is indeed a function of temperature as well as time: the loss of adatoms appears to accelerates in line with the increased adatom mobility. As noted in section 5.2.8 an increased adatom mobility will lead to an accelerated loss of adatoms, through recombination with vacancies. Adatoms may also be lost from the surface to the vacuum, though this will obviously not lead to a corresponding loss of vacancies.

The high mobility of oxygen adatoms at 220 K may explain the difficulty in imaging the $PrSr_2Mn_2O_7$ surface at this temperature: very mobile oxygen adatoms may be picked up by the STM tip during scanning, changing the tunnel junction properties. Adatoms picked up by the tip may become chemisorbed to it, making it very difficult to remove them and restore normal imaging. In practice after a few hours of scanning the $PrSr_2Mn_2O_7$ surface at 220 K a stable scan could no longer be obtained, and the STM tip had to be changed.

In order to change the STM tip in the LT-STM, the sample has to be removed from the STM stage and placed on a carousel, which is at room temperature. Warming $PrSr_2Mn_2O_7$ samples to room temperature is generally observed to disrupt the surface: stable STM imaging has not been obtained on samples which have been allowed to warm up. This may be due to the adsorption of water onto the sample surface. Some residual water will remain in the vacuum chamber, and if the sample is warmed to room temperature, water may escape from surfaces close to the sample and coat the sample surface. Also, as the sample is cooled from room temperature again for imaging, the sample surface will act as a getter for water molecules. Unfortunately this means that the $PrSr_2Mn_2O_7$ sample which had been imaged at 220

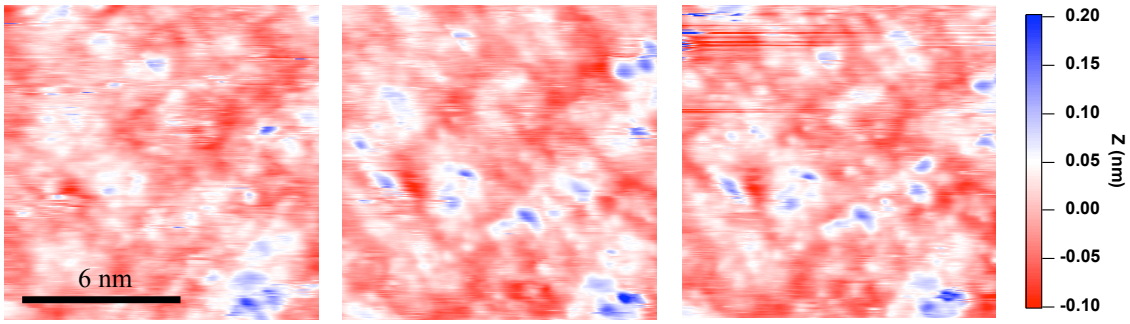

Figure 5.21: Time series of 12 x 12 nm topographic images of $PrSr_2Mn_2O_7$ collected at 220 K, +0.8 V sample bias.

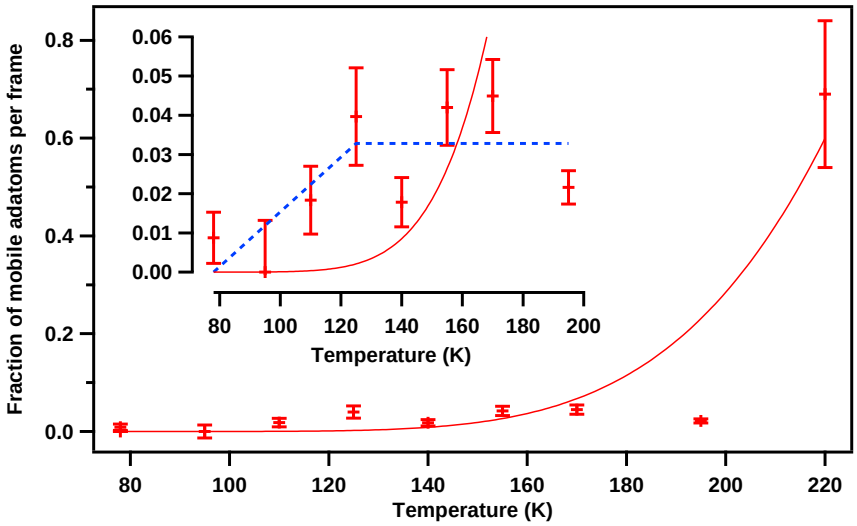

Figure 5.22: Fraction of mobile adatoms per frame as a function of temperature, including data from 220 K: thermally activated fit with $E_A = 140$ meV shown. Inset: temperature range 78 K $\leq$ T $\leq$ 195 K only, with guide to the eye (blue dashed line)

K could not be imaged again at a lower temperature as a control experiment, to see if the adatom mobility decreases again on cooling.

In general the approach adopted in the $PrSr_2Mn_2O_7$ experiments using the LT-STM described here was to keep the sample below 200 K at all times to avoid either the tip picking up adatoms, or the sample becoming contaminated with water. This approach has been successful at producing stable, repeatable imaging. In the future studies of adatom mobility could be carried out by deliberately warming a $PrSr_2Mn_2O_7$ sample, in a controlled way. For example, a $PrSr_2Mn_2O_7$ sample could be allowed to warm to around 220 K on the STM stage, without scanning, and the stage could then be cooled down again. This ought to result in a stable surface which is significantly depleted in adatoms.

5.2.11 Surface Charge Ordering in $PrSr_2Mn_2O_7$: LEED data

STM topographic images of $PrSr_2Mn_2O_7$ do not provide any evidence for any type of surface charge ordering, either CE-type or the stripe charge ordering observed by Tokunaga *et al.* [79] in X-ray diffraction data (see section 1.7). No $\sqrt{2}$a x $\sqrt{2}$a superlattice, or stripe-like structures with a periodicity of 4a, were seen in images collected at any temperature in the studied range of 78 K to 195 K. An STM image only samples a small region of the sample surface however, and it is always possible that charge ordering is only stabilised across a fraction of the surface. Also, charge ordering might be stabilised at the surface at a different temperature from the bulk, and therefore outside the temperature range of 78 K - 220 K studied with STM. Low Energy Electron Diffraction (LEED) measurements were therefore made to look for the effect of charge ordering. LEED has been used to study charge ordering on the surface of Fe_3O_4 [43]: surface charge ordering is apparent in the LEED pattern as additional diffraction peaks. The stripe-like 4a charge ordering suggested for $PrSr_2Mn_2O_7$ would result in satellite peaks around the diffraction peaks. If the charge ordering is only one-dimensional each spot will have two satellite peaks, at 1/4 the spacing of the primary peaks. If twinned domains of stripe-like charge order are present four satellite peaks will be observed, at the same spacing.

The LT-STM at the London Centre for Nanotechnology has a LEED screen mounted on the preparation chamber: samples can be transferred from the STM to the LEED station inside UHV. The spot size of the LEED beam at the sample is around 2 mm. The cryogenic manipulator can be used to cool samples, so LEED can be performed at temperatures down to 20 K. A $PrSr_2Mn_2O_7$ sample which had been previously studied in the STM was loaded onto the manipulator and studied using LEED. Figure 5.23a shows a typical LEED pattern collected at room temperature, with an electron beam energy of 174 eV, corresponding to an electron wavelength of 0.093 nm. Spots corresponding to a square lattice of spacing a = 0.43 $\pm$ 0.03 nm can be observed, where the error is based on the diffraction peak width. This is in reasonable agreement with the lattice spacing from X-ray diffraction of a = b = 0.38535 nm [79]. This result can also be compared to the lattice seen in STM data. The sample used for the LEED study had been observed to show the adatom/vacancy surface: an image from this sample is shown in figure 5.6a. The Fourier transform of this image has been repeated in figure 5.23b for comparison with the LEED image:

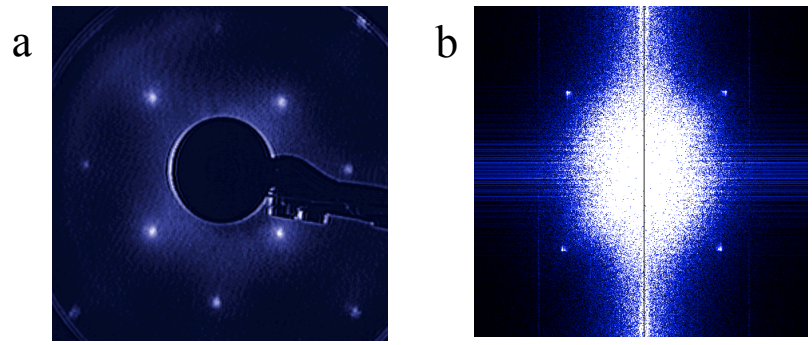

Figure 5.23: (a) Typical LEED pattern obtained from PSMO showing square lattice, at room temperature and 174V (b) FFT of 55 x 60 nm STM topograph from the same sample at 78 K, with the same orientation. This image has been shown in figure 5.6a.

a square lattice of spacing a = 0.380 ± 0.005 nm is seen in the Fourier transform. The rotational orientation of the sample is preserved in the transfer from STM to LEED station: it can be seen in figure 5.23 that the lattice seen in STM and in LEED has the same orientation as well as the same spacing. This indicates that the atomic lattice observed in STM topographic scans extends over much larger, mm-sized areas.

The cryogenic manipulator was used with liquid helium to cool the $PrSr_2Mn_2O_7$ sample at the LEED station down, so that LEED measurements could be performed in the temperature range 20 K - 300 K. No satellite diffraction peaks were observed at any temperature. The experiment was repeated with another $PrSr_2Mn_2O_7$ sample, and with different electron beam energies, with the same result. Thus we must conclude that either charge ordering is not present at the surface of $PrSr_2Mn_2O_7$, or that it is too weak to be observed by either STM or LEED.

5.2.12 Temperature and Magnetic Field Dependence of STS Measurements of $PrSr_2Mn_2O_7$

$PrSr_2Mn_2O_7$ samples were studied in the Oxford and Cryogenic STMs as well as the LT-STM. Samples were cleaved at room temperature at a pressure of around 5 x 10^{-10} mbar, around an order of magnitude higher than the pressure at which samples can be cleaved in the LT-STM. Stable atomic resolution was not achieved in either experiment, nor clear resolution of adatoms. However, atomic terraces and clear step edges were observed in all three cleaves performed. Figure 5.24a shows a 400 x 500 nm STM topograph collected at 300 K using the Oxford STM. Steps 1.00 ± 0.03 nm high can be observed, which is in good agreement with the previously measured value from LT-STM images of 1.01 ± 0.02, and the value from X-ray diffraction of c/2 = 0.9964 nm [79]. Similar images were obtained from the Cryogenic STM, giving a step height of 0.99 ± 0.03 nm. Figure 5.24a, and the cross section shown in figure 5.24b, show that the terraces are not as flat as those obtained in the LT-STM: numerous features up to 0.8 nm high can be observed. As these features are not observed in the LT-STM scans it is likely that they are due to surface contamination, possibly due to the higher vacuum chamber pressure. Most areas on the $PrSr_2Mn_2O_7$ surfaces studied show a roughness (apart from the features noted above) of around 0.2 nm peak-peak, indicative of the adatom-vacancy surface, but some areas show a flatter surface with roughness around 40 pm, indicative of the atomically flat surface.

Figure 5.24c shows a time series of 5 x 5 nm STM topographic images collected using the Oxford STM at 300 K. Each images takes around 50 seconds to acquire. Some features are seen in image 1 which might be oxygen adatoms: they have about the right height at ≈ 150 pm. These features are seen to move between images 1, 2 and 3, but the imaging quality degrades rapidly making it impossible to see any features by image 4. If these features are oxygen adatoms their high mobility would be consistent with the temperature dependence of adatom mobility identified in sections 5.2.7 and 5.2.10. The rapid degradation of the image quality is likely due to material picked up by the STM tip, either the oxygen adatoms themselves or surface contaminants.

Difficulties in imaging $PrSr_2Mn_2O_7$ at room temperature are expected due to the

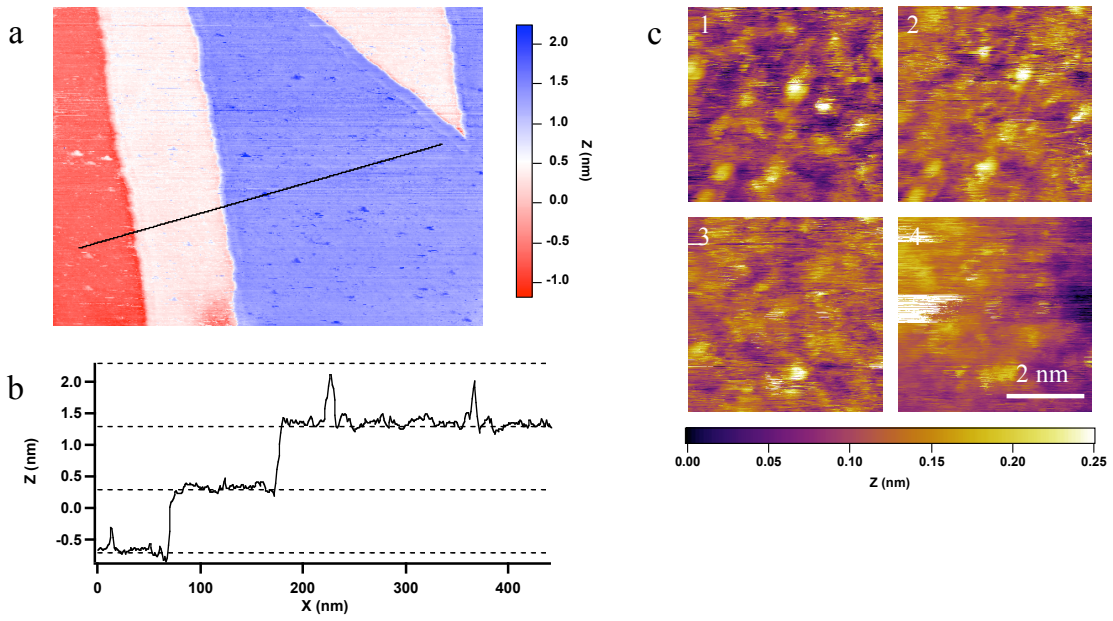

Figure 5.24: (a) 400 x 500 nm STM topographic image of $PrSr_2Mn_2O_7$ taken at 300 K using the Oxford STM (b) section showing 1 nm steps and 0.8 nm high features (c) time series of 5 x 5 nm STM topographic images taken at 300 K, covering around 200 seconds

high mobility of oxygen adatoms at 220 K and above (section 5.2.10). However good resolution could not be achieved at low temperature in either the Oxford or Cryogenic STM. This is likely due to the surface contamination. At present it is not clear if it is sufficient to reduce the vacuum chamber pressure to the 10^{-11} mbar range, as in the LT-STM, to avoid surface contamination, or if cold cleaving is also necessary, since samples were always cleaved at around 20 K in the LT-STM. If the sample is cleaved at room temperature and then cooled, the sample surface may act as a getter for water molecules and other contaminants in the vacuum chamber. Cold cleaving may help to reduce surface contamination as contaminants are efficiently cryo-pumped by the cleaving stage cryostat, which will be close to and colder than the sample. It may also be possible that a better cleave is obtained at 20 K than at room temperature, due to the sample being more brittle at low temperature and cleaving more cleanly. This would imply that some of the surface "contamination" arises from an uneven cleave of the $PrSr_2Mn_2O_7$ crystal.

Despite the poor imaging performance it ought be possible to derive information on the temperature and field dependence of the tunnelling I(V) spectrum of $PrSr_2Mn_2O_7$

from Oxford and Cryogenic STM data. Arrays of I(V) spectra can be collected across large areas at a range of temperatures and fields, and the average zero-bias conductance and energy gap parameter can be extracted. As these values will be averaged across large areas the effect of the surface contamination should be minimised, as only a small fraction of the surface is contaminated.

The Oxford STM was used to make STS measurements of $PrSr_2Mn_2O_7$ in the temperature range 75 K - 300 K. At each temperature at least 2500 I(V) spectra were collected, typically across a 100 x 100 nm area. Figure 5.25a shows example spectra from I(V) arrays collected at 126 K and 300 K. The setpoint is 200 pA, set at +0.8 V sample bias. For each temperature the gap parameter Δ and the zero bias conductance G_0 were extracted, as follows. First a straight line fit is made to each I(V) curve in the array, in the region close to zero volts (normally $\pm$ 100 mV): the slope of this fit gives the zero bias conductance G_0. The straight line fit is then subtracted from the spectrum, and the gap is measured. The gap parameter is extracted from each I(V) spectrum by measuring the positive and negative voltages at which the tunnel current exceeds a threshold value. The threshold is arbitrary but is chosen to be larger than the typical noise on the current signal, to minimise false measurements: here a threshold of 6 pA was used. For this experiment the gap parameter Δ is taken to be equal to the upper (positive bias) threshold. The full gap width 2Δ, defined as the difference between the positive and negative threshold voltages, was not used due to excess noise on the lower (negative bias) threshold. Histograms of G_0 and Δ can be produced, and Gaussian fits can be made to both, to determine G_0 and Δ for each temperature.

Figure 5.25b shows example histograms of the gap parameter Δ at 126 K and 300 K, with Gaussian fits to both. Figure 5.25c shows the temperature dependence of Δ: the error bars represent one standard deviation as measured from the Gaussian fit at each temperature. The gap parameter remains roughly constant up to 200 K and then sharply decreases at higher temperature. At all temperatures the gap distribution is unimodal: no evidence for any phase coexistence is seen. Figure 5.25d shows histograms of the zero bias conductance G_0 at 175 K, 200 K and 300 K: figure 5.25e shows the temperature dependence of G_0. The error bars again represent one standard deviation in G_0 as derived from the Gaussian fit. The temperature dependence of G_0 can be fitted with an activated curve of the form $T^{3/2}\, exp(-\Delta_0/2k_bT)$, where Δ_0 is the zero temperature gap parameter. This fit is shown in figure 5.25e:

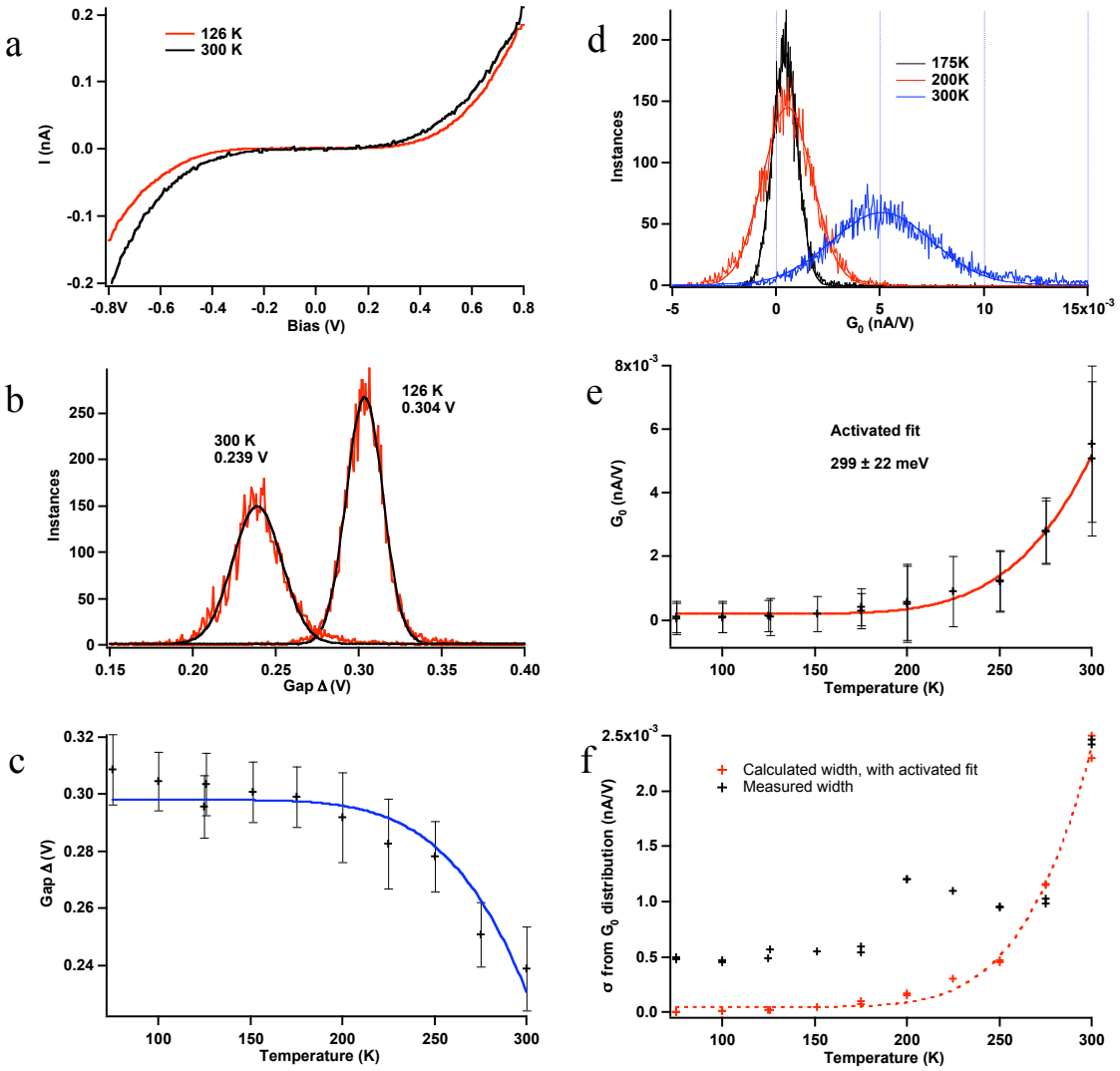

Figure 5.25: (a) example spectra from PSMO at 126K and 300K (b) histograms of gap parameter Δ at 126 and 300 K (c) temperature dependence of Δ with activated fit with $\Delta_0 = 299$ meV (d) histograms of zero bias conductance G_0 at 175 K, 200 K and 300 K (e) temperature dependence of G_0 with activated fit with $\Delta_0 = 299$ meV (f) temperature dependence of standard deviation of G_0 distribution

the value of the gap parameter Δ_0 from the fit is 299 ± 22 meV. This value is in good agreement with the gap parameter Δ measured directly from the I(V) spectra. Figure 5.25c shows an activated fit to Δ as a function of temperature: the fit has the form $\Delta_0 - AT^{3/2} exp(-\Delta_0/2k_bT)$, where A is a scaling factor. This gives a reasonable fit to Δ as a function of temperature.

The standard deviation σ of the zero bias conductance G_0 is shown as a function of temperature in figure 5.25f. We can compare this to the expected temperature dependence of the thermally broadened width of G_0. The thermal width distribution of G_0 is proportional to $T \times G_0$: this is plotted in figure 5.25f, scaled to give a similar width to the measured value at high temperature. An activated fit to this calculated width is shown. At 250 K and below the measured width is larger than the calculated value, indicating that in this experiment there is a substantial additional source of noise. This noise is likely due to the poor sample surface and imaging conditions. Interestingly there is a peak in σ at 200 K: the width in the G_0 distribution at this temperature is around twice the value at 175 K. This difference can be seen in the histograms of G_0 shown in figure 5.25d. This is around the same temperature that the oxygen adatom mobility was observed to dramatically increase (see section 5.2.10): the same effect may increase the noise in STS measurements.

Magnetic field dependent STS measurements of $PrSr_2Mn_2O_7$ were made using the Cryogenic STM, at 125 K. At this temperature the c-axis magnetoresistance at 6 T for a field applied perpendicular to the sample surface is $\Delta\rho/\rho = 20$ %. Larger magnetoresistance values can be obtained at lower temperatures, but below 78 K the sample may be too resistive to allow STM to be performed. There also appears to be some enhancement of the magnetoresistance ratio at around 125 K (see section 5.1). I(V) STS maps were collected on a 500 x 500 nm area of the $PrSr_2Mn_2O_7$ surface at magnetic fields of 0, 1, 2, 3, 4, 5 and 6 T. The maps consist of 64 x 64 spectra: the field is applied perpendicular to the sample surface. Unlike the case of the superconducting $NbSe_2$ test sample (see section 3.1.4) the $PrSr_2Mn_2O_7$ sample was found to move a substantial distance relative to the tip upon application of magnetic field, around 125 nm upon the initial application of a 1 T field. This is likely due to the non-zero magnetic moment of the $PrSr_2Mn_2O_7$ sample. However, the area studied featured a step edge and a distinctive defect which allowed the movement to be corrected for, and the same 500 x 500 nm area to be scanned at all fields.

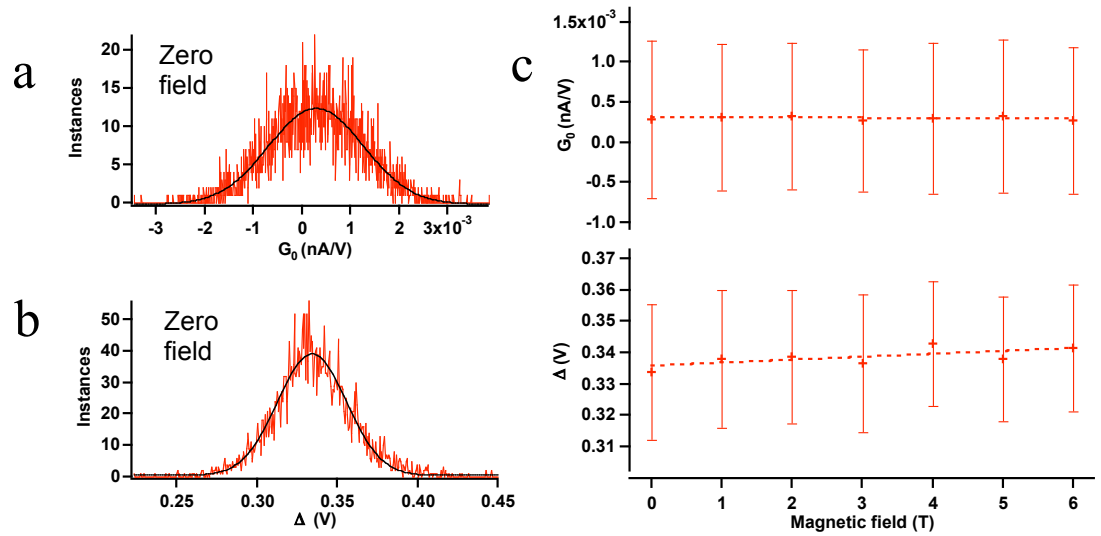

Figure 5.26: (a) Histogram of zero bias conductance G_0 at zero field at 125 K (b) Histogram of gap parameter Δ at zero field at 125 K (c) Field dependence of G_0 and Δ at 125 K. No significant dependence is seen up to 6 T

The gap parameter Δ and zero-bias conductance G_0 were extracted from the I(V) arrays in the same way as for the Oxford STM data described above. A current setpoint of 100 pA, set at +0.8 V was used: the current threshold for measuring the gap width was 3 pA. Figure 5.26 shows the results of the magnetic field-dependent study. Figures 5.26a and b show histograms of G_0 and Δ at zero field. The gap parameter was measured as $\Delta = 0.334 \pm 0.021$ V, where the error is one standard deviation as measured from a Gaussian fit to the histogram of Δ. This is larger than the gap measured using the Oxford STM at the same temperature, but the difference is less than $3.5k_B$T = 0.038 V at 125 K. The zero-bias conductance was measured as 2.9 $\pm$ 9.8 x 10^{-4} nA/V. The magnetic field dependence of G_0 and Δ is shown in figure 5.26c. No field dependence is seen in G_0: a slight increase in Δ is seen with increasing field, from 0.334 V at zero field to 0.341 V at 6 T. This difference is however less than the error on Δ and less than k_BT so it cannot be regarded as significant. Thus despite a 20 % reduction in bulk c-axis resistivity under an applied field of 6 T, no change in the zero-bias conductivity or gap parameter measured via STS is observed.

In the future a field-dependent experiment could be carried out on $PrSr_2Mn_2O_7$ at a lower temperature. This would give the advantages of less thermal noise and en-

hanced magnetoresistance ratio. At around 40 K the magnetoresistance ratio $\Delta\rho/\rho$ is larger than 50 % and k_BT is 0.015 V. The sample resistivity will be considerable at around 15 kΩ-cm. This is only 3 times the value at 78 K though, so it should still be possible to scan the surface.

5.3 Summary of $PrSr_2Mn_2O_7$ Results

STM experiments in the Omicron Nanotechnology LT-STM were successful in achieving atomic resolution on the $PrSr_2Mn_2O_7$ surface. Samples were cleaved at 20 K and studied at 78 K and above: it was found to be essential to prevent the sample warming up above ≈ 200 K in order to maintain good imaging conditions (5.2.10). The observed surface is believed to be the O - Pr/Sr layer (5.2.1). A square lattice is observed which is consistent with published X-ray diffraction data (5.2.1) and LEED data collected on the same samples (5.2.11). The lattice has a peak to peak corrugation of 4 pm: a larger modulation with a corrugation of 20 pm and a length scale of around 4 nm is also seen (5.2.1). The nature of this larger lattice is not understood, but it may be related to the distribution of Mn^{3+}/ Mn^{4+} and Pr^{3+}/ Sr^{2+} ions at the surface of $PrSr_2Mn_2O_7$. Stripe-like charge ordering, identified by X-ray diffraction [79], is not observed in STM or LEED data (5.2.11).

In some regions of the $PrSr_2Mn_2O_7$ sample a rougher surface is observed. This increased roughness is observed to be due to a population of surface adatoms and vacancies (5.2.3). The atomic lattice can still be observed and has the same spacing and similar corrugation to the lattice seen on atomically flat areas. From STS data, adatoms are found to carry a negative charge and vacancies a positive charge, relative to the rest of the surface. The adatoms have been identified as oxygen ions and the vacancies as oxygen vacancies (5.2.4). The coverage of adatoms has been related to the density of Pr^{3+} ions at the surface (5.2.5).

Adatoms are not observed to form any ordered structures commensurate with the atomic lattice. The arrangement of adatoms is almost random, although there is statistically significant anti-clustering behaviour (5.2.6). However adatoms are observed to be mobile, and show preferred positions at the surface (5.2.7). These preferred positions may be potential energy minima determined by the locations

of Pr^{3+} and Sr^{2+} ions in the surface layer and Mn^{3+} and Mn^{4+} ions below the surface layer. The mobility of adatoms is observed to increase with temperature, and appears to sharply increase between 195 K and 220 K (5.2.10). Based on Arrhenius-type fits to the mobility the activation energy for adatom motion has been estimated as being in the range $100 \leq E_A \leq 260$ meV.

The coverage of adatoms and vacancies is observed to decrease over time. In addition, elevated temperatures appear to cause an accelerated loss of adatoms and vacancies (5.2.8). This is attributed to recombination of adatoms and vacancies. Although it would not cause a decrease in vacancy coverage, loss of adatoms to the vacuum cannot be ruled out.

I(V) spectra taken on adatoms sometimes show a characteristic discontinuity caused by motion of the adatom during the I(V) measurement (5.2.9). Adatoms are not observed to move at low bias, but only at voltages higher than 300 mV.

STM experiments in the Oxford STM and the Cryogenic STM were not successful in achieving atomic resolution, perhaps due to the lack of cold cleaving or to the higher pressure in the vacuum chamber (5.2.12). Cold cleaving may help prevent contamination of the sample surface, by cryo-pumping contaminants out of the STM chamber. Also, the $PrSr_2Mn_2O_7$ samples may be more brittle and cleave more cleanly at 20 K than at room temperature. Temperature dependent measurements of the zero-bias conductance yield a measurement of the surface energy gap parameter of $\Delta = 299 \pm 22$ meV. Magnetic field-dependent measurements showed no measurable effect of a field of up to 6 T on the I(V) spectra of $PrSr_2Mn_2O_7$ at 125 K.

Chapter 6

STM experiments on $\mathbf{La_{2-2x}Sr_{1+2x}Mn_2O_7}$

6.1 Characterisation of $La_{2-2x}Sr_{1+2x}Mn_2O_7$ Samples

Single crystal and thin film samples of the bilayer manganite $La_{2-2x}Sr_{1+2x}Mn_2O_7$ were studied using STM, in the cation doping range $0.3 \leq x \leq 0.5$. Bulk single crystals of $La_{2\text{-}2x}Sr_{1+2x}Mn_2O_7$ were grown by Y. Tokura[1,2,3,4,5] and T. Kimura[4,5,6]: the samples were grown using the floating-zone technique. The crystals were grown with cation doping x = 0.3, 0.32 and 0.5: the x = 0.3 compound should be identical to that studied in colossal magneto-resistance studies [30] and by STM [59].

Thin films of $La_{2\text{-}2x}Sr_{1+2x}Mn_2O_7$ were grown by Y. Takamura[7,8]. The thin film samples are unusual in that they are grown with the [110] crystal direction normal to the sample surface. In this orientation the c axis is parallel to the surface, and the a and b axes are at 45° to the surface.

Single crystal samples were characterised at the London Centre for Nanotechnology using bulk electrical conductivity and magnetic susceptibility measurements. An Oxford Instruments MagLab was used to make conductivity measurements, and a Quantum Design MPMS based on a Superconducting Quantum Interference Device (SQUID) was used to make susceptibility measurements. The SQUID measurements were performed by Marc Warner.

MPMS measurements were performed on x = 0.3 and x = 0.32 $La_{2\text{-}2x}Sr_{1+2x}Mn_2O_7$ single crystal samples, to confirm the different low-temperature magnetic states of these two compounds (see section 1.6). A magnetic field of 20 Oe (equivalent to 0.002 T) was applied. Figure 6.1 shows the magnetic moments of $La_{2\text{-}2x}Sr_{1+2x}Mn_2O_7$, x = 0.3 and x = 0.32 as a function of temperature. Magnetic moment is given in units of the Bohr magneton μ_B, per Mn ion.

[1]Multiferroics Project, ERATO, Japan Science and Technology Agency (JST), Bunkyo-ku, Tokyo 113-8656, Japan

[2]Spin Superstructure Project, ERATO, JST, Tsukuba, Ibaraki 305-8562, Japan

[3]Correlated Electron Research Center (CERC), National Institute of Advanced Industrial Science and Technology (AIST), Tsukuba, Ibaraki 305-8562, Japan

[4]Department of Applied Physics, University of Tokyo, Bunkyo-ku, Tokyo 113-8656, Japan

[5]Joint Research Centre for Atom Technology, Tsukuba, Ibaraki 305,Japan.

[6]Bell Laboratories, LucentTechnologies, 600 Mountain Avenue, MurrayHill, New Jersey 07974

[7]Department of Materials Science and Engineering, University of California, Berkeley

[8]Lawrence Berkeley National Laboratory, Berkeley, California 94720

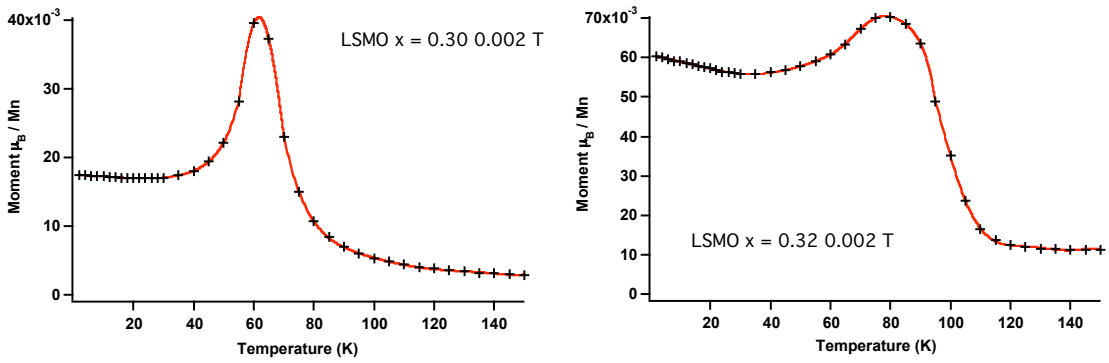

Figure 6.1: Magnetic moment of x = 0.3 and x = 0.32 single crystal samples, measured as a function of temperature using the SQUID at the LCN, at 0.002 T

The x = 0.3 compound shows a peak in magnetic moment at around 60K. A detailed study of the temperature dependent magnetic structure of $La_{1.4}Sr_{1.6}Mn_2O_7$ has been made using neutron diffraction by Argyriou et. al [2]. As noted in section 1.6, $La_{1.4}Sr_{1.6}Mn_2O_7$ is antiferromagnetic: at low temperature Mn spins are aligned close to the c-axis, but at T_N = 100 K they are tilted towards the a-b planes. The a-b plane component of the magnetic moment reaches its greatest intensity at around 80 K: below this temperature the intensity decreases as the spins rotate away from the ab-plane direction. This is likely the peak we observe at 60 K. The reduced temperature may be due to a slight variation in composition between the samples studied by Argyriou *et al.* and those studied here. T_N in these samples is around 80 K. The x = 0.32 compound is expected to be ferromagnetic. The magnetic moment of this compound shows a steep rise at around 110 K: the moment remains close to the peak value down to the lowest measured temperature, indicating a ferromagnetic state with $T_C \approx 110$ K.

Figure 6.2 shows results from an MPMS measurement of a $LaSr_2Mn_2O_7$ (x = 0.5) single crystal sample. The magnetic moment is shown as a function of temperature for magnetic field strengths of 0.002 T and 1 T: the moment is given in units of the Bohr magneton μ_B, per Mn ion. The magnetic moment of $LaSr_2Mn_2O_7$ shows a complex behaviour due to the re-entrant charge ordered state. At room temperature the sample is paramagnetic. As the temperature is decreased, the charge order state is stabilised at around 225 K: this causes a drop in magnetic moment. Around 100 K the charge ordered phase gives way to the antiferromagnetic state and the moment

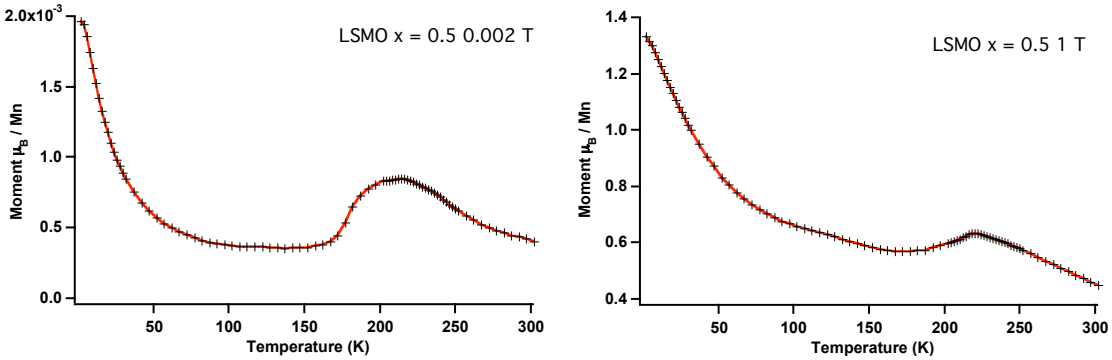

Figure 6.2: Magnetic moment of x = 0.5 $LaSr_2Mn_2O_7$ single crystal samples, measured as a function of temperature using the SQUID at the LCN, at fields of 0.002 T and 1 T

increases again. As can be seen from figure 6.2 at a higher magnetic field the effect of the charge ordered phase is suppressed, as the magnetic field stabilises the competing antiferromagnetic phase.

6.1.1 Thin Film Samples

Thin film $La_{2-2x}Sr_{1+2x}Mn_2O_7$ samples with x = 0.4 were produced by Y. Takamura by pulsed laser deposition. These films are unusual in that they are oriented in the (110) direction, with the c axis in the plane of the sample surface, and the a and b axes at 45° to the surface. The films are deposited onto a $SrTiO_3$ (110) substrate and have a range of thicknesses. The samples were characterised by Y. Takamura by X-ray diffraction, TEM and bulk transport studies [74,75]. The films show a marked tendency to be multiphase, that is to include intergrowths of n = 1 and n = ∞ (cubic perovskite) phases: this tendency is particularly notable in thinner films (200 nm thick), so films 600 nm thick were studied using STM. A TEM micrograph of a 600 nm film is shown in figure 6.3a: the c-axis unit cell parameter of $La_{1.2}Sr_{1.8}Mn_2O_7$ is 20.14 Å, and the 10.07 Å spacing corresponding with the bilayer spacing can be seen clearly. The thicker films are clearly still somewhat multiphase since a cell of reduced height corresponding to the n = 1 layer thickness can be seen. Transport data taken on a 300 nm thick film (figure 6.3b) show a highly anisotropic resistance, with resistivity in the c direction ρ_c up to two orders of magnitude higher than that in the ab plane ρ_{ab}. The films show a large magnetoresistance in fields up to 5 T, with

$\rho(0)/\rho(5\,T) \approx 100$. The temperature dependence of the zero field resistance shows a monotonic rise with decreasing temperature, whereas for single crystal samples (see sections 1.6, 1.6.2 and figure 1.8) a sharp drop in ρ_c and ρ_{ab} is observed at the metal-insulator transition at $T_{MI} \approx 125$ K. The absence of a clear transition in the thin films has been attributed to the presence of $n = 1$ and $n = \infty$ intergrowths [74].

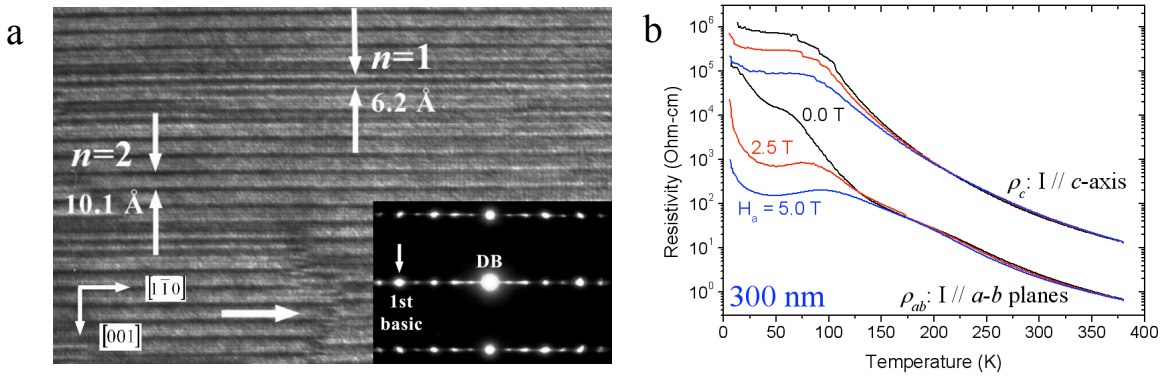

Figure 6.3: (a) TEM image of a 600 nm $La_{1.2}Sr_{1.8}Mn_2O_7$ thin film, with c-axis parallel to sample surface. The 10 Å bilayer spacing can be directly observed: an inclusion of single layer manganite with c-axis spacing 6 Å is also seen. (b) B field and temperature dependence of resistivity in a 300 nm $La_{2-2x}Sr_{1+2x}Mn_2O_7$ thin film. The films have a highly anisotropic conductivity and exhibit a CMR effect. The field is applied parallel to the ab planes [75].

6.2 Spectroscopic Variation in $LaSr_2Mn_2O_7$

Experiments on $La_{2-2x}Sr_{1+2x}Mn_2O_7$ single-crystal samples were carried out using the Cryogenic STM. Due to the lack of any suitable cleaving stage in the Cryogenic STM vacuum chamber, single crystal samples were cleaved in the loadlock. The loadlock was pumped out overnight and then left open to the preparation chamber for several hours, to achieve the best possible vacuum in the loadlock without baking. Samples were cleaved at a pressure of around 5 x 10^{-10} mbar. Initially the x = 0.3 compound $La_{1.4}Sr_{1.6}Mn_2O_7$ was studied, in order to investigate the tunnelling magnetoresistance effect (see section 1.6.2) using STM and STS. One out of four attempted cleaves was successful in producing atomically flat surfaces. STM topographic images taken at room temperature showed micron sized terraces with a peak-to-peak roughness of less than 0.1 nm, and $\approx$ 1 nm high step edges, as seen in previous measurements in the Oxford STM (section 6.4) and by Rønnow *et al.* [59]. Tunnelling spectra similar to [59] were also recorded, but no atomic resolution was observed, nor atomic resolution "islands". Unfortunately this surface degraded too rapidly for low-temperature or high magnetic field studies to be made, and subsequent cleaves of the x = 0.3 compound were not successful in producing a good surface. Further work on $La_{2-2x}Sr_{1+2x}Mn_2O_7$ in the Cryogenic STM concentrated on the x = 0.5 compound.

Single crystal samples of $LaSr_2Mn_2O_7$ (x = 0.5) were studied in the Cryogenic STM. CE-type charge order is known to be stabilised in this compound [1, 28, 34, 36]: it was hoped that atomically resolved images of the surface in both normal and charge ordered phases could be obtained. Even in the charge-ordered state the c-axis resistivity of $LaSr_2Mn_2O_7$ is still low enough, at around 20 Ω cm, to enable STM study [28]. Several cleaves were successfully performed, with three out of the eight attempted cleaves yielding reasonably flat surfaces and well resolved terraces. Figure 6.4 shows a 1 x 1 μm topographic scan showing numerous terraces. The terraces are much smaller than observed for $La_{1.4}Sr_{1.6}Mn_2O_7$ at around 50 nm across. The step height is 1.00 $\pm$ 0.06 nm: steps which are a multiple of this value are frequently observed. Atomic resolution was unfortunately not achieved on this surface: the terraces are rougher than observed on $La_{1.4}Sr_{1.6}Mn_2O_7$ [59], with 0.2 - 0.5 nm peak to peak roughness.

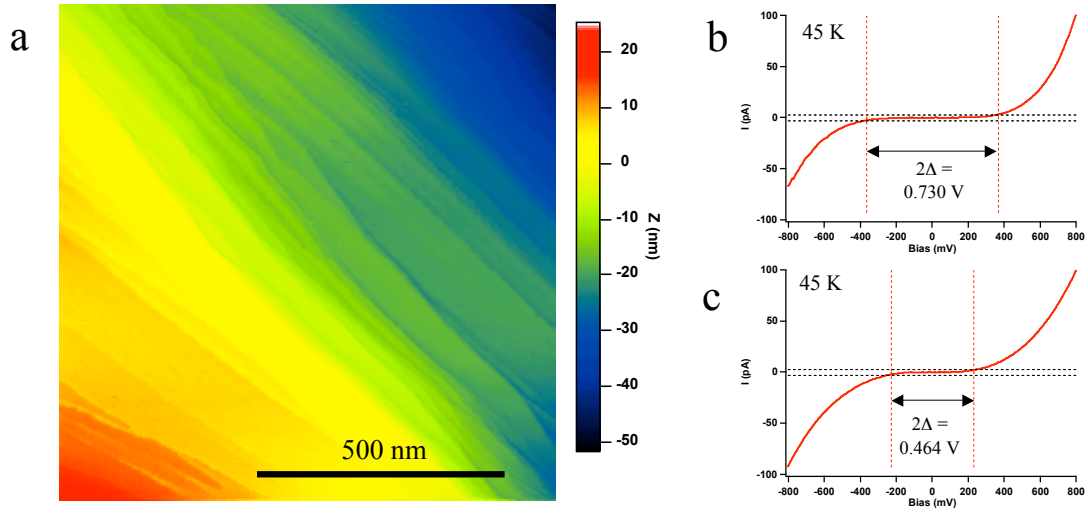

Figure 6.4: (a) 1 x 1 μm STM topographic image of $LaSr_2Mn_2O_7$ taken using the Cryogenic STM at 225 K. A large number of atomic terraces are seen: the step height is 1.00 $\pm$ 0.06 nm. (b) and (c): example spectra from a single I(V) array collected at 45 K, showing variation in gap width. Each spectrum is an average of $>$ 200 spectra, taken from the I(V) array shown in figure 6.5a

As atomic resolution could not be achieved on this surface, the charge ordered phase could not be directly imaged. The charge ordered phase may however coexist with the antiferromagnetic phase below 170 K [2]: the two phases should be distinguishable by tunnelling spectroscopy, as the charge-ordered phase should have a larger energy gap. It was therefore decided to search for phase coexistence on the $LaSr_2Mn_2O_7$ surface by collecting STS I(V) arrays at a range of temperatures, using the Cryogenic STM. Phase coexistence may be identified by a bimodal distribution of energy gap. If phase coexistence is identified, it should be possible to control the fraction of the charge-ordered phase by applying a magnetic field. A large negative magnetoresistance effect is observed in $LaSr_2Mn_2O_7$ between 100 K and 200 K [28]: this effect is explained as the "melting" of the charge ordered state under applied field. This may occur due to competition between the charge ordered state and the A-type antiferromagnetic state: the antiferromagnetic state will be stabilised by a an applied field, at the expense of the charge ordered state. A field in excess of 20 T is required to completely destroy the charge ordered state, but a 7 T field applied at 175 K is sufficient to produce a suppression of resistivity $\rho_0/\rho_H \approx 160$ %, so the maximum field of 6 T which can be applied in the Cryogenic STM ought to produce

a measurable effect. This experiment would take advantage of the ability of the Cryogenic STM to apply a field with the STM stage at an elevated temperature, since the charge ordered state is observed between 100 K and 200 K.

6.2.1 Temperature and Spatial Variation of STS spectra

STS I(V) arrays were collected on the $LaSr_2Mn_2O_7$ surface at a range of temperatures from 225 K to 10 K, using the Cryogenic STM. The STM was cooled to 132 K using liquid nitrogen only, by filling the STM helium pot with helium gas and the magnet tank with liquid nitrogen. The STM head will cool slowly by conduction and radiation in this configuration: to reach lower temperatures liquid helium was used. Arrays of 64 x 64 I(V) spectra were collected on areas of up to 1 x 1 μm. As seen in figure 6.4, due to the large number of terraces, the Z-range in the image is large, almost 80 nm across a 1 x 1 μm area: before slope subtraction, the image Z-range is 276 nm. At low temperature the Z-range of the piezo (around 300 nm at 4 K) becomes a limiting factor in the image size that can be studied. Therefore at low temperatures several smaller areas were studied, and combined to form an STS mosaic. At each temperature at least 4096 spectra were collected, either as one 64 x 64 array covering 1 x 1 μm, or where this was not possible as several smaller arrays separated by up to 1 μm. Figures 6.4b and c show two averaged spectra from an I(V) array collected at 45 K: a substantial variation in gap width is observed.

Each I(V) array was processed to produce a "gap map", as follows. First a straight line fit is made to each I(V) curve in the array, in the region close to zero volts (normally $\pm$ 0.1 V). The straight line fit is then subtracted from the spectrum, and the gap is measured. A gap is extracted from each I(V) spectrum by measuring the positive and negative voltages at which the tunnel current exceeds a threshold value. The threshold is arbitrary but is chosen to be larger than the typical noise on the current signal, to minimise false measurements. The gap 2Δ is defined as the difference between the positive and negative threshold voltages. This procedure is illustrated in figures 6.4b and c, for a threshold current of 3 pA: the method is similar to that previously used for measuring an energy gap from STS spectra [59]. The gap values are plotted on the same axes as the original array to produce a "gap map" showing the spatial variation of 2Δ.

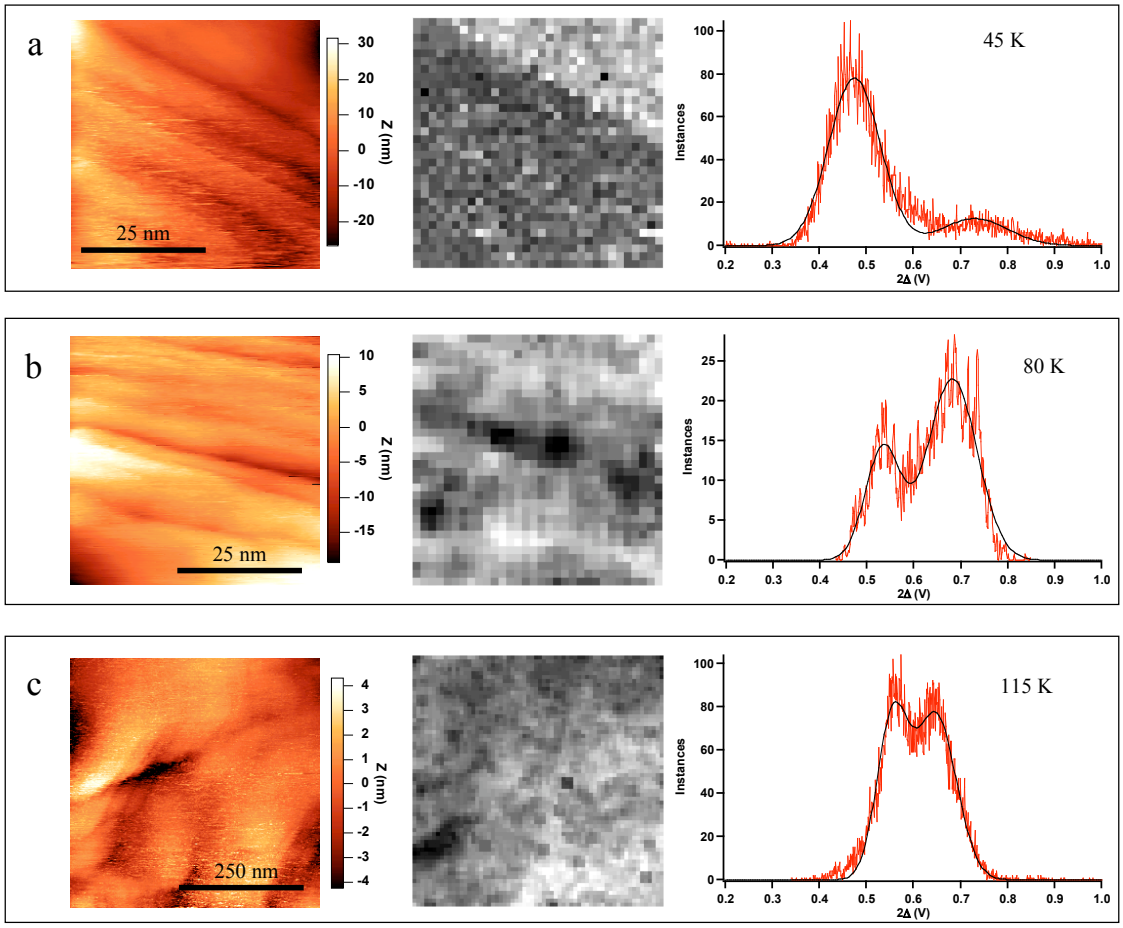

Figure 6.5: Spectroscopic variation observed in $LaSr_2Mn_2O_7$ between 115 K and 45 K. For each temperature, first column: topographic image. Second column: gap map on the same area as the image. Dark regions indicate a small gap and lighter regions a larger gap. Third column: gap histogram, fitted with the sum of two Gaussian distributions. The spectra shown in figure 6.4b and c have been extracted from the map shown in (a).

As well as a gap map, a histogram of gap values can be produced. If the gap is single-valued, the distribution of gap values will be close to a Gaussian: a Gaussian fit can be made, which will give an accurate measurement of the gap. If two gap values are present, the distribution will be the sum of two Gaussian distributions, and can be fitted as such: if the two gaps are sufficiently different the gap distribution will be bimodal, with two distinct peaks in 2Δ.

On the $LaSr_2Mn_2O_7$ surface, gap maps reveal the gap to be single-valued above 115 K, and at 10 K. Between these temperatures, at 45 K , 80 K and 115 K, spectral

variation is observed. Figure 6.5 shows the observed variation: for each temperature a topographic image is shown (first column), together with a gap map generated from an I(V) array on the same area as the image (second column). The threshold current used for the gap measurement is 3 pA. In the gap map, the dark regions indicate a small gap and lighter regions a larger gap. Also shown is a gap histogram for each temperature (third column), generated by combining the gap values generated from several I(V) arrays collected at that temperature. Each gap histogram has been fitted with the sum of two Gaussian distributions.

A bimodal distribution of the gap width 2Δ is clearly observed at 45 K, 80 K and 115 K (figure 6.5a, b and c). At 115 K the two gaps are present in roughly equal weight: at 45 K the smaller gap is more prevalent. At 80 K (figure 6.5b) the larger gap is dominant. By comparing the gap maps (second column) with the topographic images (first column) a clear correlation between gap width and the topography can be identified. At 45 K, the boundary between the large gap region and the small gap region can be seen to be aligned to a terrace edge. A similar effect is seen at 80 K where the small gap region is aligned to a terrace edge. The small gap region in the 115 K gap map also corresponds to a topographic feature, possibly a terrace edge though in this case it is not well resolved.

Figure 6.6 shows the gap width 2Δ as measured from Gaussian fits to the gap histograms, plotted as a function of temperature. The error bars represent plus or minus one standard deviation, as measured from the Gaussian fit at each temperature. At temperatures where two gaps are measured the values are plotted in different colours. In general two distinct gaps are seen, a large gap of $2\Delta = 0.72 \pm 0.07$ V and a small gap of $2\Delta = 0.52 \pm 0.05$ V. In figure 6.6 the temperature dependence of the two gaps is indicated with dotted lines as a guide to the eye. From 225 K to 140 K the gap is single valued: the gap increases with decreasing temperature before reaching a maximum at around 140 K and decreasing again. Between 115 K and 45 K two gaps are present. With decreasing temperature the two gaps diverge: the large gap increases upon cooling and the small gap decreases. In this temperature range therefore the large gap regions behave like a semiconductor with $d\rho/dT < 0$, and the small gap regions behave like a metal with $d\rho/dT > 0$. At 10 K the small gap vanishes and only the large gap is seen.

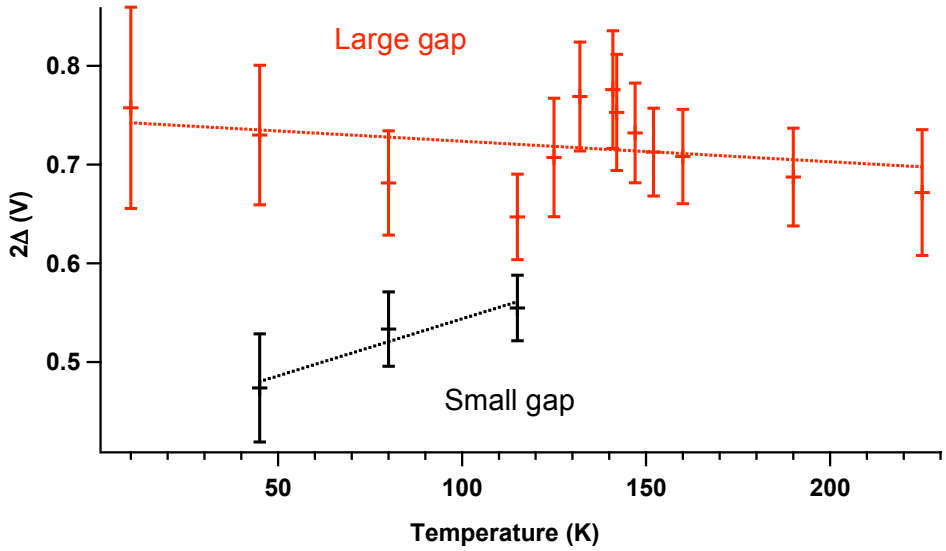

Figure 6.6: Temperature dependence of the spectroscopic gap 2Δ on the $LaSr_2Mn_2O_7$ surface. The black series represents the second, smaller gap when spectroscopic variation is observed. Dashed lines are straight line fits as guides to the eye. The large and small gaps are associated with the charge ordered and antiferromagnetic phases respectively

6.2.2 Interpretation of STS Data

The charge ordered phase of $LaSr_2Mn_2O_7$ has been determined by x-ray diffraction and bulk conductivity measurements to form at around 210 K, and collapse with decreasing temperature at 70-100 K [28, 34]. Magnetometry measurements on the samples used for this experiment (see figure 6.2) indicate that the charge ordered (CO) phase occurs in a similar temperature range to the published values. Thus charge order is expected to be be active in this material up to the highest temperature studied in the STM experiment. From X-ray diffraction data the charge ordered state appears strongest at around 150 K [28]: this corresponds with the peak in 2Δ observed at 140 K. At 115 K when the gap distribution is first observed to be bimodal, charge ordering would be starting to disappear. Neutron scattering data [1] indicate that the charge ordered and antiferromagnetic phases coexist below 170 K, with roughly equal proportions of each phase expected at 125K. The antiferromagnetic phase will be more conductive than the CO phase, so it is reasonable to assume that at 115 K the large gap represents the CO phase and the smaller gap

the AF phase.

If we adopt the same interpretation at lower temperatures, this would indicate that charge ordering is still active below 115 K. At 80 K the large gap is still seen to dominate: this is on the lower bound of the expected temperature range of charge ordering. The large gap is also observed at 45 K: if this represents charge ordering this is an apparent contradiction of X-ray and neutron diffraction results [1,28], and of magnetisation measurements (section 6.1), which indicate that the charge ordered state collapses below 70 K. However, from the gap histogram at 45 K (figure 6.5a) it seems that the smaller gap is dominant, implying that charge ordering may be present but only as a minority phase. It is possible that this phase is only stable at the surface at this temperature, explaining why it is not observed by bulk probes. From figure 6.5 it appears that the distribution of the large gap phase on the surface is influenced by surface features such as step edges: this indicates that the charge ordered phase is stabilised by some surface features, potentially explaining why the phase appears at the surface at temperatures at which it does not appear in the bulk.

At 10 K the large gap is still in evidence: the gap is single valued at this temperature on all areas studied, with $2\Delta = 0.76$ V. Again, if this is taken to be a signature of the charge ordered state this would be in apparent contradiction to bulk probe data. It is possible that the charge ordered state is stable to zero temperature, as observed by Gray *et al.* [36], but our samples show the increase in magnetisation below 100 K associated with the disappearance of the CO state. It is also possible that the charge ordered state might collapse at around 80 K and reappear at lower temperature - a phenomenon known as multiple re-entrance. The re-appearance of charge ordering at low temperature has been observed by X-ray diffraction [72]: superlattice peaks associated with the charge ordered phase are observed to reappear below 50 K. However the low-temperature charge ordering is much weaker than that observed above 100 K, with the intensity of the superlattice peaks at 9 K lower by a factor of about 100 compared to that at 175 K. Again, it is possible that this weaker charge ordered state is stabilised at the surface of $LaSr_2Mn_2O_7$ at 10 K, explaining the dominance of the large gap in the STS spectra.

To summarise, if we interpret the large spectroscopic energy gap observed in STS data as being due to the charge ordered phase, these data indicate that charge order

is stable at the surface of $LaSr_2Mn_2O_7$ in the whole temperature range 10 K $\leq$ T $\leq$ 225 K. Between 10 K and 125 K the large gap phase is suppressed, and is observed to coexist with a phase with a smaller energy gap, interpreted as the antiferromagnetic phase. Charge order may be stabilised at the surface of $LaSr_2Mn_2O_7$, so will not be apparent to bulk probes such as diffraction and magnetometry in the temperature range where it is suppressed. The large gap phase is most heavily suppressed at 45 K, and exists as a minority phase: at 10 K the surface dominated by the large gap phase.

Since atomic resolution cannot be achieved on this surface at present, it is not possible to conclusively demonstrate that the large spectroscopic gap is due to charge ordering. Also these data are only based on a single variable temperature run, which would need to be repeated to draw firm conclusions. Therefore this remains a preliminary result. In the future if atomic resolution can be demonstrated, it may be possible to unambiguously link charge ordering to a larger spectroscopic gap, as was done in the STM study of $Bi_{1-x}Ca_xMnO_3$ [54]. Until such a time the existence of spectroscopic variation is open to other interpretations: variation might be ascribed to areas of surface contamination or damage, or to different types of surface exposed upon cleaving.

6.2.3 Magnetic Field Dependence of STS spectra

The effect of magnetic field on the spatial distribution of the large and small energy gap on the surface of $LaSr_2Mn_2O_7$ was investigated using the Cryogenic STM. STS mapping was carried out at 115 K: an area of the surface was identified where the energy gap showed a clear bimodal distribution, similar to that shown in figure 6.5b. A magnetic field of 6 T was applied perpendicular to the surface, and the STS map was repeated with the tip in the same position. Initial results from gap measurements on the high-field STS map seemed to indicate a substantial change in the gap distribution: however it was apparent from the topographic images that the area scanned at 6 T was not the same as the zero-field scan area. Thus the observed change might be due to spatial variation of gap width rather than any variation under applied field. Despite the test result (see section 3.1.4) that a magnetic field of up to 6 T can be applied to the Cryogenic STM head without moving the sample

relative to the tip more that 1 nm, in this experiment the sample was observed to move more than 200 nm in the X-Y plane relative to the tip, upon application of a 6 T field. Presumably, the substantial magnetic moment of the manganite sample means that sufficient force is exerted on the sample stage to move it relative to the tip: the test sample was non-magnetic $NbSe_2$. The experiment was therefore repeated and the X-Y offset corrected for. Upon repetition no change was seen in the energy gap width 2Δ or its spatial distribution under a magnetic field of 6 T at 115 K, to an accuracy of $\pm$ 10 mV in the gap width. At 115 K $\Delta E = 3.5\ kT =$ 35 mV (see section 2.1.1) so this variation is not significant. The field dependence of the energy gap was also investigated at 140 K and 170 K, and no significant change was identified. In bulk electrical transport measurements of $LaSr_2Mn_2O_7$ a significant negative magnetoresistive effect has been identified: this is observed in the temperature range in which charge order is active, and has been identified with the suppression of the charge-ordered state by the magnetic field [28, 72]. Figure 1.10 shows the published dependence of the ab-plane resistivity on temperature and magnetic field, at fields of up to 7 T [28]. Suryanarayanan *et al.* [72] report a magnetoresistance ratio of $\Delta R/R_0 = 0.78$ ($\Delta R/R_H = 3.5$) at 150 K and 8 T. The non-observation of significant change in the surface energy gap at fields of up to 6 T could be attributed to one of two factors: either the magnetoresistive effect does not result in a measurable change in the bulk band gap at the temperatures studied, or the gap measured by STM is not representative of the bulk band gap. The former is possible: for example from figure 1.10 applying a 7 T field at 115 K produces a reduction in resistivity similar to that produced by reducing the temperature to 80-90 K. From figure 6.6 it is not clear that an equivalent change in the energy gap would be measurable. It is also possible that the bulk gap does change significantly as a result of magnetic field suppression of the charge-ordered state, but that, as noted above, the charge ordered state is stabilised at the surface, so that the surface charge ordered state is not measurably suppressed.

6.3 Polaronic Behaviour in $La_{1.36}Sr_{1.64}Mn_2O_7$

Single crystal $La_{1.36}Sr_{1.64}Mn_2O_7$ (x = 0.32) samples were studied using the Oxford UHV STM, with the intention of comparing data collected on this sample with that collected on the x = 0.3 compound, $La_{1.4}Sr_{1.6}Mn_2O_7$. In particular it was desired to study the effect of polaronic transport in the x = 0.32 compound. In $La_{1.4}Sr_{1.6}Mn_2O_7$ a polaron psuedogap has been observed in STS both above and below the metal-insulator transition: atomic resolution islands, identified as trapped polarons (see section 2.2.3), were observed on the surface. Atomic resolution was not observed on the rest of the $La_{1.4}Sr_{1.6}Mn_2O_7$ surface: this was attributed to metallic charge screening [59]. Similar phenomena might be observed in the x = 0.32 compound. In this region of the $La_{2-2x}Sr_{1+2x}Mn_2O_7$ phase diagram, samples with higher cation doping x are more resistive, as shown in figure 6.7. We may expect that the ab planes will be less metallic and more disordered, and that screening will be less effective, in $La_{1.36}Sr_{1.64}Mn_2O_7$ compared to $La_{1.4}Sr_{1.6}Mn_2O_7$.

The $La_{1.36}Sr_{1.64}Mn_2O_7$ samples were cleaved *in situ* in the STM chamber at $1x10^{-10}$ mbar, at room temperature. W tunnelling tips were used, prepared by AC electrochemical etching in KOH. The samples were studied at room and low temperature. This compound proved easier to cleave than the x = 0.3 crystals (sections 6.2 and 6.4), although only one out of the three cleaves performed yielded some atomically flat surfaces. Terraces larger than micron size were observed. Many areas of the surface were found to be rougher, with peak-peak roughness of 2-3 nm. This might be due to an uneven cleave, or to surface contamination. Figure 6.9a shows a 50 x 50 nm topographic image on an atomically flat area, together with a cross section through this image: numerous round features 3-4 nm in diameter and approximately 0.1 nm in height are observed. Figure 6.9b shows a 20 x 20 nm image of a similar area, showing the same kind of topographic features: a cross section is indicated, showing that the features are around 0.1 nm in height. Dual bias imaging has been performed to acquire images at positive and negative bias simultaneously: no significant change in the image is observed with bias polarity. The inset shows a 4 x 4 nm enlargement of the area indicated by the dashed square, centred on one of the round features. The inset has been low-pass Fourier filtered to increase the contrast. An atomic-scale lattice is visible within the round feature: the atomic contrast seems to be limited to the feature, comprising around 25 unit cells. The spacing of this

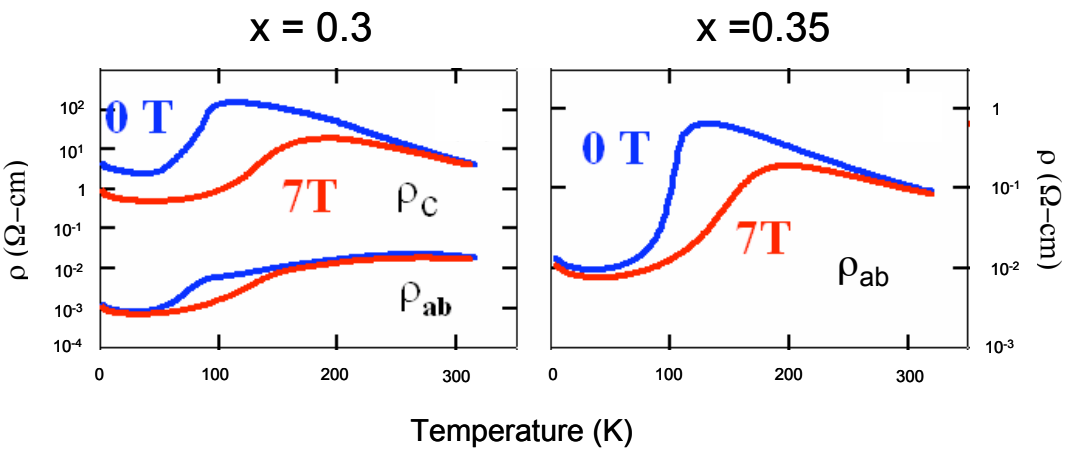

Figure 6.7: Bulk transport data for $La_{2-2x}Sr_{1+2x}Mn_2O_7$, x = 0.3 and x = 0.35. At room temperature the x = 0.3 compound has 10 times the conductivity of the x = 0.35 compound. Courtesy of T. Kimura and Y. Tokura

lattice is 0.42 ± 0.04 nm: the large uncertainty is due to the small number of unit cells available for measurement. The peak to peak corrugation of the atomic lattice is ≈ 30 pm. The step height as measured at terrace edges is 0.88 ± 0.09 nm. These measurements are in reasonable agreement with the values of a = 0.388 and c/2 = 1.007 nm, from X-ray diffraction [46].

Several spectroscopic maps were collected from the $La_{1.36}Sr_{1.64}Mn_2O_7$ sample, at room temperature and at 45 K. No spectroscopic variation was observed within the maps. Figure 6.8c shows average spectra recorded at 297 K and 45 K. Clearly the spectra are gapped at low temperature, well below the metal-insulator transition: the gap parameter Δ at room temperature is approximately 200 mV: at 45 K it is 400 mV. The observation of a gap above and below the metal insulator transition, and the larger gap at low temperature, is similar to the result for $La_{1.4}Sr_{1.6}Mn_2O_7$ [59]. This indicates that polarons are the charge carriers in the low temperature ferromagnetic metallic state of the x = 0.32 compound, as well as in the antiferromagnetic metal ground state of the x = 0.3 compound: the observed gap is the polaron pseudogap, which is a measure of the polaron binding energy.

The gap measured on the $La_{1.36}Sr_{1.64}Mn_2O_7$ surface is around twice as large as that observed on the $La_{1.4}Sr_{1.6}Mn_2O_7$ surface [59]: around 400 meV against 200 meV at around 45 K. This indicates that polarons in the x = 0.32 compound are much more

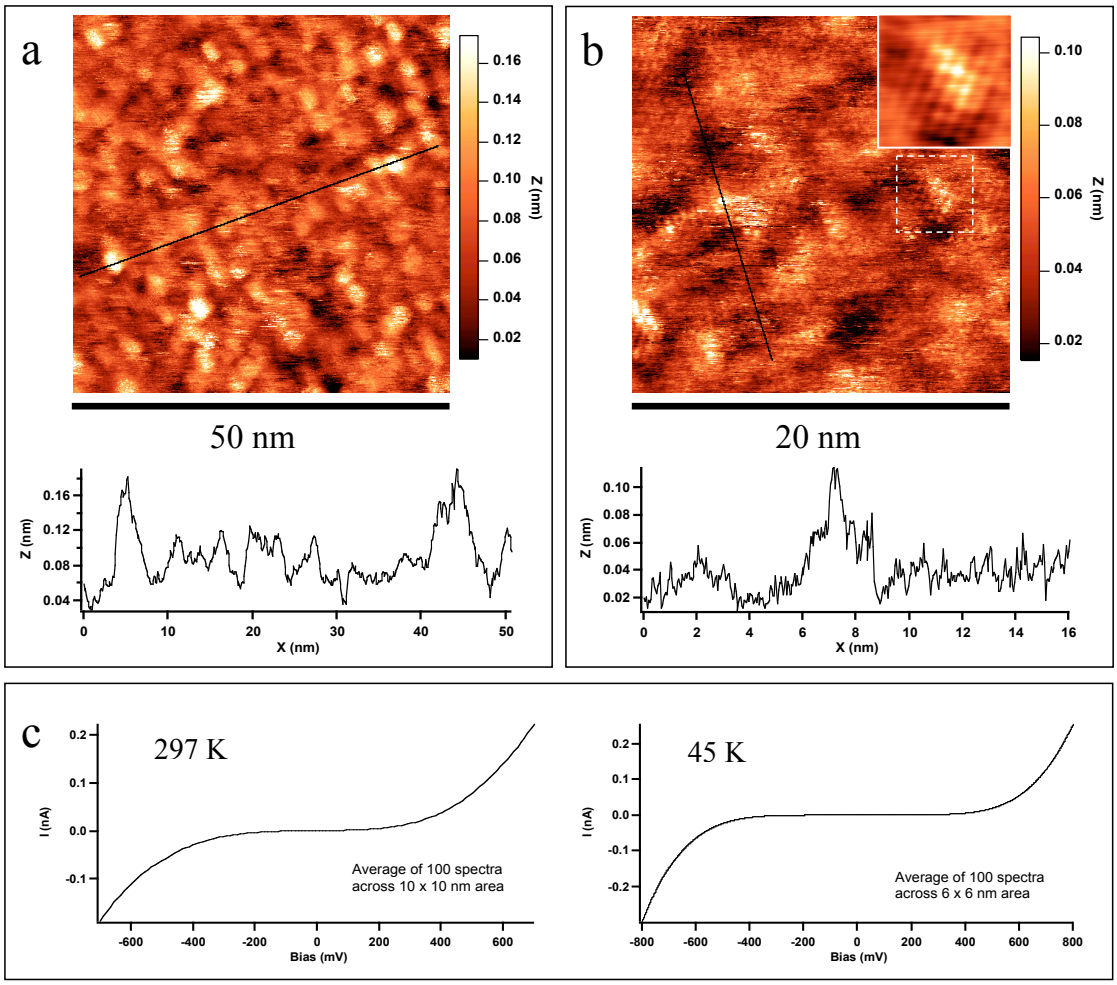

Figure 6.8: (a) 50 x 50 nm topographic image of $La_{1.36}Sr_{1.64}Mn_2O_7$ (x = 0.32), with a cross section along the line shown (b) 20 x 20 topographic image, with a cross section. The inset shows a 4 x 4 nm detail of the area delineated by the dashed square. The inset has been low-pass Fourier filtered: the lattice has a spacing of 0.42 ± 0.04 nm (c) average tunnelling spectra collected at 297 K and 45 K

tightly bound than at x = 0.3. If this is the case this would mean that the polaron binding energy is very strongly dependent on the cation doping level.

As can be seen from the cross section in figure 6.9a, the height of the round features is around 0.1 nm: the features are 3-4 nm in diameter. The size and height of these features is similar to the atomic resolution islands seen by Rønnow *et al.* [59] on the $La_{1.4}Sr_{1.6}Mn_2O_7$ compound. These islands were explained as trapped polarons: atomic resolution was not observed across most of the surface, due to charge

screening. Atomic resolution can be achieved locally on the round features on the $La_{1.36}Sr_{1.64}Mn_2O_7$ surface, as seen in figure 6.8b. This suggests that these features may represent trapped polarons, as for $La_{1.4}Sr_{1.6}Mn_2O_7$. The round features seen on the $La_{1.4}Sr_{1.6}Mn_2O_7$ surface are well separated though, whilst the features in figure 6.8a and b are almost coalescing. Since $La_{1.36}Sr_{1.64}Mn_2O_7$ is less conductive than $La_{1.4}Sr_{1.6}Mn_2O_7$, charge carriers will be scattered more frequently, and screening will be less effective. We would therefore expect a higher density of trapped polarons. It is possible that this is what is being observed in figure 6.8: the round features may represent a dense conglomeration of trapped polarons.

An alternative explanation for the structures seen on the $La_{1.36}Sr_{1.64}Mn_2O_7$ surface is related to the mixed-valence nature of the compound. La^{3+}, Sr^{2+}, Mn^{3+} and Mn^{4+} ions are all present at or near the surface. The difference in ionic radius between these ions is insufficient to account for the observed corrugation of ≈ 0.1 nm: however electronic effects due to the differing charge states on these ions might allow for this corrugation. Ma et. al [42] observed a 0.1 nm difference in height between Mn^{3+} and Mn^{4+} sites on the $La_{0.325}Pr_{0.3}Ca_{0.375}MnO_3$ surface. The features observed on the $La_{1.36}Sr_{1.64}Mn_2O_7$ surface might represent clusters of Mn^{4+} ions at or near the surface. However, if the observed corrugation were due to contrast between Mn^{3+} and Mn^{4+} ions the corrugation would be expected to be bias polarity dependent, as observed by Ma et. al [42]: so far no bias polarity dependence has been observed in STM images of $La_{1.36}Sr_{1.64}Mn_2O_7$. A second alternative interpretation of the $La_{1.36}Sr_{1.64}Mn_2O_7$ surface features might be as oxygen adatoms and vacancies, as seen on the $PrSr_2Mn_2O_7$ surface (see section 5.2.3). The features seen on the $La_{1.36}Sr_{1.64}Mn_2O_7$ surface seem too large to be individual adatoms though, at 3-4 nm in diameter. In addition, oxygen adatoms show a clear bias dependance in STM imaging (section 5.2.4). As bias dependent imaging is not observed on the $La_{1.36}Sr_{1.64}Mn_2O_7$ surface this interpretation can be ruled out.

6.4 A Minority Phase Inclusion in $La_{1.4}Sr_{1.6}Mn_2O_7$

Single crystal $La_{1.4}Sr_{1.6}Mn_2O_7$ samples (x = 0.3) were studied with a view to replicating the work of Rønnow *et al.* [59], in observing well defined atomic resolution islands. The samples used are cut from the same floating zone rod as used by Rønnow *et al.* STM experiments were carried out on $La_{1.4}Sr_{1.6}Mn_2O_7$ single crystal samples using the Oxford UHV STM. The samples were cleaved *in situ* in the STM chamber at $1x10^{-10}$ mbar, at room temperature. W tunnelling tips were used, prepared by AC electrochemical etching in KOH.

The $La_{1.4}Sr_{1.6}Mn_2O_7$ samples have proved difficult to cleave, either not cleaving at all or producing very rough surfaces. So far only one cleave of this sample has been successful in the Oxford STM. Figure 6.9a shows a 100 x 100 nm topographic scan obtained at room temperature (300 K), showing clear terrace edges. The terrace size is less than 50 nm, in contrast to the previous study [59], where atomically flat terraces of micron size were observed. The terrace step height observed here is 0.95 $\pm$ 0.09 nm, which is consistent with the terrace height of 0.94 $\pm$ 0.02 nm observed by Rønnow *et al.* [59], and the value from X-ray diffraction of 1.007 nm [46]. The error on the step height is mostly due to uncertainty in the z-calibration. With smaller scan areas regular atomic scale features could be resolved: good two dimensional atomic resolution was not achieved, but one dimensional atomic rows were observed, with a spacing measured by Fourier analysis to be 0.393 $\pm$ 0.007, very close to the Mn-Mn spacing of 0.388 nm [46]. Figure 6.9b shows a 25 x 25 nm topographic image: a step is visible, together with atomic rows. Figures 6.9c and Figure 6.9d show a 7 x 7 nm image on a different area, and a low-pass Fourier-filtered version of this image. Atomic rows are clearly visible, together with some lattice defects. The row direction is observed to rotate by 90° between 6.9b and 6.9c, indicating that the actual atomic lattice is square, and that the one dimensionality is an imaging artefact, caused perhaps by an asymmetrically shaped tip. The peak to peak corrugation of the atomic lattice is approximately 50 pm = 0.5 Å. This is comparable to the corrugation observed on atomically resolved islands [59] of around 40 pm. From images such as figure 6.9b it is clear that atomic scale rows can be resolved across wide areas, rather than being restricted to small islands, again in sharp contrast with the properties of the x = 0.3 surface seen by Rønnow *et al.* [59]. Figure 6.9e shows a typical I(V) spectrum collected on this area of the surface. The energy gap is around Δ = 200

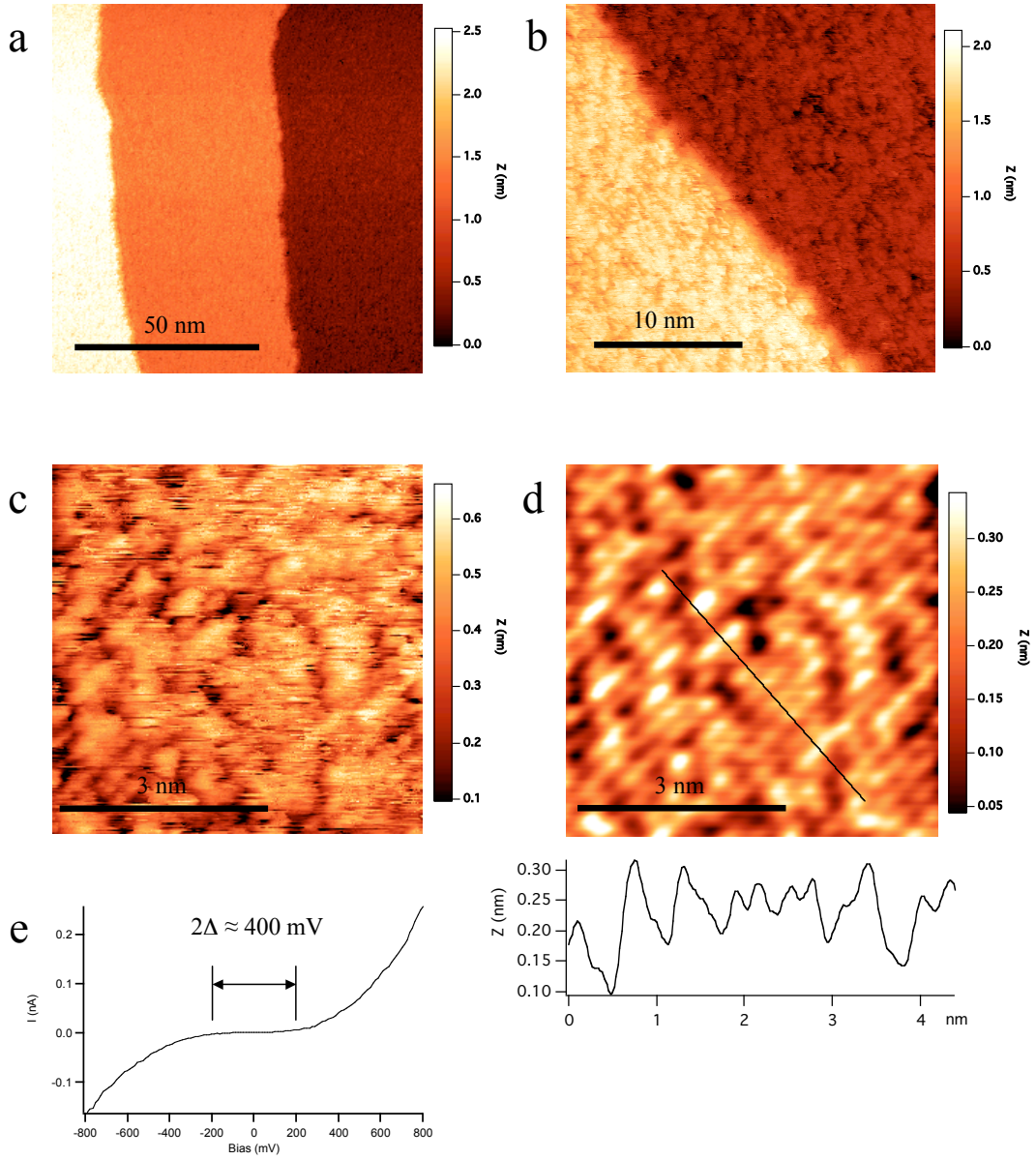

Figure 6.9: STM topographic images of $La_{1.4}Sr_{1.6}Mn_2O_7$ at 300 K (a) 100 x 100 nm: step height is 0.95 ± 0.09 nm (b) 25 x 25 nm: atomic scale stripes are visible. The stripe spacing is 0.393 ± 0.007 nm (c) 7 x 7 nm detail on a different area: the stripes have rotated by 90° (d) Same image, low-pass Fourier filtered, shown with a cross-section. Atomic scale stripes and some defects are visible. (e) Typical spectrum at 300 K, showing gap $\Delta \approx 200$ mV

mV, around twice that recorded by Rønnow *et al.* [59] at the same temperature.

Taking all the discrepancies between these $La_{1.4}Sr_{1.6}Mn_2O_7$ data and those published by Rønnow *et al.* [59], it seems clear that a fundamentally different surface is observed. One possibility is that this is an area with a local cation doping significantly different from that of the bulk, due to spatial variations in La, Sr and O content within the crystal: such an area could have different properties from the rest of the sample. The larger energy gap indicates a more insulating surface, which in turn would suggest a local doping higher than x = 0.3, as the general trend in this part of the phase diagram is for lower conductivity at higher x (see section 1.6, and also figure 6.7). The gap is similar to that measured on the x = 0.32 $La_{1.36}Sr_{1.64}Mn_2O_7$ surface (see section 6.3). This might explain the extensive atomic resolution, as screening will be less effective, and electrons more localised, on this less metallic surface. Spatial variation in cation doping has been suggested as an explanation for ferromagnetic inclusions seen in $La_{1.4}Sr_{1.6}Mn_2O_7$ [2, 31]: the inclusions are thought to have cation doping in the range $0.3 \leq x \leq 0.32$. Alternatively the surface might represent a cubic perovskite ($La_{1-x}Sr_xMnO_3$) inclusion. The observed atomic spacing is consistent with the $La_{1-x}Sr_xMnO_3$ Mn-Mn spacing of 0.386 nm: the observed steps might be double steps of 2 x 0.386 = 0.772 nm. Whilst the bilayer spacing of $\approx$ 1 nm is a better fit to the measured step height of 0.95 $\pm$ 0.09 nm, a cubic perovskite inclusion cannot be ruled out. This interpretation could also explain the extensive atomic resolution, which can clearly be achieved on some perovskite manganite surfaces [42,54]. The existence of multiphase inclusions (of single layer n = 1 and perovskite n = ∞) in n = 2 bilayer thin films has been clearly evidenced [74,75]: it is reasonable to assume that although intergrowths will be rarer in bulk single crystals, they will occur in some finite volume of the sample.

Whether the observed surface represents a portion of the bilayer crystal with a different cation doping, or a perovskite inclusion, the question remains why this effect was not observed by Rønnow *et al.* It should be stressed that this is a single measurement and has not so far been repeated: it is therefore possible that there is a low probability both of cleaving into a layer including an area of locally increased doping or a perovskite intergrowth, and happening to land on this area with the tunnelling tip, and that this is simply the first such occurrence. In addition these crystals are now several years old: manganite crystals do age, largely as a result of changes in oxygen content. If the oxygen content changes the effective cation doping

will change [36]: this can result in a change in the overall properties of the crystal. As T_N does not seem to have changed significantly in these samples (see section 6.1) a substantial change in the overall doping of the crystal seems unlikely: however local changes in oxygen content, resulting in local variations in effective cation doping could occur, which might not greatly affect the bulk sample properties.

6.5 STM Study of a-b Plane Oriented $La_{1.2}Sr_{1.8}Mn_2O_7$

Thin film samples of $La_{1.2}Sr_{1.8}Mn_2O_7$ (x = 0.4) grown in the [110] direction were studied using the Oxford UHV STM. The initial aim was to characterise the surface to determine if it is suitable for STM investigation, since it is likely to be rougher than a [001] oriented film or single crystal. Additional aims were to image the bilayer spacing if possible, and to perform position-dependent spectroscopy to see if there is any spectroscopic difference between the perovskite bilayers and the rock-salt layers that separate them. The rock-salt layers are insulating, so modulation of the STS spectra may be observed along the c-axis, with the rock-salt layers having a larger gap than the perovskite bilayers.

The $La_{1.2}Sr_{1.8}Mn_2O_7$ films were studied at room and low temperature: W tunnelling tips were used, prepared by AC electrochemical etching in KOH. 600 nm thick films were studied, as these had been found (see section 6.1.1) to have fewer inclusions of n = 1 and n = ∞ phases. The samples were studied as-grown, without any in-situ cleaning or processing. Initially scans were performed on micron sized areas, to characterise the roughness of the films. A sample 700 x 700 nm scan recorded at room temperature is shown in figure 6.10a: the peak to peak roughness is around 5 nm. The ab plane orientation can be clearly seen in figure 6.10a by the linear growth regions, which measure approximately 400 nm in the a/b plane [110] direction and 30 nm in the c-axis [001] direction.

The surface of the [110] oriented films is considerably rougher than the atomically flat terraces observed on [001] oriented single crystal samples [59]. By taking a scan area smaller than the growth regions however, regions which are sufficiently flat for high resolution imaging can be found. Figure 6.10b shows a 10 x 10 nm topographic scan: the peak to peak roughness in this image is $\approx$ 0.2 nm. Linear features aligned with the a/b plane direction can be observed. A Fourier transform of this image is shown: peaks corresponding to a stripe spacing of 1.00 $\pm$ 0.05 nm are seen. Figure 6.10c shows the same image as 6.10b, selectively Fourier filtered to enhance the stripe structure. A section through the image in the c-axis direction is shown: the 1 nm spacing can clearly be observed. We interpret these stripes as an observation of the bilayer spacing: the unit cell of $La_{1.2}Sr_{1.8}Mn_2O_7$ measures 2.014

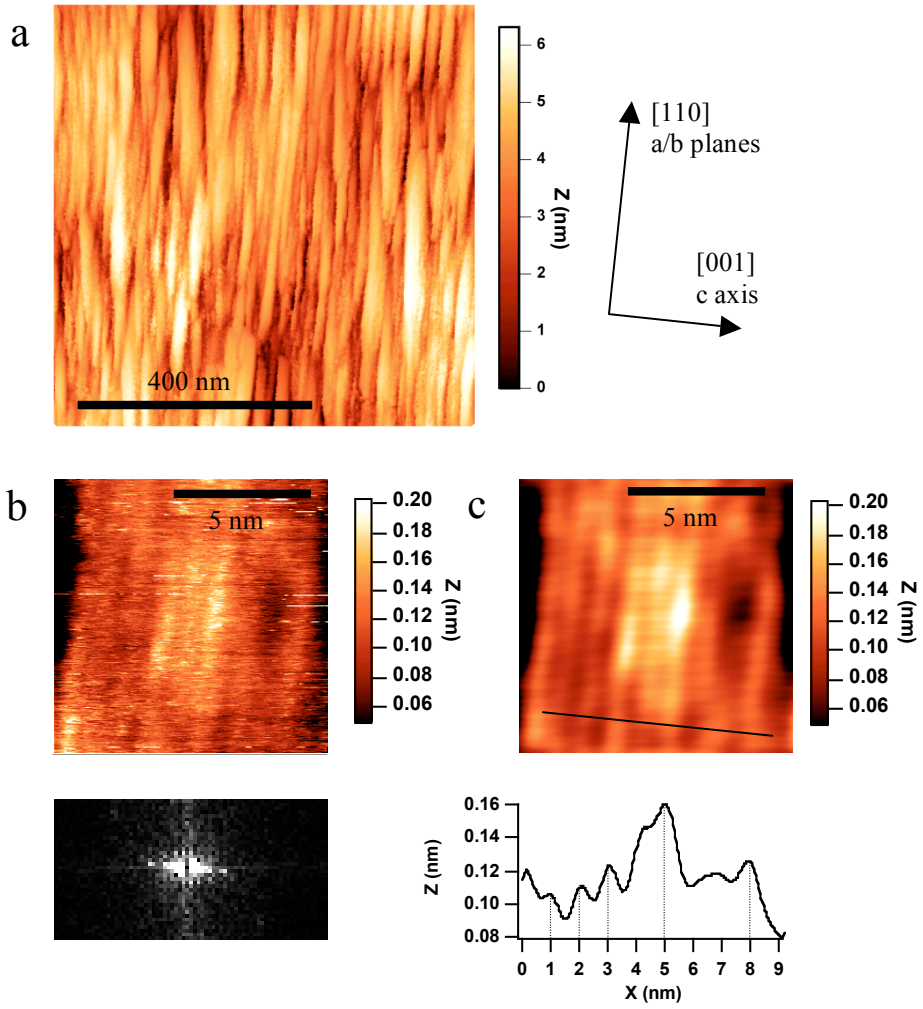

Figure 6.10: (a) 700 x 700 nm STM topographic image of a [110] oriented thin film of $La_{1.2}Sr_{1.8}Mn_2O_7$ (x = 0.4), collected at room temperature. The c axis and a/b plane directions are indicated: the growth direction of the film is clearly observed (b) 10 x 10 nm detail with the same orientation, also at room temperature. Linear structures in the a/b plane direction can be observed: an FFT of this image is also shown. The periodicity is 1.00 ± 0.05 nm. (c) The same image, Fourier filtered: a cross section is shown, indicating the 1 nm periodicity

nm in the c-axis [74], so the bilayer spacing is 1.007 nm. Troughs in the topographic image probably correspond to the rock-salt layers: these are less conducting than the bilayers, which will cause the tip to drop when passing over them: this is illustrated in figure 6.11a.

Tunnelling spectra were collected on well-resolved areas of the [110] $La_{1.2}Sr_{1.8}Mn_2O_7$ surface, at room temperature and at 44 K: example spectra are shown in figure 6.11b. Gapped spectra are observed at room temperature: the gap is around 300 mV. Bulk $La_{1.2}Sr_{1.8}Mn_2O_7$ (x = 0.4) undergoes a insulator to metal transition at $T_{MI} \approx 125$ K (see sections 1.6 and 1.6.2). Gapped spectra are also observed at 44 K. Spectroscopic arrays were recorded with spatial resolution of 0.1 nm, at room temperature and at 44 K. No spectroscopic variation was observed in the STS maps: the rock-salt insulating layers could not be distinguished spectroscopically from the perovskite bilayers.

Some experimental problems were encountered in collecting variable temperature STS data for this sample. As noted in section 6.1.1, although bulk $La_{1.2}Sr_{1.8}Mn_2O_7$ (x = 0.4) undergoes an insulator to metal transition at $T_{MI} \approx 125$ K, leading to a low resistivity state at low temperature, the resistivity of the thin films used in this experiment increases monotonically with decreasing temperature. This means that the low temperature resistivity is high: the c-axis resistivity is around 10^5 ohm-cm at 44 K. This is on the limit of what can be studied with STM, and leads to spectra whose gap is strongly dependent on the tunnel current used. This is because the sample resistance is so high that at higher tunnel current the tip is moving into the contact regime, so the tunnel signal is partially shunted by an ohmic term. At the lowest current accessible with the new preamplifier, the spectra at 44 K are certainly gapped, but the magnitude of this gap is impossible to gauge accurately.

Gapped spectra are observed on the [110] $La_{1.2}Sr_{1.8}Mn_2O_7$ surface both above and below T_{MI}: this is a similar result to that seen in STS experiments on [001] oriented single crystal $La_{1.4}Sr_{1.6}Mn_2O_7$ samples [59]. This was interpreted as an effect of polaronic transport: the charge carriers are bound states of an electron and a phonon, but as only a bare electron can tunnel from the sample to the tip, STS data always show a pseudogap equivalent to the polaron binding energy (see section 2.2.3). The same effect could be at work in this experiment: whether tunnelling perpendicular to the [001] or [110] surface, the psuedogap should always be observed.

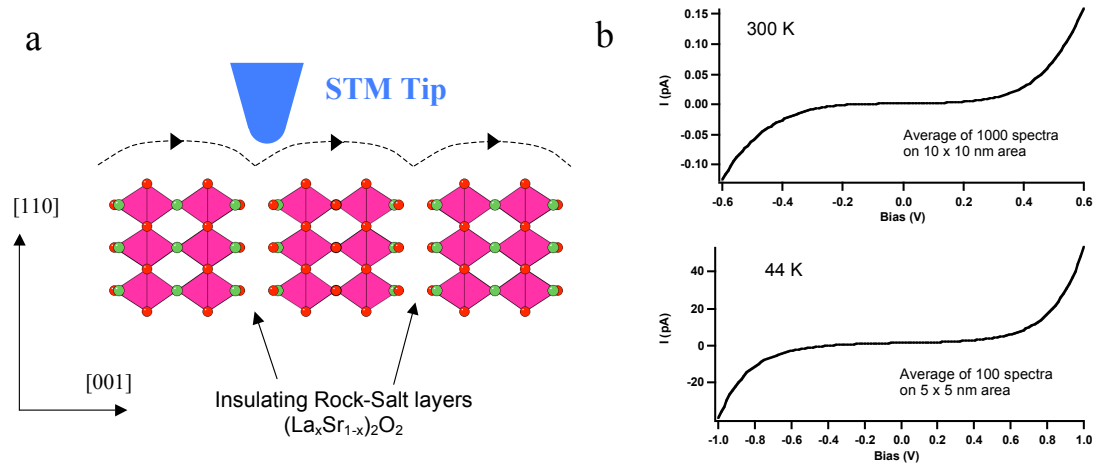

Figure 6.11: (a) schematic of STM imaging of [110] oriented $La_{1.2}Sr_{1.8}Mn_2O_7$: the tip moves closer to the insulating rock-salt layers in order to maintain the tunnel current, resulting in a depression in the topographic image (b) Averaged tunnelling spectra collected on [110] oriented $La_{1.2}Sr_{1.8}Mn_2O_7$ at 300 K and 44 K: spectra are gapped above and below the metal - insulator transition

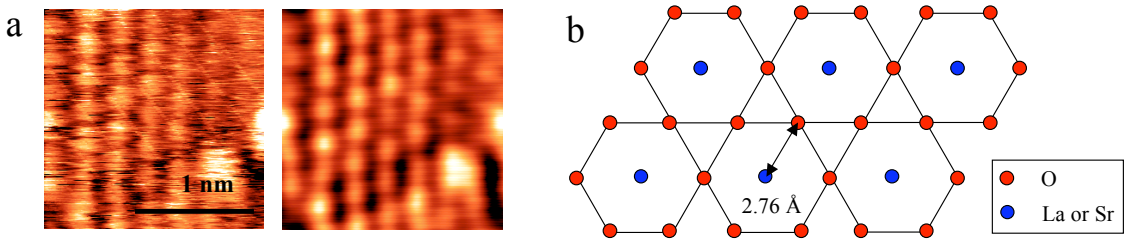

Figure 6.12: (a) 1.88 x 1.85 nm topographic image of a hexagonal inclusion in [110] - oriented $La_{1.2}Sr_{1.8}Mn_2O_7$, collected at room temperature. Raw image and low-pass Fourier-filtered images shown. (b) Possible explanation for hexagonal phase: a (111) cleave through a cubic perovskite $La_{1-x}Sr_xMnO_3$ inclusion

In some locations on the LSMO-327 [110] surface atomic resolution could be achieved, at room temperature: a hexagonal rather than square lattice is observed. A high-resolution image showing this hexagonal lattice is shown in figure 6.12a: the lattice spacing is 0.29 ± 0.02 nm. This lattice was observed repeatedly, in small areas containing approximately 200 unit cells. This represented a very small fraction of the sample surface studied at high resolution. This lattice is clearly inconsistent with the expected structure and orientation of the sample, so to explain this observation we infer an inclusion of some other phase. An investigation performed by Silvia de Santis[1] identified a possible surface which could give rise to this lattice: a cubic perovskite (n = ∞: $La_{1-x}Sr_xMnO_3$) manganite cleaved along the (111) plane can produce a hexagonal lattice with spacing 0.276 nm, if the cleave is along the (La, Sr) O layer and La, Sr and O are all visible. A schematic of the possible lattice is shown in figure 6.12b. The existence of impurity phases in the thin films samples is not surprising, since it has already been established [74, 75] that these samples are likely to contain inclusions of n = 1 and n = ∞ phases: interestingly here there is a mismatch in orientation between the majority bilayer phase and the cubic inclusion.

[1]Department of Physics, University of Rome "La Sapienza"

Chapter 7

Conclusions

7.1 Manganite Surfaces

In the experiments described in this thesis several different bilayer manganite surfaces have been studied. The quantity and quality of the data varies from compound to compound, but some general observations can be made.

Atomic resolution has been achieved in STM images of $La_{1.36}Sr_{1.64}Mn_2O_7$ and $PrSr_2Mn_2O_7$ (see sections 6.3 and 5.2.1). Atomic rows have been observed in $La_{1.4}Sr_{1.6}Mn_2O_7$, although this surface is not thought to be representative of the general surface, and may be due to an inclusion with higher cation doping (see section 6.4). The peak to peak atomic corrugation observed on the $La_{1.4}Sr_{1.6}Mn_2O_7$ surface is $\approx$ 50 pm, that observed on $La_{1.36}Sr_{1.64}Mn_2O_7$ is $\approx$ 30 pm. These both compare well with the corrugation previously observed on atomically resolved islands on $La_{1.4}Sr_{1.6}Mn_2O_7$ [59] of around 40 pm. By contrast, atomically resolved images of $PrSr_2Mn_2O_7$ show a much smaller corrugation of around 4 pm. This is contrary to what we would expect based on the relative resistivity of the compounds involved. $PrSr_2Mn_2O_7$ is more resistive than either of the La-containing compounds (compare figures 6.7 and 1.13), so we would expect weaker charge screening at the surface and increased atomic corrugation. However, it is worth noting that in the published study of the $La_{1.4}Sr_{1.6}Mn_2O_7$ surface [59] atomic resolution was not observed over most of the surface. This was attributed to effective charge screening: it was calculated that this would reduce the atomic corrugation to less than 2 pm. Only localised reduction of screening, attributed to trapping of charge carriers (polarons) by point defects, allows large atomic corrugation. A similar mechanism may be at work in $La_{1.36}Sr_{1.64}Mn_2O_7$ although a much higher density of trapped polarons is hypothesised (see section 6.3). So the corrugation of 4 pm seen in $PrSr_2Mn_2O_7$ is in fact larger than the general corrugation in $La_{1.4}Sr_{1.6}Mn_2O_7$ of < 2 pm, which is as expected based on the higher resistivity of $PrSr_2Mn_2O_7$. The low corrugation observed on $PrSr_2Mn_2O_7$ suggests that polaron trapping is not a significant feature of this surface, since this would be expected to yield local atomic corrugations larger than 40 pm. This does not imply that the charge carriers in $PrSr_2Mn_2O_7$ are not polarons however: there should still be a strong electron-phonon interaction in $PrSr_2Mn_2O_7$ due to the Jahn-Teller effect, which will result in polaron formation. The lack of trapped polarons at the surface may be due to other factors such as lower defect density.

7.1.1 Surface Superstructures

Atomic resolution has been achieved on $PrSr_2Mn_2O_7$ and $La_{1.36}Sr_{1.64}Mn_2O_7$: in both cases a superstructure is observed, which appears irregular but has features with a length scale of around 4 nm. At present it is not clear if these are due to the same phenomenon: there are some crucial differences between the two. In the case of $PrSr_2Mn_2O_7$ the corrugation amplitude is around 20 pm, and atomic resolution can be seen across the whole image area, superposed upon the superstructure. Some features of the superstructure are observed to change between positive and negative bias. In $La_{1.36}Sr_{1.64}Mn_2O_7$ the corrugation amplitude is around 100 pm. Atomic resolution appears to be confined to the superstructures seen, although this is not clear as the imaging quality is not as good as in the case of $PrSr_2Mn_2O_7$. The superstructure features do not appear to change with bias. Two models have been advanced to explain these superstructures. One involves the mixture of different ionic species present at or near the surface and has been advanced to explain the superstructure seen on $PrSr_2Mn_2O_7$ (see section 5.2.1). The bias dependence seen in images of the $PrSr_2Mn_2O_7$ superstructure would seem to support this theory, as it is established that Mn^{3+} and Mn^{4+} sites on manganite surfaces can yield markedly different contrast in filled and empty state STM images [42]. The other model is applied by analogy to the "trapped polaron" features seen in STM images of $La_{1.4}Sr_{1.6}Mn_2O_7$ [59]. This was advanced to explain the superstructure of $La_{1.36}Sr_{1.64}Mn_2O_7$ (section 6.3) and assumes a much higher density of trapping sites than was proposed for $La_{1.4}Sr_{1.6}Mn_2O_7$, creating a dense array of trapped polarons which are visible as raised structures in STM images. The lack of bias dependence in the case of $La_{1.36}Sr_{1.64}Mn_2O_7$ might be indicative of an array of trapped polarons, since these are expected to be non-dispersive [59]. Polaronic transport is clearly indicated in $La_{1.36}Sr_{1.64}Mn_2O_7$ since the material undergoes an insulator to metal transition at low temperature, but tunnelling spectra remain gapped above and below the transition temperature (see section 6.3). In principle either model might be applied to either compound: however the trapped polaron model seems unlikely for $PrSr_2Mn_2O_7$ since it should result in an atomic corrugation of order 40 pm, as observed for atomically resolved islands on $La_{1.4}Sr_{1.6}Mn_2O_7$ [59], rather than the observed corrugation of around 4 pm.

7.1.2 Preparing Manganite Surfaces for STM

The best-resolved images and most reproducible results were obtained from the $PrSr_2Mn_2O_7$ compound in experiments using the LT-STM. Whilst cold cleaving and improved vacuum conditions undoubtedly helped in producing good surfaces, the $PrSr_2Mn_2O_7$ compound clearly cleaves more reliably than any of the $La_{2-2x}Sr_{1+2x}Mn_2O_7$ compounds. Even when cleaved at room temperature and relatively poor vacuum, large, flat atomic terraces can be reliably observed (section 5.2.12). This better cleaving performance may be related to the A-site order postulated in section 5.2.5. If the A_2 sites in the centre of the bilayers are entirely occupied by trivalent ions, the electrostatic force opposing cleaving through the rock salt layers will be reduced, since the A_1 sites in these layers will be populated solely by divalent ions.

A-site ordering is observed to be more prevalent in compounds with smaller trivalent cations, for example Pr^{3+} and Nd^{3+} [67]. A family of Pr-containing bilayer manganite compounds with x = 0.5 exists as $Pr(Sr_{1-y}Ca_y)_2Mn_2O_7$ (see section 1.7). At high y these exhibit CE-type charge order: these compounds may cleave more easily and reliably than $La_{2-2x}Sr_{1+2x}Mn_2O_7$ and may be suitable for STM investigations. Nd-containing compounds such as $Nd_{2-2x}Sr_{1+2x}Mn_2O_7$ may also cleave well and be good materials to study using STM. Theoretical investigations into A-site ordering are currently underway, and may provide insight into which compounds will cleave easily.

Cleaving layered manganite samples at low temperature, and preventing them from warming up to room temperature, appears effective in producing and maintaining a clean surface suitable for STM study. So far only $PrSr_2Mn_2O_7$ has been treated in this way. In future it may be worthwhile repeating the experiments on $La_{2-2x}Sr_{1+2x}Mn_2O_7$ using cold cleaving, to see if the surface can be prepared more reliably in this way.

7.2 Research Summary

This section summarises the progress made in manganite surface research in the course of this work, in the context of the "open problems" raised in section 2.3.

- Phase separation. A clear bimodal distribution of spectroscopic energy gap values was observed for several temperatures in the $LaSr_2Mn_2O_7$ compound (section 6.2). The surface is well defined, having clear atomic terraces, although atomic resolution was not achieved. This is a clear indication of phase separation in this compound: it is suggested in section 6.2.2 that two types of spectra present may represent the charge ordered and antiferromagnetic phases. However, as this experiment has not yet been repeated this must be regarded as a preliminary result. In particular, atomic resolution imaging will be needed in order for a positive identification of the large gap phase as the charge ordered phase to be made. No evidence for phase separation was seen in the $PrSr_2Mn_2O_7$ compound in the temperature range 75 K $\leq$ T $\leq$ 300 K (section 5.2.12).

- Charge ordering. As noted above, charge ordering has been suggested as an explanation for spectroscopic variation in $LaSr_2Mn_2O_7$ but without atomic resolution data this remains speculative. In $PrSr_2Mn_2O_7$, neither CE-type, nor the stripe-type charge order identified by X-ray diffraction [79] was observed, either by atomic resolution STM or LEED (5.2.11). This indicates that either this type of charge order is too weak to be observed by STM or LEED, or that it does not occur at the surface. Ordering of A-site cations may be related to the formation of oxygen vacancies observed at the surface of $PrSr_2Mn_2O_7$ (section 5.2.5).

- Surface electronic properties compared to bulk properties. The electronic properties of $PrSr_2Mn_2O_7$ surfaces and interfaces will be strongly modified by the presence of oxygen vacancies and adatoms, which can be present at high densities (section 5.2.3). This has been observed via STS: a large change in the local density of states is recorded at vacancy and adatom locations (see figure 5.10). In $LaSr_2Mn_2O_7$, charge ordering may be present at the surface at temperatures where it is not present in the bulk (section 6.2.2).

- Surface defects. Adatoms and vacancies have been identified at the surface of $PrSr_2Mn_2O_7$ (section 5.2.3). These have been identified as oxygen adatoms and vacancies (5.2.4) based on STS data and the crystal structure of $PrSr_2Mn_2O_7$. The coverage of adatoms has been related to the density of Pr^{3+} ions at the surface (5.2.5). Adatoms are observed to be mobile, and show preferred positions at the surface (5.2.7), although they do not form ordered structures (5.2.6). Recombination of adatoms and vacancies has been observed (5.2.8). To the best of the author's knowledge this is the first STM/STS study of defects or vacancies on a manganite surface. In future it may be possible to make a combined AFM/STM study to accurately determine the voltage required to move single oxygen adatoms at the $PrSr_2Mn_2O_7$ surface (5.2.9).

- Surface preparation. It was found that $PrSr_2Mn_2O_7$ surfaces could be reliably prepared for STM study by cleaving in UHV at low temperature. This has allowed atomic resolution to be repeatedly achieved on this surface (section 5.2.1). The technique of low temperature cleaving could be used on other layered compounds, and may provide an improved surface preparation technique. Clearly some compounds cleave more easily than others: it is suggested that ease of cleaving may be related to A-site cation ordering, and that manganite compounds containing Pr^{3+} or Nd^{3+} ions may therefore be particularly well suited to surface studies (section 7.1.2).

- Technological applications for manganites. Devices based on manganite materials have previously been found to exhibit resistance switching behaviour (section 1.8). Several studies have indicated that oxygen content and motion of oxygen ions play key roles in resistance switching [3,47,60,61,69]. One proposed mechanism [69] for resistance switching in manganite-based devices is oxidation or reduction of an oxide layer, driven by the electrochemical migration of oxygen ions under applied bias. We have observed oxygen migration at the surface of $PrSr_2Mn_2O_7$: the migration rate is dependent on the polarity of the applied bias as well as temperature (see section 5.2.7). Also, single oxygen adatoms have been observed by STS to be bistable (section 5.2.9), switching between two positions on the $PrSr_2Mn_2O_7$ surface during a voltage sweep. If manganite compounds are to be developed for use as resistance switching devices, a detailed understanding of oxygen vacancies and adatoms and their behaviour at interfaces will be crucial. Accurate information, obtained from

STM data, on the motion of single oxygen adatoms under applied bias will be invaluable in modelling the resistance switching behaviour of devices based on manganites, which in turn may lead to improved resistance switching device design.

Appendix A

Supplementary Information

A.1 Improving the Cryogenic STM damping performance

As noted in section 3.1.4, low frequency noise has been found to be a particular problem with measurements on the Cryogenic STM. In particular, frequencies around 6 Hz are prevalent in STM imaging and STS spectroscopy. This section will discuss methods tried so far to improve the damping performance of the Cryogenic STM system.

Initially the air leg vibration damping system was adjusted to ensure optimum performance: cables trailing from the STM system frame to the ground were removed where possible. Where this was not possible the cables were ballasted by sandwiching them in dense foam and placing a heavy mass on top. Of particular concern were the vacuum pumping lines which run from the STM system to pumps which sit on the floor. There are two of these, one to pump on the STM helium pot, and one to back the system turbo pump.

Figure A.1a shows the vertical vibration spectrum measured on top of the Cryogenic STM frame, with the air legs inflated. The spectrum was acquired using a Wilcoxon Research accelerometer and is plotted in velocity units. Vibration measurements were made by Benjamin Bryant and Philipp Studer. The air legs were optimised

and trailing cables removed or ballasted. The red curve in A.1a shows the vibration spectrum with both pumping lines connected: a good damping curve is seen, with a broad peak at 2-3 Hz and a rapid drop at higher frequency: a sharp peak is observed at 6.1 Hz however, with an amplitude of around 0.9 $\mu m/s$. Removing both pumping lines results in a drop in amplitude of this peak to around 0.5 $\mu m/s$. The optimum suppression of the 6 Hz noise is achieved by leaving the helium pot pumping line connected, and disconnecting the turbo backing line. This is shown in the blue curve in A.1a: the noise at 6 Hz is reduced to 0.3 $\mu m/s$. The reason for this improvement is not clear, however the helium pot pumping line is heavily ballasted, which will reduce the transmission of 6 Hz noise, and may in fact provide some additional damping for the whole vibration table. This means that good vibration isolation can be achieved with the cryogenic pumping line still connected, so low temperature, low mechanical noise operation should be possible.

We attempted to improve the performance of the air leg vibration damping by adding additional mass to the system. The existing mass of the entire Cryogenic STM system is around 1800 kg. Figure A.1b shows the effect on the vertical vibration spectrum, measured as above, of adding an additional 640 kg of lead weights on top of the system frame. A modest decrease in vibration amplitude is observed below 20 Hz: the peak frequency has been shifted down to slightly less than 2 Hz. The 6 Hz noise is still present after the weight is added, though its amplitude has been slightly decreased from 0.54 to 0.46 $\mu m/s$. Adding further mass may further increase the damping performance of the air legs. Figure A.1c shows the horizontal vibration spectrum, measured in the same way as the vertical spectra. Plots for no added weight and 640 kg of added weight are shown. In this case the added weight seems to slightly increase vibration amplitudes at most frequencies. It is worth noting though that the 6 Hz peak is not visible in the horizontal vibration spectra, suggesting that this frequency is transmitted mostly in the vertical direction only. A sharp peak at 8 Hz is visible in the horizontal vibration spectrum. Figure A.1d shows the vibrational spectrum of the floor, in the vertical direction, for comparison: noise is highest in the range 2 - 20 Hz, with a sharp peak close to 6 Hz. The amplitude of this peak varies from 3 to 8 $\mu m/s$ from one measurement to another. By comparison with figures A.1a and b, we can conclude that the 6 Hz noise observed in the vertical direction originates from the floor: it is attenuated by around a factor of 10 by the air legs.

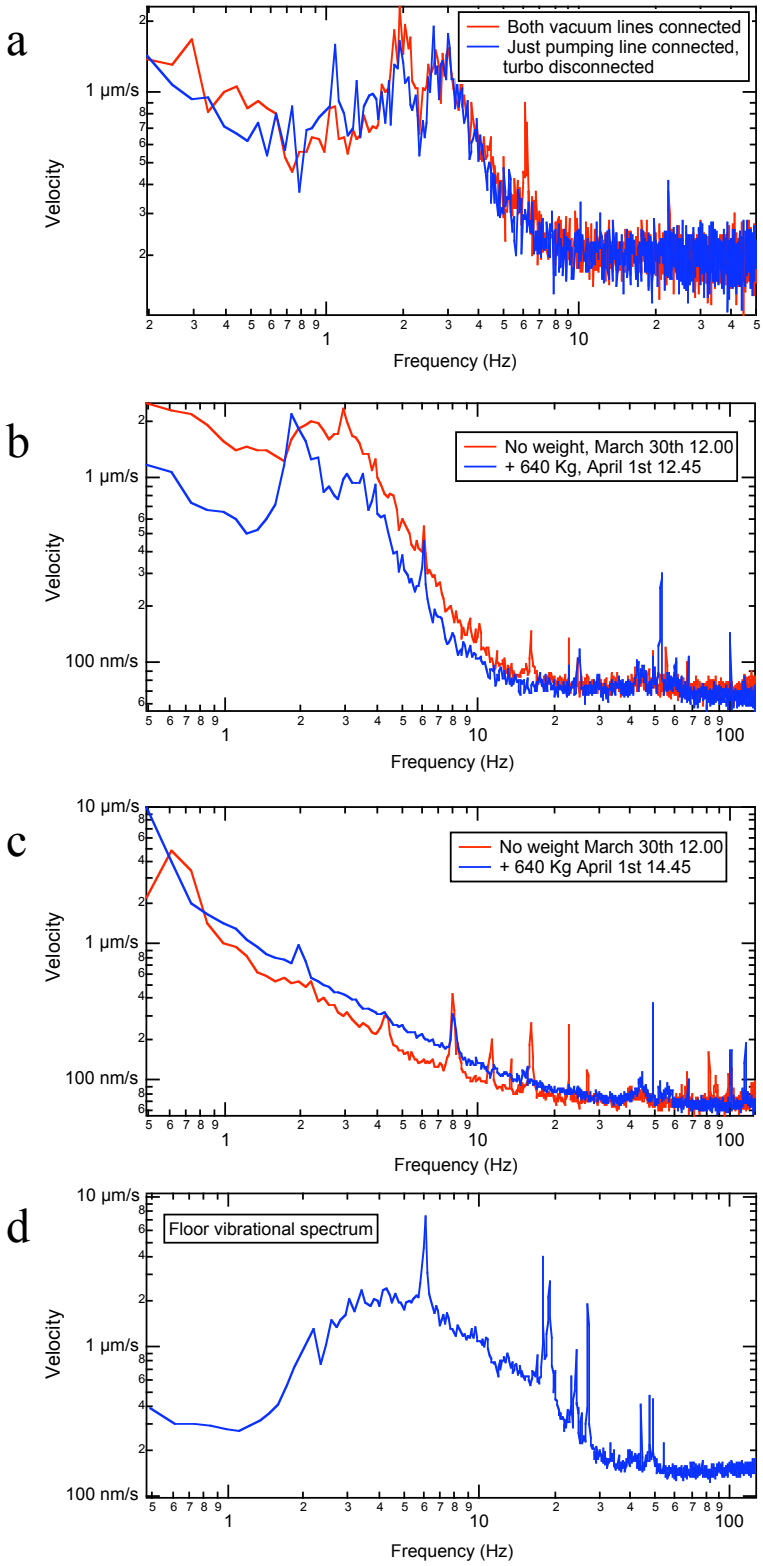

Figure A.1: (a) Vibrational noise measured on the Cryogenic STM system frame in the vertical direction, with different configurations of the pumping lines (b) Vibrational noise measured on the system frame in the vertical direction, for no added mass and 640 kg added mass (c) Vibrational noise measured on the system frame in the horizontal direction, for no added mass and 640 kg added mass (d) Vibrational spectrum of the floor in the vertical direction

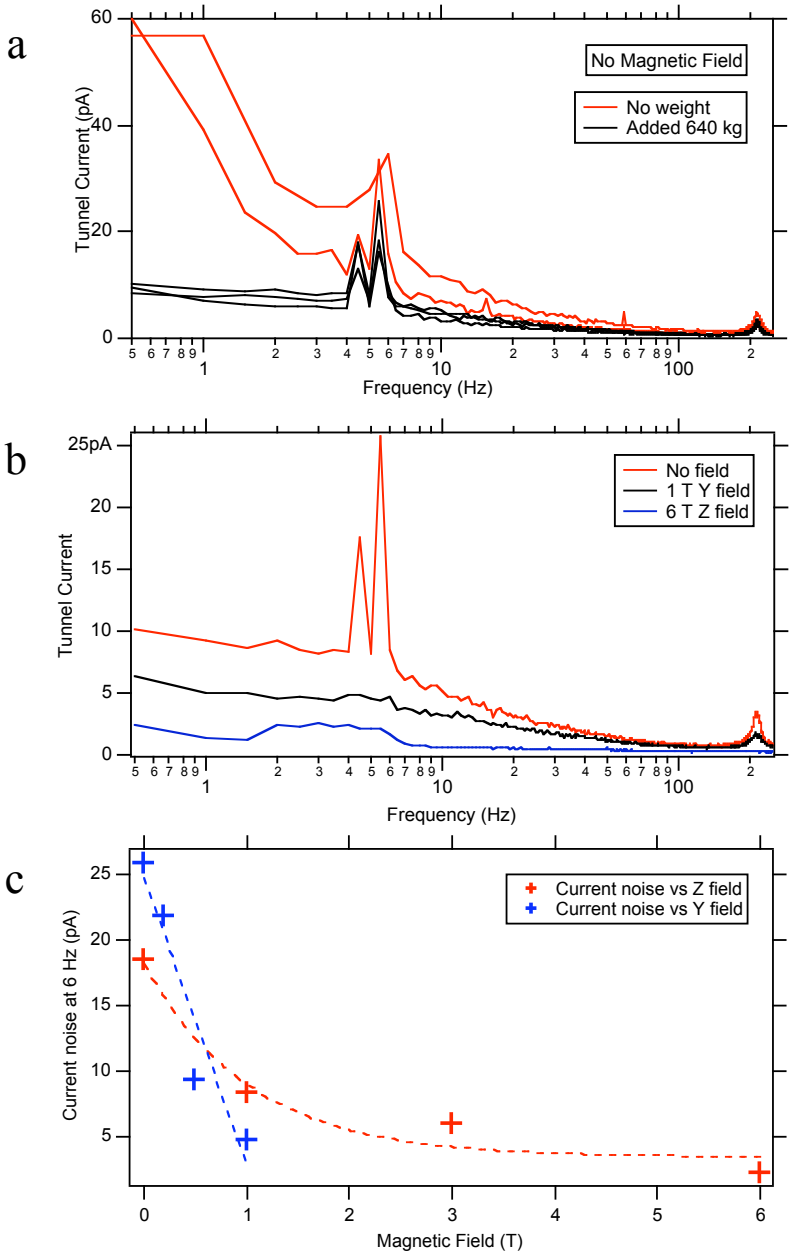

Figure A.2: (a) Frequency spectra derived from STM tunnel current, 300 pA setpoint, for no added mass and 640 kg added mass (b) Frequency spectra derived from STM tunnel current, 300 pA setpoint, for different applied fields in the Z and Y-directions, with 640 kg added mass (c) Tunnel current noise at 6 $\pm$ 0.5 Hz as a function of applied field, in the Z and Y-directions. The drop off of 6 Hz noise with field seems roughly linear for the Y-field, but saturates at high field for the Z-field: a linear guide to the eye is shown for the Y-field, and an exponential guide to the eye for the Z-field

Measurements of the vibrational spectrum of the STM system frame only provide information on how well the air damping legs are performing: the STM head also has in-vacuum spring suspension. This should provide additional vibration damping, but will also have its own resonant frequency. It is important therefore to measure the noise spectrum of the tunnel current, to determine which frequencies are being transmitted to the STM head, and whether various measures to improve the vibration performance are effective. To do this, first stable tunnelling conditions were established: usually a silicon sample surface was used. Arrays of 100 I(V) measurements were made, with the voltage set to a constant value in each I(V) spectrum. This gives a large set of data on tunnel current at fixed voltage, collected with the feedback loop off. A Fourier transform of each spectrum was made: an average was then taken of all 100 Fourier transforms to give a spectrum of tunnel current as a function of frequency. Dr. Steven Schofield wrote Igor macros to facilitate this analysis. Figure A.2a shows spectra of tunnel current as a function of frequency, for a current setpoint of 300 pA. Clear peaks are observed at 4.5 Hz and 5.5 - 6 Hz. The red curves show spectra with no weight added to the system: the black curves show spectra after 640 kg of mass was added. There is some variation but the added mass seems to significantly improve vibration performance at all frequencies below 100 Hz. Noise at 6 Hz is reduced from 34 to 26 pA. This is a relatively small decrease but indicates that further addition of mass may be beneficial. No peak is observed at 8 Hz in figure A.2a, as was seen in the vibration spectrum measured on the system frame in the horizontal direction, using the accelerometer (figure A.1c): this suggests that vibrations of the STM system in the vertical direction are transmitted more easily to the head than those in the horizontal direction.

As noted in section 3.1.4, applying a magnetic field to the STM head results in a marked decrease in low-frequency noise pickup in the tunnel current. It was decided to quantify this suppression by producing spectra of tunnel current vs. frequency for various applied fields. Figure A.2b shows tunnel current spectra, for a current setpoint of 300 pA, collected at zero field, 1 T applied in the Y-direction and 6 T applied in the Z-direction. 640 kg of mass have been added to the system. For zero applied field, the noise at 5.5 Hz has an amplitude of 26 pA: with 1 T Y-direction field applied this is reduced to 4 pA: with 6 T applied in the Z-direction this is further reduced to 2 pA. Figure A.2c shows the tunnel current noise amplitude close to 6 Hz plotted as a function of field, for Z and Y-direction fields. Although the

maximum Z-field provides twice the suppression of the 6 Hz noise as the maximum Y-field, the drop off of 6 Hz noise with field is faster for the Y-field. The 6 Hz noise is suppressed by around 50 % at 1 T Z-field, to 8 pA amplitude. This is fortuitous since it means that a 1 T field can be applied in a different directions, and a useful level of damping maintained. This means that low-noise experiments can be performed, in which the direction, but not the strength, of the applied magnetic field is varied.

In conclusion, it appears that adding mass to the Cryogenic STM system has a beneficial effect on the vibration damping performance: it may be possible to add further mass and obtain still better performance. The noise at $\approx$ 6 Hz observed in the tunnel current seems to originate from the floor, in the vertical axis: this is attenuated by a factor of ten by the existing airlegs, but this is apparently not sufficient to prevent pickup of this frequency in the tunnel current. If the addition of further mass to the existing air table is not found to provide sufficient improvement, replacing the air legs with an alternate damping system, as with the Oxford STM, may have to be considered. Active damping may be suitable as this provides improved damping performance in the 2 - 20 Hz range. Applying magnetic fields of order 1 T to the STM head results in dramatically improved vibration damping performance. This is likely due to eddy currents induced in the STM head by the applied magnetic field and vibrational motion of the head. This suggests a way to improve the vibration damping of the STM: a copper mass could be added to the head, and the magnet used at a low field to produce some eddy currents in the copper mass.

A.2 Variable Temperature Piezo Scanner Calibration for the LT-STM

For the Omicron LT-STM, extensive data for the calibration of the piezo scanners as a function of temperature was available. Si (111) was studied at 78 K and 155 K, giving absolute x, y and z calibrations at these temperatures. $PrSr_2Mn_2O_7$ was studied at a range of temperatures from 78 K to 195 K with atomic resolution, giving a good data set to determine the temperature dependence of the piezo coefficients.

The spacing of the $PrSr_2Mn_2O_7$ atomic lattice was measured at every temperature studied, using Fourier analysis. Correction factors were calculated assuming a temperature-invariant lattice spacing of 0.38535 nm [79]. The correction factor is calculated as $P(78K)/P(T)$ where $P(78K)$ is the piezo coefficient at 78 K and $P(T)$ is the coefficient at some arbitrary temperature. 78 K was used as the baseline as this is the most common operating temperature for the LT-STM, so the most calibration data is available at this temperature. The following third-order polynomial fit was made to the correction factors. This allows the piezo coefficient to be calculated for any temperature.

$$\frac{P(78K)}{P(T)} = 2.1362 - 0.0223302\,T + 1.1723 \times 10^{-4}\,T^2 - 2.3088 \times 10^{-7}\,T^3 \quad \text{(A.1)}$$

This temperature dependence is valid for the x, y and z directions since the LT-STM uses a single tube scanner for all three directions. The maximum deviation of the fit from the data is 1.4%, the average deviation is 0.8%. Since the thermal expansion coefficient of $PrSr_2Mn_2O_7$ is not known, the calculated values were checked against the ratio of $P(155K)/P(78K)$ derived from scans of Si(111) and found to agree to within 0.3% [1]. This validates the assumption that the lattice spacing of $PrSr_2Mn_2O_7$ does not change appreciably in the temperature range studied. This fit is valid for the temperature range 78 K $\leq$ T $\leq$ 195 K. For STM studies substantially outside this temperature range additional calibration data should be collected.

[1] In reality the lattice spacing of Si changes with temperature: however the thermal expansion coefficient is low, 6.9 x 10^{-7} K^{-1}at 160 K, so this can be neglected.

Table A.1 gives the piezo coefficient as a ratio of the coefficient at 78 K. Both measured values and those calculated from the polynomial fit are given. Both $P(78K)/P(T)$ and $P(T)/P(78K)$ are given for convenience. The measured values and polynomial fit for $P(78K)/P(T)$ are plotted in figure A.3. No data were collected for 220 K since atomic resolution was not achieved at this temperature: the polynomial fit has been extrapolated to this temperature.

	From PSMO data		From Fit	
T	**P(78K)/P(T)**	**P(T)/P(78K)**	**P(78K)/P(T)**	**P(T)/P(78K)**
78	1.0000	1.0000	0.9981	1.0019
95	0.8778	1.1392	0.8749	1.1430
110	0.8008	1.2487	0.7911	1.2641
125	0.7208	1.3874	0.7257	1.3780
140	0.6776	1.4757	0.6741	1.4834
155	0.6407	1.5609	0.6317	1.5830
170	0.5975	1.6735	0.5937	1.6844
195	0.5329	1.8766	0.5275	1.8956
220	No data		0.4391	2.2775

Table A.1: Piezo coefficients $P(78K)/P(T)$ and $P(T)/P(78K)$ as a function of temperature for the LT-STM, both measured and derived from the polynomial fit

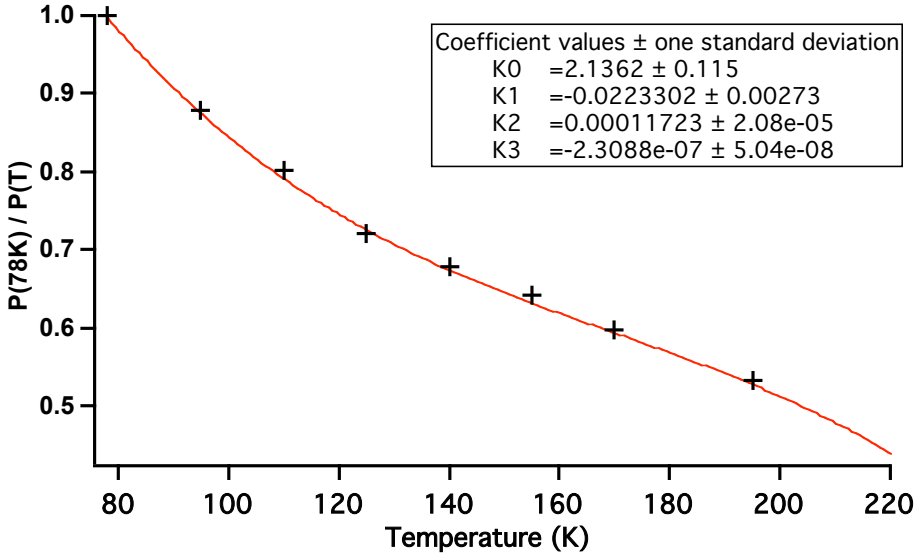

Figure A.3: Piezo coefficients $P(78K)/P(T)$ as a function of temperature for the LT-STM, plotted with the polynomial fit

A.3 Settings for the Oxford STM MATRIX Controller

The Oxford UHV STM was originally operated using a proprietary Oxford Instruments STM controller known as TOPSystem. This controller was replaced with an Omicron MATRIX SPM controller, for reasons of enhanced functionality, stability and compatibility, as noted in section 3.1.1. The MATRIX controller used with the Oxford STM requires some unique components and settings, which are documented here.

In order to supply the required signals to the Oxford piezo scanner, the piezo driver board (high voltage amplifier) in the MATRIX for the Oxford STM (PDC6) has been replaced with a modified board (PDC6 special). The output signals are modified as shown in table A.2. A jumper on the PDC special board must be changed from the default value to apply the correct polarity of Z signal. This is the polarity jumper and must be set to "−". With the polarity jumper set correctly the Z output (measured from any of the four piezo outputs) should be as follows.

- − 140 V for the tip fully forward
- + 140 V for the tip fully back.

The coarse approach motor on the Oxford STM is also wired in the opposite sense to the default value: the settings in the MATRIX remote box allow this to be corrected for. The z-direction on the remote box must be set to "+" for the coarse motor to move in the correct direction.

PDC6	PDC6 special
+ X	Z + X
− X	Z − X
+ Y	Z + Y
− Y	Z − Y
+ Z	not used

Table A.2: Outputs of standard piezo driver board PDC6 and modified PDC6 special, as fitted to the Oxford STM MATRIX controller

The MATRIX is designed to be used with Omicron's own preamplifier design: this features variable gain, and also houses the feedthrough for the bias voltage. If the bias voltage desired is less than 1 V, a signal 10 times the desired bias is sent to the preamplifier: this voltage is reduced again by a factor of 10 by a divider circuit at the preamplifier. This reduces noise pickup on the bias line between the controller and the STM for low bias voltages: the divider circuit is switched off automatically if a bias greater than 1 V is desired. For the Oxford STM we used a simple fixed gain Femto preamplifier, so for bias < 1 V a potential divider needs to be put in the bias line to achieve the correct voltage. For higher biases this divider needs to be manually removed.

Finally, in order to obtain the correct bias voltage and tunnelling current, the MATRIX software calibration settings must be changed. The Femto preamplifier has a gain of $2\text{x}10^9$ Ω, which differs from the default Omicron preamplifier. Omicron STMs normally apply an inverted bias voltage to the tip, to obtain an effective sample bias, however the Oxford STM applies the bias voltage to the sample. The MATRIX software therefore needs to be set to not invert the bias voltage to obtain the correct polarity for the Oxford STM.

Bibliography

[1] D. Argyriou, H. Bordallo, B. Campbell, A. Cheetham, D. Cox, J. Gardner, K. Hanif, A. dos Santos, and G. Strouse. Charge ordering and phase competition in the layered perovskite $LaSr_2Mn_2O_7$. *Physical Review B*, 61(22):15269–15276, Jun 1 2000.

[2] D. Argyriou, J. Mitchell, P. Radaelli, H. Bordallo, D. Cox, M. Medarde, and J. Jorgensen. Lattice effects and magnetic structure in the layered colossal magnetoresistance manganite $La_{2-2x}Sr_{1+2x}Mn_2O_7$, x = 0.3. *Physical Review B*, 59(13):8695–8702, Apr 1 1999.

[3] A. Baikalov, Y. Wang, B. Shen, B. Lorenz, S. Tsui, Y. Sun, Y. Xue, and C. Chu. Field-driven hysteretic and reversible resistive switch at the Ag-$Pr_{0.7}Ca_{0.3}MnO_3$ interface. *Applied Physics Letters*, 83(5):957–959, Aug 4 2003.

[4] W. Bao, J. Axe, C. Chen, and S. Cheong. Impact of charge ordering on magnetic correlations in perovskite (Bi,Ca)MnO_3. *Physical Review Letters*, 78(3):543–546, Jan 20 1997.

[5] A. Beck, J. G. Bednorz, C. Gerber, C. Rossel, and D. Widmer. Reproducible switching effect in thin oxide films for memory applications. *Applied Physics Letters*, 77(1):139–141, 2000.

[6] T. Becker, C. Streng, Y. Luo, V. Moshnyaga, B. Damaschke, N. Shannon, and K. Samwer. Intrinsic inhomogeneities in manganite thin films investigated with scanning tunneling spectroscopy. *Physical Review Letters*, 89(23), Dec 2 2002.

[7] S. Blundell. *Magnetism in Condensed Matter*. Oxford Master Series in Condensed Matter Physics. Oxford University Press, Great Clarendon Street, Oxford OX2 6DP, 2004.

[8] B. Campbell, R. Osborn, D. Argyriou, L. Vasiliu-Doloc, J. Mitchell, S. Sinha, U. Ruett, C. Ling, Z. Islam, and J. Lynn. Structure of nanoscale polaron correlations in $La_{1.2}Sr_{1.8}Mn_2O_7$. *Physical Review B*, 65(1), Jan 1 2002.

[9] K. Chahara, T. Ohno, M. Kasai, and Y. Kozono. Magnetoresistance in magnetic manganese oxide with intrinsic antiferromagnetic spin structure. *Applied Physics Letters*, 63(14):1990–1992, 1993.

[10] L. Chua. Memristor - the missing circuit element. *IEEE Transactions on Circuit Theory*, CT18(5):507–&, 1971.

[11] P. J. Clark and F. C. Evans. Distance to nearest neighbor as a measure of spatial relationships in populations. *Ecology*, 35(4):445–453, 1954.

[12] E. Dagotto. *Nanoscale phase separation and colossal magnetoresistance. The Physics of Manganites and Related Compounds*. Springer Series in Solid-State Sciences. Springer, 2003.

[13] E. Dagotto. Open questions in CMR manganites, relevance of clustered states and analogies with other compounds including the cuprates. *New Journal of Physics*, 7, Feb 22 2005.

[14] G. Dearnale, A. M. Stoneham, and D. V. Morgan. Electrical phenomena in amorphous oxide films. *Reports on Progress in Physics*, 33(11):1129–1191, 1970.

[15] R. Di Capua, C. Perroni, V. Cataudella, F. M. Granozio, P. Perna, M. Salluzzo, U. Scotti di Uccio, and R. Vaglio. Direct observation of spectroscopic inhomogeneities on $La_{0.7}Sr_{0.3}MnO_3$ thin films by scanning tunnelling spectroscopy. *Journal of Physics: Condensed Matter*, 18:8195–8204(10), September 2006.

[16] U. Diebold. The surface science of titanium dioxide. *Surface Science Reports*, 48(5-8):53–229, 2003.

[17] M. Fath, S. Freisem, A. Menovsky, Y. Tomioka, J. Aarts, and J. Mydosh. Spatially inhomogeneous metal-insulator transition in doped manganites. *Science*, 285(5433):1540–1542, Sep 3 1999.

[18] V. Ferrari, M. Towler, and P. Littlewood. Oxygen stripes in $La_{0.5}Ca_{0.5}MnO_3$ from ab initio calculations. *Physical Review Letters*, 91(22), November 28 2003.

[19] O. Fischer, M. Kugler, I. Maggio-Aprile, C. Berthod, and C. Renner. Scanning tunneling spectroscopy of high-temperature superconductors. *Reviews of Modern Physics*, 79(1):353, 2007.

[20] J. Freeland, K. Gray, L. Ozyuzer, P. Berghuis, E. Badica, J. Kavich, H. Zheng, and J. Mitchell. Full bulk spin polarization and intrinsic tunnel barriers at the surface of layered manganites. *Nature Materials*, 4(1):62–67, January 2005.

[21] J. B. Goodenough. Theory of the Role of Covalence in the Perovskite-Type Manganites [La, M(II)]MnO_3. *Phys. Rev.*, 100(2):564–573, Oct 1955.

[22] H. Guntherodt and R. Wiesendanger, editors. *Scanning Tunneling Microscopy I*, chapter 5. Springer-Verlag, first edition, 1994.

[23] T. Harada, I. Ohkubo, K. Tsubouchi, H. Kumigashira, T. Ohnishi, M. Lippmaa, Y. Matsumoto, H. Koinuma, and M. Oshima. Trap-controlled space-charge-limited current mechanism in resistance switching at Al/$Pr_{0.7}Ca_{0.3}MnO_3$ interface. *Applied Physics Letters*, 92(22), Jun 2008.

[24] H. F. Hess, R. B. Robinson, R. C. Dynes, J. M. Valles, and J. V. Waszczak. Scanning-Tunneling-Microscope Observation of the Abrikosov Flux Lattice and the Density of States near and inside a Fluxoid. *Physical Review Letters*, 62(2):214–216, 1989.

[25] T. Hickmott. Low-frequency negative resistance in thin anodic oxide films. *Journal of Applied Physics*, 33(9):2669, 1962.

[26] T. Ishikawa, K. Tobe, T. Timura, T. Katsufuji, and Y. Tokura. Optical study on the doping and temperature dependence of the anisotropic electronic structure in bilayered manganites: $La_{2-2x}Sr_{1+2x}Mn_2O_7$ ($0.3 \leq x \leq 0.5$). *Physical Review B*, 62(18):12354–12362, Nov 1 2000.

[27] S. Jin, T. Tiefel, M. McCormack, R. Fastnacht, R. Ramesh, and L. Chen. Thousandfold change in resistivity in magnetoresistive La-Ca-Mn-O films. *Science*, 264(5157):413–415, Apr 15 1994.

[28] T. Kimura, R. Kumai, Y. Tokura, J. Li, and Y. Matsui. Successive structural transitions coupled with magnetotransport properties in $LaSr_2Mn_2O_7$. *Physical Review B*, 58(17):11081–11084, Nov 1 1998.

[29] T. Kimura and Y. Tokura. Layered magnetic manganites. *Annual Review of Materials Science*, 30:451–474, 2000.

[30] T. Kimura, Y. Tomioka, H. Kuwahara, A. Asamitsu, M. Tamura, and Y. Tokura. Interplane tunneling magnetoresistance in a layered manganite crystal. *Science*, 274(5293):1698–1701, Dec 6 1996.

[31] M. Konoto, T. Kohashi, K. Koike, T. Arima, Y. Kaneko, T. Kimura, and Y. Tokura. Direct imaging of temperature-dependent layered antiferromagnetism of a magnetic oxide. *Physical Review Letters*, 93(10), Sep 3 2004.

[32] M. Kubota, H. Fujioka, K. Ohoyama, K. Hirota, Y. Moritomo, H. Yoshizawa, and Y. Endoh. Neutron scattering studies on magnetic structure of the double-layered manganite $La_{2-2x}Sr_{1+2x}Mn_2O_7$ ($0.30 \leq x \leq 0.50$). *Journal of Physics and Chemistry of Solids*, 60(8-9):1161–1164, Aug-Sep 1999. 7th Institute for Solid State Physics Symposium on Frontiers in Neutron Scattering Research (ISSP7), TOKYO, JAPAN, Nov 24-27, 1998.

[33] R. Kusters, J. Singleton, D. Keen, R. McGreevy, and W. Hayes. Magnetoresistance measurements on the magnetic semiconductor $Nd_{0.5}Pb_{0.5}MnO_3$. *Physica B: Condensed Matter*, 155(1-3):362 – 365, 1989.

[34] J. Li, Y. Matsui, T. Kimura, and Y. Tokura. Structural properties and charge-ordering transition in $LaSr_2Mn_2O_7$. *Physical Review B*, 57(6):R3205–R3208, Feb 1 1998.

[35] Q. Li, K. Gray, and J. Mitchell. Spin-independent and spin-dependent conductance anisotropy in layered colossal-magnetoresistive manganite single crystals. *Physical Review B*, 59(14):9357–9361, Apr 1 1999.

[36] Q. Li, K. E. Gray, H. Zheng, H. Claus, S. Rosenkranz, S. N. Ancona, R. Osborn, J. F. Mitchell, Y. Chen, and J. W. Lynn. Reentrant orbital order and the true ground state of $LaSr_2Mn_2O_7$. *Physical Review Letters*, 98(16), Apr 20 2007.

[37] C. Ling, J. Millburn, J. Mitchell, D. Argyriou, J. Linton, and H. Bordallo. Interplay of spin and orbital ordering in the layered colossal magnetoresistance manganite $La_{2-2x}Sr_{1+2x}Mn_2O_7$ ($0.5 \leq x \leq 1.0$). *Physical Review B*, 62(22):15096–15111, Dec 1 2000.

[38] H. Liu, S. Cooper, and S. Cheong. Optical study of the evolution of charge and spin ordering in the manganese perovskite $Bi_{1-x}Ca_xMnO_3$ (x > 0.5). *Physical Review Letters*, 81(21):4684–4687, Nov 23 1998.

[39] S. Liu, N. Wu, and A. Ignatiev. Electric-pulse-induced reversible resistance change effect in magnetoresistive films. *Applied Physics Letters*, 76(19):2749–2751, May 8 2000.

[40] J. Loudon, S. Cox, A. Williams, J. Attfield, P. Littlewood, P. Midgley, and N. Mathur. Weak charge-lattice coupling requires reinterpretation of stripes of charge order in $La_{1-x}Ca_xMnO_3$. *Physical Review Letters*, 94(9), March 11 2005.

[41] F. Loviat, H. M. Ronnow, C. Renner, G. Aeppli, T. Kimura, and Y. Tokura. The surface layer of cleaved bilayer manganites. *Nanotechnology*, 18(4), Jan 31 2007. International Conference on Nanoscience and Technology, Basel, Switzerland, Jul 30-Aug 04, 2006.

[42] J. Ma, D. Gillaspie, E. Plummer, and J. Shen. Visualization of localized holes in manganite thin films with atomic resolution. *Physical Review Letters*, 95(23), Dec 2 2005.

[43] G. Mariotto, S. Murphy, and I. Shvets. Charge ordering on the surface of Fe_3O_4(001). *Physical Review B*, 66(24), Dec 15 2002.

[44] A. Millis, P. Littlewood, and B. Shraiman. Double exchange alone does not explain the resistivity of $La_{1-x}Sr_xMnO_3$. *Physical Review Letters*, 74(25):5144–5147, Jun 19 1995.

[45] J. Mitra, M. Paranjape, A. Raychaudhuri, N. Mathur, and M. Blamire. Temperature dependence of density of states near the Fermi level in a strain-free epitaxial film of the hole-doped manganite $La_{0.7}Sr_{0.3}MnO_3$. *Physical Review B*, 71(9), Mar 2005.

[46] Y. Moritomo, A. Asamitsu, H. Kuwahara, and Y. Tokura. Giant magnetoresistance of manganese oxides with a layered perovskite structure. *Nature*, 380(6570):141–144, Mar 14 1996.

[47] Y. B. Nian, J. Strozier, N. J. Wu, X. Chen, and A. Ignatiev. Evidence for an oxygen diffusion model for the electric pulse induced resistance change effect in transition-metal oxides. *Physical Review Letters*, 98(14), Apr 6 2007.

[48] A. Odagawa, H. Sato, I. Inoue, H. Akoh, M. Kawasaki, Y. Tokura, T. Kanno, and H. Adachi. Colossal electroresistance of a $Pr_{0.7}Ca_{0.3}MnO_3$ thin film at room temperature. *Physical Review B*, 70(22), Dec 2004.

[49] Omicron Nanotechnology GmbH. *The LT-STM users guide, version 3.1.* Limburger Strasse 75, 65232 Taunusstein, Germany, 30 May 2008.

[50] T. Perring, G. Aeppli, T. Kimura, Y. Tokura, and M. Adams. Ordered stack of spin valves in a layered magnetoresistive perovskite. *Physical Review B*, 58(22):14693–14696, Dec 1 1998.

[51] T. G. Perring, G. Aeppli, Y. Moritomo, and Y. Tokura. Antiferromagnetic short range order in a two-dimensional manganite exhibiting giant magnetoresistance. *Physical Review Letters*, 78(16):3197–3200, Apr 1997.

[52] P. Radaelli, D. Cox, M. Marezio, and S. Cheong. Charge, orbital, and magnetic ordering in $La_{0.5}Ca_{0.5}MnO_3$. *Physical Review B*, 55(5):3015–3023, Feb 1 1997.

[53] C. Renner. *Low Temperature Scanning Tunneling Microscopy of Layered Superconductors.* PhD thesis, University of Geneva, September 1993.

[54] C. Renner, G. Aeppli, B. Kim, Y. Soh, and S. Cheong. Atomic-scale images of charge ordering in a mixed-valence manganite. *Nature*, 416(6880):518–521, Apr 4 2002.

[55] C. Renner, G. Aeppli, and H. Ronnow. Charge ordering, stripes and phase separation in manganese perovskite oxides: An STM/STS study. *Materials Science & Engineering C – Biomimetic and Supramolecular Systems*, 25(5-8, Sp. Iss. SI):775–778, Dec 2005. Symposium on Current Trends in Nanoscience - From Materials to Applications held at the 2004 EMRS Spring Meeting, Strasbourg, France, May 24-28, 2004.

[56] C. Renner and H. M. Ronnow. *Scanning Probe Microscopy*, chapter II:9: Scanning Tunneling Microscopy and Spectroscopy of Manganites. Springer New York, April 2007.

[57] S. Roessler, S. Ernst, B. Padmanabhan, S. Elizabeth, H. Bhat, F. Steglich, and S. Wirth. Polaronic state and nanometer-scale phase separation in colossal magnetoresistive manganites. *ArXiv.org*, Cond-mat:0705.4243, May 2007.

[58] S. Roessler, S. Ernst, B. Padmanabhan, S. Elizabeth, H. L. Bhat, S. Wirth, and F. Steglich. Scanning Tunneling Spectroscopy on $Pr_{0.68}Pb_{0.32}MnO_3$ single crystals. *IEEE Transactions on Magnetics*, 43(6):3064–3066, Jun 2007. 10th Joint Magnetism and Magnetic Materials Conference/International Magnetics Conference, Baltimore, MD, Jan 07-11, 2007.

[59] H. Ronnow, C. Renner, G. Aeppli, T. Kimura, and Y. Tokura. Polarons and confinement of electronic motion to two dimensions in a layered manganite. *Nature*, 440(7087):1025–1028, Apr 20 2006.

[60] A. Sawa. Resistive switching in transition metal oxides. *Materials Today*, 11(6):28–36, Jun 2008.

[61] A. Sawa, T. Fujii, M. Kawasaki, and Y. Tokura. Hysteretic current–voltage characteristics and resistance switching at a rectifying $Ti/Pr_{0.7}Ca_{0.3}MnO_3$ interface. *Applied Physics Letters*, 85(18):4073–4075, 2004.

[62] A. Sawa, T. Fujii, M. Kawasaki, and Y. Tokura. Interface transport properties and resistance switching in perovskite-oxide heterojunctions. In I. Bozovic and D. Pavuna, editors, *Strongly Correlated Electron Materials: Physics and Nanoengineering*, volume 5932 of *Proceedings of the SPIE*, pages 342–349, Jan. 2005.

[63] A. Sawa, T. Fujii, M. Kawasaki, and Y. Tokura. Interface resistance switching at a few nanometer thick perovskite manganite active layers. *Applied Physics Letters*, 88(23), Jun 5 2006.

[64] S. Seiro, Y. Fasano, I. Maggio-Aprile, E. Koller, O. Kuffer, and O. Fischer. Polaronic signature in the metallic phase of $La_{0.7}Sr_{0.3}MnO_3$ films detected by scanning tunneling spectroscopy. *Physical Review B*, 77(2), Jan 2008.

[65] S. Seiro, Y. Fasano, I. Maggio-Aprile, O. Kuffer, and O. Fischer. Homogeneous spectroscopic properties in manganite films. *Journal of Magnetism and Magnetic Materials*, 310(2, Part 1):e243 – e245, 2007. Proceedings of the 17th International Conference on Magnetism, The International Conference on Magnetism.

[66] R. Seshadri, M. Hervieu, C. Martin, A. Maignan, B. Domenges, B. Raveau, and A. Fitch. Study of the layered magnetoresistive perovskite $La_{1.2}Sr_{1.8}Mn_2O_7$ by

high-resolution electron microscopy and synchrotron X-ray powder diffraction. *Chemistry of Materials*, 9(8):1778–1787, Aug 1997.

[67] R. Seshadri, C. Martin, A. Maignan, M. Hervieu, B. Raveau, and C. Rao. Structure and magnetotransport properties of the layered manganites $RE_{1.2}Sr_{1.8}Mn_2O_7$ (RE=La, Pr, Nd). *Journal of Materials Chemistry*, 6(9):1585–1590, Sep 1996.

[68] R. Shannon. Revised effective ionic radii and systematic studies of interatomic distances in halides and chalcogenides. *Acta Crystallographica Section A*, 32(Sep 1):751–767, 1976.

[69] K. Shono, H. Kawano, T. Yokota, and M. Gomi. Origin of negative differential resistance observed on bipolar resistance switching device with $Ti/Pr_{0.7}Ca_{0.3}MnO_3/Pt$ structure. *Applied Physics Express*, 1(5), May 2008.

[70] D. B. Strukov, G. S. Snider, D. R. Stewart, and R. S. Williams. The missing memristor found. *Nature*, 453(7191):80–83, 2008.

[71] Y. Su, C. Du, P. Hatton, S. Collins, and S. Cheong. Charge ordering and the related structural phase transition in single-crystal $(Bi_{0.24}Ca_{0.76})MnO_3$. *Physical Review B*, 59(18):11687–11692, May 1 1999.

[72] R. Suryanarayanan, G. Dhalenne, A. Revcolevschi, W. Prellier, J. Renard, C. Dupas, W. Caliebe, and T. Chatterji. Colossal magnetoresistance and re-entrant charge ordering in single crystalline two layer Mn perovskite $LaSr_2Mn_2O_7$. *Solid State Communications*, 113(5):267–271, 1999.

[73] Y. Takagi, K. Hanai, H. Hosokawa, H. Ishibashi, T. Ishikawa, A. Saito, Y. Kuwahara, and Y. Taguchi. Roughening Surface of Layered Manganite $La_{0.5}Sr_{1.5}MnO_4$ by Scanning Tunneling Microscopy. *Japanese Journal of Applied Physics*, 47(8, Part 1):6456–6458, August 2008.

[74] Y. Takamura, R. Chopdekar, J. Grepstad, Y. Suzuki, A. Marshall, A. Vailionis, H. Zheng, and J. Mitchell. Thickness-dependent properties of (110)-oriented $La_{1.2}Sr_{1.8}Mn_2O_7$ thin films. *Journal of Applied Physics*, 99(8), Apr 15 2006.

[75] Y. Takamura, J. Grepstad, R. Chopdekar, Y. Suzuki, A. Marshall, H. Zheng, and J. Mitchell. Structural, magnetic, and electronic properties of (110)-

oriented epitaxial thin films of the bilayer manganite $La_{1.2}Sr_{1.8}Mn_2O_7$. *Applied Physics Letters*, 87(14), Oct 3 2005.

[76] J. Tersoff and D. R. Hamann. Theory and application for the scanning tunneling microscope. *Phys. Rev. Lett.*, 50(25):1998–2001, Jun 1983.

[77] S. M. Thompson. The discovery, development and future of GMR: The Nobel Prize 2007. *Journal of Physics D: Applied Physics*, 41(9):093001 (20pp), 2008.

[78] Y. Tokunaga, T. Lottermoser, Y. Lee, R. Kumai, M. Uchida, T. Arima, and Y. Tokura. Rotation of orbital stripes and the consequent charge-polarized state in bilayer manganites. *Nature Materials*, 5(12):937–941, Dec 2006.

[79] Y. Tokunaga, T. J. Sato, M. Uchida, R. Kumai, Y. Matsui, T. Arima, and Y. Tokura. Versatile and competing spin-charge-orbital orders in the bilayered manganite system $Pr(Sr_{1-y}Ca_y)_2Mn_2O_7$. *Physical Review B*, 77(6), Feb 2008.

[80] M. Uehara, S. Mori, C. Chen, and S. Cheong. Percolative phase separation underlies colossal magnetoresistance in mixed-valent manganites. *Nature*, 399(6736):560–563, Jun 10 1999.

[81] J. Volger. Further experimental investigations on some ferromagnetic oxidic compounds of manganese with perovskite structure. *Physica*, 20(1-6):49 – 66, 1954.

[82] R. Von Helmolt, J. Wecker, B. Holzapfel, L. Schultz, and K. Samwer. Giant negative magnetoresistance in perovskitelike $La_{2/3}Ba_{1/3}MnO_x$ ferromagnetic films. *Phys. Rev. Lett.*, 71(14):2331–2333, Oct 1993.

[83] R. Wiesendanger, editor. *Scanning Probe Microscopy and Spectroscopy*, chapter 1. Cambridge University Press, first edition, 1994.

[84] G. Xiong, Q. Li, H. Ju, S. Bhagat, S. Lofland, R. Greene, and T. Venkatesan. Giant magnetoresistive memory effect in $Nd_{0.7}Sr_{0.3}MnO_z$ FILMS. *Applied Physics Letters*, 67(20):3031–3033, Nov 13 1995.

[85] Y. Xu, K. Steenbeck, P. Das, J. Wei, M. Koblischka, and U. Hartmann. Local electronic properties of manganite films studied by STM/STS under ambient conditions. *Journal of Magnetism and Magnetic Materials*, 272(Suppl. 1):E875–E876, May 2004.